Computational Modeling of Variations in Female Anatomy to Elucidate Biomechanical Mechanisms of Pelvic Organ and Tissue Functions

by

Megan R. Routzong

B.S. Biomedical Engineering, University of Rochester, 2016

Submitted to the Graduate Faculty of

the Swanson School of Engineering in partial fulfillment

of the requirements for the degree of

Doctor of Philosophy

University of Pittsburgh

2021

UNIVERSITY OF PITTSBURGH

SWANSON SCHOOL OF ENGINEERING

This dissertation was presented

by

Megan R. Routzong

It was defended on

July 15, 2021

and approved by

Raffaella De Vita, Ph.D., Professor, Department of Biomedical Engineering and Mechanics, Virginia Tech

Spandan Maiti, Ph.D., Associate Professor, Departments of Bioengineering and Mechanical Engineering & Materials Science

Pamela A. Moalli, M.D., Ph.D., Professor, Department of Obstetrics, Gynecology & Reproductive Sciences

Anne M. Robertson, Ph.D., Departments of Mechanical Engineering & Materials Science and Bioengineering

Dissertation Director: Steven D. Abramowitch, Ph.D., Associate Professor, William Kepler Whiteford Faculty Fellow, Departments of Bioengineering and Obstetrics, Gynecology & Reproductive Sciences

Computational Modeling of Variations in Female Anatomy to Elucidate Biomechanical Mechanisms of Pelvic Organ and Tissue Functions

Megan R. Routzong, PhD

University of Pittsburgh, 2021

Pelvic floor disorders affect roughly one third of women over 50, reducing quality of life by causing pain/discomfort and/or emotional distress. These very personal and often embarrassing conditions have frequently been attributed to reduced mechanical integrity of pelvic tissues. The mechanics of female pelvic organs and tissues play a critical role in the maintenance of pelvic function, with shape and structure serving as the main drivers and indicators of biomechanical function.

For the past century, researchers have claimed that too little is known about female pelvic floor anatomy and its variation across individuals, yet its shape, soft tissue behavior, and muscle structure variability have yet to be robustly quantified. With modern computational tools and resources, we can quantify that variation and establish models that represent a broad population, rather than one individual or an exclusive cohort of women. Therefore, we aimed to quantify female anatomic variation and elucidate the relationships between that variation and female pelvic organ/tissue (dys)function.

In aim 1, statistical shape modeling (SSM) and dynamic endovaginal ultrasound established trends between urethral shape, motion, and stress urinary incontinence. Combined with a sensitivity analysis of simulated urethral passive closure, this identified the most influential tissue material properties and highlighted the importance of more robust quantification of their mechanical properties. In aim 2, SSM described bony pelvis and pelvic floor shape variation across pregnant women. From this, new, non–patient–specific geometries were generated as inputs to simulations of childbirth. This resulted in numerous finite element models that evaluated the influence of shape and pregnancy–induced remodeling on the biomechanics of vaginal birth. In aim 3, SSM and photogrammetry were utilized to define variation in female pelvic anatomy and muscle structure across an asymptomatic population of women. Differences between nulliparous (have never given birth), late pregnant,

and parous (have given birth) anatomies were identified, while photogrammetry defined variation in muscle fascicle orientations. These aims demonstrate how shape can be indicative of disease progression or tissue remodeling and influence biomechanical events, while providing critical data on anatomical variation that will improve future computational models of female pelvic floor biomechanics.

Table of Contents

List of Tables

List of Figures

Preface

The time I've spent earning my doctorate degree from the University of Pittsburgh was made enjoyable and enriching by the friends, family, and colleagues who have mentored, guided, and supported me throughout the past 5 years. I've learned and grown so much and any and all of my accomplishments may also be credited to those who have assisted me with each research project, conference abstract, manuscript, fellowship application, etc. I couldn't have done any of it alone.

First and foremost, I'd like to thank my PhD advisor and mentor, Dr. Steve Abramowitch. I didn't know exactly what I was looking for in an advisor when I applied to graduate school, but I am extremely lucky as Steve turned out to be the best advisor I could have asked for. He has always given me enough freedom to pursue my own research ideas, and without that freedom I may not have gained the confidence necessary to perform research independently. He provides feedback to make my research better without being harsh, and taught me the importance of communicating research ideas both visually and verbally. Most importantly, he made getting a PhD fun. My experiences in Steve's lab have made me realize how passionate I am about my research and that I have the skills required to pursue that research through a career in academia.

If it were not for Dr. Amy Lerner, I may not have gone to graduate school at all. As my undergraduate academic and research advisor at the University of Rochester, she played a critical role in my initial exposure to research and computational biomechanics, teaching me many of the basics of both that I still employ to this day. She was incredibly supportive as I went through one of the hardest times in my life, and that support meant the world to me (and still does). Amy has always been in my corner. She has supported me throughout my graduate journey and I know she will continue to do so as I take this next step in my education and career.

I must also thank the clinicians who make my research possible. Dr. Pamela Moalli (at Magee-Womens Research Institute and the University of Pittsburgh) provided my first exposure to Urogynecology when I attended my first clinical lab meeting during my first summer

at Pitt. She has taught me so much about the clinical aspects of our research and helped me to understand the clinical significance and implications of our findings. Dr. Ghazaleh Rostaminia (at Northshore University HealthSystem and the University of Chicago) welcomed me with open arms the first time I met her at an AUGS meeting in Chicago and made me feel so much more comfortable as I presented at my first clinical conference. Ghazaleh is so enthusiastic about her research and that enthusiasm is contagious, spreading to those she works with. Dr. Marianna Alperin (at the University of California San Diego) has advocated for me and rooted for my success from the moment I first met her at the World Congress of Biomechanics in Dublin. She took me under her wing and for that I am grateful. I am so excited to begin my postdoc under her mentorship. I'd also like to acknowledge the clinical fellows who have been a source of friendship and support; Drs. Amanda Artsen and Lindsey Burnett. Though they did not contribute to the research in my dissertation, we have collaborated on other projects and I look forward to working with them more in the future.

It would be remiss not to acknowledge my dissertation committee members who have made all of this possible: Drs. Raffaella De Vita, Spandan Maiti, Pamela Moalli, Anne Robertson, and Steve Abramowitch. In addition to other roles they've served (e.g., collaborator, professor, mentor, etc.), their contributions to my dissertation research were invaluable and I truly appreciate their support over the past few years. They helped to make this dissertation possible.

I'd also like to thank my labmates, undergraduate mentees, and colleagues who have been a source of support both in and out of the lab. Specifically, I'd like to acknowledge Shaniel Bowen, who joined the lab the year after me and has been a good friend ever since, and Liam Martin, who started out as my undergraduate mentee before joining the lab last year as a PhD student and contributed to several of the studies in my dissertation. I promised to acknowledge him as my most outstanding mentee, a title well deserved.

And finally, I'd like to conclude this by thanking my family—the people who have loved, supported, and encouraged me throughout this crazy journey and before I'd ever even thought of going to graduate school. First, my fiancé's family—his mother, Jean, father, Bill, and sister, Kendra—for the laughs and fun we've shared and for always treating me like family. Second, my siblings: Christina, Rachel, Colt, Luke, and Daniel. I appreciate my

little brother, Luke, showing an interest in and even reading some my research and Rachel, as my older twin sister, has quite literally always been there for me. Third, my parents. My dad, Doug, for always encouraging me to do what I love, and my mom, Lori, for providing me with every opportunity to pursue my interests, passions, and dreams. As a nurse, my mom introduced me to the field of medicine. She passed away while I was an undergraduate, but her memory continues to motivate and inspire me. I dedicate this dissertation to her. And finally, I'd like to thank my fiancé, Robbie (a.k.a. Dr. Robert William Gregg). In addition to his unconditional love and support, he was my comrade and companion as we both completed our PhDs from home during a global pandemic.

1.0 Introduction

1.1 Female Pelvic Anatomy

1.1.1 Bony Pelvis

The bony pelvis is composed of the sacrum, coccyx, and the left and right innominate bones—formed by the fusion of the pubis, ischium, and ilium and more commonly known as the hip or pelvic bones (Figure 1.1). The pubis is the most anterior and medial region of the innominate bone. At the most anterior point, there is a gap between the left and right pubis filled by an oval shaped, fibrocartilaginous disc, the pubic symphysis (also referred to as the symphysis pubis). This joint widens during pregnancy by roughly 3–7 mm, though there is substantial variability across individuals as pubic symphysis widths have been shown to range from 3–20 mm in women immediately following term vaginal childbirth with an intrapubic width greater than 10 mm being considered pathologic [23, 177]. It is generally believed that this widening may be the source of the symphyseal pain experienced by many pregnant women, which resolves in only 1/5 of cases within 6 months postpartum [23].

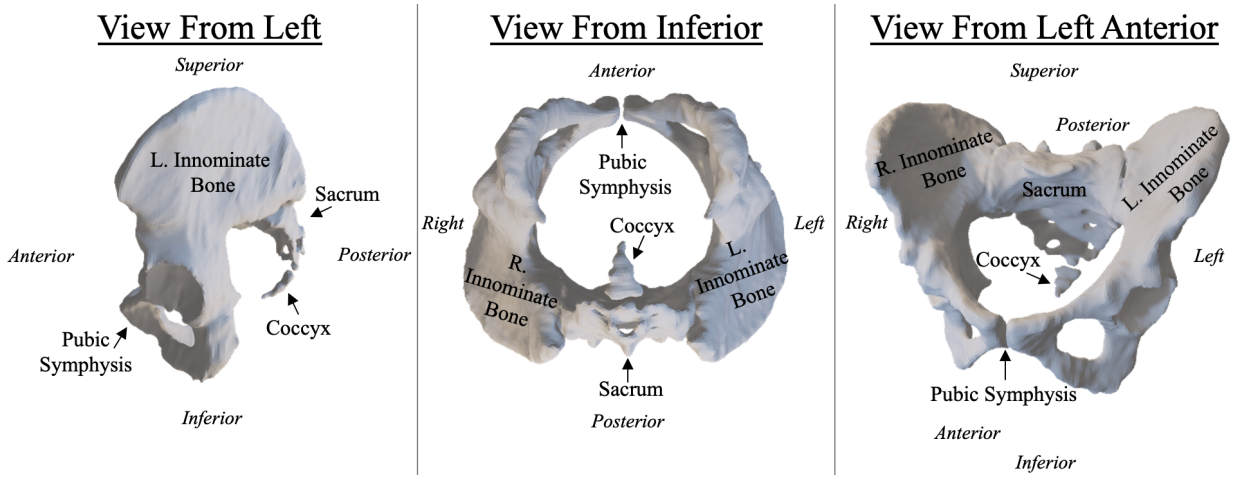

Figure 1.1: An example female bony pelvis shown from three views with relevant anatomy labelled and anatomical directions indicated (italic text). The far left depicts a pelvis from a sagittal perspective, the middle from an axial perspective, and the right from an angled perspective.

Extending laterally from the pubic symphysis are the superior and inferior pubic rami comprising the remaining sections of the pubis, the most anterior region of the innominate bones (see the left anterior view in Figure 1.1). The superior pubic rami run superiorly, posteriorly, and laterally from the pubic symphysis towards the acetabulum—the round, concave region of the innominate bones where the pubis, ischium, and ilium coalesce—also known as the socket of the hip joint where the femoral head meets the bony pelvis. The inferior pubic rami run inferiorly, posteriorly, and laterally from the pubic symphysis towards the ischial rami, forming the triangular shaped subpubic arch. A common measure is the subpubic arch angle, the angle formed by the left and right inferior pubic rami at the pubic symphysis. This angle has been used to study pregnancy and childbirth, with studies finding that a narrower subpubic arch is associated with operative birth/unplanned obstetric intervention [74, 75]. This suggests that a wider subpubic arch may better accommodate passage of the fetus during childbirth, resulting in more favorable birth outcomes.

Posteriorly, the inferior pubic rami transition into the ischium, the most inferior region of the innominate bones. Inferiorly, the inferior pubic ramus transitions into the ischial ramus, together referred to as the ischiopubic ramus (see the left anterior view in Figure 1.1). The superior pubic ramus and ischial ramus meet posteriorly at the acetabulum, forming the obturator foramen—the round hole/opening in the innominate bone allowing passage of nerves and blood vessels from the pelvis into the lower limb. The most medial point of each ischium lies at the tip of the medial and posterior pointing protrusion known as the ischial spine (see the inferior view in Figure 1.1). The left and right ischial spines are important pelvic floor muscle insertion sites and the distance between them is referred to as the interspinous distance.

The most posterior region of the innominate bone is the ilium. Its most prominent landmark is the curved superior edge, referred to as the iliac crest (see the left view in Figure 1.1). When moving anteriorly down the crest, the first landmark is the anterior superior iliac spine—the large "bump"—and then the anterior inferior iliac spine is the smaller convex curve inferior to the first. When moving posteriorly from the top of the iliac crest, the first landmark is the posterior superior iliac spine—the most posterior point on the ilium—then the posterior inferior iliac spine—the small convex curve inferior and anterior

to the previous landmark. The large concave curve located in between the iliac crest and ischial spine is the greater sciatic notch. These notches sit just anterior to each sacroiliac joint—where the sacrum meets the left and right ilium to form the only articulations between the innominate bones and the sacrum (see the left anterior view of Figure 1.1).

The sacral wings span from the sacroiliac joints and meet midsagittaly at the sacral promontory (anteriorly and superiorly) and the median sacral crest (posteriorly). The sacral promontory is the convex edge spanning from left to right at the superior sacral surface and forms the bottom of the lumbosacral joint and the anterior, superior edge of the first sacral vertebra. It is an important anatomical landmark for surgeons, particularly during pelvic organ prolapse surgeries—such as a sacrocolpopexy [136]. Inferior to the first sacral vertebra are the second through fifth sacral vertebrae and the sacral foramina—the round holes between the vertebrae that blood vessels and nerves pass through. The most inferior point of the sacrum is the apex, which forms the superior surface of the sacrococcygeal joint. The coccyx is the most mobile of the pelvic bones as it is able to pivot anteriorly–posteriorly about the sacrococcygeal joint. This motion can be observed via dynamic pelvic MRI during increases in intraabdominal pressure and vaginal childbirth [12] and has important implications for the pelvic floor muscles attached to the coccyx.

1.1.2 Muscles and Connective Tissues

The pelvic floor is composed of muscles and connective tissues that are highly interconnected, together spanning from pubis along the medial surfaces of the innominate bones to the coccyx and sacrum posteriorly. These structures serve to mechanically support the pelvic organs and allow for normal, physiologic function. Baseline muscle tone contributes to the rest configuration of not only the pelvic floor, but the pelvic viscera as well. Meanwhile, relaxation of these muscles is often necessary for physiologic events, such as defecation. Damage to and/or weakening of the pelvic floor is associated with the development of pelvic floor disorders.

The largest muscle group of the pelvic floor is the levator ani (Figure 1.2). For the majority of the past century, the levator ani were defined as being composed of the iliococcygeus,

pubococcygeus, and puborectalis [183]. In the 1970s, the term pubovisceral muscle (also referred to as the puboviscerals) was introduced to better represent the smaller muscles running from the pubis to pelvic viscera (e.g., the puboanalis) [107]. Additionally, there is still debate over the appropriateness of using the name "pubococcygeus" as many claim that no fibers run directly from the pubis to the coccyx. Therefore, in this work, we will define the levator ani as being composed of the iliococcygeus—which runs between the ilium and coccyx—and the puboviscerals—which broadly refers to muscles that attach to the pubis, such as the puborectalis and puboanalis. It should be noted that some fibers of the puboviscerals insert into the external anal sphincter. The iliococcygeus is the more posterior of the levator ani, while the puboviscerals is more anterior and medial.

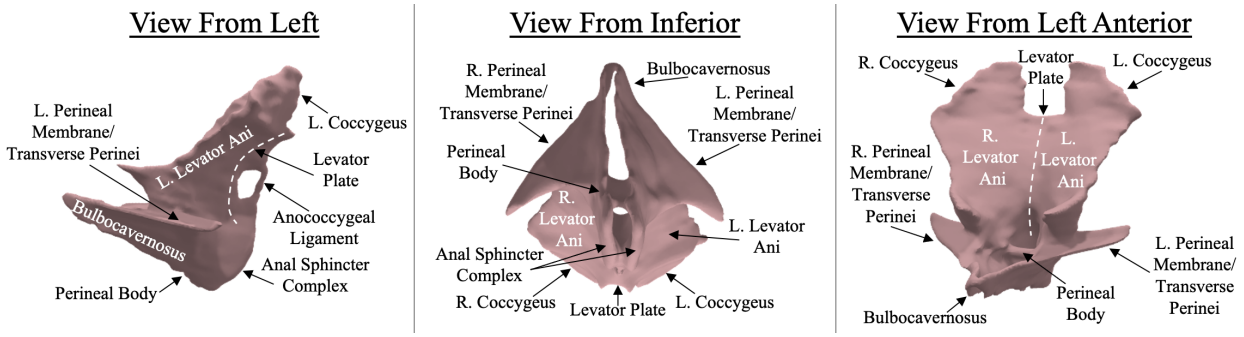

Figure 1.2: An example female pelvic floor muscle complex shown from three views with relevant anatomy labelled. This complex includes both muscles and connective tissues. The far left depicts the musculature from a sagittal perspective, the middle from an axial perspective, and the right from an angled perspective.

Where the pubovisceral muscles attach to the left and right pubis is referred to as their entheses, which is an important point of attachment and common site of injury following vaginal childbirth. In one cohort of 160 women giving birth vaginally for the first time, 18% had a pubovisceral muscle injury [57]. The medial opening in the levator ani where the urethra, vagina, and rectum reside is referred to as the levator hiatus. The minimal levator hiatus is commonly quantified via the anterior–posterior diameter, transverse diameter, and cross–sectional area. These measures have been used to quantify changes in the levator ani during pregnancy and with parity [94, 179, 180]. The levator plate (sometimes referred to as the anococcygeal raphe) is the midsagittal, posterior region of aponeurosis where the left and right sides of the levator ani coalesce. The levator plate runs from the tip of

the coccyx to the external anal sphincter and is commonly quantified via the levator plate angle, which has been associated with pelvic floor disorders and dysfunction [87, 162]. For example, the curvature of the levator plate has been shown to decrease and its position to be more posterior in women with obstructed defecation compared to controls at rest and peak evacuation—indicating it plays an important role in pelvic floor support [168].

Posterior to the iliococcygeus is the coccygeus muscles, which connect the ischial spines and coccyx. The more superior portions of the coccygeus may reach and attach to the very bottom of the sacrum. In many studies, the coccygeus muscles are not considered as part of the pelvic floor, therefore these muscles are rarely studied compared to the rate at which research is conducted on the levator ani. The sacrococcygeal joint (in between the sacrum and coccyx) allows for a fair amount of coccygeal motion about the sacrum, which has implications for the attached coccygeus muscles and surrounding muscles and connective tissues. If significant coccyx motion is present, then the coccygeus muscles and likely the closest portion of the levator ani are deforming with that motion.

The anococcygeal ligament runs from the tip of the coccyx to the anal sphincter complex superficial to and separated by fat from the levator plate. Note that though the levator plate may be referred to as the anococcygeal raphe, it is distinct from the anococcygeal ligament. The anal sphincter complex is composed of the external anal sphincter (striated muscles) and the internal anal sphincter (smooth muscles) that envelop the anus.

Anterior to the anal sphincter complex and running between the right and left sides of the most superficial portion of the puboviscerali is the perineal body. This divides the inferior region of the levator hiatus, with the anterior area occupied by the urethra and vagina being referred to as the urogenital hiatus and the rectum running posterior to the perineal body. This is a region of fibromuscular tissue composed of 3 layers of varying fiber orientations as it serves as a point of intersection for many surrounding muscles [106, 175]. It separates the superficial regions of the vagina and anus and is commonly torn during vaginal delivery. Approximately 94% of women have a perineal body tear after giving birth for the first time vs 66% of parous women (those who have given birth previously) after a subsequent childbirth [173].

The levator ani are immediately deep to a group of tissues referred to collectively as the superficial muscles and connective tissues. The bulbocavernosus muscle intersects with the perineal body posteriorly, runs lateral to the vagina and urethra on both sides, and wraps around the clitoral head anteriorly. It is held to the front of the pubic symphysis by the clitoral ligament. Spanning from the bulbocavernosus muscle to the inferior ischiopubic rami are the superficial and deep transverse perineal muscles. The superficial transverse perinei also intersect with the perineal body. The perineal membrane, a thin layer of connective tissue, also spans from bulbocavernosus to inferior ischiopubic rami immediately deep to the transverse perinei. Finally, the ischiocavernosus muscle runs from the posterior portion of the left and right ischiopubic rami along the bone to the clitoris and anterior portion of the bulbocavernosus muscle. Due to their relatively small size, difficulty to segment, and assumed insignficiant mechanical contribution, research on these tissues is scant in comparison to the larger levator ani [167].

The pelvic floor is one of the most complex systems of muscles and connective tissues in the entire body. Being so interconnected, dysfunction or defect in one muscle or connective tissue may have far reaching effects on the entire pelvic floor muscle complex. Severe enough dysfunction of the pelvic floor muscles and connective tissues will ultimately affect the physiologic function of the surrounding pelvic viscera.

1.1.3 Viscera

Organs that reside in the female pelvis include the urethra, vagina, and anorectum (a term encompassing the anus and rectum). The bladder and uterus may be considered both pelvic and abdominal as they can reside in both anatomical regions, especially when the bladder is full or the when uterus is enlarged (e.g., in late pregnancy) (Figure 1.3).

The urethra and bladder are the most anterior of these structures, with the urethra located inferiorly to the bladder. The urethra is positioned closely to the pubic symphysis. At the superior urethra there is a fat filled pocket between the urethra and pubic symphysis referred to as the space of Retzius. The bladder neck is the region of the urethra closest

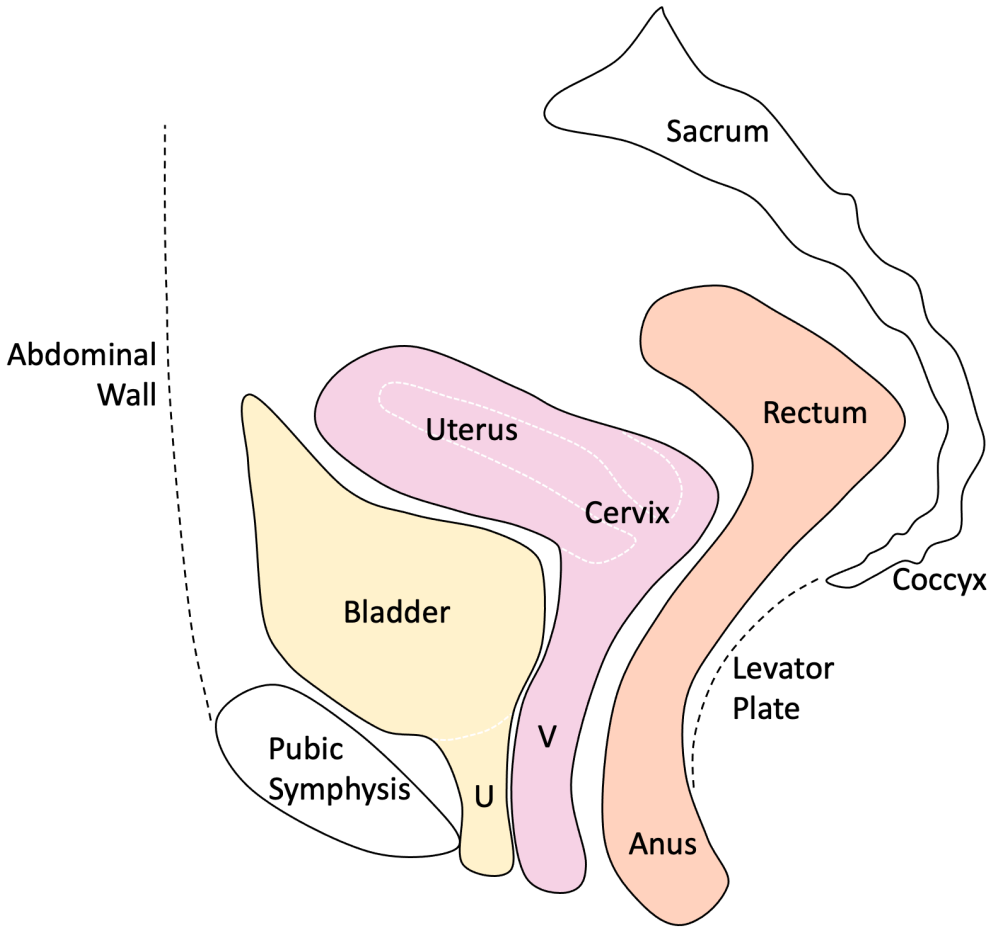

Figure 1.3: An illustration of the pelvic organs in the midsagittal plane with the anterior direction being to the left and the posterior to the right. In addition to the organs and tissues explicitly labelled, the urethra (U) and vagina (V) are also depicted.

to the bladder. The bladder is held to the abdominal wall by the median umbilical ligament, mechanically supporting the anterior superior bladder. The posterior bladder is supported by the uterus and its suspensory ligaments.

The uterus is typically positioned over the bladder, angled anteriorly while the superior vagina usually points posteriorly. In roughly 18% of women, the uterus is retroverted, meaning it points towards the sacrum and rectum instead of towards the abdominal wall [84]. The uterus is suspended to the sacrum via uterosacral ligaments located at the region of the uterus closest to the cervix. The uterus opens to the vagina via the cervix—a collagenous

structure able to dilate when necessary, such as during vaginal childbirth. The cervix and vaginal apex (the superior region of the vagina) are supported via lateral attachments to the pelvic sidewall—the cardinal ligaments. The vagina is positioned between the urethra and rectum and has three defined levels of support: level 1) the uterosacral and cardinal ligaments, level 2) lateral paravaginal attachments to the pelvic sidewall, and level 3) the superficial portion of the levator ani, the perineal body, the perineal membrane, the bulbocavernosus muscles, and the transverse perinei. Inferior to the vagina from the mid-vagina to apex is a layer of fascia referred to as the rectovaginal septum. Inferior to that is the perineal body, separating the vaginal introitus and anus.

The anorectum is supported posteriorly by the levator plate and levator ani and, more superiorly, by the sacrum and coccyx. Laterally it is also supported by the levator ani and attachments to the pelvic sidewall via the lateral rectal ligaments. The anus is enveloped by the external anal sphincter.

1.1.4 Gaps in Knowledge

Though the field of women's health has progressed in recent decades, it still falls behind many other clinical areas. The location, function, and even existence of many pelvic tissues are still being debated while frequent changes in terminology and definitions make it difficult to assess which tissues' anatomy and functions have been determined and defined with widespread confidence and which have yet to be validated. For example, as discussed previously, there is still an ongoing debate concerning the use of the term pubovisceralis and which muscles it encompasses. Over the past century, many different terms have been used to define the same origin–insertion pairs of various female pelvic floor muscles, contributing to this confusion and lack of consensus [95]. This same complaint about numerous and conflicting anatomical definitions to describe the same female pelvic floor tissues and subdivisions was also made by Smith in 1923 [183]. Smith highlighted that this was a particular issue for the female perineum and partially attributed this problem to the variability across individual women [183]. This emphasizes the importance of understanding variation in female pelvic floor anatomy, especially when generating definitions meant to reasonably approximate most

women. The advent of more powerful computational tools, improved clinical imaging, and the ability to construct larger digital patient databases in the past two decades combined with the growing number of engineers entering the field will hopefully end this 100 year old problem plaguing the study of female pelvic anatomy.

1.2 Female Pelvic Organ Functions and Pelvic Floor Disorders

1.2.1 Pelvic Floor Disorders Overview

Approximately a quarter of all women in the US have at least one pelvic floor disorder and this prevalence increases with age as roughly 32% of women in their 50s and 50% of women in their 80s have a pelvic floor disorder [126, 135, 198]. Pelvic floor disorders encompass conditions such as urinary incontinence, fecal incontinence, and pelvic organ prolapse. The presentation of a pelvic floor disorder may be structural, resulting from defects in pelvic floor tissues (e.g., levator avulsion), and/or functional, resulting from muscle/nerve dysfunction (e.g., reduced striated muscle contractile ability). Though not typically fatal, these conditions have a significant negative impact on quality of life, commonly resulting in physical, mental/emotional, and social side effects.

1.2.2 Urination and Urinary Incontinence

Urination is the process in which the bladder and urethra expel urine from the body. The bladder must also store urine until urination, expanding as the volume of urine that needs to be stored increases. During storage, the urethral lumen must remain closed to prevent leakage of urine, even in the presence of increased intra-abdominal pressure (such as during coughing). Urinary incontinence is a term encompassing disorders that result in involuntary leakage of urine.

Though bladder dysfunction, such as overactive bladder, can result in urinary incontinence, this work will focus on the urethra. Assuming normal bladder function, the urethra will use active and passive mechanisms to prevent leakage. Active mechanisms include stri-

ated and smooth muscle contraction that maintain urethral pressure so that urine does not exit the bladder and enter the urethra. The surrounding levator ani can also contract, squeezing the urethra and closing the lumen [54]. Passive closure mechanisms refer to structures and/or events that close the urethral lumen without or regardless of active muscle contraction. The pelvic floor muscles and connective tissues also contribute to passive closure, influencing urethral motion and deformation during increases in intra-abdominal pressure. This will be discussed extensively in Chapter 3.

In order to better understand urinary incontinence, researchers have taken steps to describe in detail both active and passive mechanisms of urinary continence. Existing theories include the hammock, integral, and active closure theories and the concepts of passive transmission and voluntary muscle contraction proposed by Enhorning [54, 55, 63, 146]. These theories describe different ways in which compromised mechanical integrity of urethral support structures or reduced urethral active muscle contractile ability may lead to urinary incontinence, presenting as either urethral hypermobility or intrinsic sphincter deficiency, respectively.

Approximately 16-17% of women have urinary incontinence [135, 198]. Vaginal childbirth, especially an operative delivery, is associated with urinary incontinence in comparison to non-emergency Cesarean delivery [80]. At 12 weeks postpartum, roughly 45% of women who had just given birth vaginally for the first time had urinary incontinence, with the rate of urinary incontinence being significantly influenced by birthing position [174].

Initially, conservative treatment should be considered for urinary incontinence. Conservative treatment strategies include pelvic floor muscle therapy/training (which can be performed with or without biofeedback), insertion of a pessary designed specifically for urinary incontinence, and training to use the Knack maneuver to prevent leakage [70, 130, 154]. These methods are meant to build pelvic floor muscle strength, provide additional support to the urethra, and/or teach active muscle contraction to counteract the effects of increased intra-abdominal pressure. When conservative treatment is insufficient, surgical options may be considered. Most commonly, surgical intervention consists of the

midurethral sling. Although this procedure has been determined to be effective within the first 5 years after implantation, the midurethral sling is associated with mild adverse events in roughly 40% and severe adverse events in 20% of cases [38, 68].

1.2.3 Reproduction and Pelvic Organ Prolapse

The vagina must be able to accommodate a range of biomechanical forces, such as those resulting from sexual intercourse, pregnancy, vaginal delivery, and everyday increases in intra-abdominal pressure—such as those that occur during coughing and defecation. The vagina stretches and deforms during these events and then returns to its original configuration. The vagina also provides mechanical support to surrounding pelvic organs, such as the urethra and bladder. This means that dysfunction or trauma to the vagina can have implications for other tissues of the pelvic floor and their ability to function properly.

Most relevant to this work is the ability of the uterus, cervix, and vagina to support the growing fetus during pregnancy and facilitate vaginal childbirth. As the fetus grows, so does the uterus. As they grow, the uterus becomes more abdominal and the weight of the uterus and fetus become more anterior, altering the mechanical environment of the pelvis [182]. The cervix must maintain enough mechanical integrity to support the fetus, but also be able to appropriately shorten, soften, and dilate at the onset of vaginal childbirth to allow passage of the fetus into the birth canal [104, 133]. Early initiation of cervical remodeling may contribute to preterm birth. Subsequently, during the second stage of labor, the vagina and surrounding pelvic floor muscles and connective tissues must also stretch extensively to accommodate the fetus during the descent through the birth canal. This commonly results in damage to the pelvic floor muscles and connective tissues, which will be discussed further in Chapter 4.

Pelvic organ prolapse is defined as descent of one of the pelvic organs (bladder/urethra, uterus, or rectum) into the vaginal wall. At stages of greater prolapse, this can cause portions of the vagina to distend outside of the body. Though specific mechanisms of pelvic organ prolapse progression are still being elucidated, it is known that it involves loss of mechanical support in either connective tissues or the pelvic floor muscles that support the pelvic viscera

and/or to loss in the mechanical integrity of the vagina itself. For example, if the uterosacral ligaments are no longer as able to resist downward forces, then the uterus will descend further, potentially resulting in prolapse. Alternatively, even if connective tissues allow for an appropriate amount of displacement, a mechanically compromised vagina may deform more excessively in response to the same applied loads. The connection between vaginal parity (the number of times a woman has given birth vaginally) and increased risk of pelvic organ prolapse likely lies at least partially in vaginal birth injury.

Vaginal delivery is the greatest risk factor for the later development of pelvic floor disorders [80, 119]. After a single vaginal childbirth, the odds of developing pelvic organ prolapse are approximately ten times higher [149]. Injury during vaginal childbirth is common, with roughly 94% of women having some degree of perineal tearing after their first birth and 66% after subsequent births [173]. Additionally, around 20% of women have a levator ani defect following their first childbirth [57]. Even in the absence of acute injury, these tissues may experience stretch–induced damage during vaginal childbirth that progressively, with age, leads to weakening that may predispose those women to pelvic organ prolapse.

Symptomatic pelvic organ prolapse has an approximate prevalence of 3–6%, while prolapse diagnosed via physical examination of the vagina has an approximate prevalence of 50% [19]. Pelvic organ prolapse often results in surgical intervention, with the incidence of prolapse surgery ranging from 1.5–4.9 cases per women years [19, 91]. There are many surgical techniques used to treat the various presentations of pelvic organ prolapse. For example, the surgeon can approach the vagina abdominally or vaginally while the repair may target the anterior, posterior, or apical vagina [91, 195]. Synthetic mesh is commonly used in many prolapse repairs, but pelvic tissues are an alternative used in native tissue repairs [93]. Conservative treatments include the use of a pessary and pelvic floor muscle training [91, 195].

Cesarean delivery is considered by some to be a preventative measure of pelvic organ prolapse and pelvic floor disorders, as stretch–induced birth injury to the pelvic floor muscles and connective tissues is avoided in non-emergency cases. It should be noted though that many nulliparous (have never given birth) women—approximately one fifth—still develop prolapse, meaning vaginal birth–related injury is not the only source of damage/weakening

that may predispose women to pelvic organ prolapse [195]. Additionally, planned Cesarean delivery is considered a major surgery that studies have associated with significantly increased risk of severe maternal and infant morbidity compared to planned vaginal deliveries [7, 41, 103, 114]. More recently, pelvic floor physical therapy and early exercise postpartum are being considered in order to strengthen pelvic floor muscles after the strenuous act of childbirth in hopes of preventing the later development of pelvic floor disorders [187, 199].

1.2.4 Defecation and Fecal Incontinence

The final critical function of the female pelvic organs, specifically the anorectum, is defecation. As anorectal function/dysfunction is not the focus of any of the studies discussed in this dissertation, this physiologic function will be covered in less detail.

The rectum must propagate transit of stool towards the anus and also store feces until an appropriate moment for defecation. In order to expel rectal contents, the pressure inside of the anorectum must be larger than that outside of the body. The pressure gradient is generated through intentional increase of intra-abdominal pressure, which acts on the rectum. Once stool enters the anus, the external anal sphincter and puborectalis must relax, creating a doorway, so to speak, for the feces to travel through. Because the pressure is now higher in the rectum, the stool is forced from the body. Baseline muscle tone of the external anal sphincter and puborectalis contribute to the resting pressure of the anorectum.

Fecal incontinence refers to conditions that cause loss of bowel control, resulting in the inability to either easily expel stool at the moment of or adequately store feces until defecation. Such disorders may be structural (such as rectal prolapse) or functional (such as dyssynergia). Women are disproportionately affected by fecal incontinence, and the general prevalence for men and women collectively is roughly 7-15% [29]. The disproportionate impact on women is generally attributed to vaginal childbirth, as anywhere from 12–53% of women with an obstetric anal sphincter injury (a result of severe perineal tearing that reaches the anal sphincter) will experience anal/fecal incontinence symptoms later in life [79].

1.2.5 Gaps in Knowledge

The biomechanics of many female pelvic floor functions and the dysfunction that leads to pelvic floor disorders are still not fully understood. Theories continue to be proposed and debated as the field moves towards a better understanding of these complex systems. Without being able to isolate the cause of these pelvic floor disorders, treatments cannot be designed to be as effective as possible nor ideally catered to the individual. One difficulty arises in the decades that often lie between childbirth and the development of a pelvic floor disorder, reducing the ability to isolate specific trends. Additionally, the variation in anatomy and functional ability across the general population leads to multiple presentations of each type of pelvic floor disorder, meaning a single diagnostic and/or treatment strategy will not likely be effective for every woman.

1.3 Existing Computational Research in the Field

1.3.1 Statistical Shape Models

Shape is an important aspect of biomechanics as it is a main driver and indicator of a tissue's mechanical function. There are many ways in which shape (or specific shape attributes) may be evaluated. For example, in the study of the female pelvis, length/distance and angle measures are often used to describe the "shape" of the pelvic floor. A single length/distance is not a true shape measure, but multiple lengths could be used together to describe an overall shape, so we'll consider it a measure of a specific shape attribute for the sake of this discussion. For example, the levator plate is often described by the levator plate angle, which represents how horizontal/vertical the orientation of the superior levator plate is with respect to a horizontal reference line defined by the bony pelvis [87]. The levator plate angle has been shown to be greater in women with pelvic organ prolapse compared to controls and to be correlated with increased motion of the perineal body during Valsalva [87]. The levator hiatus is commonly quantified by its transverse diameter, anterior–posterior diameter, and its area. Again, individually, these are not shape measures, but together do

describe the general shape of the levator hiatus. Hiatal dimensions have been shown to be weakly, positively correlated with age [196], asymmetric in the presence of unilateral muscle defects [60], and dynamic levator hiatal dimensions have been associated with the length of the active second stage of labor [39]. While such measures are useful and provide critical insight into the anatomy and biomechanics of the female pelvic floor, they are subject to certain biases and limitations.

Two–dimensional measures of anatomical shape and/or size only describe the regions of the tissue that define their endpoints/boundaries. For example, the levator plate angle only describes the superior levator plate, meaning the information it provides is limited to that region of the pelvic floor. Similarly, the levator hiatus only refers to one plane of the three-dimensional levator hiatus. While it is necessary to focus on specific shape attributes for such measures, other regions of the anatomy being excluded may also be important or have even stronger relationships with the outputs of interest. These measures do not consider the entire shape of the tissue, in this case, the pelvic floor muscle complex. This introduces potential bias as one may conclude that these measures are the most important, when they may actually just be the most influential of the measures (and therefore anatomical landmarks/shape attributes) evaluated.

Statistical shape modeling (to be described in more detail in Section 2.1) overcomes these limitations. It evaluates the entire shape without any bias towards specific shape attributes or anatomical landmarks when corresponding points are chose automatically. It robustly evaluates the shape variance of the given dataset, while blind to patient groups, intended comparisons, etc. When the points defining each shape are not manually chosen, that selection bias associated with the previous measures is removed.

Originally, with respect to medical research, statistical shape models were intended as a method of automatically segmenting organs/tissues from medical imaging [52]. Now, machine learning is more common for automatic image segmentation and statistical shape modeling is being used as a more robust, advanced images analysis of clinical imaging data. The idea behind a statistical shape model is to move away from individual, patient–specific descriptions of shape (in our case, anatomical shape) by using a cohort of example shapes in an attempt to describe the shape variation of a more general population (in our case, of women)

[52]. Now, the reason why the previous measures cannot be considered true shape measures is because shape is technically defined as the geometric information that remains once any variation due to differences in translation, rotation, and scale have been removed [62]. That is why a single length is not a measure of shape, but multiple lengths together could describe aspects of a shape as the ratios between them would be independent of the location, orientation, and size of the geometry. This definition of shape was originally established by Kendall in 1977 [97]. Even before Kendall's formal definition, Galileo qualitatively evaluated the difference in shape between small and large animal bones in the 1600's, observing that they differed by more than just global scaling alone, and the field of biological geometrical shape analysis was generated by Thompson in 1917 [62].

Historically, statistical shape models have been performed much more commonly on bones that soft tissues. This is likely because bones have more easily identifiable landmarks, do not generally deform enough for shape to be altered, and (in most parts of the body) have a more complicated shape than surrounding muscles and connective tissues. Hundreds of publications exist describing bony morphology via statistical shape modeling for orthopedic applications [93, 31]. The bony pelvis has also been evaluated using this methodology [21, 17]. Though quantifying muscle morphology in this way is less common, it has been done, but (before the work presented in this dissertation) only one group had evaluated any female pelvic floor muscles (they investigated the levator ani) [108]. Though it is important to note that many bony pelvis models exclude the sacrum and/or coccyx, meanwhile neither the female urethra nor the entire pelvic floor muscle complex have ever been evaluated with a statistical shape model. Even simpler two–dimensional measures have not been adequately developed to describe variation in the superficial perineal muscles and connective tissues or the coccygeus muscles. Most importantly, even if statistical shape models of these structures exist, they have not been used to study the effects of stress urinary incontinence, pregnancy, or childbirth on the shape of female pelvic tissues and organs.

1.3.2 Finite Element Models of Vaginal Childbirth

Finite element models of vaginal childbirth may investigate the effect of maternal and/or fetal model inputs on predicted maternal and/or fetal outcomes. This work focuses on maternal inputs and outcomes, while fetal parameters are simplified, and the second stage of labor specifically. For years, the study of the biomechanics of vaginal childbirth only involved the maternal pelvis and fetal skull, but in the past two decades the female pelvic floor muscles have also gained attention, and rightfully so [112]. The typical goal of such childbirth models is to determine the strain (often quantified as stretch) experienced by those maternal soft tissues during simulated vaginal childbirth, which is meant to serve as an indicator for injury (such as those discussed in Section 1.2.3) [113, 142, 143]. Such models have studied the impact of maternal soft tissue material properties [110, 111], episiotomy [141], manual perineal protection [89], and labor duration [194] on the maternal soft tissues (usually the levator ani).

For models so focused on maternal factors, the fetal head is typically represented as a sphere [113, 89] or a simplified skull [110, 111] that is rigid or so stiff as to allow negligible deformation. Some models use more advanced, full fetus models, but as the focus is still maternal, the deformation of the fetus is still minimal [143]. Though some material models allow for the incorporation of active maternal muscle material properties, only the passive mechanics and material properties of the pelvic floor are typically considered [141]. Most critical with respect to this dissertation are the usual maternal geometries used in these models. The maternal anatomy is typically patient–specific [42], simplified based on patient–specific anatomy [110, 111, 113], or obtained from cadavers [141, 143]; the only pelvic floor muscles included are the levator ani [110, 111, 113, 141, 143, 194]; the bony pelvis is excluded or incomplete [110, 111, 143, 194]; and the anatomy was not based on imaging or data from a pregnant woman [110, 111, 113, 141, 143, 194].

While many of these concessions are at times necessary to more quickly build initial models and generate hypotheses, the fact that critical features (such as geometric variation, a full pelvic floor muscle complex, allowed motion of the coccyx, etc.) are missing from most, if not every single, model is unacceptable. Only one study seemed to even discuss

multiple maternal geometries, and even then it is unclear why both were not simulated and compared [111]. For some reason, the impact of material properties and boundary conditions has been much more highly valued than the influence of maternal anatomic variation. While it is appropriate to simplify models and make assumptions, the findings must reflect those limitations and eventually the influence of those simplifications needs to be determined. Currently in the field, strong claims are being made about the biomechanics of childbirth although models have not been evaluated robustly across variation in maternal anatomy. Additionally, such oversight has a severe negative impact on women with demographics that do not match those of the these patient–specific models. Models need to be critically assessed and validated before they can become clinically meaningful, and this will be imperative moving forward.

1.4 Specific Aims

Maintenance of normal urinary, defecatory, sexual, and reproductive function is dependent on the mechanics of the female pelvic organs and pelvic floor muscles and connective tissues. As discussed in Section 1.2, pelvic floor disorders have at least partially been attributed to reduction in the mechanical integrity of these connective tissues, muscles, or the organs themselves either due to acute injury resulting from trauma (such as injury during vaginal childbirth), repetitive use injury (that may result from events such as chronic coughing), or progressive weakening (such as with age). In addition to resulting in billions of dollars in healthcare costs annually, pelvic floor disorders also reduce a woman's quality of life by inflicting physical pain/discomfort and/or social/emotional side effects, such as embarrassment and anxiety.

The shape and structure of biological tissues are the main drivers and indicators of their biomechanical functions and for 100 years it has been stated that the variability in female pelvic floor anatomy is not adequately understood [183]. Therefore, we aimed to calculate pelvic floor organ and tissue morphology to evaluate the relationship between shape and pelvic function—specifically urethral passive closure and vaginal childbirth. Then,

understanding that defining variation in pelvic tissue shape and structure would improve computational simulations of female pelvic floor biomechanics, pelvic floor muscle complex and bony pelvis morphology and pelvic floor muscle fascicle arrangement variation were quantified to generate ranges of values to be utilized in future computational models.

1.4.1 Specific Aim 1

To a) quantify urethral shape and motion associated with stress urinary incontinence and b) determine which tissues have the greatest influence on urethral passive closure. Stress urinary incontinence is associated with weakness of the urethral supportive tissues (resulting in hypermobility) and/or weakness of the urethra itself (resulting in reduced active muscle strength referred to as intrinsic sphincter deficiency). Therefore, we hypothesized that stress urinary continence would have a significant impact on urethral motion, deformation, and shape as evaluated with endovaginal ultrasound and statistical shape modeling. An extension of that inquiry was to question which tissue mechanical properties may contribute to those differences in urethral shape and motion. We hypothesized that proximal connective tissues, the perineal membrane, and urethral stiffness would have the greatest influence on urethral motion and shape in finite element simulations of Valsalva as determined by a sensitivity analysis.

1.4.2 Specific Aim 2

To a) quantify bony pelvis and pelvic floor muscle complex shape variations in pregnant women and b) determine significant geometric predictors of simulated vaginal birth-related injury. While certain aspects of female pelvic anatomy have been studied in pregnancy and associated with birth outcomes, a robust evaluation of the overall pelvic floor muscle complex and bony pelvis shape has yet to be implemented. We hypothesized that statistical shape modeling would reveal that the bony pelvis is wider, the sacrococcygeal curvature reduced, the perineal body further descended, the levator plate straighter, and the iliococcygeus more concave in late pregnancy. These morphological alterations would correspond with the increased intra-abdominal loads created by the growing fetus and would

result in more room in the pelvis for passage of the fetus, potentially reducing soft tissue strains during vaginal childbirth. To determine whether pregnancy–induced remodeling reduced the mechanical burden of vaginal childbirth by protecting against stretch–induced maternal birth injury, we performed a sensitivity analysis of finite element simulations of vaginal childbirth, sampling the statistical shape model of the combined bony pelvis–pelvic floor muscle complex in pregnant women to generate various geometric inputs. We hypothesized that shape would significantly impact the biomechanics of vaginal childbirth and morphological variation associated with late pregnancy would reduce pubovisceral muscle enthesis and perineal body strains.

1.4.3 Specific Aim 3

To quantify a) female bony pelvis and pelvic floor muscle complex shape variations and b) pelvic floor muscle fascicle orientation variations that will provide geometric and material property data to inform future models of female pelvic floor biomechanics. Many finite element simulations of the female pelvic floor are carried out with only one, patient–specific anatomy used to generate the geometric inputs. While these models still provide important information, there is no guarantee that their results apply to a broader population of women. We hypothesized that the morphology of the bony pelvis and pelvic floor muscle complex calculated via statistical shape modeling would significantly differ across nulliparous, 3rd trimester pregnant, and parous women. With significant differences in muscle shape, we could also assume variation in pelvic floor muscle fascicle orientations would be present. Therefore, we hypothesized that photogrammetry of cadaveric pelvic floor muscle complexes would demonstrate meaningful variation in muscle fascicle orientations across individuals.

2.0 Computational Methods Overview

2.1 General Statistical Shape Modeling Workflow

2.1.1 Statistical Shape Modeling Summary

Statistical shape models are designed to look only at differences in shape, not size or position, meaning variation due to rotation, translation, and scale must be removed. Briefly, this is accomplished by determining corresponding points and minimizing the distances between them via global scaling and rigid transformations. Commonly, a Procrustes analysis is used to complete this step of a statistical shape model. A principal component analysis is then performed to identify modes of variation—defined by eigenvectors and eigenvalues that describe the morphological variation of the input shapes. As a principal component analysis results in as many modes as there are shapes minus one, some analysis or threshold must be used to determine which modes are significant and warrant inclusion in subsequent analyses and statistics. It is common to use a percent variance threshold of 5% or a parallel analysis to identify significant modes. In order to perform those subsequent statistics, one must calculate principal component scores—the project of subject–specific data onto eigenvectors—which become the dependent variables in follow–up statistical analyses (Figure 2.1). Typically, an initial training set of shapes is used to define a statistical shape model and a smaller set of testing shapes is used to assess the predictive capability of that model. As this dissertation takes first steps towards robust quantification of female pelvic anatomical shapes and many of the studies had a limited sample size within patient groups of interest (though the total sample sizes were sufficient), this work will only evaluate training set as a type of advanced image analysis.

2.1.2 Shape Acquisition and Preprocessing

In the case of shape models of human anatomy, shapes are acquired via segmentation of medical images, such as magnetic resonance and computer tomography images. One

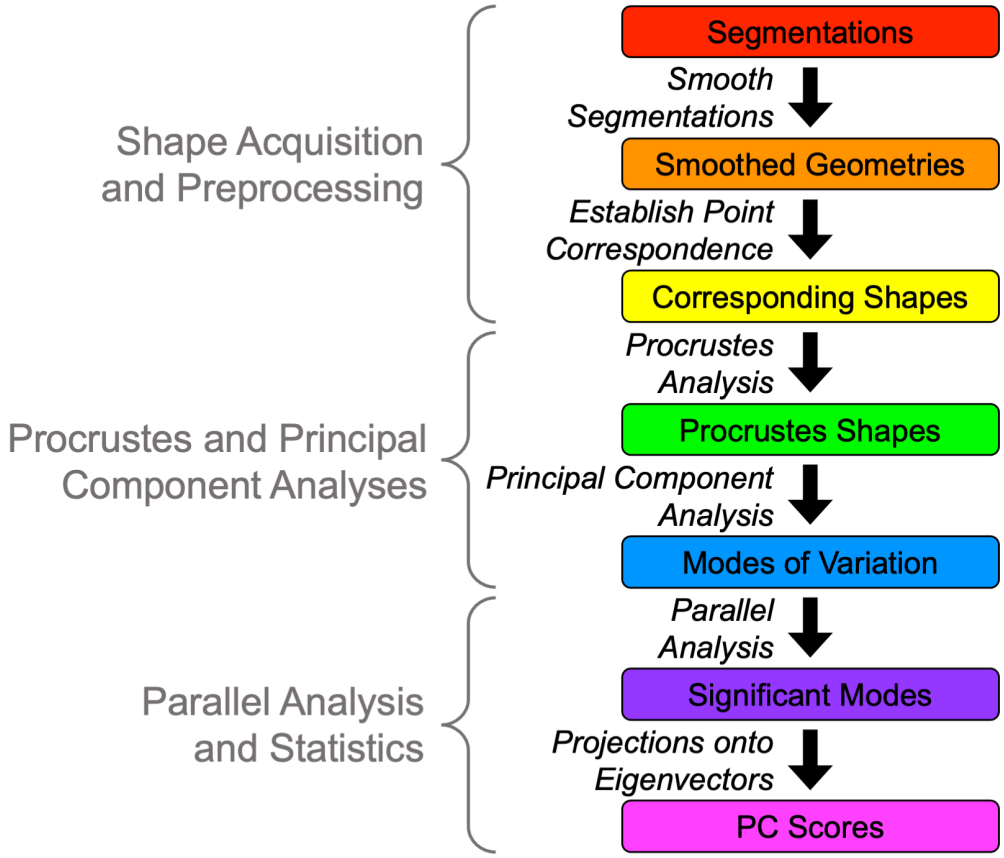

Figure 2.1: A flow chart describing a general statistical shape modelling workflow with steps categorized (gray text) based on this dissertation section (Section 2.1). Colored boxes indicate the inputs and outputs of while the italic text indicates the process/analysis carried out at each step.

consequence of this is the aliasing—step–like features that result from the slice thickness and gaps of the scans. Aliasing becomes greater and more noticeable with increasing slice thicknesses and gaps. As you do not want the shape model to measure this aliasing or for it to influence the calculated shape variance, you must remove it via a smoothing protocol.

Segmentations can be smoothed manually, automatically, or semi-automatically and in a biased or global/uniform fashion. The segmentation smoothing implemented in this work is less conventional than a straightforward manual or automatic smoothing protocol, as it served to simultaneously establish corresponding points. For the studies described here, global and fully automatic methods were not ideal as they tend to disproportionately diminish smaller anatomical features. For example, the anococcygeal ligament of the pelvic floor

muscle complex or the ischial spines of the bony pelvis would be disproportionately smoothed, and potentially decimated, by such protocols. On the other hand, manual smoothing allows for more control in order to avoid such feature decimation, but is time consuming and introduces bias. For these reasons, a semi–automatic approach was used.

Initial smoothing of 2D segmentations was carried out automatically by fitting uniform spline curves to the original dataset. Splines were pre-aligned (via translation and rotation) using custom Mathematica^{TM} scripts. This improved the results of the subsequent step where corresponding points were calculated.

The following process was used to smooth and calculate corresponding points on the 3D bony pelvis and pelvic floor muscle complex shapes. The 3D urethras analyzed as part of the study in Section 3.3 were outputs from finite element models that had identical meshes, meaning neither smoothing nor corresponding point determination were required. In all other cases, 3D shapes were initially aligned utilizing an iterative closest point (ICP) algorithm implemented in Python. ICP reduces the sum of the distances between sets of point clouds, iterating until a minimum is reached. Again, this serves to improve the results of the following step where corresponding points are established.

Corresponding points are those that refer to the same location on each object. By establishing corresponding points on geometries segmented from clinical imaging, you are ensuring that point x on each shape represents the same anatomical landmark. Corresponding points can be chosen manually or with an algorithm. Obvious cons of a manual approach include selection bias and the potential exclusion of unknown influential landmarks (as discussed previously in Section 1.3.1), therefore an automatic or semi–automatic method is highly recommended. In our statistical shape modeling workflow, we utilize the atlas–registration function within Deformetrica to semi–automatically determine corresponding points for both 2D and 3D shapes [33].

In order to smooth segmentations with Deformetrica, first a template shape must be defined. The input geometry is meant to be representative—reminiscent of an average shape if that information is available—or so simple as not to introduce bias and should be generated with the number of vertices desired for the subsequent statistical shape analysis. It needs to be adequately smooth as any major features of the template shape will be present

in every smoothed, subject–specific shape once the template fitting process is complete. For 2D shapes, simple splines were manually generated with evenly distributed points to serve as template shapes. For 3D geometries, either an ellipsoid; high–resolution, manually smoothed patient–specific geometry, or a previously calculated average shape were used as the Deformetrica templates (Figure 2.2).

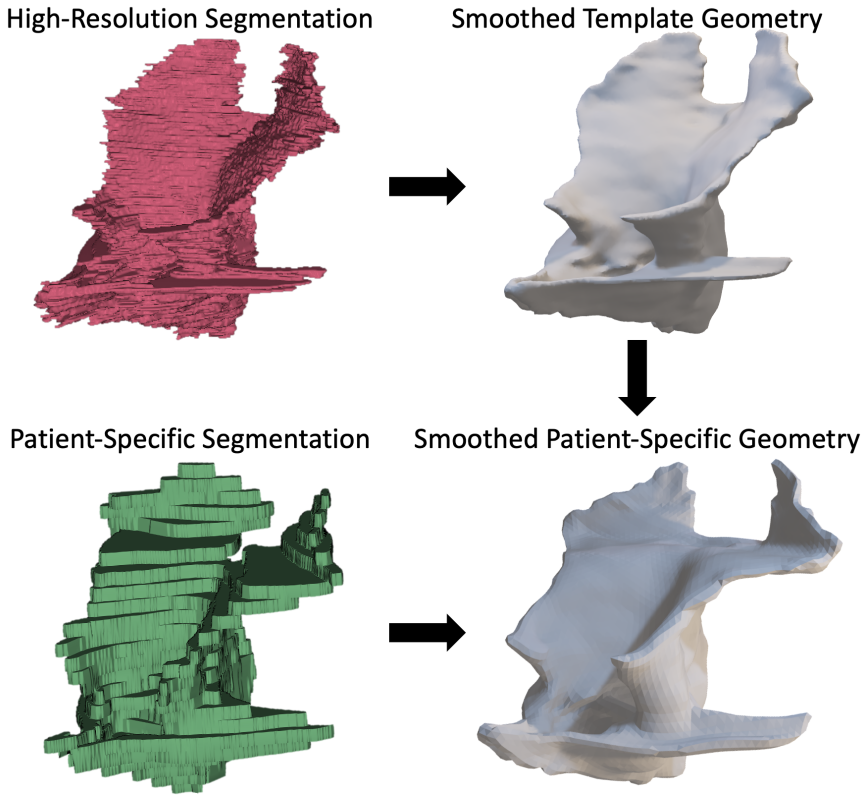

Figure 2.2: A visualization of the geometries required to semi–automatically smooth 3D patient–specific segmentations while simultaneously establishing corresponding points in Deformetrica. The top row demonstrates the creation of the pelvic floor muscle complex template from the Korean Visible Human dataset (Korea Institute of Science and Technology Information, Daejeon, South Korea), which was smoothed manually. The bottom row demonstrates the before and after for one patient–specific geometry: on the left is the original segmentation and the right depicts the template–fitted, smoothed shape after the above template had been deformed into the segmentation using Deformetrica.

In summary, the atlas–registration function within Deformetrica utilizes a large deformation diffeomorphic mapping framework to deform the given template shape into each patient–specific shape [33]. As the same template is being used and the "energy", so to speak, required to deform the template into each shape is minimized, the resulting template–fitted

shapes are both as smooth as the template and defined by the same mesh (i.e., vertices), which is what makes those vertices corresponding. This combined smoothing and corresponding point generation protocol has been evaluated for accuracy and its ability to predict missing anatomical data in an ongoing study outside the scope of this dissertation [121]. For the bony pelvis specifically, the error of the resulting smoothed, patient–specific geometries was low, with 95% of the vertices located within 2.5 mm of the original geometry—an error well within an acceptable range and less than what may result from more traditional, manual or global, automatic smoothing techniques [121].

Deformetrica deforms the template shape based on the user–defined inputs. The most important of these inputs, the kernel width and deformation kernel width, define the grid of the space in which the deformations are taking place. It is deformation of this grid that causes deformation of the template shape and these widths impact the scale of the resulting deformations. Other influential settings include the convergence tolerance and noise parameters, which impact the closeness of the final fit between the template and patient–specific segmentation. Settings were manually iterated until an optimal fit was achieved between the patient–specific segmentations and smoothed, template–fitted geometries. Statistical shape modeling results have been proven to be robust to variations in Deformetrica parameter settings [67].

The final result of this shape preprocessing workflow is a set of smoothed, patient–specific shapes with corresponding points that are ready to be input into a statistical shape model.

2.1.3 Procrustes and Principal Component Analysis

The goal of a Procrustes analysis is to remove any non–shape differences between a set of geometries. This involves aligning shapes as closely as possible via rigid translation, rigid rotation, and global scaling. When corresponding points are established, this is accomplished by minimizing the total distance between corresponding points. This ensures that any remaining differences between geometries are true shape differences. In this work, Procrustes analyses were implemented with a previously established package in Mathematica$^{\text{TM}}$ [148].

This outputs aligned versions of the patient–specific inputs, which we scaled to the average size of the dataset. Additionally, the average shape can be generated by taking the average of all of the Procrustes–aligned corresponding point coordinates.

The next step to building a statistical shape model is performing a principal component analysis (PCA) on the aligned shape coordinates. This was performed in a custom Mathematica^{TM} script (see Appendix A). It should be noted that the PCA can also be performed on the residuals of the dataset—the distance from each patient–specific dimension (e.g., x, y, z) and coordinate to the corresponding mean shape coordinates—and the PCA results will be the same. A PCA involves the calculation of linearly uncorrelated principal components (PCs) via a covariance matrix, which can be used to qualitatively and quantitatively describe the shape variance of the dataset [43, 83].

If we imagine the real world space in which our shapes reside, after the Procrustes analysis, we would see those shapes closely aligned, each defined by the same number of corresponding points, with each of those points defined by an x, y, and z coordinate (Figure 2.3). However, the PCA acts in the variable space where each entire shape is represented by an individual data point, but instead of being defined by multiple coordinates of three dimensions, each point in the variable space is defined by a single coordinate of as many dimensions as there were corresponding points multiplied by the number of original dimensions (typically three). In this variable space, the variance can be envisioned as an N-dimensional ellipsoid fit to the data in this space. As PCs (also referred to as modes of variation within the confines of statistical shape modeling) define the directions of the most variance, they can be imagined as the major then subsequent orthogonal axes of the ellipsoid. The first PC will be the longest line segment, with the largest eigenvalue. Increasing PCs describe a decreasing amount of variance. Eigenvalues are used to calculate the percent of the total variance described by each mode of variation, calculated by dividing each eigenvalue by the sum of all eigenvalues. In real space, a vector is a line defined by 3 values depicting a direction. Eigenvectors can be thought of in the same way, but in variable space and as being defined by many more values. In this way, they depict the direction in which the eigenvalues

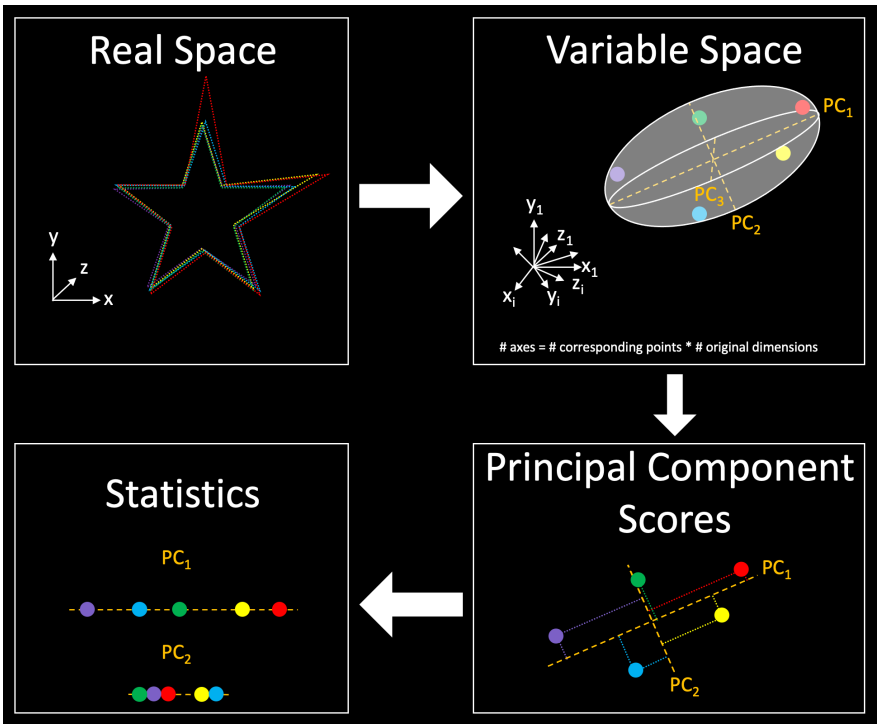

Figure 2.3: An illustration of a principal component analysis (PCA) and resulting eigenvectors, eigenvalues, and PC scores. First, example shapes (stars) are depicted in real space with each color representing an individual shape. Then we see a demonstrative illustration of those shapes projected into the variable space in which the PCA is performed, where each point now represents an entire shape from the real space. The ellipsoid is actually N-dimensional, but simplified for visualization purposes and represents the variance being calculated. The PCs represent the major and then subsequent orthogonal axes of that ellipsoid. PC scores are the projections of individual shape data onto the eigenvectors and become dependent variables in subsequent statistical analyses.

reside, describing the directions of the most variance. When projected back into real space, the eigenvectors can be used to deform the shapes in real space along those directions of greatest variance.

2.1.4 Parallel Analysis and Statistics

A PCA in a statistical shape analysis results in as many PCs as patient–specific shapes minus one. One purpose of the PCA is to reduce the dimensionality of the dataset in order to focus on truly significant shape variation and potential differences between patient groups of

interest. Therefore, only modes of variation that describe significant shape variance should be considered and included in subsequent statistical analyses. A common threshold for significance is any mode that describes at least 5% of the total shape variance, but as the number of significant modes can alter statistical comparisons we wanted to use a more robust approach [45]. In this statistical shape modeling workflow, we implement a parallel analysis within our custom Mathematica^{TM} script to determine the significant modes of variation [45, 46]. A matrix the same size as the shape dataset is generated and filled with values randomly sampled from a unit Gaussian distribution. Then a PCA is carried out on the new dataset and eigenvectors and eigenvalues calculated. This is done 10,000 times, after which the eigenvalues are averaged across all 10,000 iterations. This results in an average variance for each PC representative of the percent of the total variance associated with the noise of the dataset. Modes of variation from the original PCA on the shape data were only considered significant if they described a larger percentage of the total shape variance than the corresponding parallel analysis PCs [46]. This is visually evaluated with a scree plot (Figure 2.4).

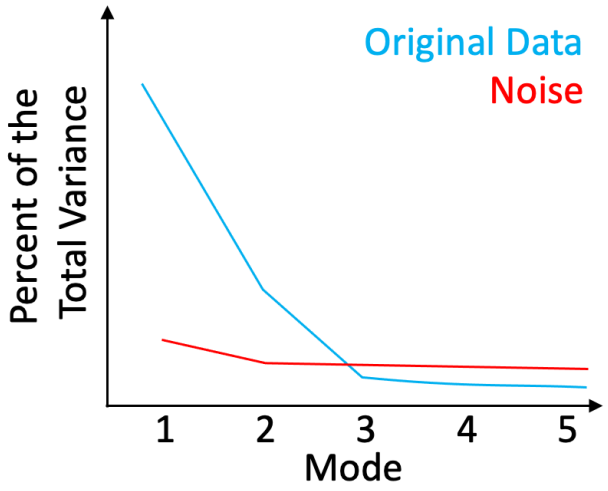

Figure 2.4: An illustrative example of a scree plot that demonstrates the percentage of the total variance explained by each mode from the original shape PCA compared to the corresponding percent of the total shape variance described by the determined noise of the dataset. In this example, only the first two modes of variation would be said to describe significant shape variance.

Once the number of significant modes of variation has been determined, those that describe significant differences between patient groups or have significant correlations with

patient data etc. can be identified. The difference between a significant mode according to the parallel analysis and those that are significant in subsequent statistics should be noted. All significant modes describe meaningful shape variation, but statistical analyses will determine which modes describe significant differences with respect to patient variables.

To evaluate a statistical shape model, statistics are performed on the principal component scores, which are projections of patient–specific data onto eigenvectors (Figure 2.3). Statistics should only be performed on PC scores calculated along significant modes. A PC score indicates where a patient's shape lies along the morphological variation described by that mode. Values closer to zero are more similar to the mean shape, while larger or smaller (more positive or more negative) values indicate increased variation from the mean shape. Typically, PC scores fall within 3 standard deviations of the mean shape. PC scores can be evaluated like any other continuous patient variable and, because they are linearly uncorrelated, they meet the independence assumption of many statistical tests.

In this work, statistical shape model results are typically evaluated with MANOVAs in order to compare patient groups of interest—such as early vs late pregnant and nulliparous vs pregnant vs parous women. Correlations and regressions can also be used to evaluate linear relationships and/or build predictive models.

2.1.5 New Shape Generation

After modes of variation have been calculated and significant modes determined, these descriptors of continuous shape variation can be used to generate new shapes that were not part of the original dataset. This often includes reconstructing the overall average shape using only significant modes and generating the average shapes of specific patient groups of interest (e.g., early vs late pregnant averages). We used the Manipulate functionality within Mathematica^{TM} to select PC scores and export these newly generated shapes (Figure 2.5). In this way, anatomy of digital patients can be created and a large variety of shapes can be used as inputs in other computational analyses (e.g., finite element simulations).

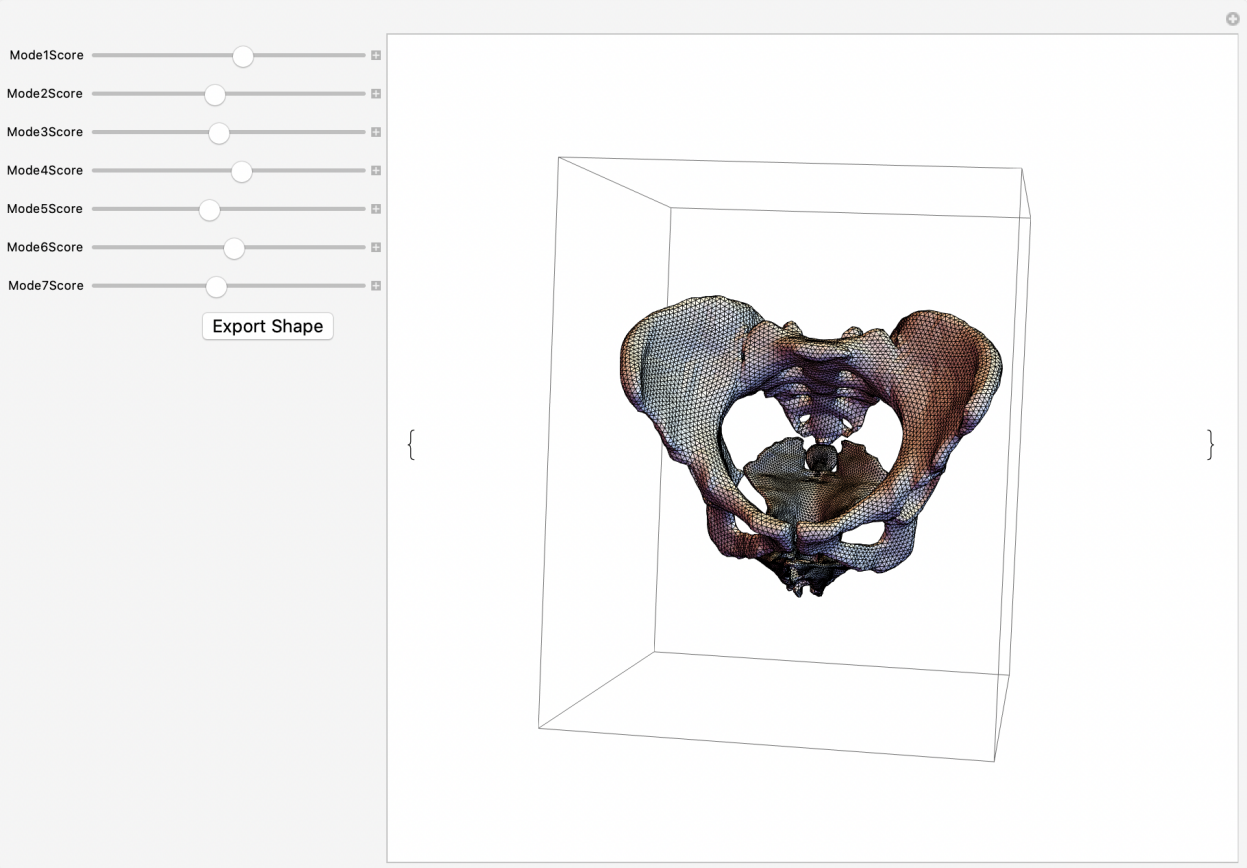

Figure 2.5: A screenshot of the Manipulate within our custom Mathematica^{TM} script used to generate brand new shapes by selecting PC scores along significant modes of variation and exporting that shape for use in other visualizations and/or computational analyses.

2.2 Finite Element Modeling Concepts

A finite element model is used to computationally simulate of the mechanics of a particular situation. The name comes from the fact that the geometries in a finite element simulation are composed of meshes made of a finite number of elements. Before a finite element simulation can run, geometry, material properties, and boundary/loading conditions must be defined.

2.2.1 Geometry

In biomechanical finite element simulations, the geometry inputs often consist of segmentations of medical imaging. As discussed with respect to statistical shape modeling in Section 2.1.2, segmentations from medical imaging are often plagued by aliasing that must be removed to ensure that it does not influence the simulation. Once the geometries are smooth, a mesh must be generated. Surfaces meshes are two-dimensional and composed of quadrilateral (i.e., squares/rectangles) and/or triangular elements. Volume meshes are three-dimensional and composed of hexahedral (composed of 6 quadrilateral faces) or tetrahedral (composed of 4 triangular faces) elements. Generally, tetrahedral elements are easier to generate for complicated geometries, while hexahedrons are better at handling large deformations. Meshes can be either uniform (consistent size) or biased (local variations in size). Utilizing a biased mesh can reduce the number of elements needed to adequately predict stresses and strains.

The number of elements in a mesh can influence the results of the simulation. In order to determine the threshold for the required number of elements, a mesh convergence study must be performed. This requires generating meshes of various densities and identifying the point at which the simulation results plateau (e.g., increasing the mesh density further affects predicted stresses/strains by less than 5%). Once this threshold has been identified, the results of any simulation with a geometry that has more elements than that threshold are not being biased by the mesh itself.

In addition to being influenced by the number of mesh vertices, mesh convergence is also influenced by the number of integration points on each element. Integration points can be thought of as invisible vertices located along the edges in between the original vertices. Integration points have a similar effect to increasing the mesh density, but without altering the mesh itself as, in addition to stresses and strains being calculated at each vertex, they are also calculated at each integration point.

2.2.2 Material Properties

Material properties in finite element modeling refer to relationships that dictate the mechanical behavior of the tissues being simulated. The discussion of material properties can be very involved and rightly so, but will only be discussed here to the extent fitting of these research studies.

A rigid body is an object that is not allowed to deform to any degree. It is infinitely stiff and cannot experience stress or strain. Bones are often assigned as rigid bodies as their *in vivo* deformation may be considered insignificant compared to that of surrounding soft tissues, but this depends on the design of the finite element model. In the case of both the urethra during Valsalva and the pelvic floor during vaginal delivery, soft tissue deformations are so great that the bony pelvic bones were treated as rigid bodies.

Though soft biological tissues demonstrate nonlinear and viscoelastic behavior *in vivo*, simpler material models are often utilized. In finite element modeling, various assumptions and concessions can be made depending on the purpose of the resulting simulation. For example, when a simulation is displacement driven and the output of interest is strain, it may be more acceptable to use a simpler material model. Additionally, the existence of the data needed to define more complicated material models and its contribution to computational costs may justify the use of simpler material models.

The studies in this dissertation most commonly employ the Neo-Hookean material model, which only requires two parameters: Young's modulus (also referred to as the material constant, C_1) and Poisson's ratio. Young's modulus refers to the stiffness (not to be confused with structural stiffness) of a material, while Poisson's ratio refers to the amount of deformation in directions perpendicular to the axis being loaded. A larger material constant will result in less deformation/strain in response to the same applied load. A larger Poisson's ratio will result in less deformation along the perpendicular axes with a maximum value of 0.5 representing a perfectly incompressible material—meaning volume is conserved. The Neo-Hookean model is an extension of Hooke's Law and widely considered the simplest material model for computational simulations. It is hyperelastic and defined by the invariants of the Left Cauchy–Green deformation tensor [101].

Having tissues or regions of tissues in close proximity with varying material properties can influence resulting stress and strain distributions. One common artifact of finite element simulations of biological tissues are high stresses along the surfaces where two materials with very different material properties meet. To avoid this pitfall, a material may be partitioned and a gradient of material properties applied to create a transitional region between the two materials. This will result in smoother stress and strain distributions more reminiscent of biological tissues *in vivo*.

2.2.3 Loading and Boundary Conditions

Loading and boundary conditions are the instructions that tell the finite element simulation what to do. Loading conditions, as implied, apply forces to geometries. Point loads can be applied at specific vertices and pressure, which can be positive or negative, applied over surfaces.

Boundary conditions dictate how geometries will respond to applied forces and displacements. Any vertex or group of vertices can be fixed or displacement prescribed in any of 6 degrees of freedom: x, y, and z translation and rotation. For example, fixing on the translations of a single point would still allow that geometry to rotate about that point. In addition to these binary constraints which allow either complete fixation or complete freedom, there are soft constraints. Depending on the capabilities of the chosen software, this may include attaching muscles to bone via springs or fixing two objects together but still allowing motion and deformation at the site of attachment with a tied constraint.

In addition to defining the behavior of finite element geometries, the interaction between multiple objects must be defined. This is referred to as contact. If contact is not assigned, two objects on a collision course would pass through one another without experiencing any stress or strain. Friction can be incorporated in contact definitions, but frictionless contact is more common. Multiple methods and algorithms may be employed to define contact depending on the finite element modeling software, but a common modifiable parameter is

the contact penalty. This dictates how repulsed two objects will be from one another. Mesh penetration, when the meshes of two objects intersect, may result from inadequate contact penalty.

2.3 Sensitivity Analysis Approach

2.3.1 Latin Hypercube Sampling

Latin hypercube sampling (LHS) is a design of experiments approach in order to minimize the number of experiments (in this case, simulations) required to perform a comparable sensitivity analysis. If you consider the most straightforward sensitivity analysis setup, one parameter is sampled evenly along its range with values chosen by the user while all other variables are set to the mean. Then each parameter is cycled through in this way (Figure 2.6). Although simple and easy to implement, this method results in more simulations than necessary to adequately describe the parameter space.

Latin hypercube sampling, on the other hand, only samples each division of each parameter once, minimizing the number of simulations needed to fully define the parameter space. In this dissertation, Latin hypercube sampling was carried out using the LHS function in the pyDOE v3.7 package in Python [122]. This requires the user to define the number of variables and regions within each variable to be sampled. The number of regions each parameter is divided into will determine the number of total simulations/experiments performed. This function generates values between 0 and 1 that can be scaled to fit any range of values and assumes an even distribution of parameter subdivisions, though the outputs can be transformed to represent a specific distribution if desired [122].

Once the LHS designed simulations have been established, additional statistics can be used to define relationships between these input parameters and output parameters of interest.

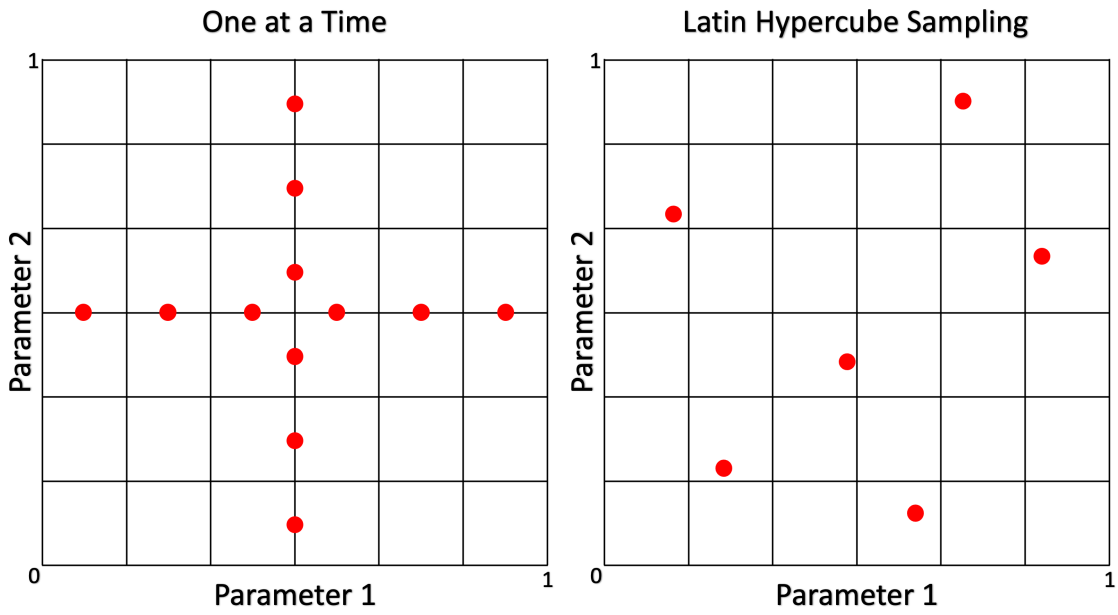

Figure 2.6: An illustration of two approaches to sampling a parameter space composed of two variables each divided into 6 regions. Latin hypercube sampling requires, in this example, half of the number of simulations to adequately define the same parameter space.

2.3.2 Partial Rank Correlation

A correlation describes a linear relationship between two variables; a partial correlation evaluates the relationship between two variables while removing any influence from other specified variables; and a rank correlation is that performed on ranked data rather than raw values [98]. A partial rank correlation is a combination of these. Within a set of values, the smallest is set to one, the second smallest to two, etc. until reaching the largest value. This transforms continuous data into ordinal data.

The partial rank correlations in this work were performed in Matlab^{TM} using the partial correlation function, partialcorri, which performs a partial correlation between given variable matrices while adjusting for internal variables (see Appendix B). This means that the influence of all remaining inputs and outputs are controlled for [66].

The outputs of this function are correlation coefficients and p–values. A larger coefficient indicates a stronger relationship while the sign of the coefficient determines whether the two variables are inversely (negative coefficient) or directly (positive coefficient) related. The p–value indicates the significance of the relationship.

2.3.3 LHS–PRCC Sensitivity Analysis

The use of the LHS–PRCC methodology as a finite element model sensitivity analysis workflow has been established previously [66, 76]. When utilized in conjunction, the LHS sampled finite element model inputs and measured outputs are ranked and correlated to determine PRCCs. To determine which inputs had the greatest influence across all outputs, cumulative influence factors, previously defined by Feola et. al., were calculated for each input variable [66]. The cumulative influence factor indicates how influential an input variable is when all outputs are considered simultaneously. It is a normalized value, calculated by dividing the sum of each input variable's ranks by the highest possible sum of all ranks (this sum is equal to the number of input variables multiplied by the number of output variables). The largest possible CIF value is 1—indicating the most influential variable—while smaller values represent less influential parameters. In these studies, parameters with a CIF ≥ 0.5 were considered to meaningfully influence the chosen output variables.

3.0 The Role of Urethral Support in Female Urinary Continence and Passive Urethral Closure

3.1 Summary

Stress urinary incontinence (SUI) has been associated with urethral hypermobility and alterations in urethral and surrounding muscle and connective tissue material properties. Yet, mechanisms of the development of SUI and the failure of midurethral slings to correct SUI in many cases remain undefined. In Section 3.2, we utilized statistical shape modeling and dynamic endovaginal ultrasound to quantify differences in midsagittal urethral shape, motion, and deformation between women with no, mild, and severe SUI. In Section 3.3, we performed a sensitivity analysis on finite element simulations of Valsalva (urethral passive closure) to identify tissue material properties that significantly contributed to urethral shape, motion, and deformation at peak Valsalva. By measuring those variables associated with SUI severity in Section 3.2 in these simulations of urethral passive closure in Section 3.3, we were able to draw conclusions concerning which tissue material properties may contribute to various presentations of SUI.

3.2 Dynamic Measurements of Midsagittal Urethral Shape and Motion

3.2.1 Limitations of Existing Female Urinary Continence Theories

The mechanisms of urethral closure and dysfunction in the presence of female stress urinary incontinence (SUI) have been researched for decades, with a number of hypotheses being proposed to explain the role of the urethral support structures within these mechanisms. SUI severity depends upon the urethra's ability to maintain a robust urethral closure pressure during fluctuations in intra–abdominal pressure [13, 172]. This pressure is sustained through a combination of active and passive closure forces generated by the urethral wall and surrounding structures. At rest, closure forces resulting from submucosal vessels, elastin and connective tissue, smooth muscle, and neuronal stimuli seal off the lumen [78, 88]. During increases in intra–abdominal pressure, the levator ani muscles (actively) and the endopelvic fascia (passively) interact to further maintain continence and provide pelvic support [115].

The "hammock" [55] and "integral" [146] theories hypothesized that the downward force resulting from increased abdominal pressure applied to the bladder base and urethra during a cough would compress the urethra against the underlying layer of endopelvic fascia. It is the underlying stability of this layer formed by the connection of the endopelvic fascia and anterior vaginal wall to the arcus tendineus fascia pelvis and levator ani muscles that would allow this to happen rather than the position of the urethra relative to the pelvis [55, 146]. The abdominal pressure acts transversely across the urethra, altering the stresses such that its anterior wall is deformed toward its posterior wall, thereby helping to close the urethral lumen and prevent leakage caused by increased intravesical pressure [16]. Though this hypothesis has not been tested with biomechanical studies, the success rate of the mid–urethral sling was accepted universally as validation of these theories. However, this hypothesis does not explain the high failure rates observed several years after sling implantation.

A large, multicenter, comparative–effectiveness trial comparing retropubic versus transobturator mid–urethral slings for SUI (TOMUS study) showed the success rate of mid–urethral slings (regardless of surgical technique) at 2– and 5–year follow–up to be 77% and 50%, respectively [99, 155]. Additionally, the Stress Incontinence Surgical Treatment Efficacy Trial (SISTEr), a randomized controlled trial of the Burch urethropexy and the pubovaginal fascial sling, revealed success rates of 66% vs 49% for pubovaginal fascial sling vs

Burch urethropexy at 2–year follow–up and 30.8% vs 24.1% at 5–year follow–up, respectively [4, 37]. While it seems that the "hammock" and "integral" theories explain why slings can work, they do not explain why they fail in almost 50% of patients or why Burch procedures may work in only 24% of patients 5 years postoperatively. These increasing failure rates over time suggest that a sling's mechanical environment changes slowly after sling implantation, likely because of changes in the position and shape of the urethra resulting from alterations in the mechanical integrity of surrounding tissues. Improved understanding of urethral support structures is needed to improve sling designs and surgical techniques and cater these procedures to the anatomy and mechanical environment of individual women.

Pelvic floor ultrasound is a useful tool to visualize urethral shape and motion during voluntary squeeze and Valsalva. We aimed to use this tool to quantify the voluntary and passive closure mechanisms of the urethra by evaluating urethral shape and position/motion during these maneuvers in women with and without SUI. Our main hypothesis was that dynamic anterior compartment pelvic floor ultrasound would be able to visualize and resulting position measures be used to quantify the voluntary urethral closure mechanism (the effect of pelvic floor muscle squeeze) and passive urethral closure mechanism (how urethral support structures affect compression and motion of the urethra during Valsalva). A secondary hypothesis was that shape and position measures would be significantly influenced by SUI severity (no vs mild vs severe SUI).

3.2.2 Patient Recruitment, Ultrasound, and Urodynamics

This was a prospective cohort study, approved by the Institutional Review Board committee at NorthShore University HealthSystem. Women presenting to our tertiary urogynecology center for urodynamic study for urinary incontinence evaluation or preoperative assessment for occult urinary incontinence from October 2018–January 2019 were recruited to the study. We set two levels of screenings for exclusion criteria. The first was at recruitment before signing the consent form: Women with urinary retention, history of significant central nervous system disease, history of pelvic floor reconstructive surgery, history of anti–incontinence surgery including sling procedure, bulking agent injection, third–line treatment

for overactive bladder including intravesical botox injection, and sacral neuromodulation were excluded from the study. The second was at the end of the urodynamic study: Patients with newly diagnosed urinary retention (post–void residual $>$ 150 ml), low bladder capacity ($<$ 300 ml), high pressure detrusor instability (detrusor pressure $>$ 40 cmH2O), or a low maximum urethral closure pressure (MUCP $<$ 40 cmH2O) were excluded from the study. This allowed us to isolate the influence of the supportive tissues specifically on the urethral closure mechanisms as the influence of variable functional integrity of the bladder and urethra was removed. Recruited patients underwent a comprehensive interview including a detailed urinary symptoms assessment and pelvic examination with POP–Q assessment.

Imaging was obtained at the time of the study visit using the BK Medical BK3000 (Peabody, MA) X14L4 12 MHz transducer. All ultrasound studies were performed in the office setting with the patient in the dorsal lithotomy position, with hips flexed and abducted. No preparation was required, and no rectal or vaginal contrast was used. Patients voided before ultrasound imaging. The probe was inserted into the vagina in a neutral position. Three hundred sixty–degree endovaginal ultrasound volumes and dynamic ultrasound videos were saved for further analysis. It has been previously shown that the endovaginal probe has no adverse effect on anatomy compared to transperineal ultrasound [185].

The dynamic imaging takes a 5 second video of a midsagittal view of the bladder and urethra. The urethral meatus, pubic symphysis, and bladder neck were landmarks included in these videos. Patients were asked to perform a squeeze maneuver first and then a Valsalva maneuver. For the latter, patients were instructed to bear down as if having a bowel movement. Maneuvers were practiced with patients several times before starting the imaging to ensure they were performed correctly. Patients made multiple attempts at each maneuver. From those, the attempt that demonstrated the strongest squeeze/Valsalva was included in the analysis. Images were saved for future analysis. All measurements were performed during rest, squeeze, and maximum Valsalva.

Dynamic measurements included:

- Urethral length: the distance between the proximal opening of the urethra (to the bladder) to the urethral meatus along the lumen.
- Retropubic bladder neck angle: the angle between the line connecting the bladder neck to the inferior-posterior point of the pubic symphysis and the line following the superior edge of the pubic symphysis from that point (Figure 3.1).
- Urethral anterior–posterior diameter: the diameter of the urethra measured at the level of the meatus (5 mm from the distal end of the urethra), mid–urethra, and bladder neck (5 mm from the proximal end of the urethra) from the anterior border to the posterior border.
- Bladder neck–pubic bone angle: the angle between the line connecting the center of the bladder neck to the inferior–posterior pubic symphysis and the vertical (moving posteriorly from the pubic symphysis) line from that point.
- Meatus–pubic bone angle: the angle between the line connecting the center of the urethral meatus to the inferior–posterior pubic symphysis and that same vertical line.
- Urethral knee–pubic bone angle: the angle between the line connecting the posterior side of the urethral knee (approximately 1 cm from the distal urethral opening) to the inferior-posterior pubic symphysis and that same vertical pubic bone line (Figure 3.1).
- Urethral knee–pubic bone distance: the distance from the posterior urethral knee to the superior–inferior pubic symphysis point.

In a well–supported female, the distal urethra is thought to be relatively fixed at the level of the perineal membrane (the sheet of connective tissues immediately deep to the superficial perineal muscles) compared to the proximal urethra, which is relatively mobile. The fixation of the distal urethra results from attachments to the pubocervical fascia as well as direct attachment to the pubic bone via the perineal membrane and lower portions of the striated urogenital sphincter. The point of inflection between the mobile and immobile portion of the urethra has been called the "knee" of the urethra and lies approximately 1–2 cm from the meatus [128, 186]. This is the region referred to as the urethral knee in this study.

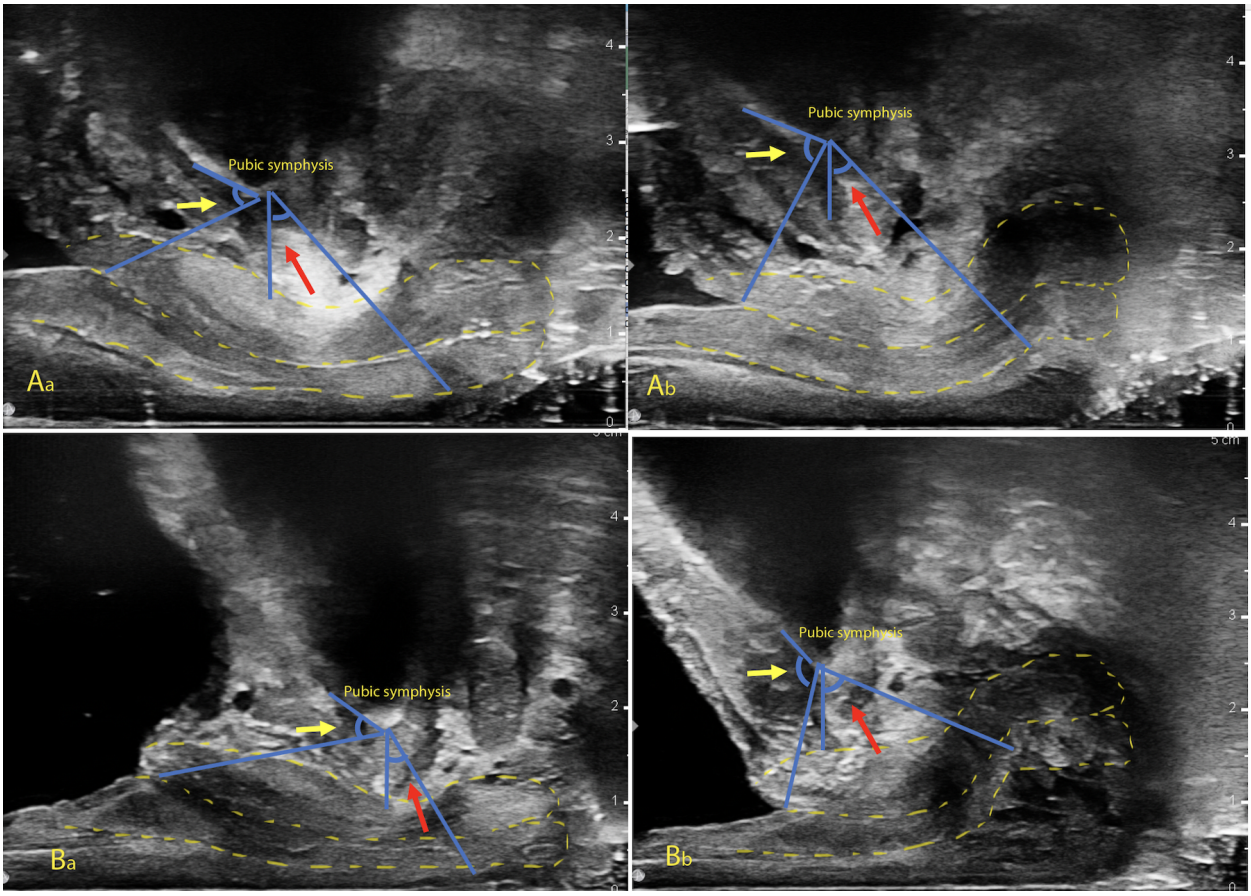

Figure 3.1: The anterior compartment visualized via dynamic endovaginal ultrasound in a urinary continent patient at (Aa) rest and (Ab) Valsalva and in a urinary incontinent patient at (Ba) rest and (Bb) Valsalva. The anterior and posterior urethral walls (outlined in yellow), retropubic bladder neck angles (yellow arrow), and urethral knee–pubic bone angles (red arrow) are indicated [164]. This figure was reprinted by permission from The International Urogynecological Association: Springer; International Urogynecology Journal; Megan R Routzong, Cecilia Chang, Roger P Goldberg, Steven D Abramowitch, and Ghazaleh Rostaminia. Urethral support in female urinary continence part 1: dynamic measurements of urethral shape and motion. *International Urogynecology Journal*, 2021; © 2021 The International Urogynecological Association.

This urodynamic study was performed according to the International Continence Society criteria, using a 7–Fr transurethral double–lumen catheter and an 8–Fr rectal/vaginal pressure sensor immediately following the previously described ultrasound imaging [2, 159]. The bladder filling rate was 80 ml/min. Patients were asked to indicate the first sensation

of bladder filling, the first desire to void, and the moment of a strong desire to void. Serial cough and Valsalva maneuvers were performed during the filling phase to replicate stress urinary leakage.

A urethral pressure profile, a graph indicating the intraluminal pressure along the length of the urethra, was obtained for each patient, and urethral closure pressure was calculated by the subtraction of the intravesical pressure from the urethral pressure. The maximum difference between the urethral pressure and the intravesical pressure was documented as the maximum urethral closure pressure. Permission to void was then given, and postvoid residual volume was determined through the catheter.

3.2.3 Statistical Shape Modelling of the Midsagittal Urethra

In this study, we carried out a statistical shape modeling workflow previously developed by our laboratory [168, 169]. Statistical shape modeling involves calculating corresponding points for each shape and minimizing the distances between them. Midsagittal urethral shapes were segmented from each patient's rest and maximum squeeze and Valsalva ultrasound images (Figure 3.1). Corresponding points were calculated across all patients and maneuvers using the deterministic atlas application within Deformetrica [33]. These corresponding shapes were imported into Mathematica v12.1.1.0 (Wolfram Research, Champaign, IL, USA) where the Procrustes method was used to align these shapes and remove differences due to scale, and a principal component analysis (PCA) quantified their variance [148]. Each PC, or mode of variation, is defined by an eigenvector and eigenvalue, but to determine which were significant and should be included in subsequent statistical analyses, a parallel analysis was used. Modes of variation were only considered significant if they explained a percent of the total variance greater than that explained by noise [46]. PC scores—the projections of subject–specific coordinates onto eigenvectors—were calculated only for significant modes of variation.

Patients with a normal maximum urethral closure pressure (MUCP $\geq$ 40 cmH2O) were categorized as having no, mild, or severe SUI based on their reported symptom severity and urodynamic study findings. Patients who denied having SUI (i.e., had an asymptomatic his-

tory) and did not demonstrate SUI during their urodynamic study (with any prolapse being supported) were considered continent and categorized into the "no SUI" group. Patients with SUI were categorized into the "mild SUI" group if they reported having urine leakage on average less than once daily or into the "severe SUI" group if they reported having urine leakage daily.

Patients' demographics, symptoms, POP–Q, urodynamics, and changes in dynamic ultrasound measurements were compared between these SUI groups using Fisher's exact or chi–squared test for categorical variables and ANOVA (parametric) or Kruskal–Wallis test (nonparametric) for continuous variables. Changes in dynamic ultrasound were quantified by subtracting values at rest from those at squeeze or Valsalva. Position and shape variables were evaluated together using a multinomial logistic regression. These analyses were conducted using SAS 9.4 (SAS Institute Inc., Cary, NC), and a p value < 0.05 was considered statistically significant. PC scores were analyzed with a two–way mixed MANOVA with univariate ANOVAs and Benjamini–Hochberg corrections (with a false discovery rate of 10%) performed post hoc in IBM SPSS Statistics v26 (International Business Machines Corporation, Armonk, NY, USA) to evaluate the influence of the between–subjects variable, SUI severity, and the within–subjects variable, maneuver (rest vs squeeze vs Valsalva). Results are depicted as mean $\pm$ standard deviation unless stated otherwise.

3.2.4 Patient Demographics and Urodynamic Study Results

One hundred one women met the initial inclusion criteria, and then 25 were excluded as they had an MUCP < 40 cmH2O while 76 were included with an MUCP ≥ 40 cmH2O. The latter patients were categorized as 23 with no SUI, 31 with mild SUI, and 22 with severe SUI. There were no statistically significant differences in age, parity, or BMI across SUI groups, though urge urinary incontinence and POP–Q point C did ($p = 0.0116$ and 0.0384, respectively) (Table 3.1). Volume with or without leak while sitting was largest in those with no SUI and smallest in those with severe SUI ($p = 0.0003$) while leak in UPP was more prevalent in those with SUI ($p < 0.0001$) (Table 3.2).

Table 3.1: Patient Demographics, symptoms, and POP-Q measures across SUI groups [164]. This table was reprinted by permission from The International Urogynecological Association: Springer; International Urogynecology Journal; Megan R Routzong, Cecilia Chang, Roger P Goldberg, Steven D Abramowitch, and Ghazaleh Rostaminia. Urethral support in female urinary continence part 1: dynamic measurements of urethral shape and motion. *International Urogynecology Journal*, 2021;

	Total		**No SUI**		**Mild SUI**		**Severe SUI**		**p-value**
	n	%	n	%	n	%	n	%	
of patients	76	100.00	23	30.26	31	40.79	22	28.95	
Demographics									
Age (years), mean ± SD	57.08 ± 13.02		57.09 ± 12.93		58.16 ± 13.49		55.55 ± 12.89		0.7759
Race									
African American	5	6.58	2	8.70	2	6.45	1	4.55	
Asian	0	0.00	0	0.00	0	0.00	0	0.00	
Caucasian	58	76.32	18	78.26	25	80.65	15	68.18	
Hispanic	8	10.53	2	8.70	3	9.68	3	13.64	0.9079
Indian	2	2.63	0	0.00	1	3.23	1	4.55	
Middle Eastern	1	1.32	0	0.00	0	0.00	1	4.55	
Mongolian	2	2.63	1	4.35	0	0.00	1	4.55	
BMI (kg/m^2), mean ± SD	28.35 ± 5.88		28.78 ± 6.88		27.79 ± 5.29		28.68 ± 5.74		0.7962
Gravidity, median (range)	2 (0-10)		2 (0-9)		2 (1-10)		2 (0-5)		0.7073
Parity, median (range)	2 (0-8)		2 (0-6)		2 (1-8)		2 (0-5)		0.7607
Symptoms, mean ± SD									
Urinary Frequency (inter-void intervals by hour)	2.59 ± 1.18		2.57 ± 1.14		2.53 ± 1.26		2.71 ± 1.16		0.8585
Urge Urinary Incontinence (incidents per day)	0.88 ± 1.42		0.70 ± 1.15		0.48 ± 0.93		1.61 ± 1.93		**0.0116**
Nocturia	1.07 ± 1.23		0.78 ± 0.98		1.03 ± 1.19		1.41 ± 1.46		0.2296
POP-Q, mean ± SD									
Ba	-0.95 ± 1.25		-0.59 ± 1.59		-1.00 ± 0.99		-1.27 ± 1.12		0.1772
C	-5.36 ± 2.19		-4.74 ± 2.34		-5.13 ± 2.34		-6.32 ± 1.45		**0.0384**
Gh	3.75 ± 0.66		3.78 ± 0.77		3.82 ± 0.67		3.61 ± 0.51		0.5057
PB	2.96 ± 0.46		3.00 ± 0.50		3.00 ± 0.34		2.86 ± 0.56		0.5096
Bp	-1.24 ± 1.00		-1.54 ± 1.05		-0.92 ± 0.88		-1.39 ± 1.01		0.0531

Statistically significant p-values shown in **bold**.

Table 3.2: Urodynamic Study Measures across SUI groups [164]. This table was reprinted by permission from The International Urogynecological Association: Springer; International Urogynecology Journal; Megan R Routzong, Cecilia Chang, Roger P Goldberg, Steven D Abramowitch, and Ghazaleh Rostaminia. Urethral support in female urinary continence part 1: dynamic measurements of urethral shape and motion. *International Urogynecology Journal*, 2021; © 2021 The International Urogynecological Association.

	Total (N=76)		**No SUI (N=23)**		**Mild SUI (N=31)**		**Severe SUI (N=22)**		**p-value**
	n	mean ± SD or %	n	mean ± SD or %	n	mean ± SD or %	n	mean ± SD or %	
First Sense									
Sitting	73	121.71 ± 81.44	22	149.91 ± 92.53	31	113.48 ± 74.98	20	103.45 ± 73.56	0.1381
Standing	24	385.88 ± 106.99	15	376.33 ± 131.01	5	378.60 ± 57.07	4	430.75 ± 9.43	0.6747
Strong Desire									
Sitting	69	371.62 ± 143.62	22	418.00 ± 161.75	28	355.64 ± 138.06	19	341.47 ± 121.73	0.1768
Standing	23	487.65 ± 126.91	14	495.64 ± 156.64	5	446.20 ± 57.35	4	511.50 ± 58.95	0.7135
Capacity									
Sitting	75	498.43 ± 130.87	22	518.77 ± 135.32	31	502.19 ± 143.10	22	472.77 ± 107.90	0.5021
Standing	25	586.60 ± 153.79	15	601.20 ± 178.94	6	537.83 ± 101.74	4	605.00 ± 127.48	0.6901
VLPP with leak (cmH2O)									
Sitting	37	106.78 ± 39.89	0		19	109.26 ± 41.63	18	104.17 ± 39.00	0.7034
Standing	12	101.33 ± 18.27	2	96.00 ± 25.46	5	102.60 ± 22.72	5	102.20 ± 14.92	0.9286
VLPP without leak (cmH2O)									
Sitting	38	91.21 ± 31.63	23	94.00 ± 36.14	11	83.73 ± 24.52	4	95.75 ± 21.45	0.6572
Standing	18	100.78 ± 22.51	16	101.38 ± 23.61	1	106.00	1	86.00	0.8009
Volume with or without leak									
Sitting	76	343.99 ± 159.47	23	443.78 ± 162.13	31	327.23 ± 144.40	22	263.27 ± 123.92	**0.0003**
Standing	30	487.77 ± 170.36	18	532.94 ± 190.29	6	432.67 ± 78.81	6	407.33 ± 142.29	0.2030
DO Pressure (cmH2O)									
Sitting	71	11.92 ± 11.47	20	12.10 ± 11.77	30	13.17 ± 11.49	21	9.95 ± 11.44	0.6200
Standing	25	26.80 ± 62.44	13	17.92 ± 14.00	7	13.00 ± 16.15	5	11.40 ± 13.50	0.5577
DO Volume									
Sitting	53	425.43 ± 158.69	16	483.69 ± 160.63	25	429.16 ± 153.20	12	340.00 ± 140.43	0.0564
Standing	17	458.88 ± 229.08	9	545.56 ± 904.21	5	302.80 ± 238.93	3	459.00 ± 210.07	0.1670
MUCP (cmH2O)	76	68.67 ± 24.72	23	75.48 ± 34.49	31	69.65 ± 19.92	22	60.18 ± 15.55	0.1108
Leak in UPP									
Yes	39	52.70	0	0.00	21	72.41	18	81.82	**<0.001**
No	35	47.30	23	100.00	8	27.59	4	18.18	

Statistically significant p-values shown in **bold**.

VLPP, Valsalva leak point pressure; DO, detrusor overactivity; MUCP, maximum urethral closure pressure; UPP, urethral pressure profile.

3.2.5 Dynamic Ultrasound Differences with Maneuver and SUI Severity

Squeeze maneuvers elongated the urethra by 9% of its resting length and compressed the distal, mid–, and proximal urethra by 32%, 20%, and 3.5% of its original anterior–posterior diameters (Table 3.3, Figure 3.2A). The squeeze lifted the bladder neck and closed the retropubic angle by 26%, increased the length of the urethra behind the pubic symphysis by 30%, and decreased the length in front of the pubic symphysis by 8%. There were no statistically significant differences between continent and SUI patients.

Valsalva maneuvers, on the other hand, shortened the urethra by 8% of its resting length, compressing the urethra longitudinally, which increased the urethral anterior–posterior diameters at the distal, mid–, and proximal urethra by 16%, 23%, and 27% of its resting thickness, respectively (Table 3.3, Figure 3.2A). The superior–inferior swinging motion of the bladder neck and the urethral knee about the pubic symphysis were, on average, 44° (77% change relative to rest) and 20° (98% change relative to rest), respectively. This motion opened the retropubic bladder neck angle by 41° (a 96% increase from rest), reducing the retropubic urethral length by 66.5% and increasing the infrapubic urethral length by 56%.

While comparing across SUI groups, changes in three measurements from rest to Valsalva differed significantly: the retropubic bladder neck angle ($p = 0.0157$), infrapubic urethral length ($p = 0.0154$), and urethral knee–pubic bone angle ($p = 0.0098$) (Table 3.3, Figure 3.2B). For all three measures, the difference between rest and Valsalva increased with SUI severity. The receiver–operating characteristic (ROC) curves for these three ultrasound measurements showed a relatively strong sensitivity and specificity to predict the presence of severe SUI (Figure 3.3). We entered the calculated threshold into the multinomial logistic regression model for predictors of the presence of SUI symptoms, and a urethral knee–pubic bone angle $> 18°$ was associated with the presence of severe SUI (OR = 7.969, $p = 0.0172$) (Table 3.4).

Table 3.3: Dynamic ultrasound measurements across SUI groups during squeeze and Valsalva [164]. This table was reprinted by permission from The International Urogynecological Association: Springer; International Urogynecology Journal; Megan R Routzong, Cecilia Chang, Roger P Goldberg, Steven D Abramowitch, and Ghazaleh Rostaminia. Urethral support in female urinary continence part 1: dynamic measurements of urethral shape and motion. *International Urogynecology Journal*, 2021; © 2021 The International Urogynecological Association.

	Total (N=76)			No SUI (N=23)			Mild SUI (N=31)			Severe SUI (N=22)			p-value[1]
	Rest	Maneuver	Change (%)	Rest	Maneuver	Change	Rest	Maneuver	Change	Rest	Maneuver	Change	
Squeeze													
Urethral Length (cm)	3.90 ± 0.48	4.24 ± 0.52	8.96 ± 7.85	4.01 ± 0.60	4.29 ± 0.65	0.28 ± 0.25	3.91 ± 0.44	4.25 ± 0.47	0.34 ± 0.31	3.79 ± 0.37	4.19 ± 0.44	0.40 ± 0.28	0.3414
Meatus AP Diameter (cm)	1.20 ± 0.27	0.81 ± 0.28	-32.12 ± 20.03	1.23 ± 0.26	0.88 ± 0.29	-0.35 ± 0.25	1.21 ± 0.27	0.77 ± 0.24	-0.45 ± 0.29	1.16 ± 0.30	0.80 ± 0.32	-0.37 ± 0.23	0.3648
Mid-Urethra AP Diameter (cm)	1.24 ± 0.31	0.97 ± 0.26	-20.49 ± 15.87	1.26 ± 0.26	1.07 ± 0.24	-0.19 ± 0.15	1.20 ± 0.27	0.95 ± 0.27	-0.25 ± 0.21	1.27 ± 0.41	0.92 ± 0.26	-0.36 ± 0.34	0.0846
Bladder Neck AP Diameter (cm)	1.40 ± 0.20	1.35 ± 0.20	-3.46 ± 10.35	1.39 ± 0.27	1.39 ± 0.27	0.01 ± 0.19	1.42 ± 0.14	1.35 ± 0.15	-0.07 ± 0.12	1.39 ± 0.21	1.29 ± 0.17	0.09 ± 0.13	0.0620
Retropubic Bladder Neck Angle (°)	55.39 ± 20.93	40.61 ± 18.77	-26.20 ± 21.24	57.34 ± 23.57	44.33 ± 24.51	-13.00 ± 10.46	54.18 ± 21.45	39.34 ± 16.52	-14.84 ± 14.86	55.03 ± 18.06	38.55 ± 14.89	-16.47 ± 17.60	0.7349
Retropubic Urethral Length (cm)	1.97 ± 0.61	2.44 ± 0.66	29.68 ± 40.14	2.09 ± 0.68	2.43 ± 0.78	0.34 ± 0.30	1.90 ± 0.61	2.40 ± 0.57	0.51 ± 0.39	1.97 ± 0.56	2.52 ± 0.64	0.55 ± 0.46	0.1601
Infrapubic Urethral Length (cm)	1.88 ± 0.55	1.72 ± 0.57	-7.86 ± 17.38	1.88 ± 0.64	1.74 ± 0.66	-0.14 ± 0.34	1.99 ± 0.46	1.79 ± 0.53	-0.20 ± 0.38	1.75 ± 0.56	1.60 ± 0.51	-0.15 ± 0.41	0.8449
Valsalva													
Urethral Length (cm)	3.90 ± 0.48	3.58 ± 0.53	-8.00 ± 10.26	4.01 ± 0.60	3.60 ± 0.58	-0.41 ± 0.36	3.91 ± 0.44	3.65 ± 0.49	-0.26 ± 0.41	3.79 ± 0.37	3.48 ± 0.53	-0.31 ± 0.47	0.4283
Meatus AP Diameter (cm)	1.20 ± 0.27	1.35 ± 0.18	16.44 ± 26.52	1.23 ± 0.26	1.44 ± 0.22	0.21 ± 0.28	1.21 ± 0.27	1.31 ± 0.14	0.12 ± 0.21	1.16 ± 0.30	1.29 ± 0.16	0.11 ± 0.26	0.3758
Mid–Urethra AP Diameter (cm)	1.24 ± 0.31	1.45 ± 0.27	22.58 ± 26.45	1.26 ± 0.26	1.54 ± 0.32	0.28 ± 0.25	1.20 ± 0.27	1.37 ± 0.25	0.19 ± 0.24	1.27 ± 0.41	1.45 ± 0.20	0.19 ± 0.37	0.5272
Bladder Neck AP Diameter (cm)	1.40 ± 0.20	1.79 ± 2.47	27.17 ± 162.54	1.39 ± 0.27	2.43 ± 4.33	1.04 ± 4.30	1.42 ± 0.14	1.51 ± 0.23	0.08 ± 0.24	1.39 ± 0.21	1.46 ± 0.26	0.07 ± 0.19	0.3408
Retropubic Bladder Neck Angle (°)	55.39 ± 20.93	96.66 ± 23.67	95.97 ± 75.02	57.34 ± 23.57	88.33 ± 22.71	30.99 ± 23.58	54.18 ± 21.45	97.93 ± 23.08	44.81 ± 21.78	55.03 ± 18.06	103.36 ± 23.90	48.34 ± 15.30	**0.0157**
Retropubic Urethral Length (cm)	1.97 ± 0.61	0.74 ± 0.70	-66.47 ± 30.25	2.09 ± 0.68	1.04 ± 0.68	-1.05 ± 0.61	1.90 ± 0.61	0.63 ± 0.69	-1.29 ± 0.64	1.97 ± 0.56	0.59 ± 0.66	-1.38 ± 0.44	0.1535
Infrapubic Urethral Length (cm)	1.88 ± 0.55	2.79 ± 0.67	56.29 ± 45.23	1.88 ± 0.64	2.48 ± 0.61	0.60 ± 0.55	1.99 ± 0.46	3.01 ± 0.66	1.04 ± 0.61	1.75 ± 0.56	2.80 ± 0.65	1.05 ± 0.58	**0.0154**
Bladder Neck–Pubic Bone Angle (°)	64.04 ± 18.42	19.85 ± 27.03	-76.97 ± 53.28	65.40 ± 22.00	28.25 ± 28.37	-37.16 ± 21.27	62.23 ± 18.14	18.32 ± 24.87	-44.78 ± 22.55	65.06 ± 15.28	13.40 ± 27.39	-51.66 ± 23.42	0.1081
Meatus–Pubic Bone Angle (°)	55.97 ± 14.26	69.66 ± 11.51	30.68 ± 33.22	54.49 ± 18.22	65.97 ± 12.93	10.35 ± 13.2	57.96 ± 12.78	69.57 ± 11.87	12.36 ± 13.75	54.84 ± 11.79	73.46 ± 8.36	18.63 ± 12.83	0.1146
Urethral Knee–Pubic Bone Angle (°)	25.74 ± 12.68	46.15 ± 12.93	98.08 ± 74.77	26.07 ± 13.35	41.01 ± 13.87	14.94 ± 12.34	26.88 ± 14.78	46.70 ± 12.34	20.65 ± 14.27	23.92 ± 8.76	50.58 ± 11.35	26.65 ± 9.33	**0.0098**
Urethral Knee–Pubic Bone Distance (cm)	2.06 ± 0.47	2.59 ± 0.45	30.66 ± 28.73	2.16 ± 0.59	2.56 ± 0.50	0.40 ± 0.52	2.07 ± 0.42	2.65 ± 0.48	0.59 ± 0.43	1.94 ± 0.40	2.56 ± 0.37	0.61 ± 0.44	0.2284

[1]Comparison of Change across SUI groups.

Statistically significant p-values are shown in **bold**.

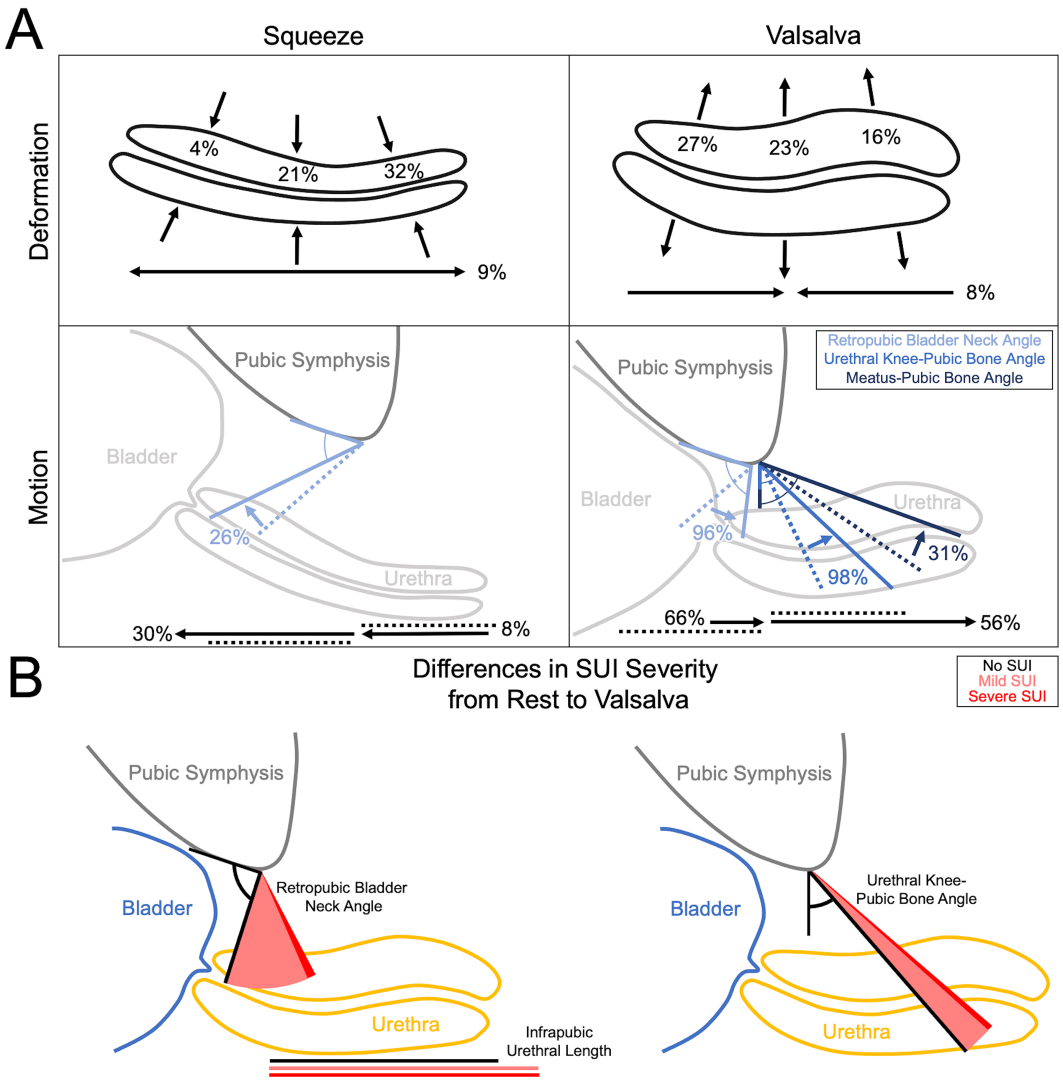

Figure 3.2: Visual summarizations of the results from the shape and position measures taken via dynamic anterior compartment ultrasound. A) Average (across no, mild, and severe SUI groups) axial and longitudinal urethral deformations and motions with respect to the pubic symphysis are depicted during squeeze and Valsalva. For the motions, dotted lines portray the rest values, solid lines the maneuver values, and arrows the direction from rest to the maneuver values. B) The only significant differences observed across SUI severity groups (change in the retropubic bladder neck angle, infrapubic urethral length, and urethral knee–pubic bone angle from rest to Valsalva) are illustrated. Black indicates the angle/length of the no SUI group at Valsalva, while pink and red represent the change from rest to Valsalva for the mild and severe SUI groups, respectively. This depiction highlights the change from rest to Valsalva as if all groups had started at the same rest value [164]. This figure was reprinted by permission from The International Urogynecological Association: Springer; International Urogynecology Journal; Megan R Routzong, Cecilia Chang, Roger P Goldberg, Steven D Abramowitch, and Ghazaleh Rostaminia. Urethral support in female urinary continence part 1: dynamic measurements of urethral shape and motion. *International Urogynecology Journal*, 2021; © 2021 The International Urogynecological Association.

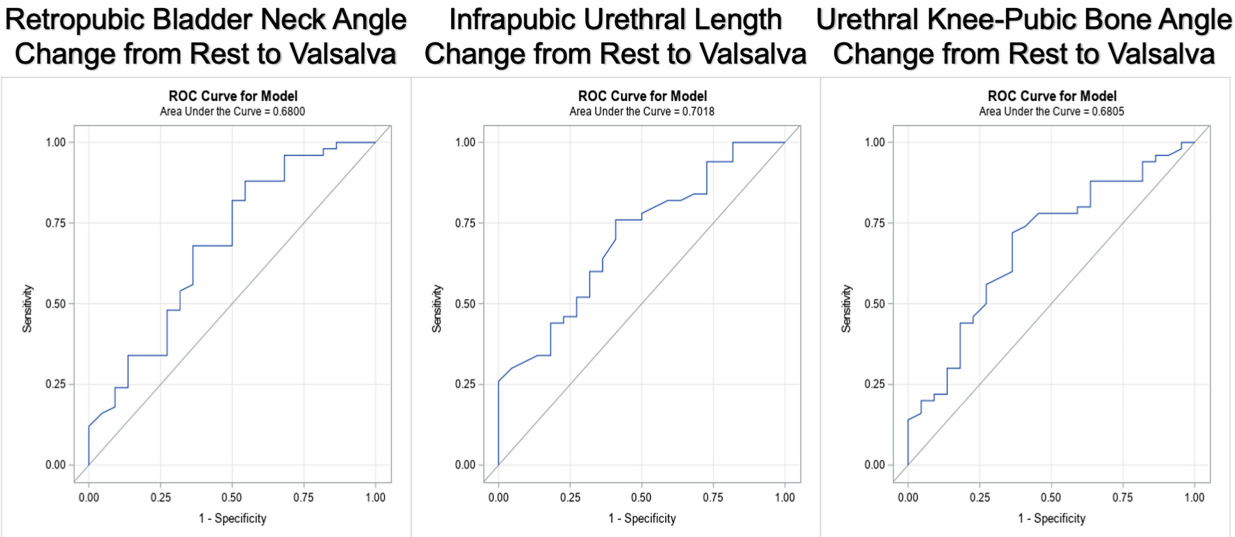

	Presence of Symptoms	
Changes from Rest to Strain	**AUC (95% CI)**	**Optimal Threshold (Se, Sp)**
Retropubic Bladder Neck Angle	0.68 (0.54-0.82)	37.0 (68.0, 63.6)
Infrapubic Urethral Length	0.70 (0.57-0.83)	0.6 (76.0, 59.1)
Urethral Knee-Pubic Bone Angle	0.68 (0.54-0.82)	18.0 (72.0, 63.6)

Figure 3.3: The receiver operating characteristic (ROC) curves for the three variables that had dynamic ultrasound measures that differed across SUI severity groups when looking at the change from rest to Valsalva. The area under the curve (AUC) and the sensitivity (Se) and specificity (Sp) of the optimal threshold are given in the table below the ROC curves [164]. This figure was reprinted by permission from The International Urogynecological Association: Springer; International Urogynecology Journal; Megan R Routzong, Cecilia Chang, Roger P Goldberg, Steven D Abramowitch, and Ghazaleh Rostaminia. Urethral support in female urinary continence part 1: dynamic measurements of urethral shape and motion. *International Urogynecology Journal*, 2021; © 2021 The International Urogynecological Association.

3.2.6 Shape Differences with Maneuver and SUI Severity

Twelve modes of variation were deemed significant to explain the variance in shape observed in this study, both between patients and with each maneuver. Modes 1–12 are ranked based on the variance they describe: 51%, 18%, 7.0%, 4.6%, 3.3%, 2.8%, 2.5%, 1.7%, 1.4%, 1.3%, 1.1%, and 0.92%, respectively. Both SUI severity and maneuver significantly influenced the entire urethral shape ($p < 0.001$). The shape differences between maneuvers were significant for modes 1 and 2, specifically ($p < 0.001$) (Table 3.5). Based on the ranked order of our modes, this indicates that shape changes of the urethra during these maneuvers are responsible for more variation than the modes that distinguish between SUI severity.

Table 3.4: Multinomial logistic regression predicting the presence of SUI symptoms with no SUI as the reference [164]. This table was reprinted by permission from The International Urogynecological Association: Springer; International Urogynecology Journal; Megan R Routzong, Cecilia Chang, Roger P Goldberg, Steven D Abramowitch, and Ghazaleh Rostaminia. Urethral support in female urinary continence part 1: dynamic measurements of urethral shape and motion. *International Urogynecology Journal*, 2021; © 2021 The International Urogynecological Association.

	Mild SUI				**Severe SUI**			
	Odds Ratio	95% CI		p-value	Odds Ratio	95% CI		p-value
Age (years)	1.051	0.994	1.111	0.0777	1.034	0.974	1.098	0.2671
BMI (kg/m^2)	0.990	0.888	1.103	0.8536	1.030	0.918	1.155	0.6197
Changes from Rest to Strain								
Retropubic Bladder Neck Angle (>37.0s $\leq$ 37.0	2.077	0.539	8.008	0.2885	1.630	0.371	7.160	0.5173
Infrapubic Urethral Length (>0.6 cm vs $\leq$ 0.6cm)	2.892	0.695	12.029	0.1441	3.027	0.590	15.528	0.1843
Urethral Knee–Pubic Bone Angle (>18.0s $\leq$ 18.0	1.624	0.393	6.717	0.5032	7.969	1.444	43.975	**0.0172**

Statistically significant p-values shown in **bold**.

SUI, stress urinary incontinence; CI, confidence interval.

This suggests that shape differences identifying SUI severity based on clinical measurement alone are likely masked by the more gross shape changes caused by the maneuver. In terms of maneuver, mode 1 qualitatively described variation in "c"–shaped concavity and mode 2 variation in "s"–shaped concavity, which exists in all SUI severity groups (Figure 3.4). During squeeze, the urethra became more "c" shaped (hugging the pubic bone) with distal urethral pinching, and, during Valsalva, the urethra became more "s" shaped with distal urethral wall thickening in all SUI groups (Figure 3.5).

SUI severity was significant for modes 5 (p = 0.001), 7 (p = 0.001), and 11 (p = 0.009) specifically (Table 3.5). For these modes, the no and severe SUI groups differed significantly (p = 0.001, 0.002, and 0.007, respectively), and the continent and mild SUI groups differed for mode 7 (p = 0.007) (Table 3.5). Modes 5, 7, and 11 describe variation in the proportional wall thickness of specific regions of the urethra, indicative of more or less "pinching" or "squeezing" across SUI severity, regardless of maneuver (Figure 3.6). Together, these modes

Table 3.5: Univariate ANOVAs (evaluating the significance of maneuver and SUI severity) and post-hoc comparisons (evaluating the differences between no, mild, and severe SUI) of the PC scores of significant modes of variation from the statistical shape model. To be considered significant, p-values had to be greater than corresponding Benjamini-Hochberg critical values [164]. This table was reprinted by permission from The International Urogynecological Association: Springer; International Urogynecology Journal; Megan R Routzong, Cecilia Chang, Roger P Goldberg, Steven D Abramowitch, and Ghazaleh Rostaminia. Urethral support in female urinary continence part 1: dynamic measurements of urethral shape and motion. *International Urogynecology Journal*, 2021; © 2021 The International Urogynecological Association.

	p-value	Rank	Benjamini-Hochberg Critical Value		p-value	Rank	Benjamini-Hochberg Critical Value
Univariate ANOVAs				***Post-hoc Multiple Comparisons***			
Maneuver Mode 1	**<0.001**	1	0.004	Mode 5: No vs Severe SUI	**0.001**	1	0.011
Maneuver Mode 2	**<0.001**	2	0.008	Mode 7: No vs Severe SUI	**0.002**	2	0.022
SUI Severity Mode 7	**0.001**	3	0.013	Mode 7: No vs Mild SUI	**0.007**	3	0.033
SUI Severity Mode 5	**0.001**	4	0.017	Mode 11: No vs Severe SUI	**0.007**	4	0.044
SUI Severity Mode 11	**0.009**	5	0.021	Mode 5: Mild vs Severe SUI	0.080	5	0.056
Maneuver Mode 11	0.028	6	0.025	Mode 11: Mild vs Severe SUI	0.147	6	0.067
SUI Severity Mode 9	0.072	7	0.029	Mode 5: No vs Mild SUI	0.217	7	0.078
Maneuver Mode 8	0.134	8	0.033	Mode 11: No vs Mild SUI	0.496	8	0.089
SUI Severity Mode 4	0.141	9	0.038	Mode 7: Mild vs Severe SUI	1.000	9	0.100
SUI Severity Mode 1	0.179	10	0.042				
Maneuver Mode 6	0.192	11	0.046				
SUI Severity Mode 12	0.229	12	0.050				
SUI Severity Mode 10	0.284	13	0.054				
SUI Severity Mode 2	0.374	14	0.058				
Maneuver Mode 9	0.377	15	0.063				
Maneuver Mode 7	0.457	16	0.067				
SUI Severity Mode 8	0.496	17	0.071				
Maneuver Mode 4	0.554	18	0.075				
Maneuver Mode 5	0.751	19	0.079				
Maneuver Mode 12	0.759	20	0.083				
Maneuver Mode 10	0.805	21	0.088				
Maneuver Mode 3	0.913	22	0.092				
SUI Severity Mode 3	0.950	23	0.096				
SUI Severity Mode 6	0.997	24	0.100				

Statistically significant p-values shown in **bold**.

describe less "c"–shaped concavity during squeeze and more "s"–shaped concavity, urethral wall thickening at the urethral knee, and proximal urethral "pinching" during Valsalva in mild and severe SUI urethras compared with those in the no SUI group (Figure 3.5). At rest, those with severe SUI have proportionally thicker mid–urethras with an overall straighter urethral shape.

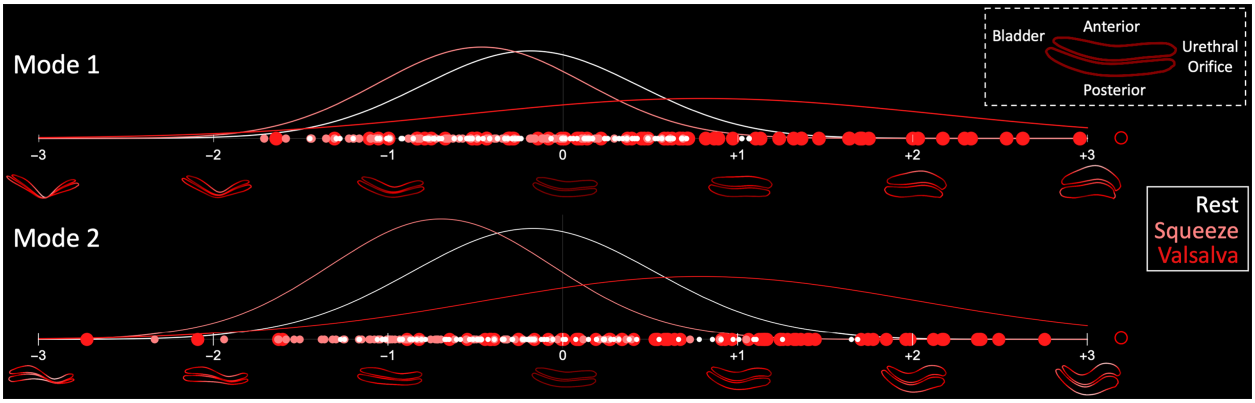

Figure 3.4: An illustration of modes 1 and 2 with normal curves depicting the distribution of all rest, squeeze, and Valsalva PC scores (color-coded as indicated in the right middle legend). Individual PC scores are depicted by points with outliers as open circles. The color map on the shapes (white showing the greatest displacement from the mean shape, located at 0 for each mode) reveal the aspects of urethral shape being described by each mode. The normal curves demonstrate a shift towards the left from rest to squeeze and a shift towards the right from rest to Valsalva. Relevant anatomy and the urethra's general orientation are shown in the top right legend [164]. This figure was reprinted by permission from The International Urogynecological Association: Springer; International Urogynecology Journal; Megan R Routzong, Cecilia Chang, Roger P Goldberg, Steven D Abramowitch, and Ghazaleh Rostaminia. Urethral support in female urinary continence part 1: dynamic measurements of urethral shape and motion. *International Urogynecology Journal*, 2021; © 2021 The International Urogynecological Association.

The multinomial logistic regression evaluating position and shape measures to compare mild and severe SUI patients to those with no SUI demonstrated that proportionally thicker walls at the mid–urethra and urethral knee (described by modes 5, 7, and 11) were significant predictors of severe SUI as indicated by their respective odds ratios (OR = 0.378, 0.181, and 5.490) and p–values (p = 0.0029, $<$ 0.0001, and 0.0034) (Table 3.6).

3.2.7 Dynamic Anterior Compartment Ultrasound Effectively Captures Urethral Shape, Motion, and Variations with SUI Severity

Our study used dynamic anterior compartment endovaginal ultrasound to evaluate urethral shape and position changes resulting from squeeze and Valsalva maneuvers and how those changes are altered in the presence of SUI. Regardless of SUI severity, the urethra moved superiorly, stretched longitudinally, and thinned axially during squeeze, resulting in

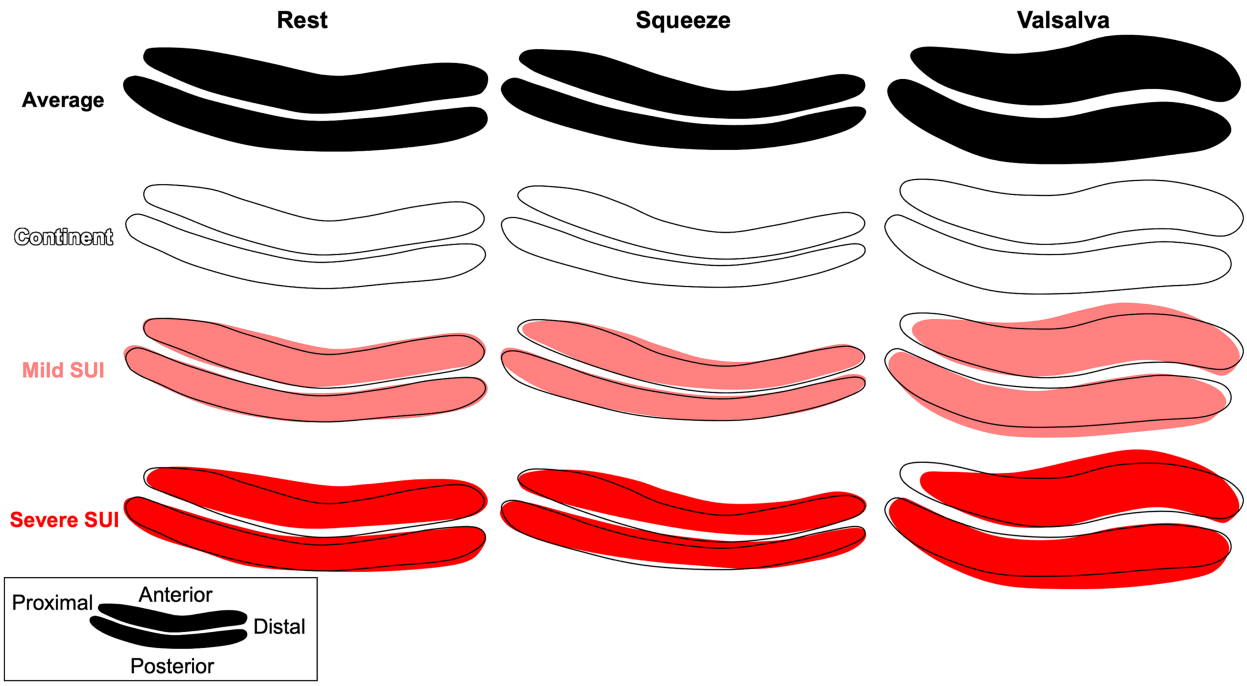

Figure 3.5: The average shape from each maneuver and SUI severity subgroup calculated using modes 1, 2, 5, 7, and 11 to emphasize differences due to maneuver and SUI while ignoring general population shape variation not attributed to a specific variable in this study. The black lines on the mild and severe SUI shapes depict the corresponding no SUI/continent shape so differences due to SUI (such as increased proportional thickness in the mid–urethra) can be easily observed. Relevant anatomy and the urethra's general orientation are shown in the bottom left legend [164]. This figure was reprinted by permission from The International Urogynecological Association: Springer; International Urogynecology Journal; Megan R Routzong, Cecilia Chang, Roger P Goldberg, Steven D Abramowitch, and Ghazaleh Rostaminia. Urethral support in female urinary continence part 1: dynamic measurements of urethral shape and motion. *International Urogynecology Journal*, 2021; © 2021 The International Urogynecological Association.

an overall more "c" shape. During Valsalva, inferior urethral swinging resulted in longitudinal compression (reducing the urethral length and thickening the urethral wall) and an overall "s" shaped urethra with a "knee" at the level of the perineal membrane.

During a voluntary squeeze, the striated muscles of the urethra (three distinct muscles: m. sphincter urethrae, m. compressor urethrae, and m. urethrovaginal sphincter) [139] and the levator ani muscles that laterally attach to the arcus tendineus fascia pelvis contract to close the urethral lumen [131]. The importance of the compressor urethrae to continence is demonstrated by the occurrence of SUI after radical vulvectomy [152] when the distal

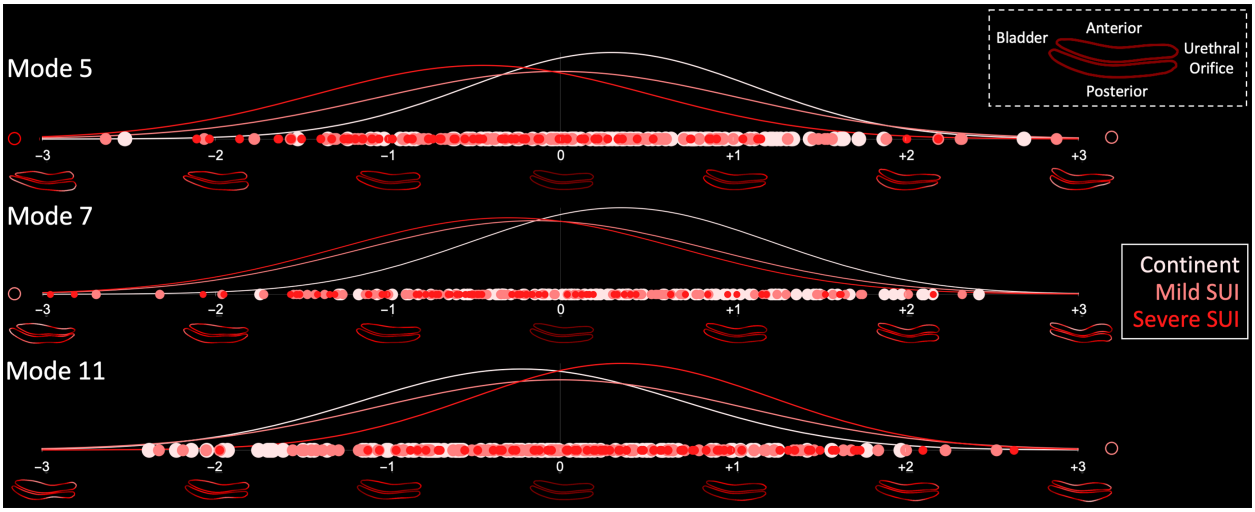

Figure 3.6: An illustration of modes 5, 7, and 1 with normal curves depicting the distribution of all no, mild, and severe SUI PC scores (color-coded as indicated in the right middle legend). Individual PC scores are depicted by points with outliers as open circles. The color map on the shapes (white showing the greatest displacement from the mean shape, located at 0 for each mode) reveal the aspects of urethral shape being described by each mode. Mode 5 demonstrates a shift between no and severe SUI shapes while the mild straddle both distributions. Mode 7 demonstrates a shift between no and both SUI groups—mild and severe SUI distributions are almost identical. Finally, mode 11, like mode 5, only demonstrates a difference between no and severe SUI shape distributions. Relevant anatomy and the urethra's general orientation are shown in the top right legend [164]. This figure was reprinted by permission from The International Urogynecological Association: Springer; International Urogynecology Journal; Megan R Routzong, Cecilia Chang, Roger P Goldberg, Steven D Abramowitch, and Ghazaleh Rostaminia. Urethral support in female urinary continence part 1: dynamic measurements of urethral shape and motion. *International Urogynecology Journal*, 2021; © 2021 The International Urogynecological Association.

urethra, containing the compressor urethrae and urethrovaginal sphincter, is excised. This is thought to provide a back-up mechanism for continence, aiding the 50% of continent, climacteric women who demonstrate bladder neck incompetence with coughing [192]. Using dynamic endovaginal anterior compartment ultrasound during squeeze, we could visualize and quantify urethral elongation, elevation to a more retropubic position, axial compression, bladder neck lift, and closure of the retropubic angle. Although urethral motion did not differ with SUI, shape did. The less prominent "c"–shaped concavity observed in women with severe SUI at rest and during squeeze may be indicative of less effective muscle contraction. These findings are important for evaluating active closure mechanisms, identifying candidates for pelvic floor physical therapy, and following up with the response to physical therapy.

Table 3.6: Multinomial logistic regression for the predictors of severe SUI with no SUI as the reference [164]. This table was reprinted by permission from The International Urogynecological Association: Springer; International Urogynecology Journal; Megan R Routzong, Cecilia Chang, Roger P Goldberg, Steven D Abramowitch, and Ghazaleh Rostaminia. Urethral support in female urinary continence part 1: dynamic measurements of urethral shape and motion. *International Urogynecology Journal*, 2021; © 2021 The International Urogynecological Association.

	Odds Ratio	**95% Confidence Interval**		**p-value**
Mode 1	1.066	0.798	1.424	0.6638
Mode 2	1.246	0.853	1.821	0.2554
Mode 5	0.378	0.199	0.716	**0.0029**
Mode 7	0.181	0.078	0.421	**<0.0001**
Mode 11	5.490	1.759	17.136	**0.0034**
Retropubic Bladder Neck Angle	1.005	0.967	1.043	0.8097
Infrapubic Urethral Length	0.410	0.137	1.225	0.1104
Bladder Neck–Pubic Bone Angle	0.998	0.955	1.043	0.9254
Urethral Knee–Pubic Bone Angle	1.026	0.991	1.061	0.1486

Statistically significant p-values are shown in **bold**.

During Valsalva, we observed a synchronized, though limited, inferior swinging motion of the urethra about the pubic symphysis. Patients with SUI experienced more exaggerated swinging of the bladder neck and urethral knee that resulted in proportionally thicker urethras, suggesting that controlled swinging is part of the urethral passive closure mechanism. This phenomenon is not adequately described by existing theories concerning female urinary continence and will be explored further in Part 2 of this work (see Section 3.3).

3.2.8 The Swing Theory for Passive Female Urinary Continence

Assuming the urethra is primarily supported proximally by connections from the endopelvic fascia and anterior vaginal wall to the arcus tendineus fasciae pelvis and levator

ani muscles (via paraurethral connective tissue) and distally at the urethral knee to the inferior pubic rami (via the perineal membrane), a simulated increase in intra–abdominal pressure naturally results in this coordinated swinging motion with urethral shape deformations and displacements resembling those quantified via ultrasound in the present study as demonstrated by Part 2 (Section 3.3) of this study (Figure 3.7). This demonstrates how this urethral swinging caused by these support structures contributes to the passive closure mechanism. As the bladder neck swings toward the distal supports, the urethral knee and meatus also swing, but not quite as much. This results in (1) longitudinal compression of the urethra and (2) a kink or "knee" that forms in the urethra at the level of the perineal membrane.

Theoretically, concomitant smooth muscle contraction with passive longitudinal compression closes the urethral lumen [185]. This explains the swinging motion and shape changes observed during Valsalva, but not why excessive swinging and a proportionally thicker shape corresponds with SUI. It is possible that reduced urethral muscle tone allows the excessive longitudinal compression observed in women with SUI and may explain why that compression does not always result in the smooth muscle contraction that aids continence mechanisms. It is also likely that connective tissue integrity contributes to the passive urethral closure mechanism—lack of which may describe why the urethras of women with SUI swing further during Valsalva. It is thought that the urethral knee created by this swinging motion may cause a kink in the urethra that stops urine flow as a last resort to prevent leakage. We would hypothesize that some combination of reduced urethral muscle tone and connective tissue integrity renders the urethral knee ineffective, meaning more swinging is needed to result in a kink that is effective.

In summary, the urinary continence mechanism is a complex interplay of both dynamic and passive support and sphincteric function. This suggests that symptoms of SUI could result from various and even multiple pathophysiologic insults. As a result, SUI likely does not result from a single anatomical defect; therefore, a "one surgery fits all" treatment option is not logical. This study proved that urethral voluntary and passive closure mechanisms can be evaluated in detail using dynamic anterior compartment pelvic floor ultrasound. Additionally, we identified significant differences in these mechanisms (quantified via urethral

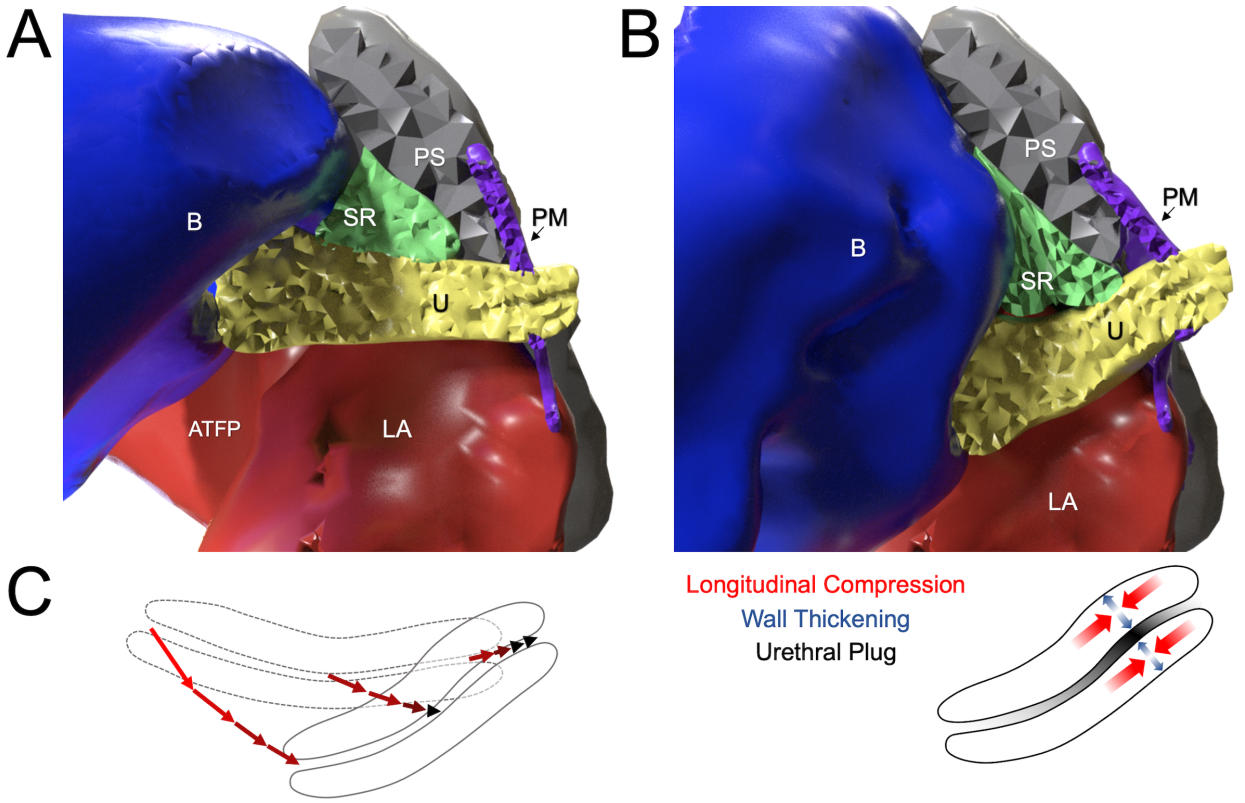

Figure 3.7: A finite element simulation of the urethra during Valsalva at (A) rest and (B) maximum Valsalva demonstrates the likely role of urethral support structures in the passive urethral continence mechanism. Shown are the urethra (U, yellow), bladder (B, blue), perineal membrane (PM, purple), pubic symphysis (PS, gray), space of Retzius (SR, green), and the levator ani muscles and pelvic sidewall (LA and ATFP, red). The paraurethral connective tissues cannot be seen but are present in the simulation, acting on the lateral portions of the urethra. C) Illustrates how the motion of the bladder neck, mid–urethra, and distal urethra (which is greater proximally) from rest (dashed outline) to peak Valsalva (solid outline) results in an "s"–shaped urethra, corresponding with longitudinal compression and wall thickening that creates the urethral plug (at the urethral knee). Together, these motions and deformations form the knee–like kink at the mid–distal urethra [164]. This figure was reprinted by permission from The International Urogynecological Association: Springer; International Urogynecology Journal; Megan R Routzong, Cecilia Chang, Roger P Goldberg, Steven D Abramowitch, and Ghazaleh Rostaminia. Urethral support in female urinary continence part 1: dynamic measurements of urethral shape and motion. *International Urogynecology Journal*, 2021; © 2021 The International Urogynecological Association.

shape and motion) across women with varying SUI severity. In the future, these analyses can improve our understanding of conservative versus surgical management of SUI and even help determine which type of surgical procedure would be most successful for individual women.

3.3 Biomechanical Simulations of Urethral Passive Closure

3.3.1 Summary of the Biomechanics of Female Urethral Passive Closure and SUI

Female stress urinary incontinence (SUI) is a prevalent condition affecting approximately 35% of all women and accounting for 50% of all UI [25, 118]. As discussed in Part 1 [164] of this study (Section 3.2), the fascinating problem of SUI has gained attention from researchers during the last century, yet opinions concerning the role of urethral support in maintaining continence are controversial. Kelly observed an open vesical neck in women with SUI in 1912 [96], Bonney observed abnormal displacement of the anterior vaginal wall [34], and Jeffcoate and Roberts observed a loss of the urethrovesical angle in 1949 [90]. In 1960, Enhorning described "transmission" of abdominal pressure to the urethra and noticed that transmission was reduced in women with SUI. He hypothesized that loss of pressure transmission occurred because the urethra fell "below" the influence of abdominal pressure [63]. In the 1990s, Petros and Ulmsten [146] and DeLancey [55] proposed hypotheses of varying complexity concerning why restoring or maintaining urethral support would translate to improved closure and stress continence. Although these theories differ, both necessitate the anterior urethral wall to be pushed into the posterior wall to close the urethra. The "hammock theory," despite recognition that urethral support and pressure transmission are both critical in understanding SUI, hypothesized that increases in urethral closure pressure (transmitted intra–abdominal pressure observed by Enhorning) during a cough probably arise because the urethra is compressed against a hammock–like supportive layer, rather

than the urethra being truly "intra–abdominal" [9].

In Part 1 (Section 3.2), our team studied urethral motion and shape changes caused by increases in intra–abdominal pressure using dynamic anterior compartment ultrasound and noticed that (1) the intra–abdominal pressure applied on the peritoneal surface will be transmitted to infra–peritoneal structures creating a force that pushes the viscera toward the pelvic outlet, (2) its attachments to the pubic bone and pelvic sidewall cause the urethra to "swing" inferiorly during Valsalva, (3) the support structures limit the range of this swinging proximally at the bladder neck and distally at the level of the perineal membrane (the layer of connective tissue deep to the superficial perineal muscles), (4) this motion longitudinally compresses the mid–urethra against the distal urethra at the level of the perineal membrane, which thickens the urethral wall and creates the urethral plug, and (5) this swinging and compression together create a knee–like kink at the mid–distal urethra resulting in an overall s–shape (Figure 3.7). It should be noted that while both this "swing theory" and the "integral theory" emphasize two closure mechanisms—the bladder neck and distal urethra—the descriptions of urethral closure fundamentally differ. The discussion of these findings in Part 1 generated the hypotheses investigated in the current study.

To evaluate whether established theories and/or this hypothesized "swing theory" accurately describe the urethral motions and deformations observed previously via ultrasound, a finite element model of Valsalva was created to simulate passive urethral motions and deformations. This model utilized the anatomy of a young, nulliparous, urinary continent woman to determine which boundary conditions and material properties simulated that patient's urethra during Valsalva, as observed with dynamic magnetic resonance imaging (MRI). We hypothesized that the presence of connective tissue supports at the bladder neck and at the level of the perineal membrane would be required to recreate the patient's peak Valsalva configuration and would result in the urethral swinging and longitudinal compression observed previously in Part 1 in continent women without prolapse. Additionally, we ran a sensitivity analysis on the resulting finite element model to determine which tissues (i.e., changes in their stiffness) had the greatest influence on resulting urethral deformation, motion, and shape. We hypothesized that changes in the stiffness of the urethra, proximal connective tissues, and perineal membrane would be the most influential.

3.3.2 Baseline Model Generation

The pelvic and dynamic MR defecography images of a 26–year–old, nulliparous, continent female who was recruited with IRB approval at NorthShore University HealthSystem as a control in a prior study [160] were used to acquire the anatomy for this biomechanical analysis. Relevant anatomy was segmented from a high–resolution MRI scan in the supine position at rest with a 1.5–T MRI scanner (Trio Tim, Siemens, Germany) (slice thickness 3 mm; matrix 320 × 160; field of view 430 mm; pixel size 1.344 mm). Images were acquired in the midsagittal plane approximately every 1.5 s while the patient performed several Valsalva maneuvers.

The urethra, bladder, perineal membrane, paraurethral connective tissues, space of Retzius, arcus tendineus fascia pelvis, levator ani muscles, pubic symphysis, and bony pelvis were segmented from the patient's rest images using 3D Slicer v4.10.1 [64] and imported into Houdini FX v18.0.499 (SideFX, Toronto, CA) for finite element simulation (Figure 3.8). Houdini was used because its procedural workflow allowed for efficient model development. Additionally, its dynamic solver is robust for simulations that include large degrees of nonlinearity and contact. Valsalva was simulated by applying a pressure of 90 cmH_2O to the inside wall of the bladder, the urethra, the anterior surfaces of the paraurethral connective tissues, and the superficial surface of the perineal membrane, so forces were pushing these surfaces inferiorly. This was accomplished using custom code written in Houdini and verified based on the application of external forces and pressures of simple geometric shapes that were discretized to varying degrees and for which solutions were known. The mid– and proximal urethra was connected to the pelvic sidewall (arcus tendineus fascia pelvis) via two lateral paraurethral connective tissues and to the pubis anteriorly via the perineal membrane (Figure 3.8). The bladder was held in place via a soft constraint from the anterior, superior portion of the bladder to the abdominal wall, simulating the median umbilical ligament. A second soft constraint was used on the posterior portion of the bladder to simulate the support normally provided by the uterus and its suspensory ligaments.

Soft tissues were modeled as linear elastic solids with the initial Young's moduli (a measure of stiffness describing a material's mechanical behavior) of the bladder, urethra,

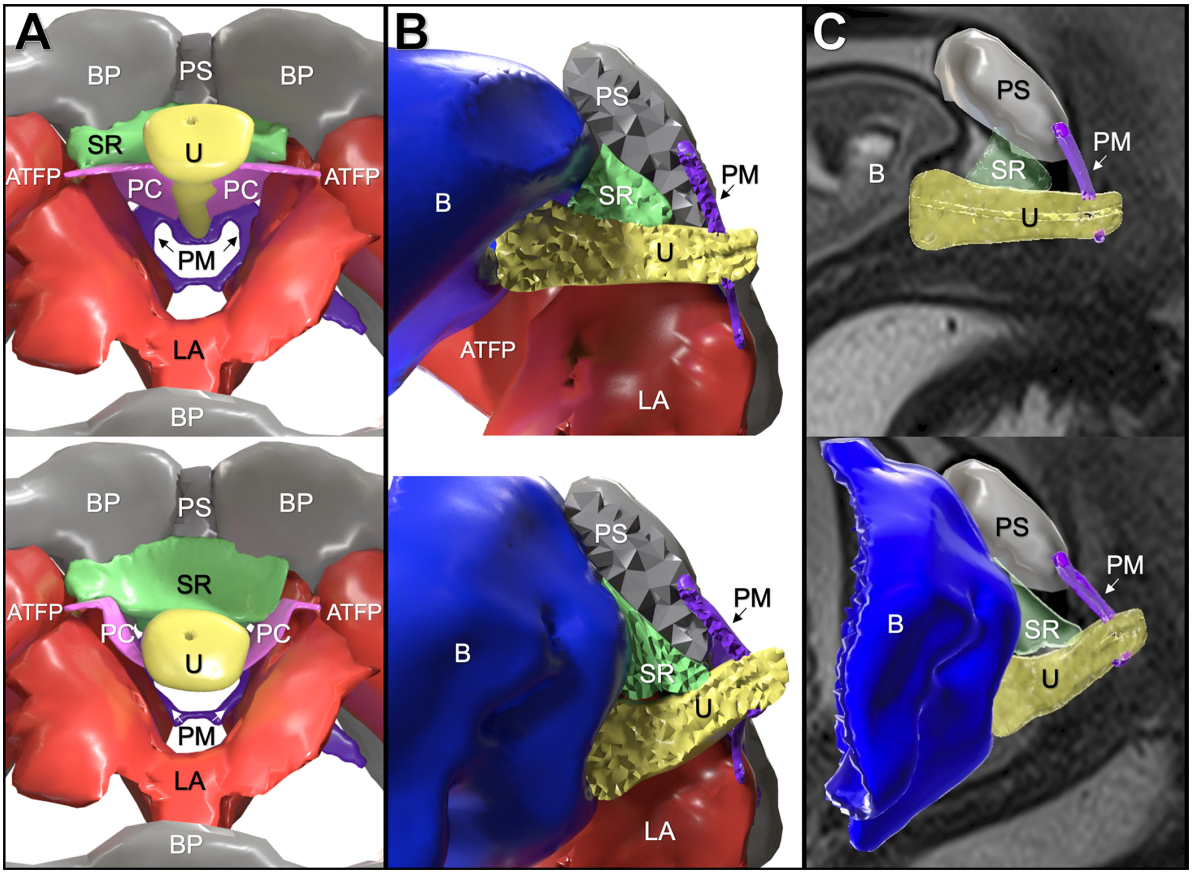

Figure 3.8: Screenshots of the baseline finite element model at rest (top) and peak Valsalva (bottom). A) Images from the perspective of the sacrum facing anteriorly and inferiorly. B) Images from the patient's right side with a midsagittal cut so the urethra can be seen clearly. C) Displays the same model view as B, but with the patient's dynamic MRI images overlain to demonstrate the agreement between the final model and *in vivo* imaging. The urethra (U, yellow), perineal membrane (PM, purple), space of Retzius (SR, green), and pubic symphysis (PS, gray) can be seen in all three image sets. The bony pelvis (BP, gray) and paraurethral connective tissues (PC, pink) can only be seen in A, the bladder (B, blue) in B and C, and the levator ani and arcus tendineus fascia pelvis (LA and ATFP, red) in A and B [166]. This figure was reprinted by permission from The International Urogynecological Association: Springer; International Urogynecology Journal; Megan R Routzong, Liam C Martin, Ghazaleh Rostaminia, and Steven D Abramowitch. Urethral support in female urinary continence part 2: a computational, biomechanical analysis of Valsalva. *International Urogynecology Journal*, 2021; © 2021 The International Urogynecological Association.

and connective tissues set as 0.05, 0.03, and 1.2 MPa, respectively [145]. The bony pelvis and pubic symphysis were modeled as rigid bodies as they do not deform meaningfully compared to the soft tissues. Material properties were calibrated until the deformed urethra from the simulated Valsalva had a comparable position and shape to the urethra in the

dynamic MRI at maximum Valsalva (Figure 3.8C), which was also consistent with position measures taken from dynamic anterior compartment ultrasound of continent women without prolapse, a subset of patients from the no SUI group described in Part 1 (Section 3.2). This resulted in a baseline simulation representative of Valsalva in a healthy, continent woman. A temporal convergence study was then performed to determine the point in which changes in the timestep value no longer influenced the simulation, i.e., $< 3.5\%$ differences for all output parameters.

Though material property values (i.e., Young's moduli and soft constraints) would be altered in the sensitivity analysis, the presence of the tissues in this baseline model was required to successfully simulate urethral motion and shape changes during Valsalva. The sensitivity analysis was designed to determine which parameter changes had the most influence on the urethra specifically. Note that an insignificant result in this type of analysis does not mean that the presence of the tissue is unimportant, rather that large changes in its material parameters did not significantly alter the urethra during simulated Valsalva.

The literature was searched to determine a range of Young's moduli for each tissue of interest using both computational and experimental studies as references; however, it was observed that these values varied widely, and there seemed to be an overall lack of consensus in the field. Due to the scarcity of published data, finding recent and relevant data was difficult, and some Young's moduli defined by the literature, like that of the urethra, included values that we know to be unrealistic (e.g., reaching the same order of magnitude as acrylic) [47, 132, 134, 170]. Additionally, many existing computational models of the urethra [50, 102, 184] derived their material properties from the same two original sources [69, 71] while other computational studies [22] pulled theirs from publications [157, 184] that also used those same two original sources. Though these studies are still valuable to the field, this demonstrates the need for more robust quantification of pelvic organ and tissue material properties. The analyses performed in the current study will suggest which should receive priority in future mechanical testing. Several experimental studies were incorporated to round out these parameter ranges, including data from porcine and equine [105, 134] and human cadaver [5, 47, 123, 132, 156] tissues. Several tissues included in our model did not have enough data in the literature to generate parameter ranges (such as the paraurethral

Table 3.7: Organ and tissue Young's moduli from literature and the ranges used to define the parameter space of the sensitivity analysis [166]. This table was reprinted by permission from The International Urogynecological Association: Springer; International Urogynecology Journal; Megan R Routzong, Liam C Martin, Ghazaleh Rostaminia, and Steven D Abramowitch. Urethral support in female urinary continence part 2: a computational, biomechanical analysis of Valsalva. *International Urogynecology Journal*, 2021; © 2021 The International Urogynecological Association.

	Range from Literature			**Baseline Model**	**Sensitivity Analysis Range**		**References Used**
Organ/Tissue	Minimum	Maximum	Average		Minimum	Maximum	
Urethra	3 kPa	10 MPa	1.9 MPa	1 MPa	3 kPa	10 MPa	[22, 69, 132, 134, 184]
Perineal Membrane	0.82 MPa	1.63 MPa	1.12 MPa	1 MPa	0.82 MPa	1.63 MPa	[102]
Connective Tissue	0.2 MPa	4.62 MPa	2.04 MPa	0.8 MPa	0.2 MPa	4.62 MPa	[47, 156]
Bladder	0.23 MPa	1 MPa	0.28 MPa	0.245 MPa	0.23 MPa	1 MPa	[47, 69, 123, 170, 184]
Trigone	1.9 MPa	4.1 MPa	3 MPa	3 MPa	1.9 MPa	4.1 MPa	[123]
Space of Retzius	1 kPa	2.9 kPa	1.95 kPa	2.25 kPa	1 kPa	2.9 kPa	[5, 50]

connective tissues). For these tissues, data from analogous pelvic tissues assumed to have similar material properties (like the uterosacral ligament) were used. Due to these limitations and the desire to structure the study around a baseline model representative of a continent female, the final parameter ranges used in the sensitivity analysis were determined using those found in the literature as described, but such that the baseline model's parameter values were the mean of each range (Table 3.7).

3.3.3 Sensitivity Analysis Overview

To carry out this sensitivity analysis, first, values were selected within the defined parameter ranges using Latin hypercube sampling (LHS), implemented via the LHS function in the pyDOE v3.7 package [122] in Python with an n of 8 and 10 samples (dividing each input parameter range into 10 sections while assuming normal distributions). This LHS was repeated 5 times, resulting in a total of 50 simulations. The eight input parameters with ranges being semi–randomly sampled were the Young's moduli of the urethra, perineal membrane, paraurethral connective tissues, bladder, and space of Retzius; the penalty of the soft constraints dictating the effective stiffness of the bladder's connective tissues to the sacrum and the tissue holding the perineal membrane to the anterior vagina; and the stiff-

ness of the bladder trigone defined by a factor by which the bladder modulus was multiplied. Reducing a tissue's material stiffness/Young's modulus will cause it to be "softer," while increasing these values would result in a "harder" material. Meanwhile, increased constraint values mean more force is required to displace/deform the regions being constrained. The six length and swing–related outputs of interest measured at peak Valsalva were the urethral length, retropubic urethral length, retropubic bladder neck angle, bladder neck–pubic bone angle, meatus–pubic bone angle, and urethral knee–pubic bone angle, as defined in Part 1 (Section 3.2.2). Additionally, the geometry of the urethra was exported from each simulation at maximum Valsalva, and a statistical shape analysis was performed utilizing a workflow previously established by our laboratory [168, 169] and described in Part 1 (Section 3.2.3), but, because these urethras had identical meshes, the existing vertices served as the corresponding points and did not need to be recalculated. The significant modes of variation of this shape model were included as outputs of interest in the following statistical analyses by calculating a principal component (PC) score for each simulation and mode.

Once all results were obtained, the values of each input and output variable were ranked across all 50 simulations so that partial rank correlation coefficients (PRCCs) could be obtained. This LHS–PRCC methodology has been used previously and established for finite element model sensitivity analyses [66, 76]. A few trials could not reach the final timepoint due to deformations being so extreme, so maximum Valsalva was reached before the full pressure had been applied. This was not considered a major limitation as the outputs are ranked (therefore exact output values are less critical) and using earlier timepoints would only result in a slight underestimation of the actual urethral motion and deformation of what are already the largest and likely physiologically unrealistic values. PRCCs were obtained using the partial correlation function within MATLAB R2018a (MathWorks Inc., Natick, MA, USA) on the input and output ranks, while controlling for all other inputs and all outputs, respectively. The absolute values of the PRCCs were ranked across each output, so values ranged from 1 through 8 with 8 indicating the most influential input for each output. To determine which factors were overall the most influential, the cumulative influence factor (CIF), as defined previously by Feola et al., was calculated for each input across all outputs and for each output category [66]. The CIF is a normalized factor calculated by dividing

the sum of each input variable's ranks by the highest possible sum, so the highest possible CIF value is 1—indicating the most influence—while smaller values indicate less influence. A CIF ≥ 0.5 was considered meaningful while p–values < 0.05 were considered statistically significant.

3.3.4 Incorporation of Previously Established SUI Thresholds

In Part 1 (Section 3.2), we elucidated relationships between SUI and specific variables measured via dynamic ultrasound; however, they do not explain what led to those observed urethral motions and deformations. We wanted to generate hypotheses regarding the biomechanics of SUI by drawing relationships between our finite element model inputs and the presence of SUI symptoms via those variables found to significantly increase with SUI severity in Part 1: the infrapubic urethral length, retropubic bladder neck angle, urethral knee–pubic bone angle, and modes of variation describing greater proportional mid–distal wall thickening during Valsalva [164]. We defined thresholds dividing our simulations into those representing continent– or SUI–like scenarios. These thresholds were either the optimal threshold defined via the receiver–operating characteristic curve for the prediction of the presence of severe SUI defined in Part 1 or +1 standard deviation from the mean. For each simulation, we calculated the change in infrapubic urethral length, retropubic bladder neck angle, and urethral knee–pubic bone angle from rest to Valsalva and calculated PRCCs between those and all model inputs, though evaluating variables from rest to Valsalva vs at Valsalva in this study does not change resulting PRCCs as the rest configuration was the same for all simulations. Note that this also means analyzing PC scores at Valsalva provides indistinguishable results from analyzing scores from rest to Valsalva, so PC scores from the mode that best described urethral knee thickening were also used in this threshold analysis. Model inputs with stronger associations to these measures ($0.6 > \text{PRCC} > 0.6$) would be hypothesized to have similar relationships with SUI severity.

3.3.5 Baseline Model and Simulation Urethral Swing Values

The urethral swing values for the baseline simulation reasonably agreed with the ranges defined by continent women without prolapse from Part 1 at rest and Valsalva. After calibration, the input parameter values for the baseline model were as follows: urethra stiffness of 1000 kPa, perineal membrane stiffness of 1000 kPa, paraurethral connective tissue stiffness of 800 kPa, bladder stiffness of 245 kPa, space of Retzius stiffness of 2.25 kPa, bladder soft constraint of 0.125, perineal membrane soft constraint of 25, and trigone factor of 5. While the constraint values are unitless, an increase or decrease in their values relative to baseline indicates that the corresponding tissues are either providing more or less resistance, respectively. The resulting urethral length, swing, and shape measures for the baseline model at rest and peak Valsalva, respectively, were as follows: urethral length of 4.8 cm and 4.28 cm, retropubic urethral length of 3.31 cm and 2.34 cm, retropubic bladder neck angle of 52.7° and 82.1°, bladder neck–pubic bone angle of 68.2° and 32.9°, meatus–pubic bone angle of 46.8° and 62.1°, and urethral knee–pubic bone angle of 22.0° and 38.7°. The urethral swing values for the baseline simulation reasonably agreed with the ranges (mean ± standard deviation in degrees) defined by continent patients without prolapse from Part 1 at rest and Valsalva, respectively: retropubic bladder neck angle of 50.03 ± 15.52 and 82.70 ± 13.39, bladder neck–pubic bone angle of 72.84 ± 7.95 and 39.87 ± 12.02, meatus–pubic bone angle of 55.97 ± 8.95 and 66.93 ± 7.07, and urethral knee–pubic bone angle of 25.81 ± 5.49 and 39.86 ± 11.67. Four modes from the statistical shape analysis were found to be significant, and the baseline model had PC scores of 0.039, 0.007, 0.003, and 0.013 for modes 1, 2, 3, and 4, respectively, at Valsalva.

3.3.6 Sensitivity Analysis Findings

Of the 50 simulations performed, 5 reached peak Valsalva before the final timestep (see Appendix C). All 50 urethral shapes at peak Valsalva were included in the statistical shape model. Four significant modes of variation explained 77%, 8.5%, 5.8%, and 1.4% of the total shape variance. Qualitatively, mode 1 described overall urethral shape variation, modes 2 and 4 defined anterior–posterior and left–right variation, respectively, in the very distal end

of the urethra, and mode 3 portrayed deformation of the bladder neck. Additionally, mode 2 also demonstrated various levels of mid–distal proportional thickness changes while mode 3 described proportional changes in bladder neck thickness, both indicative of varying degrees of longitudinal compression in distinct regions of the urethra (Figure 3.9).

In descending order, urethra stiffness, perineal membrane soft constraint, and bladder, paraurethral connective tissue, and perineal membrane stiffness were the five most influential inputs (Table 3.8, Figure 3.10A). To better understand the nature of these influential factors and evaluate how the choice of output variables may have influenced our results, we broke the output variables down into four categories: length (urethral and retropubic urethral lengths), proximal swinging (retropubic bladder neck and bladder neck–pubic bone angles), distal swinging (meatus–pubic bone and urethral knee–pubic bone angles), and shape (significant modes of variation) (Figure 3.10B). These category–specific CIFs were calculated as if only the output variables in that category were considered (Table 3.8). The influence of urethral stiffness was meaningful (CIF $\geq$ 0.5) for every category, although greatest (CIF = 1) for urethral length (Figure 3.10B). The perineal membrane soft constraint CIF was largest for distal swinging (CIF = 1), the bladder stiffness CIF largest for proximal swinging (CIF = 1), paraurethral connective tissue stiffness contributed the most towards proximal swinging (CIF = 0.88), and the influence of perineal membrane stiffness was greatest for length (CIF = 0.75).

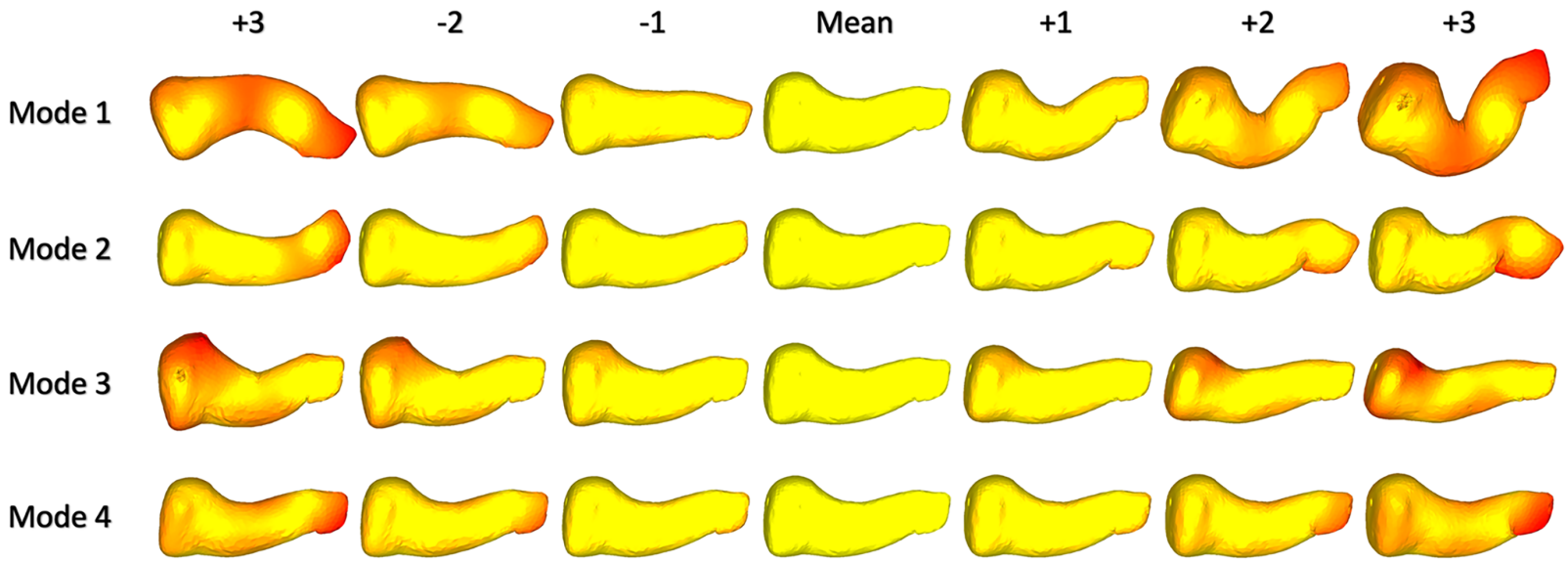

Figure 3.9: The urethral shapes within ± 3 standard deviations of the mean shape from a sagittal view along all 4 significant modes of variation as determined by the statistical shape analysis on the 50 urethras simulated at peak Valsalva. These modes explained 77%, 8.5%, 5.8%, and 1.4% of the total shape variance, respectively. For orientation, the bladder neck is to the left, the meatus is to the right, and the anterior side (where the pubic symphysis would be) is to the top of each urethra. The colormap is defined based on the distance from each vertex on the meshes defining the urethras to the corresponding vertex on the mean urethra; yellow indicates no displacement from the mean (therefore the mean shape is completely yellow) while red indicates the maximum distance from the mean for each mode separately [166].

Table 3.8: Partial rank correlation coefficients (PRCCs), their ranks, and cumulative influence factors (CIFs) [166]. This table was reprinted by permission from The International Urogynecological Association: Springer; International Urogynecology Journal; Megan R Routzong, Liam C Martin, Ghazaleh Rostaminia, and Steven D Abramowitch. Urethral support in female urinary continence part 2: a computational, biomechanical analysis of Valsalva. *International Urogynecology Journal*, 2021; © 2021 The International Urogynecological Association.

Output Categories	**Urethral Length**		**Proximal Urethral Swinging**		**Distal Urethral Swinging**		**Urethral Shape**			
Output Variables	Urethral Length	Retropubic Urethral Length	Retropubic Bladder Neck Angle	Bladder Neck–Pubic Bone Angle	Meatus–Pubic Bone Angle	Urethral Knee–Pubic Bone Angle	Mode 1	Mode 2	Mode 3	Mode 4
PRCCs (p–values)										
Urethra Stiffness	**0.893 (<0.001)**	**0.911 (<0.001)**	**-0.481 (0.001)**	**0.507 (0.001)**	**0.594 (<0.001)**	**0.638 (<0.001)**	**-0.626 (<0.001)**	**-0.761 (<0.001)**	**0.361 (0.017)**	0.272 (0.078)
Perineal Membrane Stiffness	**-0.487 (0.001)**	**-0.490 (0.001)**	**-0.388 (0.010)**	**0.404 (0.007)**	-0.162 (0.298)	-0.197 (0.206)	0.154 (0.323)	-0.110 (0.484)	**-0.339 (0.026)**	-0.003 (0.985)
Paraurethral Connective Tissue Stiffness	-0.044 (0.780)	0.096 (0.540)	**-0.589 (<0.001)**	**0.645 (<0.001)**	**-0.635 (<0.001)**	**-0.625 (<0.001)**	**-0.757 (<0.001)**	0.085 (0.590)	**-0.320 (0.036)**	**-0.392 (0.009)**
Bladder Stiffness	-0.262 (0.090)	**-0.511 (<0.001)**	**-0.814 (<0.001)**	**0.802 (<0.001)**	-0.016 (0.919)	0.131 (0.401)	**0.637 (<0.001)**	**-0.536 (<0.001)**	**-0.581 (<0.001)**	0.259 (0.093)
Space of Retzius Stiffness	-0.056 (0.720)	-0.133 (0.394)	0.102 (0.513)	-0.097 (0.536)	0.198 (0.203)	0.207 (0.183)	-0.076 (0.628)	0.096 (0.540)	-0.060 (0.704)	0.189 (0.225)
Bladder Soft Constraint	**-0.458 (0.002)**	**-0.381 (0.012)**	-0.280 (0.069)	0.282 (0.067)	-0.035 (0.826)	0.048 (0.761)	**-0.392 (0.009)**	0.170 (0.277)	-0.082 (0.602)	-0.032 (0.838)
Perineal Membrane Soft Constraint	**-0.637 (<0.001)**	**-0.453 (0.002)**	-0.265 (0.086)	0.259 (0.093)	**-0.889 (<0.001)**	**-0.893 (<0.001)**	**-0.502 (0.001)**	**0.786 (<0.001)**	-0.115 (0.463)	**0.487 (0.001)**
Trigone Factor	-0.217 (0.162)	-0.241 (0.119)	-0.047 (0.765)	0.056 (0.720)	-0.008 (0.959)	0.014 (0.927)	-0.120 (0.445)	0.003 (0.985)	-0.020 (0.901)	-0.136 (0.385)
Ranks										
Urethra Stiffness	8	8	6	6	6	7	6	7	7	6
Perineal Membrane Stiffness	6	6	5	5	4	4	3	4	6	1
Paraurethral Connective Tissue Stiffness	1	1	7	7	7	6	8	2	5	7
Bladder Stiffness	4	7	8	8	2	3	7	6	8	5
Space of Retzius Stiffness	2	2	2	2	5	5	1	3	2	4
Bladder Soft Constraint	5	4	4	4	3	2	4	5	3	2
Perineal Membrane Soft Constraint	7	5	3	3	8	8	5	8	4	8
Trigone Factor	3	3	1	1	1	1	2	1	1	3
CIFs										**Overall**
Urethra Stiffness	**1.00**		**0.75**		**0.81**			**0.81**		**0.84**
Perineal Membrane Stiffness	**0.75**		**0.63**		**0.50**			0.44		**0.55**
Paraurethral Connective Tissue Stiffness	0.13		**0.88**		**0.81**			**0.69**		**0.64**
Bladder Stiffness	**0.69**		**1.00**		0.31			**0.81**		**0.73**
Space of Retzius Stiffness	0.25		0.25		**0.63**			0.31		0.35
Bladder Soft Constraint	**0.56**		**0.50**		0.31			0.44		0.45
Perineal Membrane Soft Constraint	**0.75**		0.38		**1.00**			**0.78**		**0.74**
Trigone Factor	0.38		0.13		0.13			0.22		0.21

Statistically significant PRCCs and p–values ($p<0.05$) are shown in **bold**.

Meaningful CIFs (≥ 0.5) are also in **bold**.

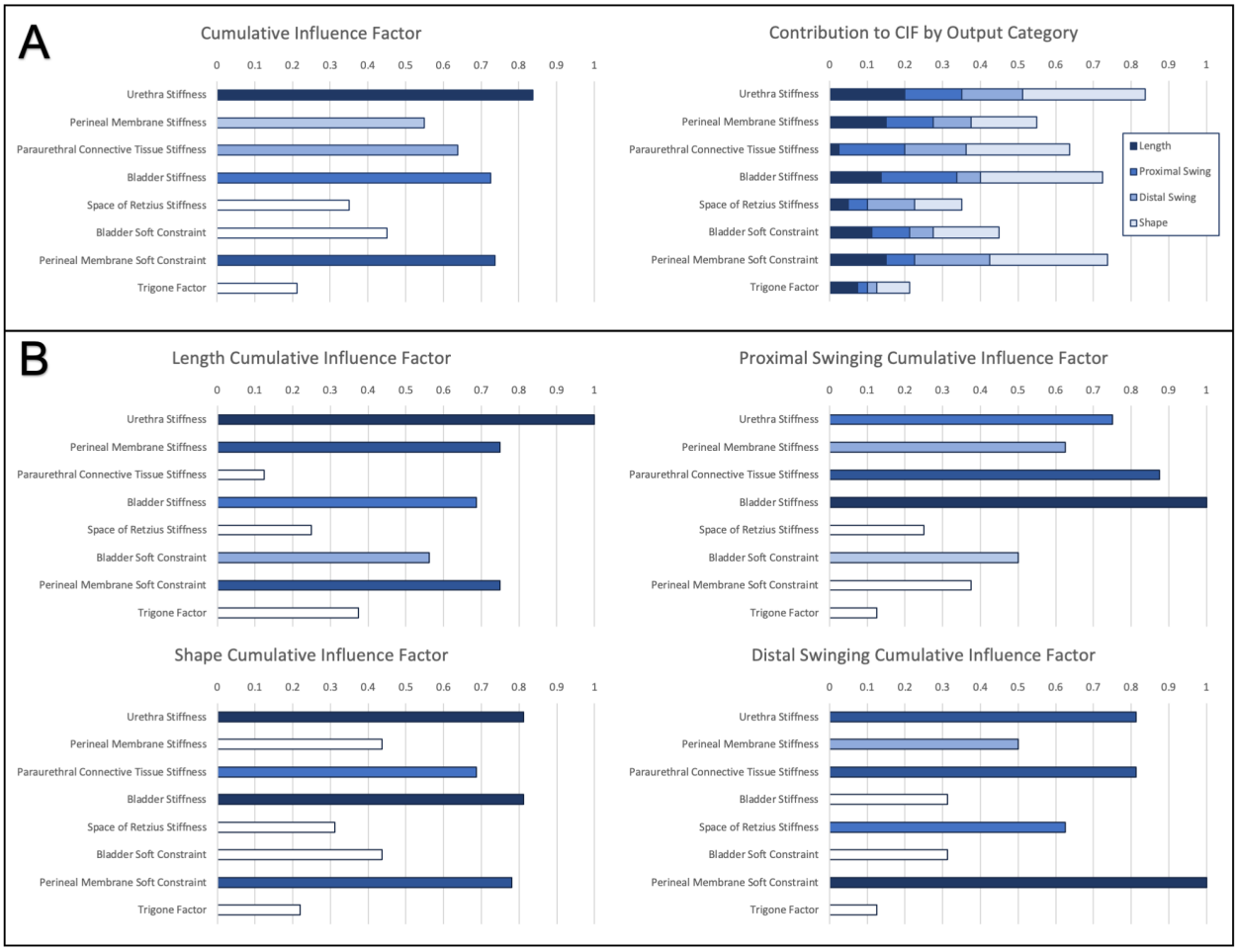

Figure 3.10: Graphs of the final Latin hypercube sampling–partial rank correlation coefficient results—the cumulative influence factors (CIFs). A) Displays the overall CIF for each input variable. The darkest color indicates the overall most influential input and the lightest the overall least influential input, while white bars indicate variables that did not reach meaningful influence (CIF ≥ 0.5). On the right, the CIFs are broken down by output variable category. B) Displays the CIFs as if the output variables within each output category were considered individually, demonstrating how an input variable's influence may change with the choice of output variables. The bars are color coded using the same convention as that of the overall CIF graph [166]. This figure was reprinted by permission from The International Urogynecological Association: Springer; International Urogynecology Journal; Megan R Routzong, Liam C Martin, Ghazaleh Rostaminia, and Steven D Abramowitch. Urethral support in female urinary continence part 2: a computational, biomechanical analysis of Valsalva. *International Urogynecology Journal*, 2021; © 2021 The International Urogynecological Association.

3.3.7 Potential Relationships Between Model Inputs and SUI via Model Output SUI Thresholds

Infrapubic urethral length, retropubic bladder neck angle, and urethral knee–pubic bone angle from rest to Valsalva and mode 2 had stronger associations with urethra, paraurethral connective tissue, and bladder stiffnesses and the perineal membrane soft constraint (see Appendix C). Mode 2 was chosen for this threshold analysis as it best described isolated urethral knee thickening. These thresholds were defined by the optimal threshold for the retropubic bladder neck angle (37°) and urethral knee–pubic bone angle (18°) and +1 standard deviation from the mean for the infrapubic urethral length (1.11) and mode 2 (0.0318). These results demonstrated both positive and negative correlations with SUI (Figure 3.11). To determine how threshold categories may be interrelated, urethral stiffness and perineal membrane soft constraint were plotted with surpassed thresholds identified (Figure 3.12A) and then simplified for clearer interpretation (Figure 3.12B). Regardless of urethral stiffness, excessive swinging due to a very low perineal membrane soft constraint (< 10) always resulted in a surpassed threshold. We also see how a very soft urethra frequently corresponds with simulations that surpassed one or more thresholds.

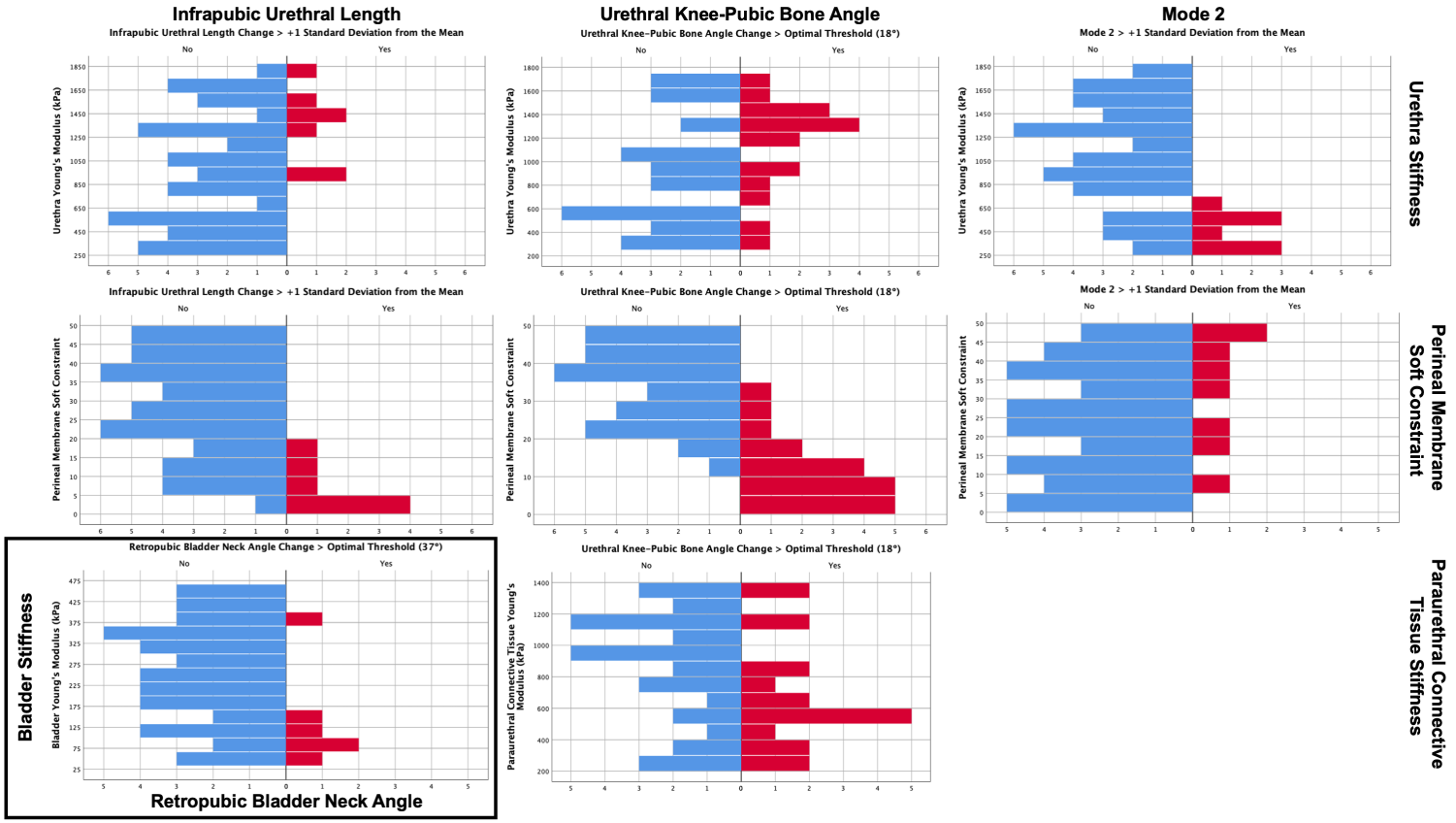

Figure 3.11: Histograms of finite element model input parameters (rows) categorized by whether the output variable's (columns) threshold for SUI symptoms was surpassed (blue/left for "no" and red/right for "yes") to demonstrate how these model input parameters may be related to SUI. These thresholds were defined as either the optimal threshold determined in Part 1 (Section 3.2) that corresponds with increased likelihood of having severe SUI (retropubic bladder neck angle and urethral knee–pubic bone angle) or as +1 standard deviation from the mean value (infrapubic urethral length and mode 2). Mode 2 was evaluated only at Valsalva (as only peak Valsalva shapes were analyzed) while the other variables were evaluated as the change in that parameter from rest to peak Valsalva [166]. This figure was reprinted by permission from The International Urogynecological Association: Springer; International Urogynecology Journal; Megan R Routzong, Liam C Martin, Ghazaleh Rostaminia, and Steven D Abramowitch. Urethral support in female urinary continence part 2: a computational, biomechanical analysis of Valsalva. *International Urogynecology Journal*, 2021; © 2021 The International Urogynecological Association.

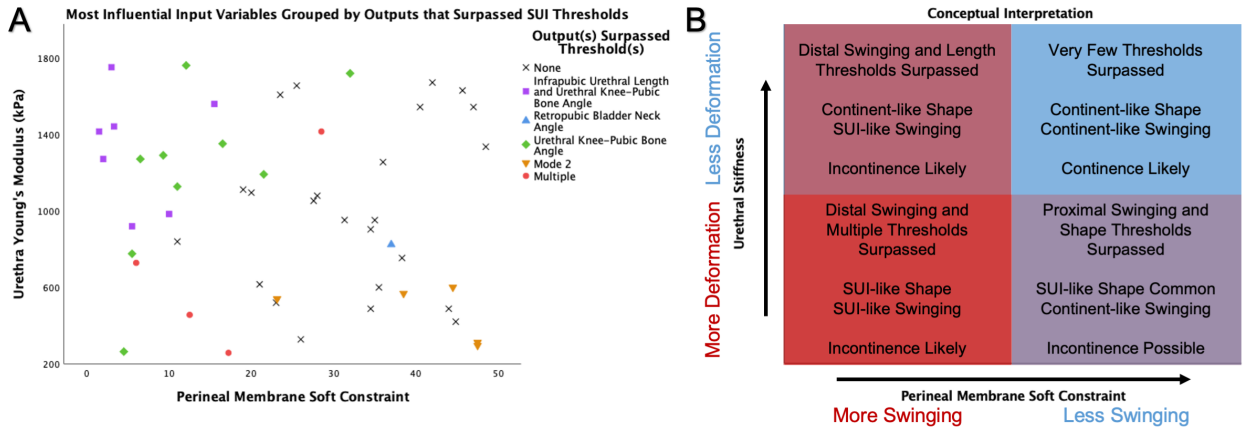

Figure 3.12: A) A scatterplot of the two most influential finite element model inputs for all 50 simulations labeled by which (if any) SUI thresholds were surpassed, meaning those simulations likely resemble a Valsalva of a patient with SUI. B) Our conceptual interpretation of the different regions defined by that scatterplot based on the conditions in which specific thresholds were surpassed [166]. This figure was reprinted by permission from The International Urogynecological Association: Springer; International Urogynecology Journal; Megan R Routzong, Liam C Martin, Ghazaleh Rostaminia, and Steven D Abramowitch. Urethral support in female urinary continence part 2: a computational, biomechanical analysis of Valsalva. *International Urogynecology Journal*, 2021; © 2021 The International Urogynecological Association.

3.3.8 Sensitivity Analysis Findings Support the Swing Theory

These finite element simulations demonstrate that the behavior of the urethra during Valsalva as observed via both MRI and endovaginal ultrasound can be accurately described by an alternative theory of passive female urinary continence that we are terming the Swing Theory, which is based on dynamic study of urethral motion and shape and explains the biomechanical mechanism of passive urethral closure (i.e., swinging and then kinking that forms the urethral knee). The urethral shape changes and swinging observed *in vivo* in Part 1 (Section 3.2) and simulated here in Part 2 (Section 3.3) are inconsistent with the expected urethral shape and motions described by the existing hammock and integral theories.

According to those theories, increased intra–abdominal pressure would have pushed the anterior urethral wall into the posterior wall and the entire urethra into the endopelvic fascia and vagina, creating a backstop (or hammock) that resists posterior urethral motion. Not only were these urethral motions and deformations not observed, but the current model demonstrates that *in vivo* urethral motions and deformations can be accurately simulated

without a vagina, pubourethral ligament, or a "hammock" of posterior connective tissues. This makes sense clinically as continence can be achieved without a vagina. For example, one study found that 47% of women with vaginal agenesis did not have urinary symptoms prior to surgery [127].

A major finding of this study was that the material properties of the urethra, perineal membrane, bladder, and paraurethral connective tissues were the main contributors to changes in the length, swinging motion, and/or shape of the urethra during Valsalva (with CIFs ≥ 0.5). While these results closely align with our original hypothesis, formulated based on the results of Part 1 [164], they demonstrate that tissue material properties and the mechanical integrity of attachments between soft tissues and to bone are important in elucidating the passive mechanisms of the urethra.

3.3.9 Model Material Properties May Explain Potential Mechanisms of SUI

By applying thresholds delineating patients with SUI from those without in Part 1 onto our simulations in Part 2, we were able to understand how the material properties of the urethra and surrounding structures may explain potential mechanisms of SUI with regard to urethral swinging and deformation during Valsalva. It is likely that excessive distal swinging inhibits effective urethral kinking observed during passive closure, as every simulation with a perineal membrane soft constraint value below 10 passed a SUI threshold regardless of urethral stiffness. In this way, SUI symptoms may be present even if the urethral shape seems to resemble that of a continent woman (Figure 3.12B). The urethral support structures are so compromised that the passive role of urethral mechanical integrity (an adequately stiff urethra) becomes inconsequential relative to non–ideal swinging motions. When the urethra was soft (Young's modulus < 700 kPa), a mix of "continent" and SUI results was observed. There were more "continent" simulations with increasing perineal membrane soft constraint within this soft urethra range, suggesting that controlled proximal swinging may be able to passively close the urethra—even when it is soft—by directing longitudinal forces such that the mid–urethra is pushed towards the perineal membrane, forming an adequate urethral knee to maintain continence. However, the mix of results in this region also indicates that,

in some cases, the urethra may be so soft that even controlled swinging resembling that of a continent woman may not prevent leakage. This is clinically consistent with data showing the variable effectiveness of procedures that aim to stabilize the proximal urethra.

These observations support the novel Swing Theory of urinary continence mechanisms for urethral passive closure which describes how urethra and supportive tissue mechanical integrity contribute to the urethral motions and deformations observed during Valsalva. Importantly, this framework can explain mid–urethral sling success and failure, where existing theories could not. Because this theory allows for definitions of multiple mechanisms of continence and SUI—defined by whether the urethral swinging motion and/or shape/deformations (or neither) are contributing to the observed continence or SUI—we could then speculate that a mid–urethral sling may be more effective in women with one presentation of SUI versus another. Although this will require robust clinical and computational validation, we speculate that a mid-urethral sling addresses non–ideal swinging by aiding compromised supportive structures and may be less successful in women with compromised urethral but adequate supportive tissue mechanical integrity. This is consistent with existing ideas concerning diverse presentations of SUI based on the presence of urethral hypermobility but defined more explicitly and only for passive closure by the Swing Theory. While passive urethral mechanical integrity is likely influenced by urethral tone or lack thereof (i.e., the urethras of women with intrinsic sphincter deficiency likely demonstrate softer passive mechanical behavior), the mechanisms of passive continence described in this work only become important if urethral pressures being generated by active mechanisms (e.g., the striated urethral sphincter and smooth muscle) are exceeded. Though active closure is undoubtedly very important, the goal of this study was to isolate the mechanisms of passive closure.

3.3.10 Study Limitations and Future Directions

Although the use of dynamic MR images from a continent patient allowed thorough segmentation and the ability to calibrate our baseline model, the differences in urethral visibility between 2D ultrasound (Part 1 [164]) and 3D MRI (Part 2 [166]) made it such that lengths and modes of variation could not be directly compared between Parts 1 and 2.

This, however, did not change our ability to identify landmarks necessary for defining the proximal and distal swinging angles. Additionally, it is unknown how accurately continent rest anatomy can be used to simulate the urethra of a women with SUI during Valsalva. A major challenge was finding material properties in the literature, and the sparsity of the data meant that material property ranges could not be utilized to perfectly match a specific cohort of women. Nevertheless, this study identified which properties need to be well defined for eventual patient–specific models (such as those to simulate surgical repairs). Until those data are obtained, the clinical applications of all computational models will remain limited. Finally, this study likely included combinations of material property values that would not normally be observed together *in vivo*. However, the current study design is adequate for forming new hypotheses, and the robust sensitivity analysis allowed us to use the most extreme conditions to isolate trends and draw conclusions about SUI.

In summary, dynamic endovaginal ultrasound of the urethra in women with and without SUI in Part 1 of this study showed that controlled, coordinated swinging of the proximal and distal urethra during Valsalva results in longitudinal compression as the bladder neck is pushed against the perineal membrane. This results in shortening of the urethra, thickening of the urethral walls, and kinking at the level of the perineal membrane (formation of the urethral knee) that, together, likely contribute to passive closure of the urethral lumen (Figure 3.7). These ideas were the basis behind the Swing Theory, for which the current study explored potential mechanisms. These finite element simulations demonstrate how urethral motion and deformation during Valsalva are better explained by the Swing Theory than the existing integral and hammock theories and that this motion is likely dictated by the stiffnesses of the urethra, perineal membrane, bladder, and paraurethral connective tissues. These findings are an important step towards improved evaluation of SUI and the design of patient–specific surgical treatments. In future studies, it will be critical to evaluate the effect of the mid–urethral sling and urine flow on the urethral motions and deformations described by the Swing Theory.

3.4 Conclusions

In Section 3.2, we defined average changes in urethral motion, deformation, and shape during Squeeze and Valsalva. Differences between women with no, mild, and severe SUI—after controlling for low maximum urethral closure pressure—were only observed during Valsalva. During passive urethral closure, the urethra swings about the pubic symphysis, and this swinging was more exaggerated and resulted in more longitudinal compression and a more pronounced "s"–shaped urethra in women with SUI, which indicates that controlled swinging of the urethra is likely part of the passive closure mechanism. This idea of controlled swinging resulting in passive closure was deemed the Swing Theory, which was evaluated in Section 3.3. The sensitivity analysis of urethral passive closure revealed that the stiffness of the urethra, perineal membrane, bladder, and paraurethral connective tissues significantly influenced urethral motion, deformation, and shape. Additionally, by drawing connections between SUI and finite element model tissue material properties via the urethral length, angle, and shape measures from Section 3.2 that differed significantly with SUI severity, we discovered that urethral stiffness and the perineal membrane soft constraint (which dictates the strength of its attachment to the bony pelvis) contribute to the hypermobility and and urethral shapes associated with severe SUI. Together, these studies support that the Swing Theory, which describes how controlled swinging and then kinking at the urethral knee results in passive closure of the urethral lumen, provides a better, more accurate explanation of mechanisms of urethral passive closure than existing theories of female urinary continence.

4.0 Significant Geometric and Material Property Predictors of Simulated Vaginal Birth-Related Injuries

4.1 Summary

Many existing models of vaginal childbirth utilize single, patient–specific geometries and, frequently, the only pelvic floor muscles included in these simulations are the levator ani. In Section 4.2, we aimed to determine the impact of superficial perineal muscles and connectives on predicted perineal body and pubovisceral muscle strains. Meaningful differences between the model that included vs the model that omitted the superficial perineal structures would suggest that these structures warrant inclusion in future computational simulations and analyses of the female pelvic floor muscle complex. In section 4.3, we calculated the shape variance of combined bony pelvis–pelvic floor muscle complex geometries and of the bony pelvis and pelvic floor muscle complex individually. Early–mid vs late pregnant shapes were compared to determine the influence of pregnancy–induced remodeling of the shape of maternal pelvic anatomy. In section 4.4, shapes generated from the previously described SSM were used to build numerous, non–patient–specific computational models of vaginal childbirth. This allowed us to determine which aspects of maternal pelvic shape significantly influenced the pubovisceral muscle and perineal body—common sites of injury during vaginal birth—and to test the hypothesis that pregnancy–induced shape remodeling would reduce the mechanical burden of vaginal childbirth.

4.2 Novel Inclusion of Superficial Perineal Structures to Determine their Impact on Vaginal Delivery

Vita, and Steven D Abramowitch. Novel simulations to determine the impact of superficial perineal structures on vaginal delivery. *Interface Focus*, 9:20190011, 2019; © 2019 The Author(s).

4.2.1 Motivation for Studying Superficial Perineal Structures

Injury to the soft tissues that provide pelvic organ support during vaginal delivery can lead to the development of pelvic floor disorders decades later [85, 198]. Previous finite element simulations predicted pubovisceral muscle enthesis injury during vaginal delivery, an injury which has been identified with medical imaging in 18% of parous women after delivery [57, 92]. Meanwhile, other studies have found that 65.8% of parous women experience perineal body disruption during vaginal delivery [173]. In existing finite element models of childbirth, however, the maximum stretch values at the pubovisceral muscle are approximately 10% larger than those at the perineal body [92]. If stretch positively correlates with injury, then these numbers do not coincide with the relative prevalence of these injuries observed clinically. Thus, a clear understanding of stretching during vaginal delivery is critical to simulating mechanisms of injury.

Finite element models of vaginal delivery commonly include only the levator ani muscles, the major components of pelvic organ support that maintain the genital hiatus, which may be adequate for certain research questions [15, 171, 181, 194]. However, they generally exclude superficial perineal structures—such as the bulbocavernosus, ischiocavernosus, and deep and superficial transverse perinei—striated muscles with high connective tissue content that are superficial to the levator ani and intersect at the perineal body [56, 85] (Figure 4.1). These structures are commonly omitted from simulations as they are difficult to segment from imaging, and, based on visual inspection, seem to be mechanically insignificant compared to the levator ani [112]. Anatomically, superficial perineal structures resist caudal motion of the perineal body, meaning their exclusion may allow non–physiological movement of maternal soft tissues [56, 112]. Our objective was to determine the impact of these superficial perineal

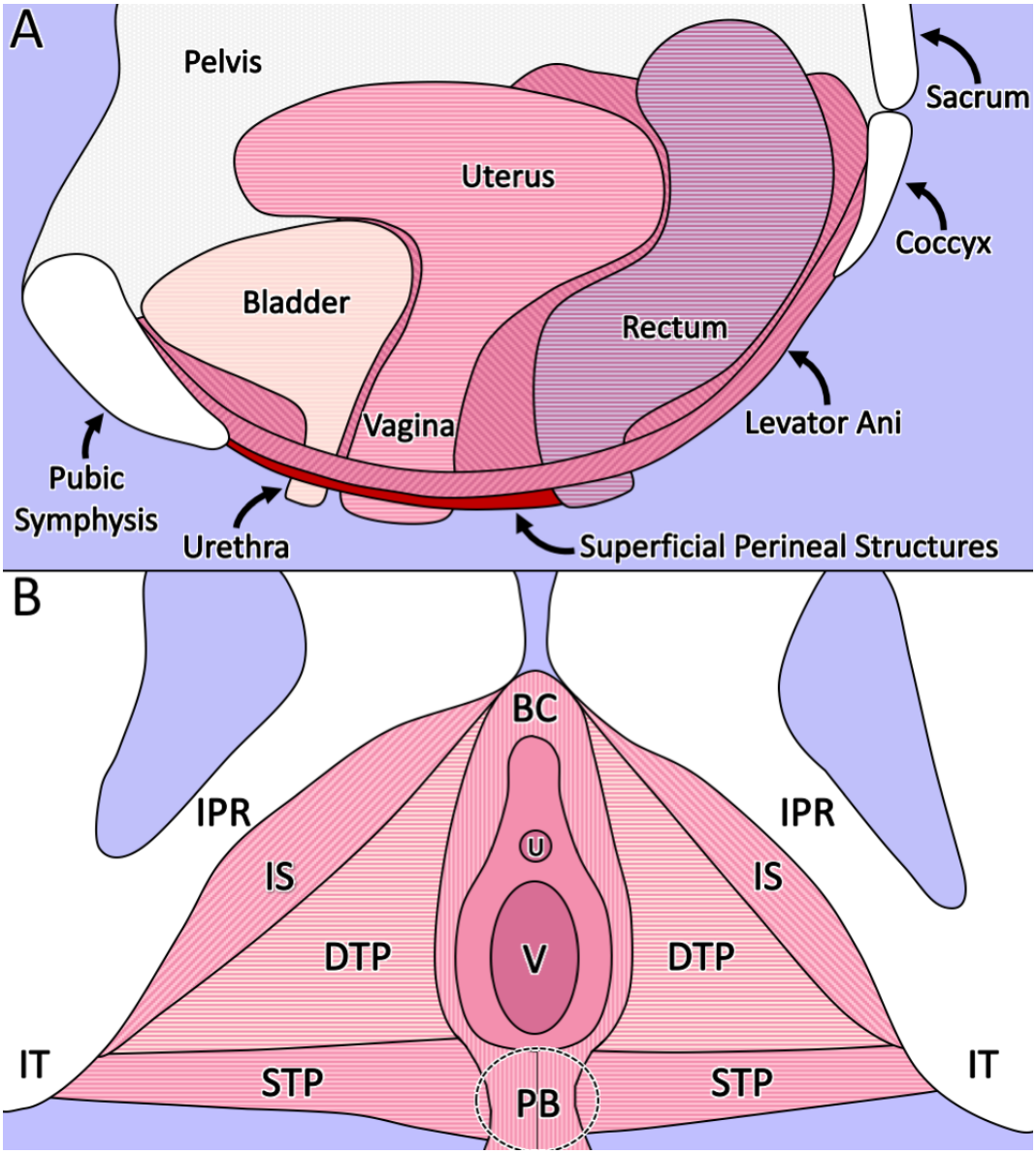

Figure 4.1: An illustration of A) the female pelvis from the midsagittal plane with the region where the superficial perineal structures are located emphasized in red and B) the superficial perineal structures (the bulbocavernosus (BC), ischiocavernosus (IS), deep transverse perinei (DTP), and superficial transverse perinei (STP)) in detail. Shown for reference are the inferior pubic rami (IPR), urethra (U), vagina (V), ischial tuberosities (IT), and the perineal body (PB) [167]. This figure was reprinted by permission from The Author(s): Royal Society; Interface Focus; Megan R Routzong, Pamela A Moalli, Spandan Maiti, Raffaella De Vita, and Steven D Abramowitch. Novel simulations to determine the impact of superficial perineal structures on vaginal delivery. *Interface Focus*, 9:20190011, 2019; © 2019 The Author(s).

structures on the stretch ratios measured in the pubovisceral muscle and perineal body during a simulation of vaginal delivery. The hypothesis, based on the assumptions of previous literature, was that they would have minimal impact (differences $< \pm 10\%$).

4.2.2 Finite Element Model Generation

The geometry of the finite element model developed in this study was composed of 6 parts: the maternal bony pelvis (right and left pelvic bones, sacrum, and coccyx), the maternal musculature (which includes the levator ani and superficial perineal muscles), and the fetal head (Figure 4.2). The muscles and bony pelvis were manually segmented from frozen cryosection images (with a 0.33mm slice thickness) of the female cadaver (parous, deceased at age 59 from a heart attack) from the Visible Human Project (U.S. National Library of Medicine, Bethesda, MD, USA), the use of which required a license but not consent or IRB approval. This anatomy was chosen as the unusually thin slice thickness allowed for visualization and segmentation of the difficult to identify superficial perineal structures in greater detail than MRI or CT are currently capable of. These geometries were then manually smoothed in 3D-Coat v.4.1.16 (Pilgway, Kiev, Ukraine) to remove aliasing, the step-like formations created around the edges of shapes due to discrete image slices, by filling the gaps and smoothing the peaks between slices. This biased smoothing approach was chosen as global smoothing techniques led to the decimation of relatively thinner regions of these complex geometries.

The fetal head was represented as an ellipsoid created within PreView v1.19.0 (University of Utah, Salt Lake City, UT, USA) and therefore did not require smoothing. The dimensions of the fetal head were approximated based on clinical averages, but the width was limited by the shape of the maternal bony pelvis—in particular the interspinous distance (the distance between the ischial spines). This resulted in a fetal head circumference of 254.6 mm, which is more representative of a term fetus at 27–29 weeks or a preterm fetus at 25.5–31.5 weeks rather than a term fetus at 40 weeks [48, 65, 117]. This was the largest fetal head possible given the material properties and boundary conditions of this first–generation model (described in the following section).

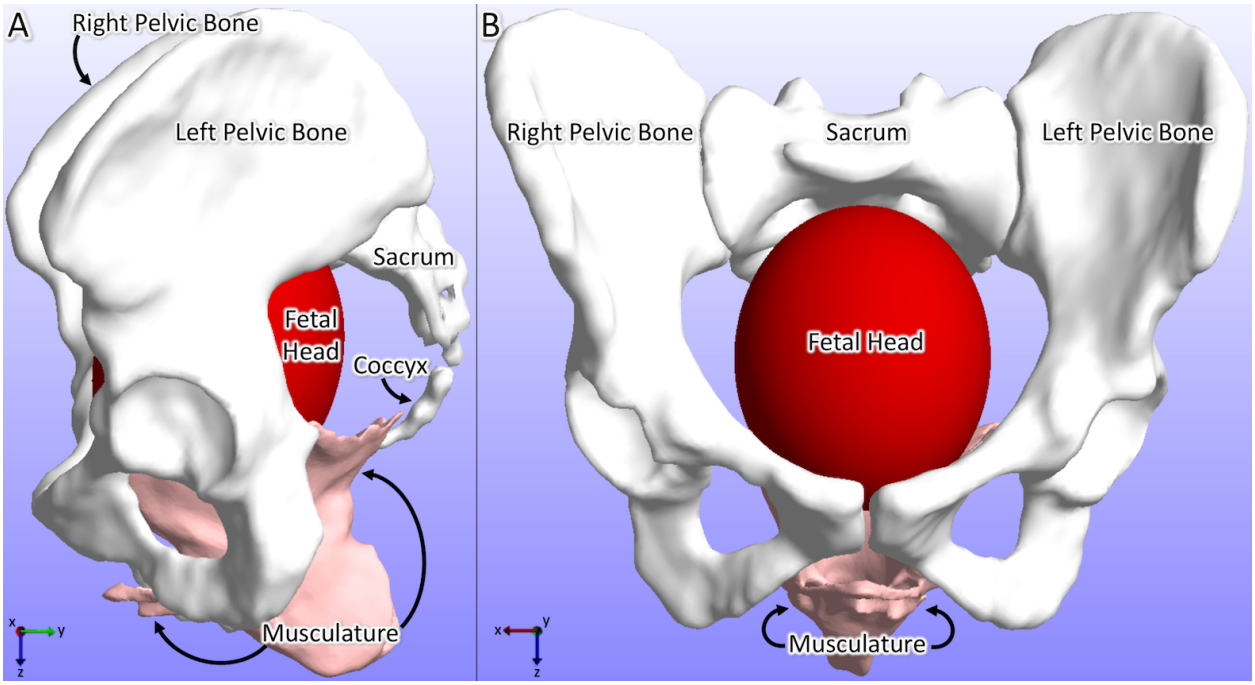

Figure 4.2: A) A sagittal view and B) coronal view of the six separate geometries included in these finite element simulations. The maternal bony pelvis is shown in white, the maternal musculature in pink, and the fetal head in red [167]. This figure was reprinted by permission from The Author(s): Royal Society; Interface Focus; Megan R Routzong, Pamela A Moalli, Spandan Maiti, Raffaella De Vita, and Steven D Abramowitch. Novel simulations to determine the impact of superficial perineal structures on vaginal delivery. *Interface Focus*, 9:20190011, 2019; © 2019 The Author(s).

Triangle surface meshes were created for all maternal geometries using Instant Meshes (Interactive Geometry Lab ETH Zurich, Zurich, Switzerland), as forming a surface of triangular elements is computationally easier for complex geometries. These meshes were then imported into PreView where volume meshes composed of tetrahedral elements, which are made of 4 triangular faces, were generated for the deformable maternal geometries (the coccyx and musculature) using the TetGen function. The hexahedral volume mesh of the fetal head was also generated within PreView. In total, the pelvic bones and sacrum consisted of 43,190 triangular elements, the coccyx had 1,042 4–noded tetrahedral elements, the fetal head had 27,648 8–noded hexahedral elements, and the muscle had 518,542 4–noded tetrahedral elements which was determined as a sufficient mesh density by a mesh convergence

study (Figure 4.3). The mesh was considered converged once increasing the density consistently resulted in corresponding strain values measurements with differences of less than 5%, which is where the mesh convergence curve plateaus.

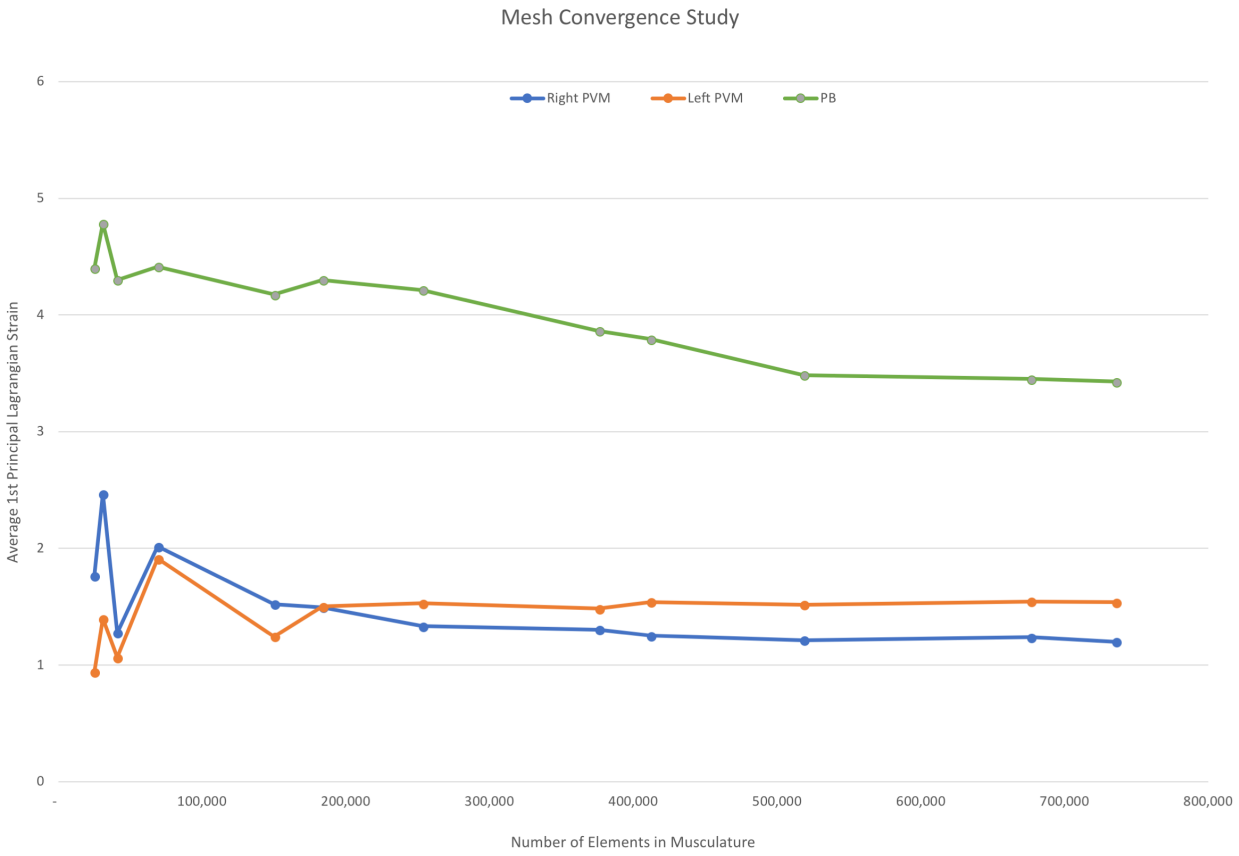

Figure 4.3: The results of our mesh convergence study demonstrating that convergence was reached for the strain outputs at all three anatomical regions of interest when the maternal musculature was composed of approximately 519,000 tetrahedral elements [167]. This figure was reprinted by permission from The Author(s): Royal Society; Interface Focus; Megan R Routzong, Pamela A Moalli, Spandan Maiti, Raffaella De Vita, and Steven D Abramowitch. Novel simulations to determine the impact of superficial perineal structures on vaginal delivery. *Interface Focus*, 9:20190011, 2019; © 2019 The Author(s).

The pelvic bones and sacrum were assigned as rigid bodies and fixed in all degrees of freedom, so they could not translate or rotate. The coccyx was deformable only to achieve the desired boundary conditions (sagittal rotation about a single point) but was given a stiffness 10 times greater than that of the muscle so that it essentially behaved as a rigid body. All maternal muscles were modelled as a single, isotropic, homogeneous, nearly incompressible, neo-Hookean, 3D continuum. Since representative values of the material parameters for many

of the involved tissues are unknown, especially at the time of delivery, material properties were selected to be the same for all muscles. The perineal body was represented as the medial region between the ends of the bulbocavernosus and superficial transverse perinei muscles, while the pubovisceral muscle was the medial portion of the levator ani near the attachment sites to the superior pelvic rami. The fetal head was a rigid body; free to translate in any direction during a prescribed downward (z) displacement of 60 mm, but fetal head crowning for both models was reached long before this displacement was achieved. All fetal head rotations were fixed with an initial orientation chosen to maximize the overall size of the fetal head, but minimize the circumference passing through the maternal bony pelvis.

Connective tissues were simulated as springs defined by force–displacement curves with a stiffness of 0 N/mm in compression, meaning they did not resist compressive loads. The connective tissues of the superficial perineal structures simulated included the attachments from the ischiocavernosus and bulbocavernosus muscles to the inferior pubic rami, from the superficial transverse perinei muscles to the ischial tuberosities, and from the deep transverse perinei muscles to the inferior pubic rami (Figure 4.4A and 4.4C). Other connective tissues simulated were the attachments from the sacrum to the coccyx (representing the sacrococcygeal ligaments), from the posterior levator ani to the sacrum (representing the anococcygeal raphe/levator plate), from the posterior levator ani to the tip of the coccyx (representing the anococcygeal raphe/levator plate and anococcygeal ligament), from the levator ani to the superior pubic rami (representing the origin of the arcus tendineus fascia pelvis and anterior portion of the arcus tendineus levator ani), and from the levator ani to the ischial spines (representing the insertion of the arcus tendineus fascia pelvis [86] (Figure 4.4B and 4.4D). Initially, all connective tissue stiffness values in tension were equal and then altered iteratively, where the final values selected restricted non-physiological movement (Figure 4.4E). Assuming material properties are roughly equivalent across these connective tissues, using structural properties (i.e. stiffness) ensures that thicker tissues, represented with more spring attachments, will provide more resistance to stretch. As resulting stresses were not the focus of this study, neither pressures nor forces were prescribed, and the mechanical behaviour of these tissues remains undefined for women at term, relative stiffness

and material parameter values were assigned to recreate the gross mechanical behaviour of delivery while avoiding additional computational complexities (such as element locking) and non–physiological motion.

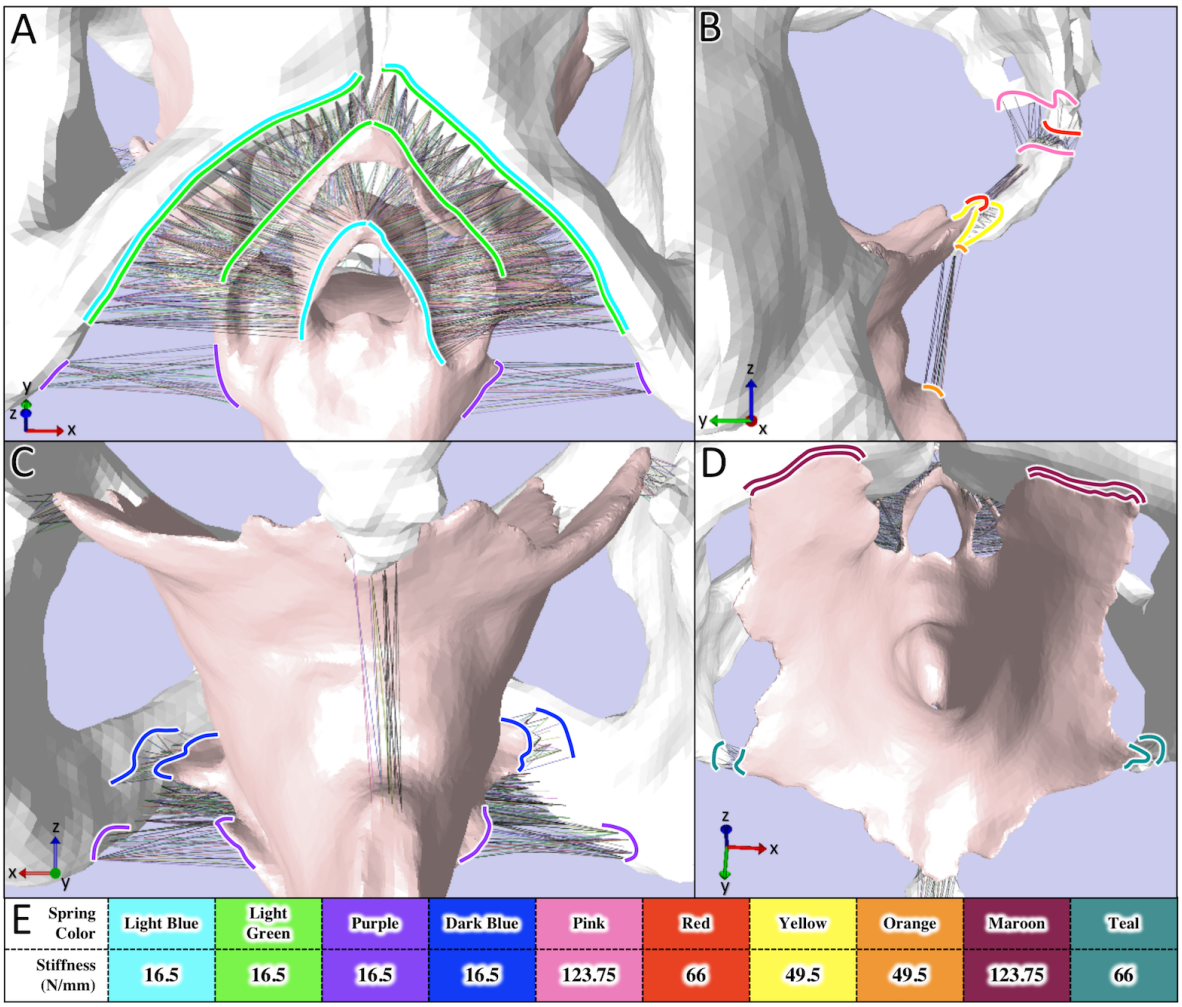

Figure 4.4: Images highlighting the A) superficial connective tissues from an inferior, anterior view, B) posterior connective tissues from a left, sagittal view, C) remaining superficial tissues from a posterior, coronal view, D) superior connective tissues from a superior view, and E) stiffness values colour coded with their corresponding attachment site outlines. Shown explicitly are the connective tissue components of the bulbocavernosus (light blue), ischiocavernosus (light green), superficial transverse perinei (purple), and deep transverse perinei (dark blue) muscles and the following connective tissues: sacrococcygeal ligaments (pink), anococcygeal raphe/levator plate (red and yellow), anococcygeal ligament (orange), origin of the arcus tendineus fascia pelvis and anterior portion of the arcus tendineus levator ani (maroon), and insertion of the arcus tendineus fascia pelvis (teal) [86, 167]. This figure was reprinted by permission from The Author(s): Royal Society; Interface Focus; Megan R Routzong, Pamela A Moalli, Spandan Maiti, Raffaella De Vita, and Steven D Abramowitch. Novel simulations to determine the impact of superficial perineal structures on vaginal delivery. *Interface Focus*, 9:20190011, 2019; © 2019 The Author(s).

To allow appropriate movement of the muscles and fetal head, contact conditions were created between the fetal head and maternal musculature, fetal head and maternal bony pelvis, and bony pelvis and musculature where their surfaces were expected or found to meet. Contact between all bodies was assumed to be frictionless sliding and was enforced with a penalty parameter determined by trial and error and then adjusted as part of the mesh convergence study (as penalty is mesh dependent). The fetal head displacement occurred linearly over 10,000 seconds (2.78 hours) with automatically adjusted time steps ranging from 1e-05 to 1,000 s. The analysis was dynamic so that temporal evolution could be studied, and all tissues were given the same density value. Numerical damping was employed to eliminate elastic wave propagation/amplification by adjusting the Newmark time integration parameters β and γ to 1 and 2, respectively. Although density can influence dynamic simulations, mass–scaling by 5 orders of magnitude in preliminary trials resulted in stretch ratio differences of less than 1% in corresponding anatomical regions. This indicated that these simulations were slow enough that density was not meaningfully influencing results of interest. All simulations were performed using FEBio v.2.5 (University of Utah, Salt Lake City, UT, USA).

4.2.3 Study Design to Isolate the Influence of Superficial Perineal Structures

To answer the research question motivating this study, in addition to the Included Model generated using the above methods, an Omitted Model was created with the same geometry, material properties, and boundary conditions, but the influence of the superficial perineal structures (the bulbocavernosus, ischiocavernosus, and deep and superficial transverse perinei muscles, and their connective tissues) was removed. This only required the removal of all contact conditions assigned to these structures and the springs connected to them, so none of the geometries or meshes were altered, allowing for a direct comparison between models. The fetal head and maternal musculature behaved as if these superficial structures, although visible, were not physically there. This assured that the contribution of these structures specifically was the only difference between the two models, allowing us to determine where the superficial perineal structures alone notably influence the outcomes of this child-

birth simulation. As 5% is the approximate error associated with the mesh density used, differences of 10% (twice that error) or greater between models were considered meaningful. The Omitted Model is meant to represent the majority of existing childbirth models as in these models the levator ani are the only maternal muscles resisting fetal head motion during simulated vaginal delivery [111, 112, 113, 143, 189].

1st principal Lagrangian strain versus time data was generated for both models using PostView v1.9.1 (University of Utah, Salt Lake City, UT, USA) to find the peak strain for the perineal body and right and left pubovisceral muscle entheses individually, only considering time points before any non-physiological motion of the coccyx or musculature occurred due to elastic recoil after fetal head crowning. Because the mesh was not altered to create the Omitted Model, the exact same elements could be sampled from both models to obtain strain values of identical anatomical regions. These strains were converted to stretch ratio values and percent differences calculated to directly compare the Included and Omitted models.

The positions of the fetal head vertex (the leading portion of the head during delivery) and perineal body centroid were measured in PostView and analysed in Wolfram Mathematica Student Edition v11.0.0 (Wolfram Research, Inc., Champaign, IL, USA) using a custom code which allowed for the generation of displacement versus time plots (Appendix D). Using these displacements, the angle of progression was calculated at each available time point for both models from the onset of the 2nd stage of labour (t=0 in these simulations) to fetal head crowning (defined as the instant of maximum perineal body strain). Angle of progression is a 2D angle between the midsagittal, long (or semi-major) axis of the ellipse-shaped pubic symphysis and a line connecting the inferior end of this axis to the vertex of the fetal skull measured at approximately the midsagittal plane [30, 109]. This has been shown to be a more reliable, robust method for measuring fetal head progression during vaginal delivery and easier to define within a finite element model than fetal head stations [30, 109]. In this study, the concept of the angle of progression was also applied to the perineal body, where the first line is still the long axis of the pubic symphysis but the second extends to the centroid of the perineal body instead of the fetal head. This served as a repeatable measure to describe and compare perineal body movement within the midsagittal plane during simulations of vaginal delivery.

4.2.4 Included vs Omitted Model Differences

In the Included Model, which incorporates the superficial perineal structures, the perineal body experienced higher and the pubovisceral muscle entheses lower stretch values in comparison to those in the Omitted Model. The fetal head paths in both models were identical until the point of maximum perineal body strain; however, in the Included Model, the path is longer as crowning occurred at a later time point due to the longer delivery time. The path of the perineal body in the two models differed after the fetal head made initial contact with the levator hiatus. Specifically, the perineal body of the Included Model reached a larger peak inferior displacement and a larger peak and final angle of progression, accounting for the increased stretch values in that region.

Table 4.1: The maximum average stretch ratio value at each anatomical site of injury of interest and the corresponding percent differences when looking from the Omitted to the Included Model [167]. This table was reprinted by permission from The Author(s): Royal Society; Interface Focus; Megan R Routzong, Pamela A Moalli, Spandan Maiti, Raffaella De Vita, and Steven D Abramowitch. Novel simulations to determine the impact of superficial perineal structures on vaginal delivery. *Interface Focus*, 9:20190011, 2019; © 2019 The Author(s).

Anatomical Location	**Omitted Model Stretch Values**	**Included Model Stretch Values**	**Percent Difference**
Perineal Body	1.98	4.10	+107%
Right Pubovisceral Muscle	1.93	1.74	-9.84%
Left Pubovisceral Muscle	2.20	1.88	-14.6%

From the Omitted to the Included Model, the changes in stretch were +107% in the perineal body, -9.84% in the right pubovisceral muscle, and -14.6% in the left pubovisceral muscle (Table 4.1). The Omitted Model had maximum stretch values of 1.98, 1.93, and 2.20 in the perineal body, left pubovisceral muscle, and right pubovisceral muscle respectively, while corresponding maximal stretch values were 4.10, 1.74, and 1.88 in the Included Model (Table 4.1). The differences in the stretch values in the perineal body and left pubovisceral muscle exceed our ±10% threshold while the difference between the right pubovisceral muscles nearly reaches it.

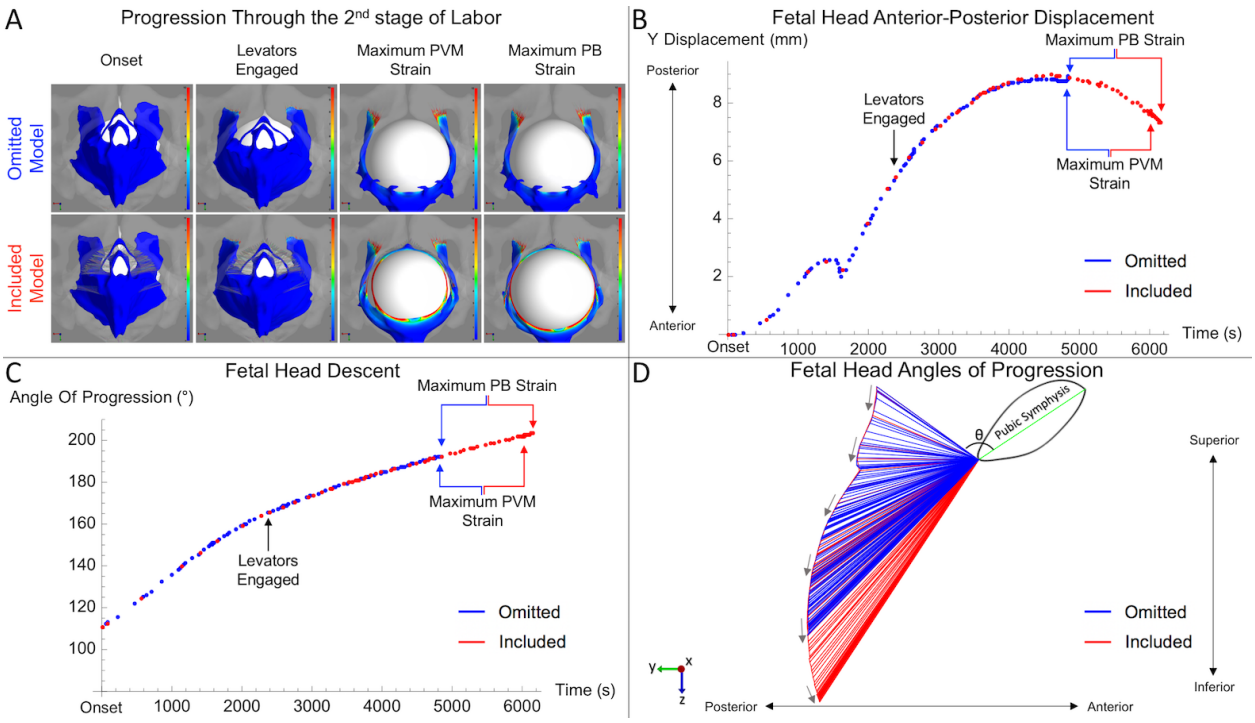

Figure 4.5: A) Screenshots from both the Omitted (top row) and Included (bottom row) models at the onset of the 2nd stage of labour (far left column), when the fetal head engages the levator hiatus (2nd column), average time point between maximum right and left pubovisceral muscle (PVM) strains (3rd column), and maximum perineal body (PB) strain (far right column). B) A plot of fetal head anterior–posterior displacements with labelled arrows pointing to the instances shown in A). C) A labelled plot of the angle of progression values for the fetal head. D) A visualization of those angles in the midsagittal plane. The arrows are guides pointing away from the onset of labour towards the moment of maximum perineal body strain, θ represents the initial angle of progression, and the green line emphasizes the long axis of the pubic symphysis [167]. This figure was reprinted by permission from The Author(s): Royal Society; Interface Focus; Megan R Routzong, Pamela A Moalli, Spandan Maiti, Raffaella De Vita, and Steven D Abramowitch. Novel simulations to determine the impact of superficial perineal structures on vaginal delivery. *Interface Focus*, 9:20190011, 2019; © 2019 The Author(s).

Because the superior–inferior displacement of the fetal head was a prescribed boundary condition, the fetal head paths were the same until the Omitted Model reached the time of maximum perineal body strain despite the freedom given in the anterior–posterior and mediolateral directions (Figure 4.5A and 4.5B). This time point arrived noticeably sooner in the Omitted Model (at t $\approx$ 4844 s with an angle of progression of 192.3°) compared to the Included Model (at t $\approx$ 6146 s with an angle of 203.3°), but that was the only noticeable difference (Figure 4.5C). Adding the superficial perineal structures resulted in a 11.0°, or +5.71%, increase in the final fetal head angle of progression in the Included Model (Figure

4.5D). Although this was not considered significant, the +26.9% difference in final fetal head superior–inferior displacement was. Mediolateral (x) displacements, which represent deviation from the midsagittal plane, were minimal (for both the fetal head and the perineal body) and fetal head superior–inferior displacements were prescribed; therefore, these specific results are not shown.

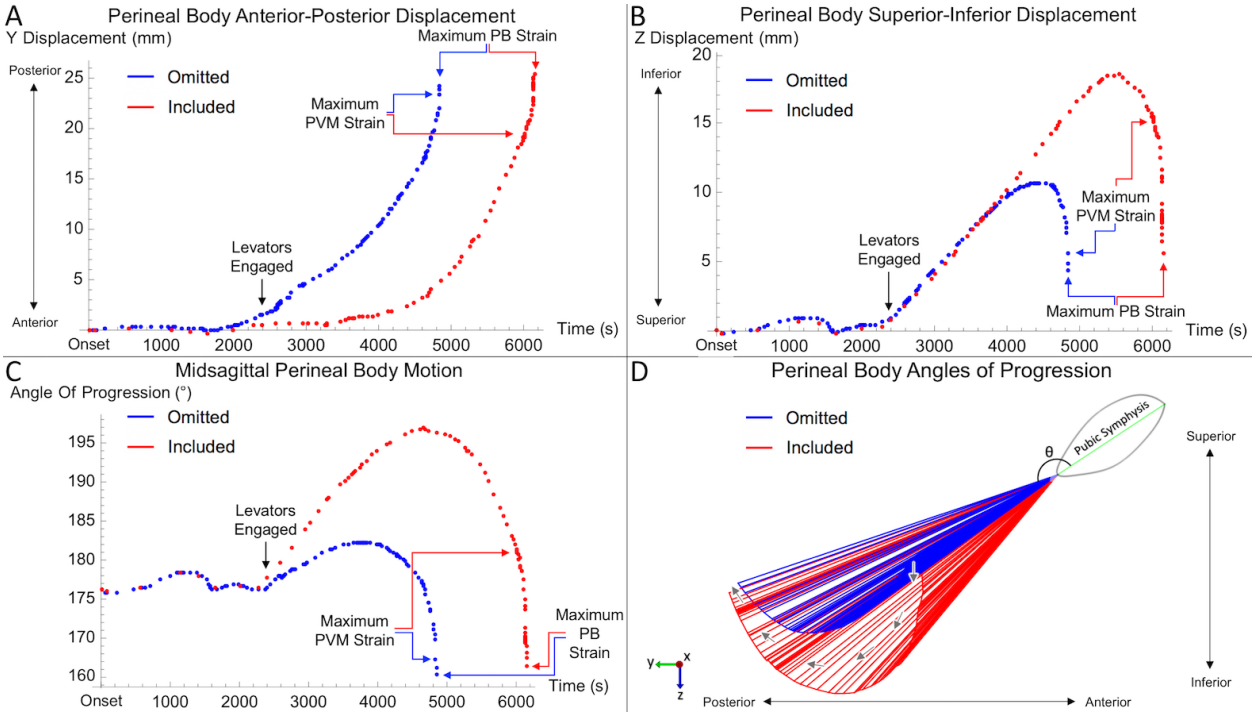

Figure 4.6: A) A plot of perineal body (PB) anterior–posterior displacements with the same timepoints from Figure 5 labelled. B) A labelled plot of perineal superior–inferior displacements. C) A labelled plot of the modified angle of progression values for the centroid of the perineal body. D) A visualization of those angles in the midsagittal plane. The arrows are guides pointing away from the onset of labour towards the moment of maximum perineal body strain, θ represents the initial angle of progression, and the green line emphasizes the long axis of the pubic symphysis [167]. This figure was reprinted by permission from The Author(s): Royal Society; Interface Focus; Megan R Routzong, Pamela A Moalli, Spandan Maiti, Raffaella De Vita, and Steven D Abramowitch. Novel simulations to determine the impact of superficial perineal structures on vaginal delivery. *Interface Focus*, 9:20190011, 2019; © 2019 The Author(s).

As expected, until the fetal head engaged the levator hiatus, the displacement and angle of progression curves for the perineal bodies were almost identical. Following this contact, the perineal body paths diverged. The anterior–posterior displacements only differed in timing as the slopes and magnitudes were otherwise quite similar (Figure 4.6A). Although the fetal head path was not significantly altered, the perineal body was forced to inferiorly

displace 7.8 mm, or +72.5% (greater than our ±10% threshold), further at its peak in the Included Model due to the presence of the superficial perineal structures (Figure 4.6B). This corresponds with an angle of progression 14.6°, or +8.00%, larger in the Included Model (Figure 4.6C). The peak superior–inferior displacement and maximum angle of progression of the Included Model were 18.5 mm and 196.9°, respectively, while those of the Omitted Model were 10.7 mm and 182.3°. For the perineal body in each model to reach the same final anterior–posterior and superior–inferior displacement, the perineal body in the Included Model had to deform more in the inferior direction (Figure 4.6D). This resulted in the higher stretch ratio, superior–inferior displacement, and angle of progression values observed in the Included Model.

4.2.5 Superficial Perineal Structures Impact Simulations of Vaginal Delivery

These results refute the stated hypothesis, suggesting that superficial perineal structures play a critical role in maternal birth injury pathophysiology and should be included in future computational models. This work also supports that the perineal body is more vulnerable to injury than previously appreciated, which is consistent with the relatively large quantity of perineal tears observed clinically [82, 173]. Inclusion of the superficial perineal structures resulted in higher stretch values in the perineal body and lower values in the pubovisceral muscle, indicating that the Omitted Model, and those with geometries like it, underestimate perineal body and overestimate pubovisceral muscle stretch. The percent differences imply that this perineal body underestimation is much more severe than the pubovisceral muscle overestimation. When maternal musculature is modelled as a simple, sling–like shape, the levator ani—specifically the pubovisceral muscle entheses—take on a higher proportion of the load. In contrast, when the superficial perineal structures are present to decrease urogenital hiatus size and restrict the perineal body, as demonstrated in the Included Model, the perineal body can no longer move as easily and must stretch instead. This is more similar to what is observed *in vivo* as the perineum stretches drastically while its motion is restricted during fetal head crowning.

These stretch values are reasonable compared to previous studies (with models similar to the Omitted Model) as values range from 1.6 to 3.5 in the levator ani [86]. The perineal body in the Included Model surpasses this range, which could potentially be explained by the variation in perineal body location across childbirth models. The perineal body is commonly described as the fibromuscular structure between the anus and vagina and superficial to the pelvic diaphragm, but its exact boundary and composition are widely debated [85, 106]. Studies have determined that it is comprised of 3 layers, but do not agree on the location and makeup of each layer [106, 175]. When childbirth models only include structures at the same depth as the levator ani, they are only including the deepest layer of the perineal body, if any true layer at all [106, 175]. The Included Model contains the thickness of more, if not all three, layers as well as corresponding connective tissue attachments. This could explain the increased perineal body stretching as, in addition to the levator ani, the superficial perineal structures were also pulling it in opposing directions.

The fetal head in both models started at an angle of progression of 100°, but at the moment of fetal head crowning—defined here as the point of maximum perineal body strain, as in previous studies—the Included Model had a larger value [14, 30, 109]. The superficial perineal structures increased the final fetal head angle of progression, indicating that the soft tissues in the Included Model were pushed further to reach an analogous moment of fetal head crowning. This is corroborated by the perineal body data.

The perineal body in the Included Model was forced to stretch and inferiorly displace further to reach a similar final anterior–posterior and superior–inferior displacement as the Omitted Model (Figure 4.7). Although both models reach similar final displacements, the Included Model took longer to do so. This acts as a form of validation as the anatomical function of the superficial perineal structures *in vivo* is to restrict caudal, or anterior–posterior, motion of the perineal body [56]. These structures forced the perineal body to stretch further by creating tension that restricted its anterior–posterior motion as it was being pushed posteriorly by the fetal head. When the superficial perineal structures were not present, it was easy for that tissue to be pushed out of the way (as demonstrated by the smaller perineal body angle of progression values in the Omitted Model). Although angle of progression is typically used to assess fetal head progression, it was employed here as a robust method

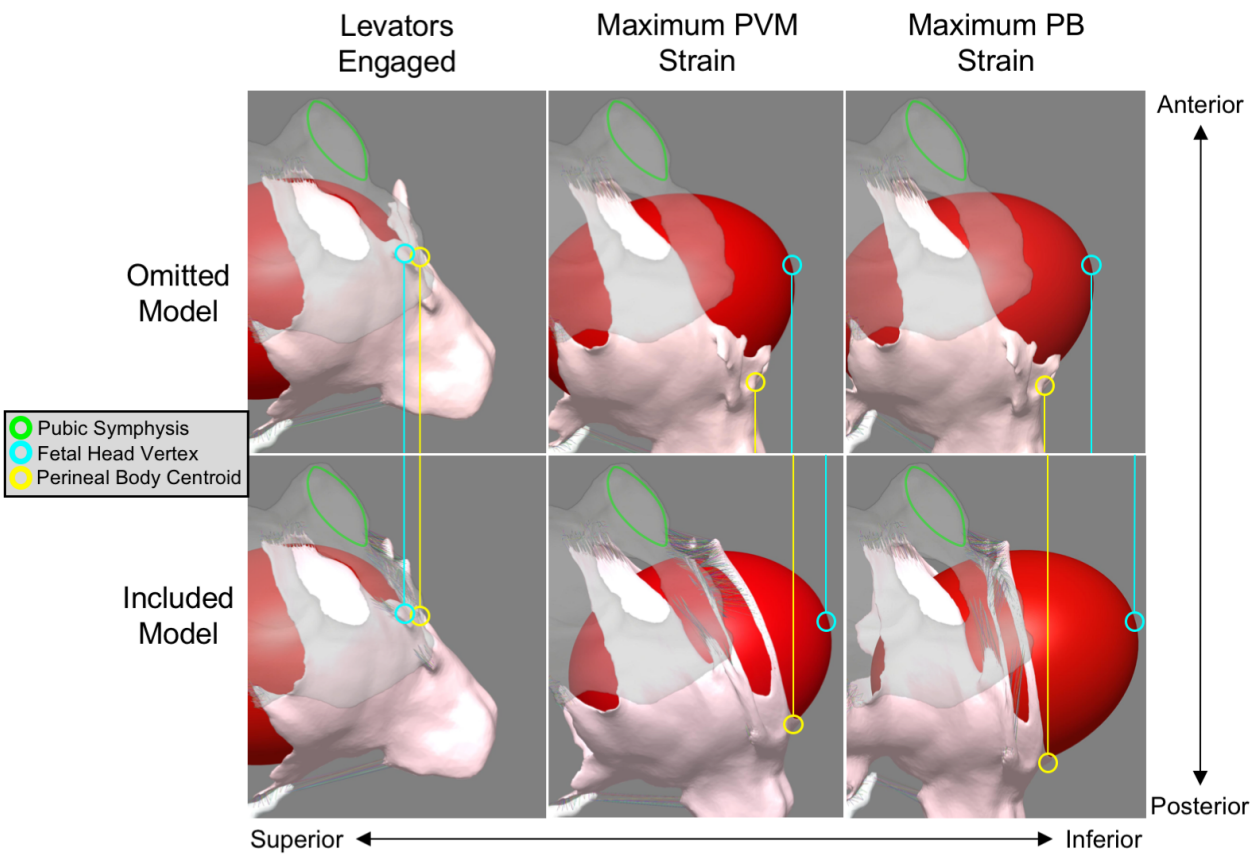

Figure 4.7: Screenshots from both the Omitted (top row) and Included (bottom row) models at the moment the fetal head engages the levator hiatus (far left column), the average time point between maximum right and left pubovisceral muscle (PVM) strains (2nd column), and the moment of maximum perineal body (PB) strain (far right column). The pubic symphysis (outlined in green) serves as a point of reference. The differences in the superior–inferior positions of the fetal head vertex (circled in blue) and PB centroid (circled in yellow) between models are emphasized with vertical lines coming from each [167]. This figure was reprinted by permission from The Author(s): Royal Society; Interface Focus; Megan R Routzong, Pamela A Moalli, Spandan Maiti, Raffaella De Vita, and Steven D Abramowitch. Novel simulations to determine the impact of superficial perineal structures on vaginal delivery. *Interface Focus*, 9:20190011, 2019; © 2019 The Author(s).

for measuring and a basis for a more quantitative evaluation of midsagittal perineal body movement during the 2nd stage of labour that could be used in future computational and experimental studies.

As a first attempt to quantify the importance of superficial perineal structures in finite element models of vaginal delivery, this study has several limitations. The maternal geometry was from an older, parous, female cadaver, which likely does not appropriately represent a

woman at full–term. All maternal muscles were continuous, hyper–elastic, passive, lacked fibre directions, and assigned the same, simplified material properties meant to serve as initial estimates for future experiments. While many of these muscles are continuous anatomically, there are identifiable boundaries, varying fibre orientations, and possibly varying material properties in women at full–term, making it unclear how stresses are transferred *in vivo* during delivery. The fetal head was small, rigid, and rotation was restricted, although the small size was not considered a considerable limitation as the fetal head moulds during vaginal delivery *in vivo* in order to fit through the birth canal by reducing the fetal head circumference. This model does not incorporate fetal head moulding, so using measurements of a fetal head at term would have resulted in an overestimation of stretch ratio values throughout the simulated delivery. Work is currently being done to overcome these limitations, but, as they affect both models equally, it is assumed that the direct comparisons reported here are minimally affected.

After thorough observation and analysis, it is believed that the Included Model in this study provides a better gross impression of the maternal geometry and biomechanics in response to the passage of the fetal head during the seconds stage of labour. These results suggest that the superficial perineal structures likely warrant more focus in future computational and experimental studies of childbirth biomechanics than given previously.

4.3 Morphological Differences in the Bony Pelvis and Pelvic Floor Muscle Complex of Pregnant Women

4.3.1 Pregnancy–Induced Remodeling and Female Pelvic Shape

During gestation, maternal pelvic organs and tissues undergo dramatic remodeling due to the biochemical changes initiated by fluctuating hormones and the altered mechanical environment created by the growing fetus [8]. For the pelvic floor muscles, rat models have been used to determine that these changes likely involve increasing muscle fiber length [11], sarcomere elongation [44], and muscle stiffness [10]. In humans, reduced levator ani muscle

active force [51] and less shortening during contraction [179] have been observed. In contrast, the stiffness of pelvic connective tissues decrease during pregnancy [8], which corresponds with observed pelvic organ descent and increased urethral mobility [73, 176]. It is believed that these changes are preparing the maternal pelvic tissues to bear the load of the fetus until full term and/or for the strenuous act of vaginal delivery [44].

Evidence provided by existing literature and clinical knowledge suggests that this maternal remodeling and response to a changing mechanical environment results in visible changes to the shape of the maternal pelvic floor and bony pelvis. Imaging studies have identified increased levator hiatus dimensions during pregnancy [176]. Additionally, statistical shape modeling has been used to identify midsagittal pelvic floor shape differences between 1st/2nd vs 3rd trimester pregnant women: The levator plate was found to be straighter and positioned more posteriorly and inferiorly with a more vertical orientation in late pregnancy (see Section 5.3) [169]. Image analyses have also been used to quantify differences in the midsagittal sacrum–coccyx shape and found straighter and more posteriorly positioned coccyxes in pregnant women compared to nulliparous controls [120]. We believe that, with robust quantification, the shape of pelvic anatomy could be used to determine the degree of remodeling undergone during pregnancy, which, in turn, could eventually determine who may be at increased risk for stretch-related injury during vaginal childbirth.

The aim of this study was to utilize statistical shape modeling to objectively quantify shape variation in the pelvic floor and bony pelvis of gravid (i.e., pregnant) women of varying gestational ages (1st and 2nd vs 3rd trimester). We hypothesized that the levator plate and sacrococcygeal joint would be straighter and that there would be greater perineal descent in 3rd trimester women.

4.3.2 3D Female Pelvic Shape Acquisition

This was a retrospective study approved by the Institutional Review Board at the University of Pittsburgh and considered exempt at Northshore University HealthSystem. Gravid women age 20-49 who underwent pelvic MRI without contrast as instructed by their physician for medical indications (such as abdominal/pelvic pain, appendicitis, abnormal placentation,

or fetus anomalies) at Magee-Womens Hospital or Northshore University HealthSystem between 2005 and 2018 were included in this study. Exclusion criteria were history of pelvic surgery (not including Cesarean delivery), pelvic masses, scans that did not completely capture the bony pelvis or pelvic floor, and incomplete birth history information. As these patients were pregnant, imaging had been performed in the lateral decubitus position.

The pelvic floor muscle complex and bony pelvis were segmented from each patient. In this study, the pelvic floor included the coccygeus, levator ani (composed of the iliococcygeus and pubovisceralis), external anal sphincter, perineal body, and superficial perineal structures (including the bulbocavernosus, ischiocavernosus, superficial and deep transverse perinei, and perineal membrane) all segmented as one continuous structure (Figure 4.8). To reduce computational costs and improve point correspondence, the perineal membrane and other superficial tissues were segmented as one instead of leaving holes or gaps in between individual structures. This also meant that some of the lateral, posterior portions of the clitoris were segmented as part of the pelvic floor to avoid regions where there would be multiple thin muscles/connective tissues in close proximity. The bony pelvis included the coccyx, which was physically separate from the sacrum, and left and right innominate bones (each composed of the pubis, ischium, and ilium) which were segmented as a continuous structure (Figure 4.8).

To smooth these segmentations while simultaneously calculating corresponding points for subsequent statistical shape analyses, a template pelvic floor and bony pelvis were generated and deformed onto the patient–specific segmentations (see Section 2.1.2). The pelvic floor template was segmented from one of the Visible Korean Human's female cadaveric pelvis cryosection images (Korea Institute of Science and Technology Information, Daejeon, South Korea). This segmentation was smoothed in 3D–Coat (Pilgway, Kiev, Ukraine) and contained 8,327 vertices. The bony pelvis template in this study was the average shape calculated from 25 female bony pelvises segmented from CT images as part of a previous study [27]. Because the coccyx bones exhibited a high amount of shape variability relative to the size of the coccyx, a simple ellipsoid was used as the coccyx template.

The pelvic floor, bony pelvis (sacrum and innominate bones), and coccyx templates were applied to the corresponding pregnant segmentations separately using the atlas–registration

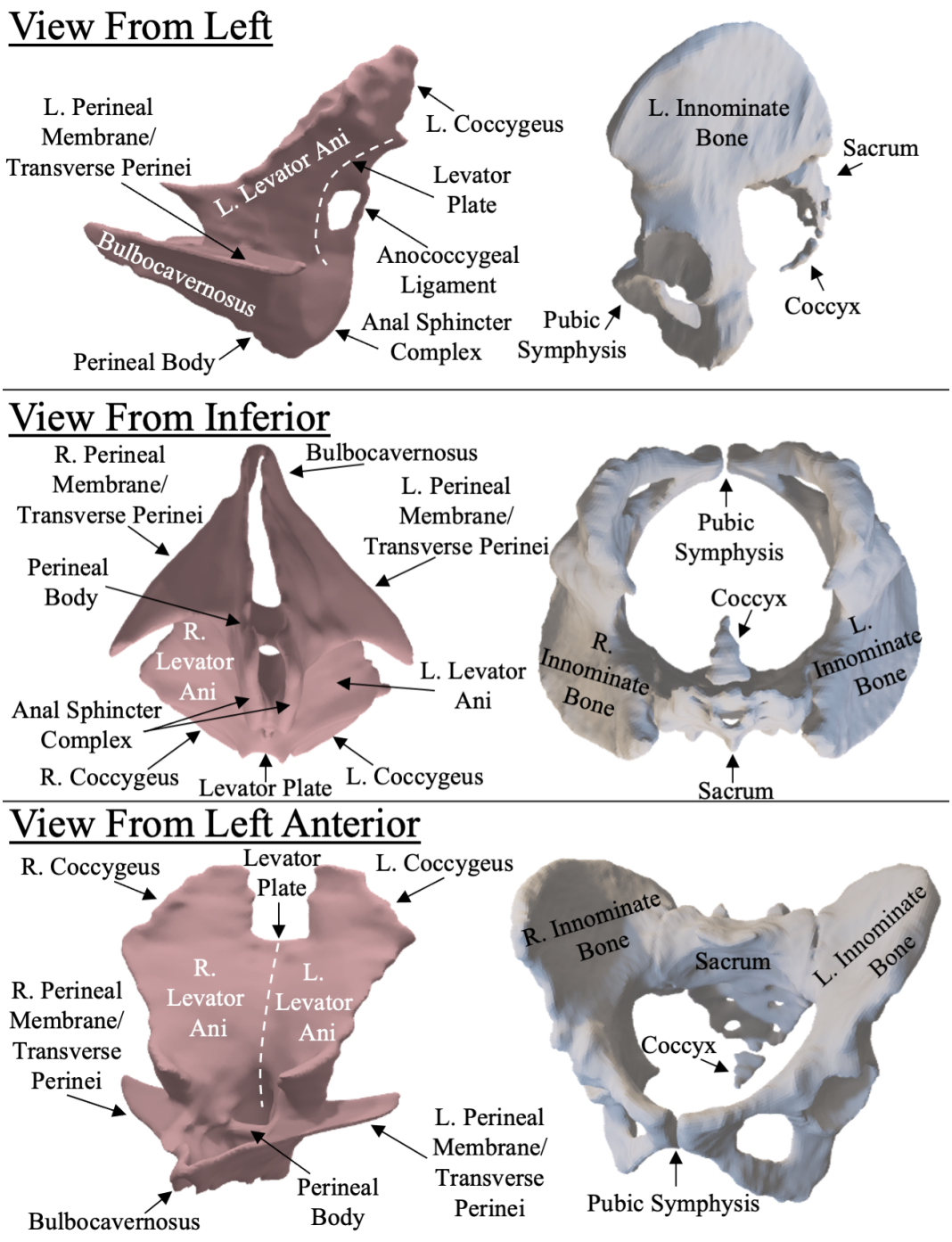

Figure 4.8: A representative pelvic floor muscle complex and bony pelvis from left (top), inferior (middle), and angled left anterior (bottom) perspectives with relevant structures labelled.

function in Deformetrica. Due to the complexity of the pelvic floor muscle complex shape, the template was scaled to match the size of each subject–specific segmentation. This scaling improved the fit of the smoothed shapes and ensured that the Procrustes determined average shape would still be representative of the average scale of the subject–specific segmentations. The bony pelvises were smoothed using the previously described average composed of 11,086 vertices. Due to the large amount of aliasing relative to the total size of the coccyx (some coccyxes consisted of as little as 3 MRI slices) they had to be fitted twice using two different templates. The first template was an ellipsoid generated specifically for each coccyx. This initial smoothing pass was designed to remove the largest level of aliasing present in some of the coccyxes. The second ellipsoid template was used to apply the corresponding points to all every coccyx and had 872 vertices.

4.3.3 3D SSM of the Bony Pelvis and Pelvic Floor

Once corresponding points were determined, each patient's pelvic floor, bony pelvis, and coccyx were recombined in Houdini FX (SideFX, Toronto, Canada) into the correct relative positions. Each set of geometries consisted of 20,285 vertices. Once combined and aligned, these combined bony pelvis–pelvic floor geometries (referred to as combined geometries) were imported into Mathematica (Wolfram Research, Champaign, IL, USA) to carry out the rest of the statistical shape modeling (SSM) workflow previously established by our lab [169] (see Sections 2.1 and 5.3). This process involves performing a Procrustes analysis to remove any differences due to translation, rotation, or scale; a principal component (PC) analysis to identify eigenvectors, eigenvalues, and modes of variation; and a parallel analysis to determine which modes are significant (i.e., explain more variance than noise). This results in PC scores—the projection of patient-specific data onto eigenvectors—for each patient and significant mode which were used as the dependent variables in subsequent statistical analyses. This SSM workflow was also carried out on the bony pelvises and pelvic floors individually for more representative statistical comparisons, as the scale of the combined

geometries may potentially hide smaller shape differences (e.g., small pelvic floor muscle shape differences may be insignificant when evaluating the combined geometries but not the pelvic floors by themselves).

Patient demographics were compared between 1st and 2nd vs 3rd trimester patients via independent t–tests for continuous and Pearson Chi–Square tests for categorical variables utilizing SPSS v.25 (International Business Machines Corporation, Armonk, NY, USA). Parity and vaginal parity were categorized as either =0, =1, or >1, while gravidity was categorized as =1, =2, or >2 for these statistics. 1st and 2nd vs 3rd trimester shapes were compared across all three SSMs with MANCOVAs. Maternal age was included as a covariate in order to isolate the influence of gestational age on maternal pelvic morphology. ANCOVAs were performed to assess significant modes individually, which allows for qualitative descriptions of specific differences in shape attributes. The Benjamini–Hochberg (BH) method with a false discovery rate of 10% was used to correct MANCOVA and ANCOVA p–values for multiple comparisons [24]. A p–value less than the corresponding BH critical value was considered statistically significant.

4.3.4 Significant Shape Variation and Differences Between Early and Late Pregnancy

Table 4.2: Patient Demographics and 1st and 2nd vs 3rd Trimester Comparisons

Trimester	**Gestational Age (weeks)**			**Maternal Age (years)**			**Parity**			**Vaginal Parity**		
	Mean ± SD	N	p-value	Mean ± SD	N	p-value	Median (Min-Max)	N	p-value	Median (Min-Max)	N	p-value
1st/2nd	15.2 ± 5.5	17	**<0.001**	30.5 ± 4.4	17	0.105	1(0-3)	17	0.18	0(0-2)	15	0.083
3rd	31.5 ± 3.4	17		33.5 ± 6.2	17		1(0-6)	17		0(0-2)	16	

Trimester	**Race/Ethnicity**					**Gravidity**		
	Asian (N)	Black (N)	White (N)	White Hispanic (N)	p-value	Median (Min-Max)	N	p-value
1st/2nd	1	4	11	0	0.187	2(1-5)	17	**0.033**
3rd	1	1	11	3		4(1-10)	17	

As expected, gestational age (weeks) significantly differed between 1st and 2nd vs 3rd trimester shapes (p<0.001, Table 4.2). Maternal age, parity, vaginal parity, and race/ ethnicity did not significantly differ between these groups while gravidity did (p=0.033).

Table 4.3: Percent Variance Explained by Each Mode and ANCOVA p-values

	N	Mode 1	Mode 2	Mode 3	Mode 4	Mode 5	Mode 6	Mode 7	Mode 8
Combined SSM	25	22.30%	20.50%	8.40%	6.80%	6.30%	5.30%	4.30%	
p-value		0.079	0.153	0.122	0.157	**0.021**	0.367	0.244	
Pelvic Floor SSM	28	27.30%	14.90%	10.90%	9.10%	5.30%	3.90%		
p-value		0.204	0.973	0.288	**0.024**	0.35	0.447		
Bony Pelvis SSM	33	23.20%	12.50%	9.90%	7.90%	6.60%	4.60%	4.10%	2.80%
p-value		**0.008**	0.931	0.498	0.246	**0.022**	0.424	0.481	0.036

The combined SSM resulted in 7 significant modes of variation, the pelvic floor SSM in 6, and the bony pelvis SSM in 8 (Table 4.3). At the multivariate level (when all significant modes are considered simultaneously), both the combined geometries and bony pelvis shapes differed significantly between 1st/2nd trimester and 3rd trimester women (p=0.002 and 0.001, respectively). At the univariate level (when each significant mode was considered individually), mode 5 from the combined SSM (p=0.021), mode 4 from the pelvic floor SSM (p=0.024) and modes 1 and 5 from the bony pelvis SSM (p=0.008, and 0.022, respectively) were significantly influenced by gestational group (Table 4.3).

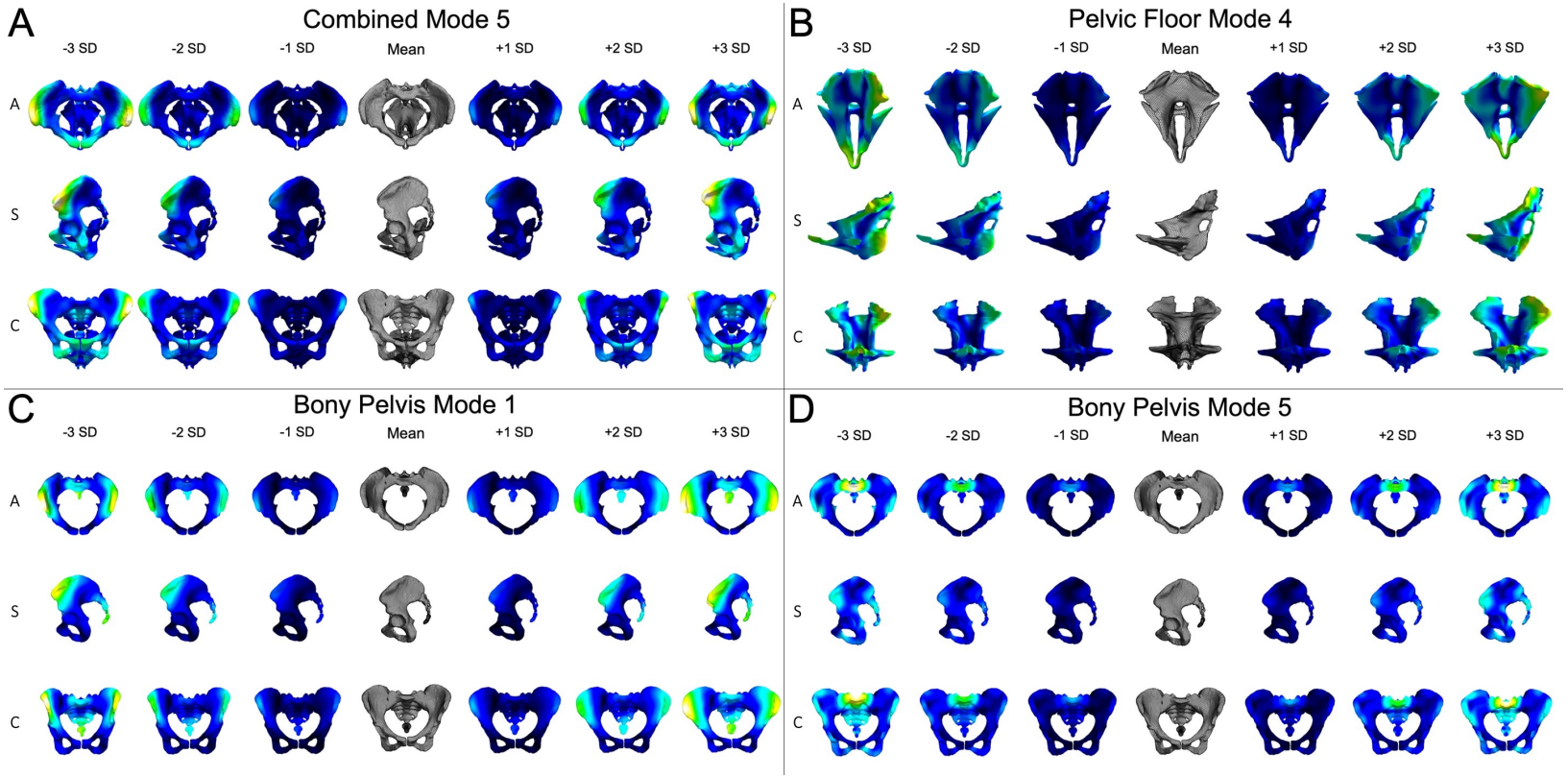

Figure 4.9: Representative shapes from axial (A), sagittal (S), and coronal (C) views within 3 standard deviations (SD) of the mean shapes demonstrating the shape variation described by each mode with significant differences between 1st/2nd and 3rd trimester women. Black/dark blue indicates mesh vertices/regions with minimal displacement from the mean shape while white/yellow indicates maximal displacement. A) Combined bony pelvis-pelvic floor mode 5 highlights variation in the width of the pelvis at the iliac crests, the angle of the obstetric inlet at the pubic rami, and descent of the perineal body. B) Pelvic floor mode 4 highlights variation in the orientation of the coccygeus muscles, the curvature of the levator plate, and in the relative position of the perineal membrane and external anal sphincter. C) Bony pelvis mode 1 highlights variation in the medial-lateral orientation (width) of the iliac crests and in the curvature and relative position of the sacrum and coccyx. D) Bony pelvis mode 5 highlights variation in the curvature of the lumbosacral joint.

As expected, due to the size of the bony pelvis relative to the pelvic floor muscle complex, the combined pelvic floor–bony pelvis modes demonstrated more bony pelvis shape variation. Mode 5 described variation in the width of the pelvis (most prominently at the iliac crests), the angulation of the left and right pubic rami, and relative descent of the perineal body (Figure 4.9A). Women in their 3rd trimester had significantly smaller combined mode 5 PC scores than women earlier in their pregnancy, suggesting that later in pregnancy women have wider pelvises, larger subpubic arch angles, and more descent of the perineal body (Figure 4.10A). Pelvic floor mode 4 describes variation in the orientation of the coccygeus, the levator hiatus proportions, the curvature of the levator plate, and in the relative position of the perineal membrane and external anal sphincter (Figure 4.9B). Women in their 3rd trimester had larger PC scores than those in the 1st/2nd trimester. Specifically, these group differences suggest that 3rd trimester women have more superiorly–inferiorly orientated coccygeus muscles, proportionally larger levator hiatus transverse diameters, straighter and more vertical levator plates, relatively longer anococcygeal ligaments, and further descended perineal membranes and external anal sphincters relative to the coccyx and ischial spines (Figure 4.10B). Bony pelvis mode 1 described iliac crest and sacrococcygeal joint variation, while mode 5 demonstrated lumbosacral joint, sacral promontory, and coccyx variation (Figure 4.9C and D). The women in their 3rd trimester in this study had wider pelvises (with left and right iliac crests that were further apart), straighter sacrococcygeal angles, more relatively anteriorly–inferiorly located sacral promontories, and slightly more vertical left iliac crests (Figure 4.10C and D).

When the average 1st/2nd trimester and 3rd trimester shapes were generated and compared via a surface–to–surface distance mapping algorithm and by overlapping those shapes, we see the greatest differences in similar regions of the bony pelvis and pelvic floor as described by the discussed SSM modes (Figure 4.11). The most notable difference is the wider pelvis at the iliac crests in the 3rd trimester average shape.

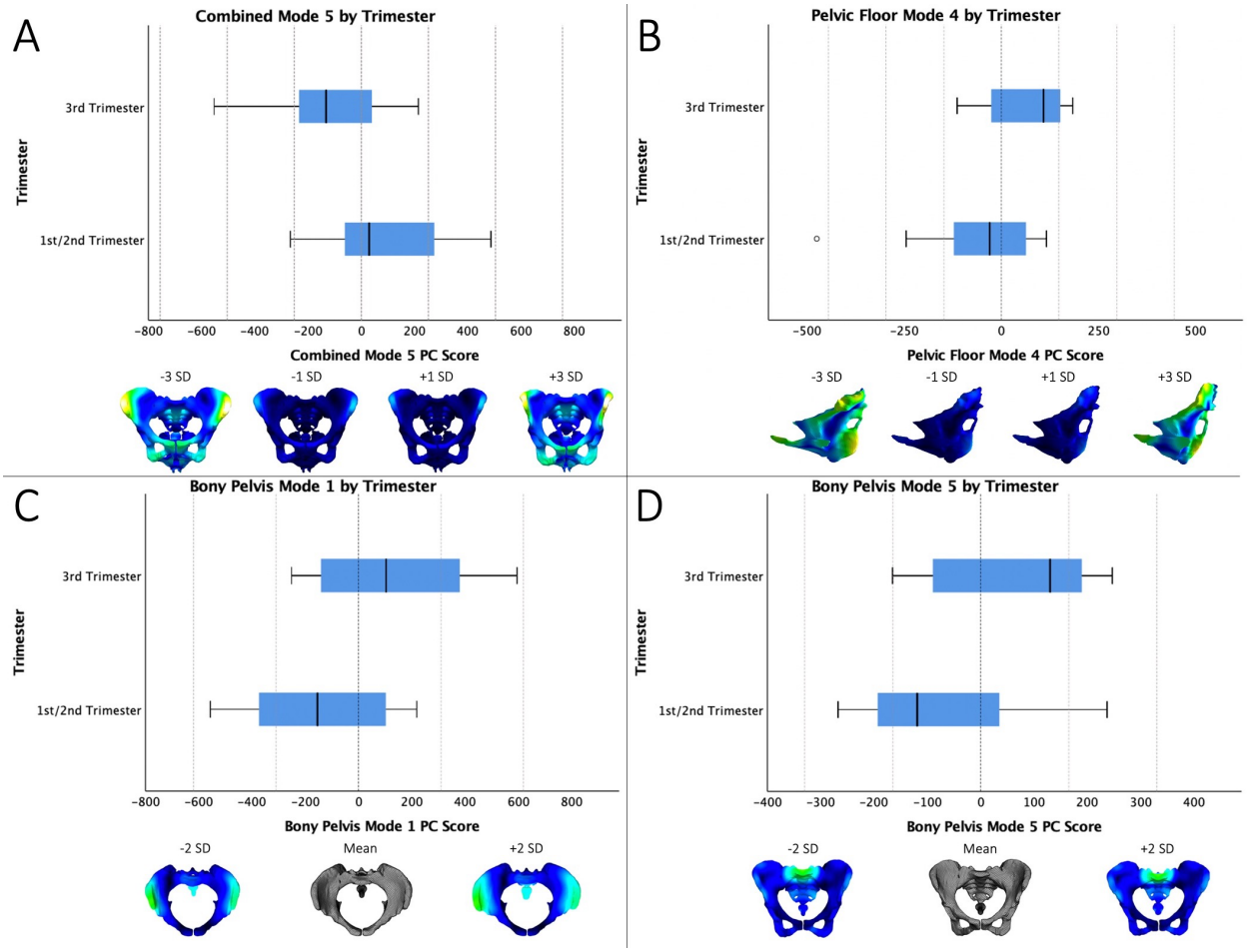

Figure 4.10: Horizontal boxplots demonstrating the group distributions of A) combined bony pelvis-pelvic floor mode 5, B) pelvic floor mode 4, C) bony pelvis mode 1, and D) bony pelvis mode 5 PC scores. Below each plot are illustrative shapes from Figure 4.9 highlighting these group differences. 3rd trimester pelvic floors had more vertically oriented coccygeus muscles, increased relative descent of the perineal membrane and external anal sphincter, and proportionally wider levator hiatuses. 3rd trimester bony pelvises were wider at the iliac crests and had less sacrococcygeal curvature, relatively more anterior-inferior positioned sacral promontories, and more vertically oriented left iliac crests.

4.3.5 Pregnancy–Induced Remodeling Impacts Pelvic Shape

This statistical shape modeling study revealed that there are significant differences in the bony pelvis and pelvic floor muscle complex morphology of pregnant women in the 1st/2nd vs 3rd trimester. Importantly the overall (when all significant modes are considered simultaneously) combined bony pelvis–pelvic floor and overall bony pelvis shapes demonstrated

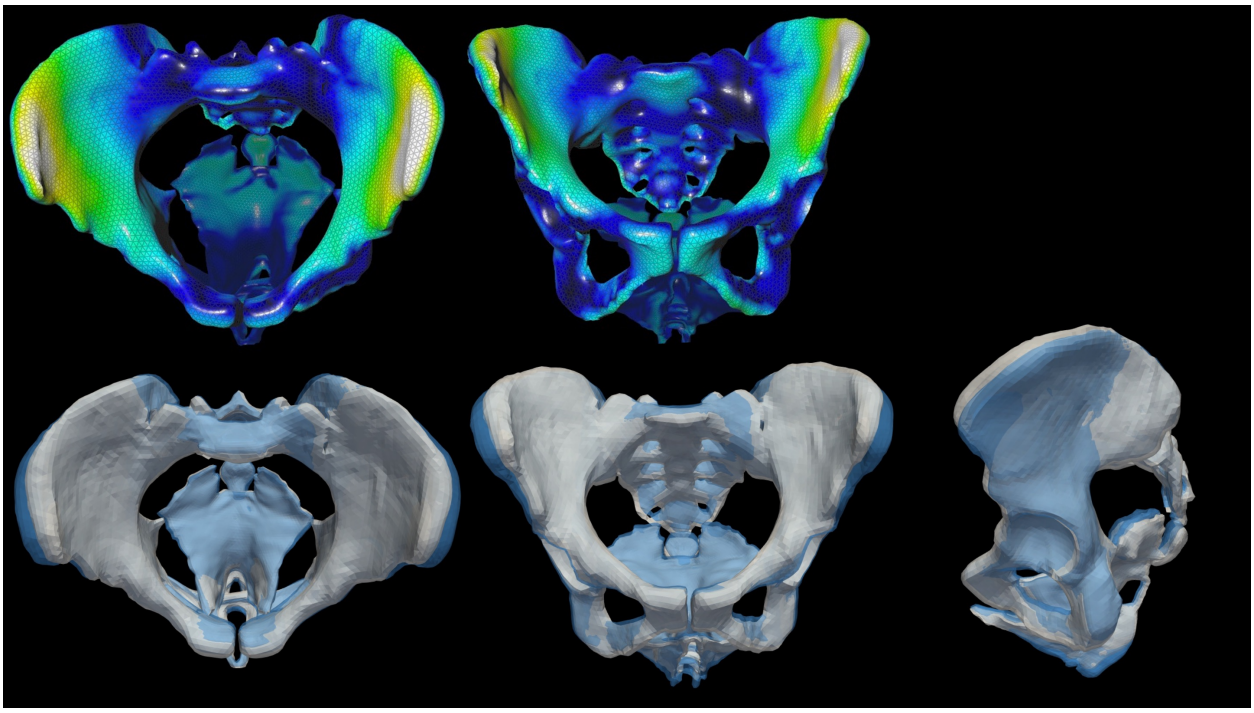

Figure 4.11: Depicts the average 1st/2nd trimester (top: lighter colors, bottom: white) and 3rd trimester (top: darker colors, bottom: blue) combined bony pelvis–pelvic floor shapes to demonstrate the most general morphological differences between these groups. The top depicts the 1st/2nd trimester shape with colors representative of the differences from the late pregnant shape, while the bottom depicts both shapes overlaid on top of one another.

significant differences across trimester groups. This, and the fact that more bony pelvis modes explained a larger percent of the total shape variance (even when the bony pelvis and pelvic floor muscle complex were considered individually), suggests that bony pelvic morphological changes in pregnancy may be more prominent than those of the pelvic floor muscle complex. Though the morphological alterations in the 3rd trimester stated in our hypothesis were verified by this study (i.e., greater perineal descent, straighter levator plate, and straighter sacrococcygeal joint), greater shape variation was found in the iliac crests and obstetric inlet.

While this study cannot isolate which morphological changes are associated with alterations in the mechanical environment, alterations in hormone levels, or, most likely, some combination of both, we can hypothesize which shape variations would better support the

fetus or reduce the burden of vaginal childbirth. The role of the increased proportional pelvic width linked to 3rd trimester shapes likely changes depending on the region of the pelvis being considered. The iliac crests, for example, are outside of the obstetric inlet/outlet and likely have little influence on vaginal childbirth. When the pelvic width increases at the iliac crests, it is likely a response to increased mechanical loads on the bony pelvis, rather than a hormonal response meant to facilitate vaginal childbirth. This would be the case for the shape variation described by bony pelvis mode 5 as well, which was very localized, isolated to the part of the sacrum that composes the bottom of the lumbosacral joint and a potential result of changes in gait and spine loading conditions later in pregnancy. A larger subpubic arch angle and corresponding widening of the obstetric inlet at the pubic symphysis (as described by combined mode 5 and bony pelvis mode 1), on the other hand, would create more room within the bony pelvis for passage of the fetal head, reducing the risk of maternal birth injury. This is supported by literature that has shown that a smaller subpubic arch angle is associated with operative delivery [74]. The bulk of these morphological changes in the obstetric inlet/outlet are without doubt facilitated by the pubic symphysis, as it has been shown to increase in width during pregnancy due to remodeling of the fibrocartilaginous tissue induced by circulating hormones [23].

The differences in the pelvic floor muscle complex shape between 1st and 2nd vs 3rd trimester women corroborates previous findings that only looked at the midsagittal plane [169] (see Section 5.3). This previous study also observed relative perineal descent, anterior–inferior bulging of the bulbocavernous muscle, and straightening of the levator plate in 3rd trimester pelvic floor muscle complexes. Additionally, in this 3D analysis, we noted proportionally longer anococcygeal ligaments, relatively taller coccygeus muscles, and proportionally wider levator hiatuses. These findings agree with increased levator hiatus dimensions [176] and pelvic organ descent [73] in late pregnancy documented in the literature. All of these soft tissue morphological changes correspond with what we would expect from increased mechanical loads being applied to the pelvic floor and likely reduce the strains experienced by these tissues during the 2nd stage of labor.

Although this study was retrospective and cross–sectional, enough patients were included to adequately define normal distributions of shape variation. While confirming previous find-

ings from studies that used two–dimensional variables and/or analyses to evaluate morphological changes in pregnant women, these statistical shape models also deliver robust shape quantification and generated shapes along significant modes that can be used as geometric inputs to improve computational simulations of pregnant female anatomy. One important application of such geometries would be for computational simulations of vaginal childbirth, which are currently limited by the use of single, patient–specific anatomy frequently segmented from scans of non–pregnant women [112, 167]. The resulting modes of variation from this study will allow for the generation of anatomies representative of a population of pregnant women so that simulation results can be aptly applied to more than one individual at a time.

4.4 Biomechanical Simulations of Vaginal Childbirth to Evaluate the Influence of Maternal Pelvic Morphology

4.4.1 Maternal Shape and Vaginal Childbirth

The leading risk factor for the development of pelvic floor disorders later in life is vaginal childbirth [80, 119]. It is believed that this is at least partially due to acute injury and/or microdamage sustained by the female pelvic floor muscles and connective tissues during the second stage of labor. These soft tissues must stretch to an incredible degree to accommodate the fetus, and it is still unknown how pregnancy–induced remodeling (potentially impacting both soft tissue material properties and pelvic morphology) relates to maternal birth injuries.

It is clear that the morphology of the maternal pelvic anatomy indeed plays a role in the biomechanics of vaginal childbirth. Obstructed labor, when the fetus cannot physically fit through the obstetric inlet, has been attributed to cephalopelvic disproportion [61]. This means that the maternal bony pelvis is too narrow to accommodate passage of the wider fetus. Obstructed labor frequently results in maternal morbidity and mortality and the only current treatment is Cesarean delivery [6]. Meanwhile, fewer associations have been made between soft tissue shape and birth outcomes. Although it is clear that the maternal pelvic

floor soft tissues remodel during pregnancy [8], likely at least partially to reduce the burden of vaginal childbirth, the influence of soft tissue morphology on childbirth biomechanics has yet to be investigated.

This study aimed to evaluate the influence of maternal pelvic morphology on the biomechanics of vaginal childbirth—specifically, distension of the pubovisceral muscles and perineal body, which are two common sites of maternal birth injury. We expected for shape attributes associated with pregnancy–induced remodeling to reduce the mechanical burden of vaginal childbirth (i.e., reduce the predicted strains in these maternal soft tissues).

4.4.2 Finite Element Model Geometries

The geometries for the finite element models in this study came from the combined bony pelvis–pelvic floor statistical shape model of pregnant women (see Section 4.3). These geometries were imported into Houdini FX (SideFX, Toronto, CA) for finite element simulation. In Houdini, the combined geometries were separated into individual bony pelvis (sacrum and innominate bones), coccyx, and pelvic floor muscle complex meshes using the Split function. Importantly, at this point in the model workflow, these meshes are still defined by the corresponding points of the previously mentioned statistical shape model. Houdini provides the capability to develop a procedural workflow. For this study, this meant that once a simulation was generated using the corresponding points to define the various model parameters—such as those for boundary conditions—then any shape with the same corresponding points could be imported and those same settings would be automatically applied.

A Geometry node was used to define regions of interest based on corresponding point coordinates and to generate volume meshes for each geometry. Additionally, a Geometry node was used to create the fetal head. The fetal head was the same for each simulation, simplified as a sphere with a diameter of 90 mm—a typical diameter used in other vaginal childbirth finite element models [111, 113]—composed of 8,048 tetrahedrons. As the other geometries were generated outside of Houdini and the TetRemesh and TetEmbed nodes used to generate biased tetrahedral meshes are shape dependent, the patient–specific geometries

do not have identical volume meshes, though they are similar in density.

Each coccyx was composed of roughly 10,000 tetrahedral elements. Before generating the volume mesh, corresponding points were manually selected to define regions of interest. For the coccyx, this included the region of the coccyx in close contact with the pelvic floor muscle complex, the very tip of the coccyx, and the region at the top of the coccyx closest to the sacrum. Once the coccyx was remeshed, a GroupTransfer node was used to define the vertices on the new mesh that encompass those previously defined regions of interest. To avoid initial mesh penetration that causes finite element simulation errors, regions of the coccyx were shaved off if they penetrated with the pelvic floor muscle complex mesh at rest. This mesh penetration occurred, in part, because, while we wanted the muscle and bony pelvis attachments to remain in close proximity, some modes of variation defined shapes that penetrated one another at these locations, especially in shapes with principal component scores further from the mean shape. This trimming was accomplished with Boolean functions while VDB from Polygons and VDB Convert nodes were used to fill the new holes, resulting in non–penetrating, smooth surfaces.

The pelvis geometries were setup in a way very similar to that of the coccyxes. The same functions were used to remove penetration between the pelvic floor muscle complex and bony pelvis, which sometimes occurred at the pubovisceral muscle entheses, the attachments to the inferior ischiopubic rami, and at the ischial spines. Tetrahedral meshes were also generated, with these geometries being composed of approximately 50,000 tetrahedral elements, and regions of interest were defined based on manually selected corresponding points. For the bony pelvis, these definitions included the superior and inferior portions of the pubis for later definition of the long axis of the pubic symphysis and the interior, anterior tip of the sacrum for later definition of the sacrococcygeal to inferior pubis point (SCIPP) line. These landmarks and measures are not mentioned in the results of this study, but are incorporated into the procedural workflow and are important for calculating angles of progression and perineal descent in the future.

For the pelvic floor muscle complex geometries, regions of interest consisted of the attachments at the pubovisceral muscle entheses, ischial spines, inferior ischiopubic rami, and coccyx. Additionally, the superior edge of the coccygeus muscles, the anococcygeal ligament

(with the top/superior portion of the ligament also individually defined for a specific boundary condition), the region that is held to the front of the pubis by the clitoral ligament, the perineal membrane, perineal body, and the tips of the pubovisceral muscle entheses. Some of these regions were generated for the later definition of boundary conditions, and others for later post–simulation measurements. The pelvic floor muscle complexes in these preliminary simulations were made of roughly 25,000–30,000 tetrahedrons.

4.4.3 Finite Element Model Boundary Conditions and Contact

FEM Target Constraints were used to strictly enforce fixed or prescribed displacement boundary conditions, though an FEM Attach Constraint with a high Strength could generate similar fixed constraints. In Houdini, Hard refers to a very strict boundary condition definition with little freedom allowed, while a Soft constraint can be made more or less strict via the Strength parameter. The bony pelvis (sacrum and innominate bones) was fixed in place in all degrees of freedom using a Hard Target Constraint.

A Soft FEM Target Constraint was used to attach the superior coccyx to the inferior sacrum, with a Strength chosen to minimize rigid translation while still allowing rotation of the coccyx about the sacrum. The inferior coccyx was also attached to the surrounding pelvic floor muscles and the superior portion of the anococcygeal ligament via FEM Attach Constraints. Additionally, another Attach Constraint with a lower strength loosely held the entire pelvic floor towards the coccyx. This simulated the resistance provided *in vivo* by the fat, skin, and other tissues that surround the pelvic floor muscles—particularly posteriorly and inferiorly.

Soft Target Constraints held the pelvic floor to the bony pelvis at the ischial spines, inferior ischiopubic rami, and where the clitoral ligament would be. This constraint was also used to secure the top of the coccygeus in place, using a much lower Strength that still allowed for some displacement. The pubovisceral muscle entheses were attached to the nearest regions of the left and right pubis via an FEM Attach Constraint, but, unlike with the other similar constraints, the initial configuration was set as an absolute distance of approximately 1 mm. This ensured that any pubovisceralis entheses originally located

potentially several millimeters from the bony pelvis would be pulled to the bony pelvis at the beginning of the simulation. We attempted to minimize such discrepancies as we generated the statistical shape model, but, as the inverse to mesh penetration, having some distance between the muscle attachments and bones initially was sometimes unavoidable.

Contact in Houdini is defined by a Repulsion parameter. This dictates to what degree each geometry will or will not allow penetration with any other object. The Repulsion values of the fetal head, bony pelvis, coccyx, and pelvic floor muscle complex, were optimized through trial and error and adjusted slightly across simulations. This was necessary as an ideal Repulsion for one geometry may have prevented fetal head motion or allowed too much muscle penetration for another geometry.

4.4.4 Material Properties and Fetal Head Motion

Each object in these simulations was defined using the Stable Neo–Hookean Variant in Houdini, which is intended for simulating organic tissue and/or large deformations. The material parameters of this model are defined with Lamé parameters (referred to as the Volume Stiffness and Shape Stiffness, respectively, in Houdini). To essentially treat the fetal head and bones as rigid bodies, their stiffness parameters were set as 3 orders of magnitude larger than that of the pelvic floor muscle complex.

As the focus of this study was on the effect of pelvic morphology, the pelvic floor muscle stiffness parameters were determined by approximating the slope of stress–strain curves from literature. *Ex vivo* mechanical testing was previously conducted on female human cadaveric pelvic floor muscles by Burnett et. al. [40]. The slope of the iliococcygeus stress–strain curve of data obtained from younger donors in the 0.6–0.8 strain region was used to estimate a Young's modulus of 200 kPa. Then a Poisson's Ratio of 0.49 was chosen. When converted to first and second Lamé parameters, this equated to stiffness values of 3288.59 and 67.1141, respectively.

In order for the simulations to run successfully, the anococcygeal ligament needed to be significantly stiffer than the surrounding musculature. Stress–strain data previously obtained from human uterosacral ligaments by Baah-Dwomoh et. al. was used to approximate

the stiffness of the anococcygeal ligament [18]. The secant modulus of the human data from specimens loaded in the main *in vivo* loading direction was roughly 8 MPa, so the anococcygeal ligament was assigned as 40 times stiffer than the rest of the pelvic floor muscle complex. Additionally, the regions of the musculature attached at the pubovisceral muscle entheses, inferior ischiopubic rami, and coccyx were set to be 5 times stiffer and then parts of the musculature next to those elements set to be 2 times stiffer than the rest of the pelvic floor muscle complex. This created a stiffness gradient at those attachment sites to improve the quality of the attachment and reduced the prevalence of negative Jacobians.

Each geometry underwent 2 simulations, with the only major difference being how the fetal head displacement was prescribed (minor Repulsion and Constraint settings may have needed adjustment from the first to the second simulations). In the first simulations, an algorithm was used to prescribed a downward (-x direction) force onto the fetal head while it was allowed to move along the other axes. This ensured that the fetal head path was following the shape of the pelvic anatomy. Unfortunately, this force–driven model frequently resulted in mesh penetration and instability. To circumvent these issues while still utilizing geometry–specific fetal head paths, we devised a second simulation in which the fetal head displacements derived from the first simulation are used to completely prescribe the fetal head in the second simulation. This increased stability and reduced penetration issues. Additionally, to avoid other computational problems in the second simulation (such as unrealistic pinching at the pubovisceral muscle entheses), this fetal head path was smoothed in between simulations and defined such that the fetal head in the second simulation would remain at least one millimeter from the surface of the pelvis (leaving room for the muscle). These second simulations were used to measure output parameters of interest (Figure 4.12).

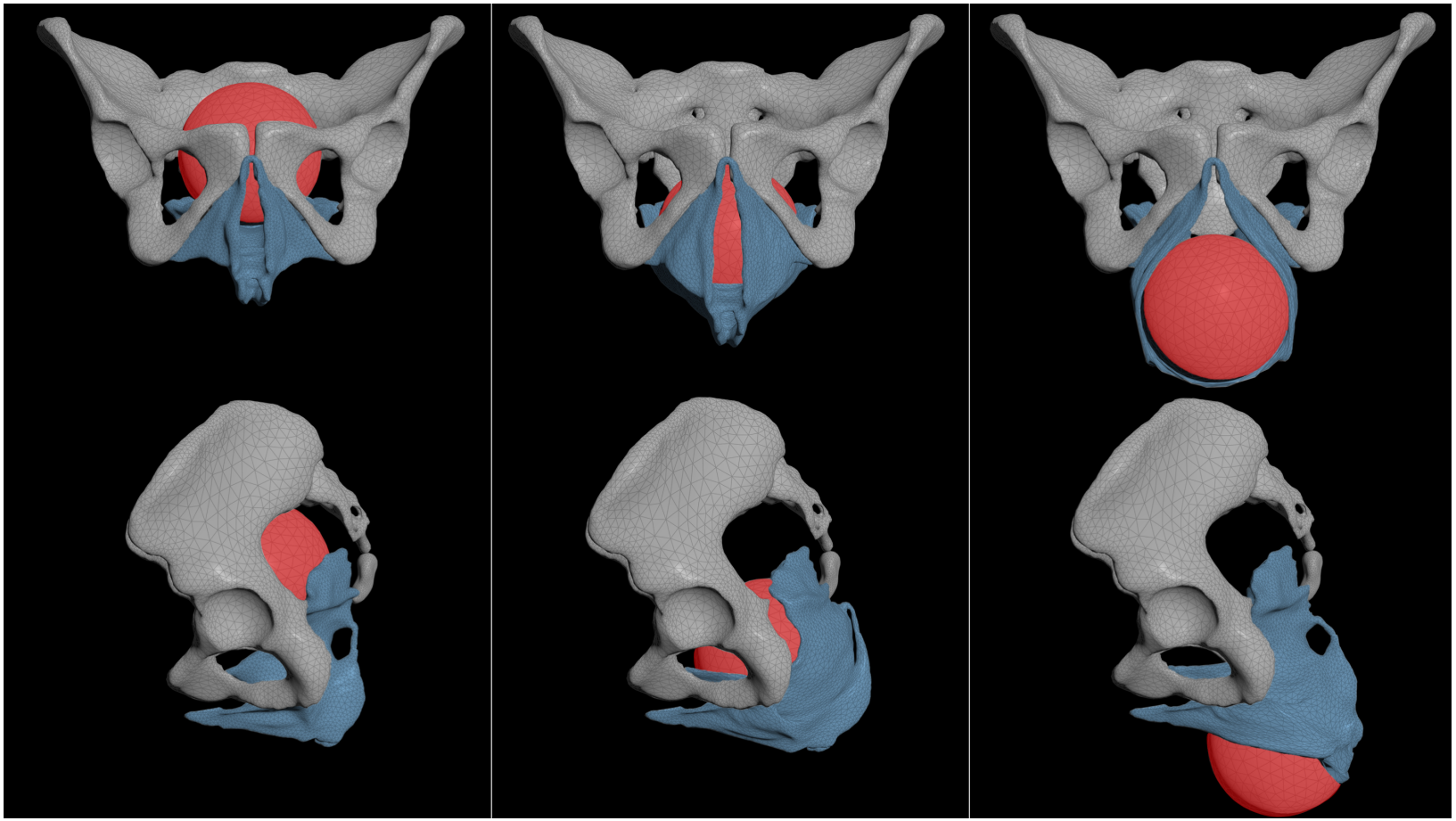

Figure 4.12: Screenshots of the average 3rd trimester geometry during simulated vaginal birth. Images in the top row were taken from an inferior (-x) perspective with respect to the sagittal screenshots. This is the direction the fetal head (red) was predominantly traveling in. The bottom row depicts the same images but from a left, sagittal perspective. The far left demonstrates the simulation at rest, the middle at the halfway point, and the right the approximate moment of peak pubovisceral and perineal body strain/distension. The bony pelvis is gray while the pelvic floor is blue.

4.4.5 Simulation Output Measures

Though this Houdini workflow incorporates additional parameters that may be of interest in future studies (such as angles of progression), the current study only investigated the influence of pelvic morphology on the estimated strain (referred to here as distension) of the pubovisceralis and perineal body. Issues with negative Jacobians are still being resolved so that, in the future, strain can be measured directly at the element level.

The length of the pubovisceral muscle was approximated by averaging the length of the left and right sides. The midpoint between the tip of the left and right entheses was calculated based on previously described regions of interest along with the centroid of the perineal body. The distance between these points was calculated at each time step and strain was approximated as the change in this length divided by the original length.

Similarly the strain in the perineal body was approximated using the left and right endpoints. As the perineal body curves significantly around the fetal head later in the 2nd stage of labor, its length was calculated as the sum of the distance from each endpoint to the perineal body centroid. To approximate strain, the change in this length was divided by the original length. The peak perineal body and peak pubovisceral muscle approximate strains were evaluated in the sensitivity analysis. For qualitative comparisons, length and distension were also evaluated at rest and halfway between rest and the peak strains.

4.4.6 Sensitivity Analysis

In this preliminary study, 6 individual geometries were generated based on values selected using Latin Hypercube Sampling (LHS) (see Section 2.3) (Table 4.4). The LHS function within the PyDOE package [122] was utilized to divide each significant mode of variation from the combined SSM generated previously (Section 4.3) into 6 sections and generate a combination of principal component scores that sampled each region of each mode with only 6 total simulations. In addition to these 6 LHS generated geometries, the average 1st/2nd trimester and 3rd trimester geometries were also included in these analyses.

Due to the small number of simulations, bivariate correlations were performed to analyze the relationships between the significant modes of variation and the pubovisceral muscle

Table 4.4: The principal component scores of the Latin hypercube sampled combined bony pelvis–pelvic floor geometries and those of the 1st/2nd and 3rd trimester average shapes. These principal component scores correspond with the combined statistical shape model described in Section 4.3.

	Mode 1	**Mode 2**	**Mode 3**	**Mode 4**	**Mode 5**	**Mode 6**	**Mode 7**
Simulation 1	250.5	-228.4	-321.4	304.2	-256.9	-338.8	156.3
Simulation 2	-293.6	572.7	-433.9	-116.7	-460.2	-68.9	318.9
Simulation 3	-491.8	769.3	13.8	389.2	161.5	350.8	-354.4
Simulation 4	746.6	76.4	495.3	-282.8	-127.3	123.8	-7.3
Simulation 5	496.5	-515.5	-23.0	148.9	348.8	283.4	-184.2
Simulation 6	-684.5	-699.4	268.1	-439.7	184.7	-174.8	24.6
1st/2nd Trimester Average	-152.3	137.2	62.9	-76.4	109.6	-30.2	56.8
3rd Trimester Average	165.0	-148.6	-68.2	82.8	-118.7	32.8	-61.6

and perineal body distension variables. This allowed for the evaluation of significant correlations between morphology and the biomechanics of vaginal childbirth. In the future, with the execution of more simulations, this evaluation could be made more robust with the incorporation of the previously described LHS–PRCC protocol (see Section 2.3).

4.4.7 Sensitivity Analysis Findings

The bivariate correlations revealed that mode 3 was significantly, positively correlated with both the approximate perineal body and pubovisceral muscle strain measures (ρ = 0.799 and 0.755 and p = 0.017 and 0.030). Mode 3 positive principal component scores are associated with less bulbocavernosus bulging and perineal descent, a proportionally smaller pelvic floor relative to the pelvis, increased iliococcygeus convexity, and a more anteriorly positioned and proportionally larger coccyx (Figure 4.13). These correlations indicate that these shape attributes are also associated with increased pubovisceral muscle and perineal body distension.

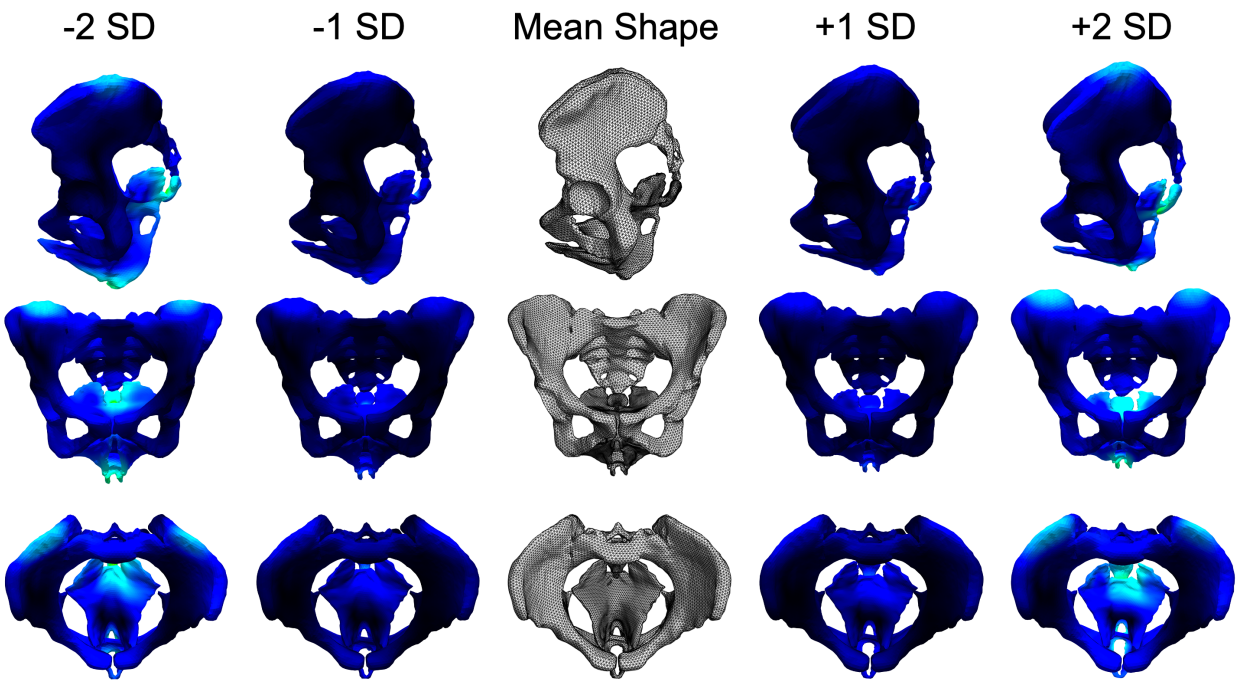

Figure 4.13: This figure depicts shapes generated by mode 3 of the combined bony pelvis–pelvic floor muscle complex statistical shape model within 2 standard deviations (SD) of the mean shape. Lighter colors indicate regions of more and darker colors regions of less variation from the mean shape (middle, gray). The top row shows these shapes from a left sagittal view, the middle row from an anterior view, and the bottom row from a superior view. Shapes attributes associated with more positive/larger principal component scores were directly correlated with pubovisceral muscle and perineal body distension as calculated from finite element simulations of vaginal childbirth.

4.4.8 Tissue Length and Approximate Strain

As expected, pubovisceral muscle and perineal body distension increased throughout the progression of each simulation of vaginal birth (Figure 4.14). General trends indicate that a greater initial length results in less distension during childbirth, which makes intuitive sense given that the fetal head size remained constant in each simulation.

4.4.9 Differences between Average Trimester Shapes

Though included in the sensitivity analysis, we also evaluated the average early/mid (1st/2nd trimester) and late pregnant (3rd trimester) average geometries separately (Fig-

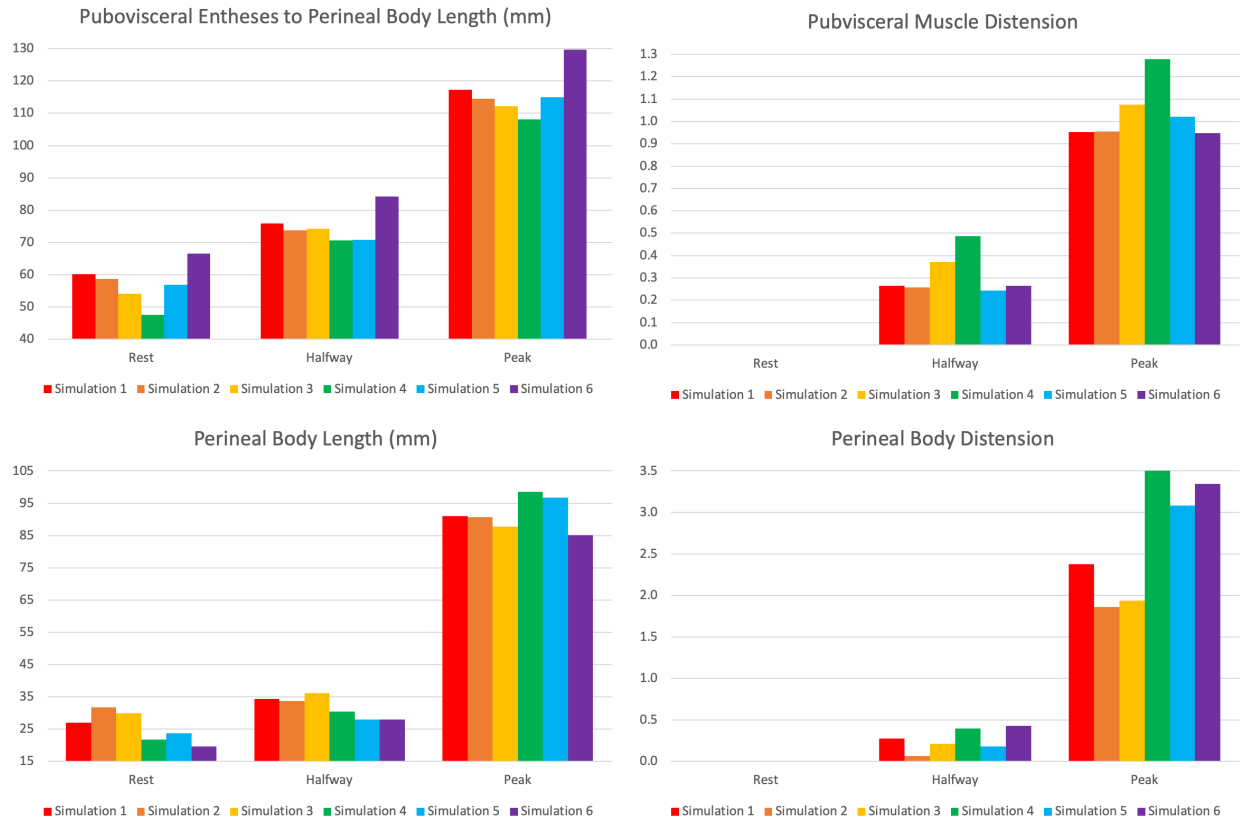

Figure 4.14: These plots illustrate the pubovisceral muscle and the perineal body distension (approximate strain) values and the distances that went into those strain calculations for each of the LHS sampled simulations (1–6) at rest (left), at the halfway point of each simulation (middle), and at peak pubovisceral muscle/perineal body distension (right). The variation across these 6 simulations should be appreciated.

ure 4.15). This data suggests that maternal pelvic morphology representative of an earlier gestational stage will undergo more strain (at least at the pubovisceral muscle and perineal body) if fetal factors remain comparable to the late pregnant morphology.

4.4.10 Pregnancy–Induced Morphological Alterations and Maternal Birth Injury

Although this was a preliminary study, these initial findings suggest that pregnancy–induced remodeling may alter maternal pelvic morphology in a way that reduces the me-

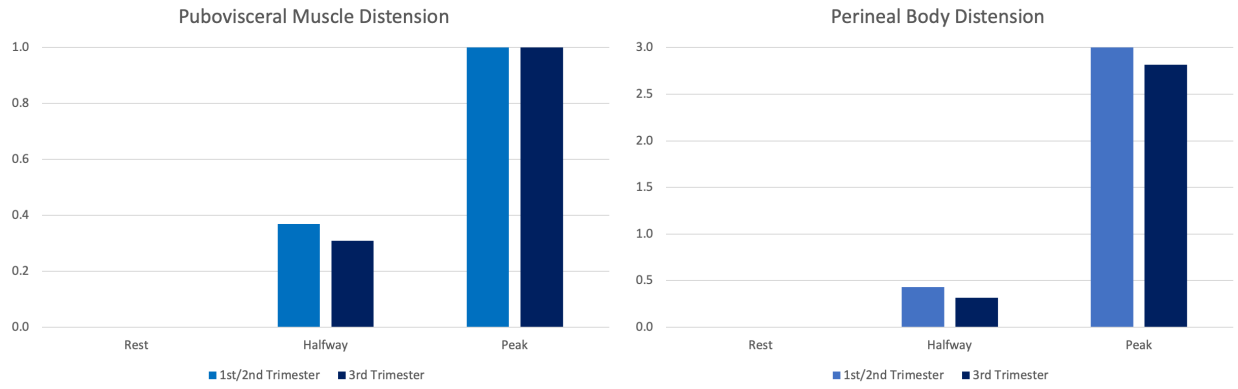

Figure 4.15: These plots illustrate the pubovisceral muscle and the perineal body distension (approximate strain) values for the 1st/2nd trimester and 3rd trimester average shapes at rest (left), at the halfway point of each simulation (middle), and at peak pubovisceral/perineal body distension (right). Though not dramatic, the early/mid pregnant values were consistently larger.

chanical burden of vaginal childbirth. Though mode 5 (associated with differences between early/mid pregnant and late pregnant maternal shape in Section 4.3) was not significantly correlated with these biomechanical measures of childbirth, mode 3 was and described shape attributes associated with pregnancy by other statistical shapes models, such as iliococcygeus convexity (see Sections 5.2 and 5.4). These trends indicate that some of the shape attributes associated with late pregnancy (e.g., increased bulbocavernosus bulging, perineal descent, iliococcygeus concavity) are inversely correlated with pubovisceral muscle and perineal body strain. Together, these results combined with the direct comparison of the 1st/2nd trimester and 3rd trimester average shapes describe how pregnancy–induced shape alterations may reduce the strains experienced by the pelvic floor muscle complex during vaginal childbirth.

The posterior and inferior displacement of the fetal head, and, therefore, the corresponding displacement of the pelvic floor tissues, is going to significantly impact the strains those tissues experience. For example, if the iliococcygeus muscle enters labor with a more convex shape, the muscle needs to be pushed further posteriorly and inferiorly compared to a more convex iliococcygeus to accommodate a fetal head of comparable size. Although this particular study did not investigate the iliococcygeus directly, it is likely that the mechanics of the iliococcygeus will impact other regions of the pelvic floor muscle complex. In addition,

if the perineal body and bulbocavernosus begin in a more inferior position, a fetal head of a similar size may not have to push those structures as far inferiorly and posteriorly during the 2nd stage of labor. If true, this has important implications for using shape as a proxy for childbirth outcomes and the development of predictive and preventative strategies to address maternal birth injury. Future studies would need to isolate specific shape attributes (rather than the entire shape at once) to confirm such specific potential trends.

Although this would also need to be verified with additional analyses, there also seems to be a potential compensatory relationship between the pubovisceralis and perineal body. The perineal body and pubovisceral muscle both compose the U–shaped soft tissue, pelvic floor opening that the fetal head passes through in these simulations. One could then surmise that increased strain in one of these structures would reduce the amount the other structure must stretch to accommodate passage of the same fetal head. This could be investigated with sensitivity analyses of the soft tissue material properties in addition to pelvic morphology.

It should be noted that this is a limited, preliminary study. Strain could not be measured directly due to mesh penetration issues (that ongoing efforts aim to troubleshoot) and the appearance of negative Jacobians near the moment of peak pubovisceral muscle and perineal body strains (representative of fetal head crowning). Additionally, more LHS sampled simulations need to be generated in order to evaluate other variables already calculated in this childbirth model workflow (such as fetal head and perineal body angles of progression) [167]. We cannot deem the modes other than mode 3 truly insignificant until more robust analyses have been completed. However, in its current form, this study demonstrates the utility of a very robust finite element model sensitivity analysis workflow and the ability to perform post–simulation calculations automatically on any geometries defined by those same corresponding points. This was a novel attempt to evaluate the role that shape plays in the biomechanics of vaginal childbirth and to investigate the potential impact of pregnancy–induced morphological alterations on those biomechanical measures.

4.5 Conclusions

These computational studies demonstrate the importance of critically evaluating maternal pelvic morphology and quantifying its impact on finite element simulations of vaginal childbirth. Notably, we've shown that the inclusion/omission of specific muscles (i.e., the superficial perineal muscles and connective tissues) in addition to their morphology can significantly impact predicted strains in the perineal body and pubovisceral muscle. The inclusion of superficial perineal muscles and connective tissues decreased the measured pubovisceral muscle and increased the perineal body stretch values, indicating that finite element models that omit these structures overestimate pubovisceral muscle and underestimate perineal body strains. Meanwhile, mode 3 of the combined bony pelvis–pelvic floor statistical shape model of pregnant women was positively correlated with pubovisceral muscle and perineal body strains, demonstrating that perineal descent, anterior bulging of the bulbocavernosus muscle (and surrounding superficial tissues), and a proportionally smaller and more posteriorly positioned coccyx are associated with smaller maternal soft tissue strains. In addition to the importance of shape in general, it seems that specific attributes of pelvic morphology associated with pregnancy–induced alterations may reduce the burden of vaginal childbirth (i.e., decrease the strains experienced by maternal pelvic soft tissues thereby reducing the risk of injury). This was shown as the predicted strains in the simulation of the 1st/2nd trimester average shape were larger than those of the 3rd trimester average, indicating that the shape remodeling undergone during pregnancy (regardless of soft tissue remodeling) resulted in less soft tissue stretch. This workflow for evaluating pelvic shape and its influence on a specific biomechanical event could be adapted to other anatomical regions/clinical fields and/or to address other female pelvic biomechanical conditions/pathophysiology.

5.0 Variations in Female Bony Pelvis Shape and Pelvic Floor Muscle Complex Shape and Fascicle Orientations

5.1 Summary

The majority of studies that carry out simulations of female pelvic floor biomechanics are performed with models based on one (or very few) patient–specific pelvis. When population–based variation is not evaluated, it can not be said how applicable those research findings are to the general population. In extreme instances, those findings may be untrue or reversed for women whose anatomy was not evaluated. To help future computational studies overcome these pitfalls and define anatomical variation in female pelvic anatomy, we performed statistical shape modeling on the bony pelvis and pelvic floor of nulliparous, late pregnant, and parous women and carried out pelvic floor muscle fascicle orientation quantification via cadaveric photogrammetric reconstructions.

5.2 Variation in the Shape of the Female Bony Pelvis and Differences between Nulliparous, Late Pregnant, and Parous Women

5.2.1 Bony Pelvis Shape, Obstructed Labor, and Parity

One of the primary roles of the bony pelvis is to provide mechanical support to pelvic viscera and tissues via direct load bearing against gravitational forces and indirectly by providing points of attachment for pelvic floor muscles and connective tissues. For the female pelvis during pregnancy, this supportive role also translates to the growing fetus and uterus that increase the forces acting on the pelvis and pelvic floor, but the pelvis must also be able to accommodate passage of the fetus during vaginal childbirth [144]. Mechanically, these roles are somewhat conflicting as any pelvic features/alterations that may improve mechanical support to organs, when too far in the extreme, would likely also hinder vaginal

childbirth. For example, a narrow pelvis would better resist downward forces from gravity and increased intraabdominal pressure but would make passing a large fetus through the birth canal more difficult.

Obstructed labor occurs when the fetus is physically unable to pass through the obstetric inlet/outlet of the bony pelvis in the presence of adequate uterine contractions and is most commonly attributed to cephalopelvic disproportion—meaning the pelvic inlet/outlet is proportionally too narrow to accommodate the fetus [61]. Obstructed labor is a major contributor to maternal morbidity and mortality, especially in parts of the world where Cesarean delivery—the primary treatment for obstructed labor—is not readily available [6, 61]. We hypothesize that the remodeling undergone during pregnancy prepares the pelvis for vaginal childbirth and that a larger degree of remodeling would prevent maternal birth injury.

Parity, the number of times a woman has given birth, has also been associated with changes in bony pelvic shape. A deeper sacral hollow, wider intertuberous diameter, wider pelvic arch, and larger transverse inlet diameter have been associated with pelvic floor disorders (such as fecal incontinence, urinary incontinence, and pelvic organ prolapse) [81]. It may be that these bony pelvic features create a non–ideal mechanical environment for the attached pelvic floor muscles and connective tissues that support the pelvic viscera. While greater pelvic width, for example, reduces the burden of vaginal delivery, it seems that it also appears to contribute to compromised mechanical support decades later in menopausal women. This suggests that remodeling of the bony pelvis postpartum towards the pre–pregnancy state may prevent the development of pelvic floor disorders later in life.

Therefore, the aim of this study was to robustly quantify bony pelvis shape variation and morphological alterations caused by pregnancy–induced or postpartum remodeling via a statistical shape analysis comparing nulliparous, late pregnant, and parous women. We hypothesized that pelvic width would increase and sacrococcygeal curvature would decrease in late pregnant women compared to nulliparous controls. Additionally, we postulated that the distribution of parous values would span both the nulliparous and parous groups—indicative of varying degrees of postpartum remodeling.

5.2.2 Bony Pelvis Shape Acquisition

This study was approved by the Institutional Review Board at the University of Pittsburgh and considered exempt at Northshore University HealthSystem. Pelvic magnetic resonance and computer tomography images of women age 20–49 who underwent imaging as instructed by their physician for medical indications (such as abdominal/pelvic pain, appendicitis, abnormal placentation, or fetus anomalies) at Magee–Womens Hospital or Northshore University HealthSystem between 2005 and 2018 were collected retrospectively. Exclusion criteria were history of pelvic surgery (not including cesarean delivery), pelvic masses, scans that did not completely capture the bony pelvis or pelvic floor, and incomplete birth history information. All of the pregnant women in this study were in their 3rd trimester. Pregnant patients were imaged in the lateral decubitus position, while nulliparous and parous women were supine during imaging.

The bony pelvis, which includes the left and right innominate bones, sacrum, and coccyx, was segmented from each image set. The innominate bones and sacrum were segmented together, attached at the sacroiliac joints, while the coccyx remained separated from the sacrum via an intentional gap at the sacrococcygeal joint.

The atlas–registration functionality within the open–source software, Deformetrica, was used to smooth the bony pelvis segmentations while simultaneously calculating corresponding points, which are required for the statistical shape analysis [33]. This was accomplished by deforming a high–resolution, previously manually smoothed template shape into each patient–specific segmentation (see Section 2.1.2). In this study, the template shape for the sacrum/innominate bones geometry was an average of 25 female bony pelvises segmented from pelvic CT images as part of a previous study [27] and composed of 11,086 vertices. The coccyx template was a simple ellipsoid composed of 872 vertices. Because the degree of shape variability of the coccyx is large with respect to the size of the coccyx, utilizing a simple shape provided better template fitting results than the use of an average coccyx. Additionally, due to this high degree of variability, the template had to be fit to each coccyx twice: The first pass removed large aliasing and the second was an improved fit that applied the desired number of corresponding points. The number of combined vertices on

these templates determined the number of corresponding points that would be incorporated into the statistical shape analysis. The number of vertices were chosen by minimizing the number of surface mesh elements required to adequately define the template geometry as to avoid unnecessary computational costs. This method for segmentation smoothing has been shown to be very accurate, with 95% of vertices having an error less than 2.5 mm [121]. The template meshes were uniform, rather than biased, as not to introduce bias into the shape analysis—given that regions of greater mesh density would be weighted more heavily.

5.2.3 3D Bony Pelvis SSM

This statistical shape analysis workflow was carried out in Mathematica (Wolfram Research, Inc., Champaign, IL, USA) and has been used previously to build 2D and 3D shape models of pelvic organs and tissues [164, 166, 168, 169]. The first step of a statistical shape analysis is a Procrustes analysis which aligns all shapes in order to remove differences due to translation, rotation, and scale—this way only true shape differences remain to be evaluated (see Section 2.1). The next step is a principal component analysis (PCA), which calculates the variance of the dataset. The outputs of a PCA include modes of variation which describe continuous variation in specific shape attributes, eigenvalues (used to determine the percent of the total variance described by each mode), and eigenvectors (which indicate the vertices involved in and directions of the shape variation described by each mode). Finally, a parallel analysis is utilized to determine which modes of variation describe significant shape variance. A PCA results in as many modes as the number of individual input shapes minus one, but to reduce dimensionality and focus on only truly important shape attributes, only modes describing more variance than the noise of the dataset are used in subsequent statistical comparisons. PC scores—the projections of patient–specific data onto eigenvectors—become the dependent variables in the statistical analyses.

Maternal age was compared between nulliparous, pregnant, and parous women via a One–Way ANOVA and included as a covariate in the MANCOVA and follow–up ANCOVAs comparing the PC scores across patient groups. The MANCOVA evaluated the effect of patient group on all modes simultaneously while the ANCOVAs consider each significant

mode individually. Multiple pairwise comparisons are used to assess specific group differences across modes with significant ANCOVA p–values. The Benjamini-Hochberg (BH) method with a false discovery rate of 10% was used to correct ANCOVA and pairwise comparison p–values for multiple comparisons [24]. A p–value less than the corresponding BH critical value was considered statistically significant.

5.2.4 Significant Bony Pelvic Morphological Differences

This study evaluated 49 bony pelvises. The nulliparous group included 15 women, the pregnant group included 17 women in their 3rd trimester, and the parous group was composed of 17 women. Age significantly differed across groups ($p<0.001$), with the average age increasing from the nulliparous (24.6±5.1 years), to the pregnant (33.5±6.2 years), and then the parous group (38.4±5.6 years). Though age was significantly influenced by group in this cohort of women, its influence was removed from the statistical comparisons of shape via its inclusion as the covariate.

Table 5.1: ANCOVA and Multiple Comparison p-values

	Mode 1	**Mode 2**	**Mode 3**	**Mode 4**	**Mode 5**	**Mode 6**	**Mode 7**	**Mode 8**	**Mode 9**	**Mode 10**
ANCOVA p-value	**<0.001**	**<0.001**	0.511	0.505	0.470	0.165	0.540	0.711	0.275	0.666
Nulliparous vs Pregnant Comparison	**<0.001**	**<0.001**								
Parous vs Pregnant Comparison	**0.002**	**<0.001**								
Parous vs Nulliparous Comparison	0.418	0.630								

The statistical shape model had 10 significant modes of variation. These modes described 22.3%, 20.4%, 8.4%, 6.8%, 6.3%, 5.3%, 4.3% 3.6%, 3.1%, and 2.7% of the total shape variance. When all 10 modes were considered together, the overall bony pelvis shape different significantly between nulliparous, pregnant, and parous women ($p<0.001$). Of these 10 modes, modes 1 and 2, which account for roughly 40% of the total shape variance, were significantly impacted by patient group ($p<0.001$ each). The trends of both of these modes were similar—the pregnant group significantly differed from the nulliparous and parous groups (Table 5.1).

Mode 1 demonstrated significant morphological variation at the iliac crests and coccyx, affecting the width of the pelvis and the proportional width of the coccyx (Figure 5.1).

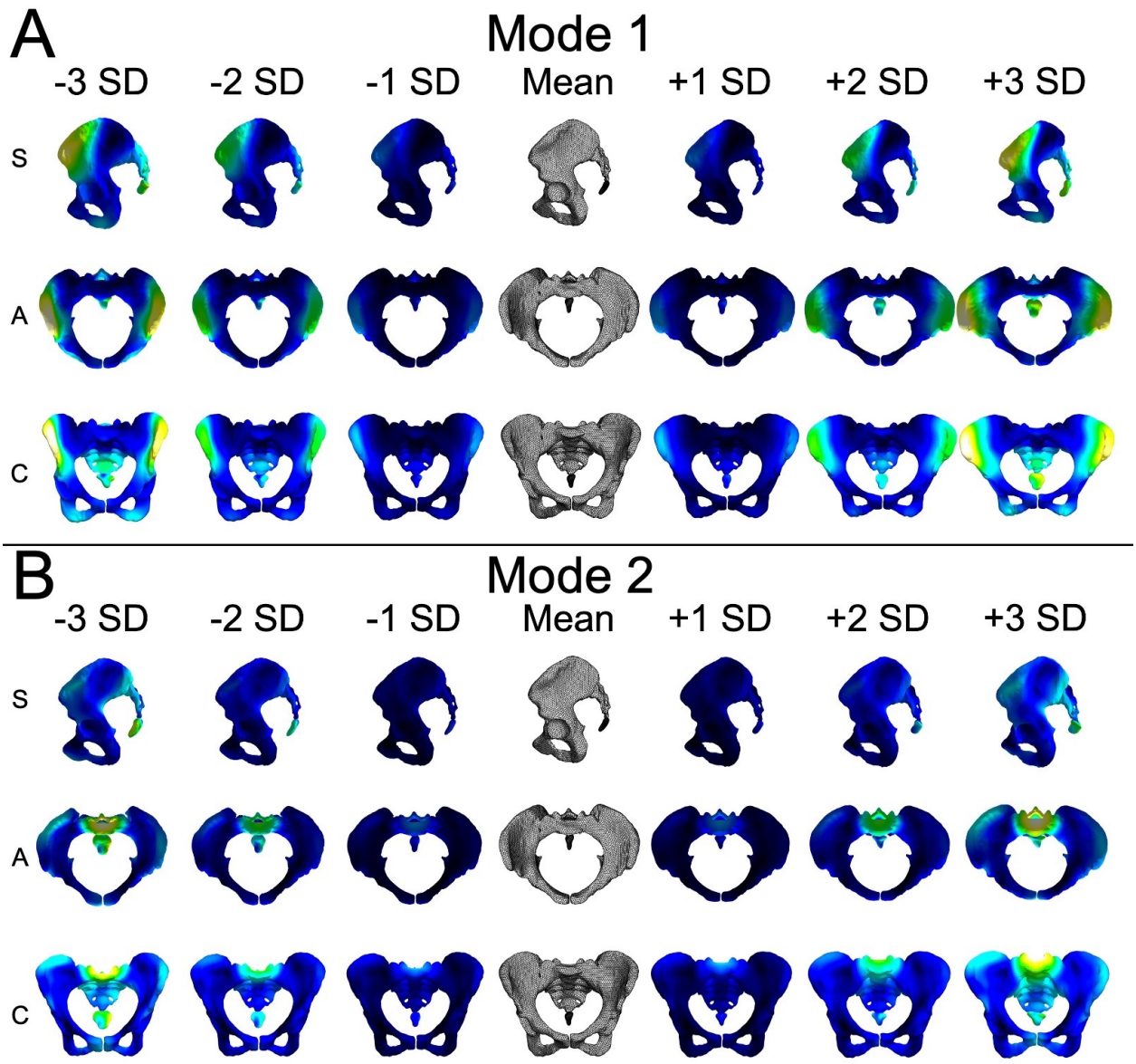

Figure 5.1: Shapes from sagittal (S), axial (A), and coronal (C) views within 3 standard deviations (SD) of the mean shape along modes 1 and 2. Black/dark blue indicates mesh vertices/regions with minimal displacement from the mean shape while white/yellow indicates maximal displacement. A) Mode 1 describes variation in the proportional width of the pelvis (particularly at the iliac crests) and the relative width of the coccyx. B) Mode 2 describes variation in the relative position of the sacrum in the region that composes the bottom of the lumbosacral joint and in the proportional length and width of the coccyx.

Pregnant women had significantly larger mode 1 PC scores representative of greater pelvic width and a wider coccyx compared to nulliparous and parous women (Figure 5.2). Mode 2 described significant shape variation in the coccyx and at the sacral promontory. Pregnant women had significantly smaller mode 2 PC scores, corresponding with a proportionally longer coccyx and relatively more inferiorly located sacral promontory, influencing the lumbosacral joint which this region of the sacrum composes the bottom portion of.

The average nulliparous, pregnant, and parous bony pelvis geometries were generated by averaging the PC scores of each group across all 10 significant modes, allowing for visual evaluation of average differences (Figure 5.3). The most apparent differences were in the iliac crests, pubic bones, ischial spines, and coccyxes. Pregnant women had the most lateral iliac crests, contributing to the differences in proportional pelvic width. At the region of the left and right pubis enclosing the pubic symphysis, pregnant women had the most relatively anterior and parous women the most relatively posterior pubic bones. Similarly, pregnant women had the most anteriorly positioned ischial spines relative to the rest of the bony pelvis. Finally, the pregnant average pelvic shape had the proportionally widest and longest coccyx, while the parous average had the thinnest coccyx.

5.2.5 Significant Bony Pelvis Shape Changes in Pregnancy and Full Recovery Postpartum

The maternal bony pelvis shape significantly differed between nulliparous, pregnant, and parous women. Our hypothesis—that the bony pelvises of pregnant women would be wider—was supported by these findings, though differences, while statistically significant with very low p–values, were more subtle than anticipated. Although morphology did not demonstrate meaningful variation in sacrococcygeal curvature as predicted. Our second hypothesis concerning parous morphology was not supported as the parous group significantly differed from the pregnant group and was statistically similar to the nulliparous group. We expected that the parous group distribution would not differ from that of the pregnant group for at least one mode. This suggests that pregnancy–induced remodeling significantly impacts bony pelvis shape and, on average, fully recovers to nulliparous values postpartum.

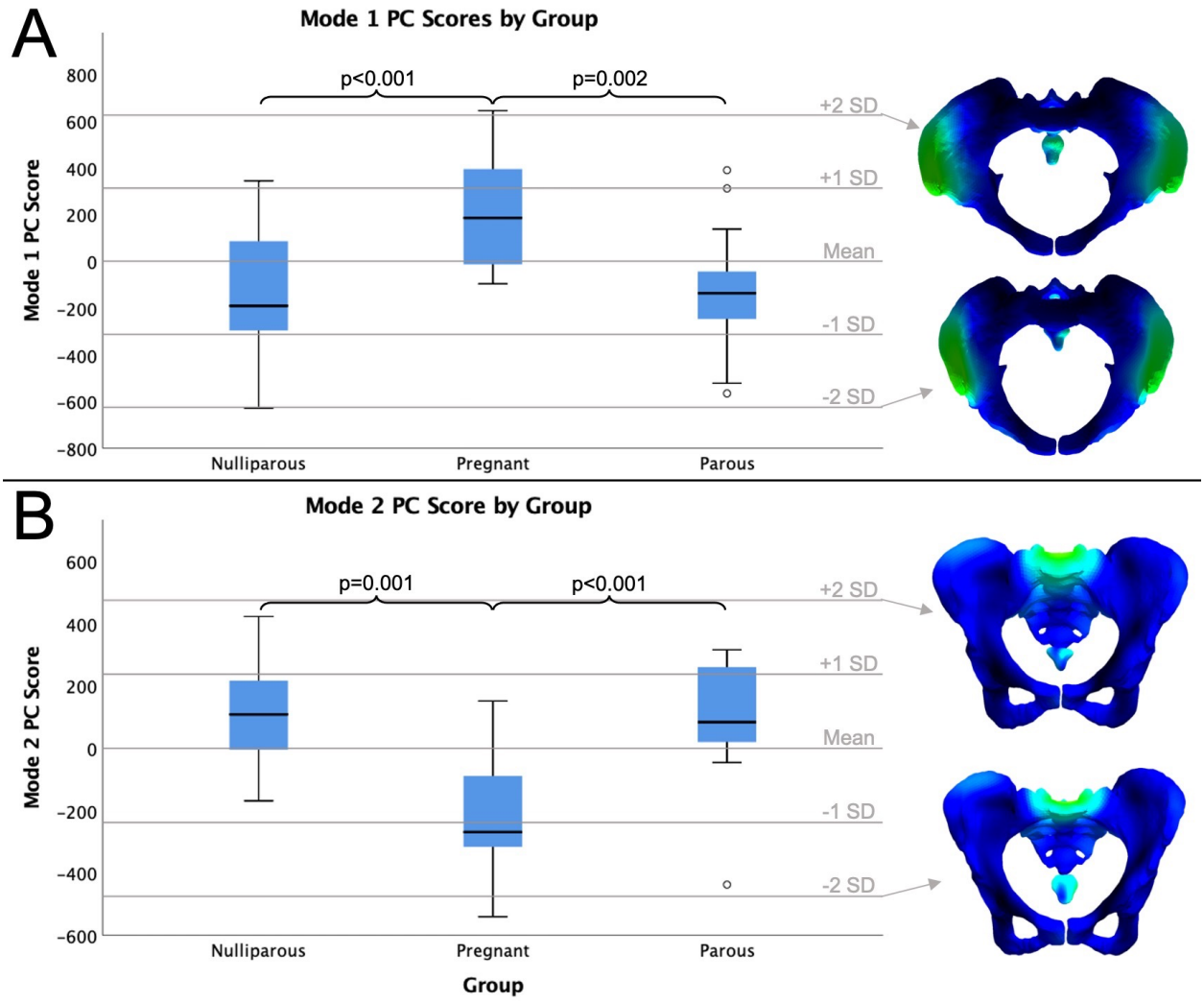

Figure 5.2: Horizontal boxplots exhibiting the group distributions of A) mode 1 and B) mode 2 principal component scores. Next to each boxplot are the shapes 2 standard deviations (SD) from the mean along each mode from the perspective that best represented the morphological variation defined by that mode. Significant multiple comparison p-values are shown. Pregnant women had proportionally wider pelvises (particularly at the iliac crests) and coccyxes and relatively more inferior sacral promontories (impacting the sacral portion of the lumbosacral joint).

The largest and most expected morphological differences between groups concerned the proportional width of the pelvis. Mode 1 highlights the increased proportional width in pregnant women compared to nulliparous and parous women. While this effect is greatest at the iliac crests, the variation in obstetric inlet dimensions can also be observed along this mode. The larger mode 1 PC scores of the pregnant group are associated with a propor-

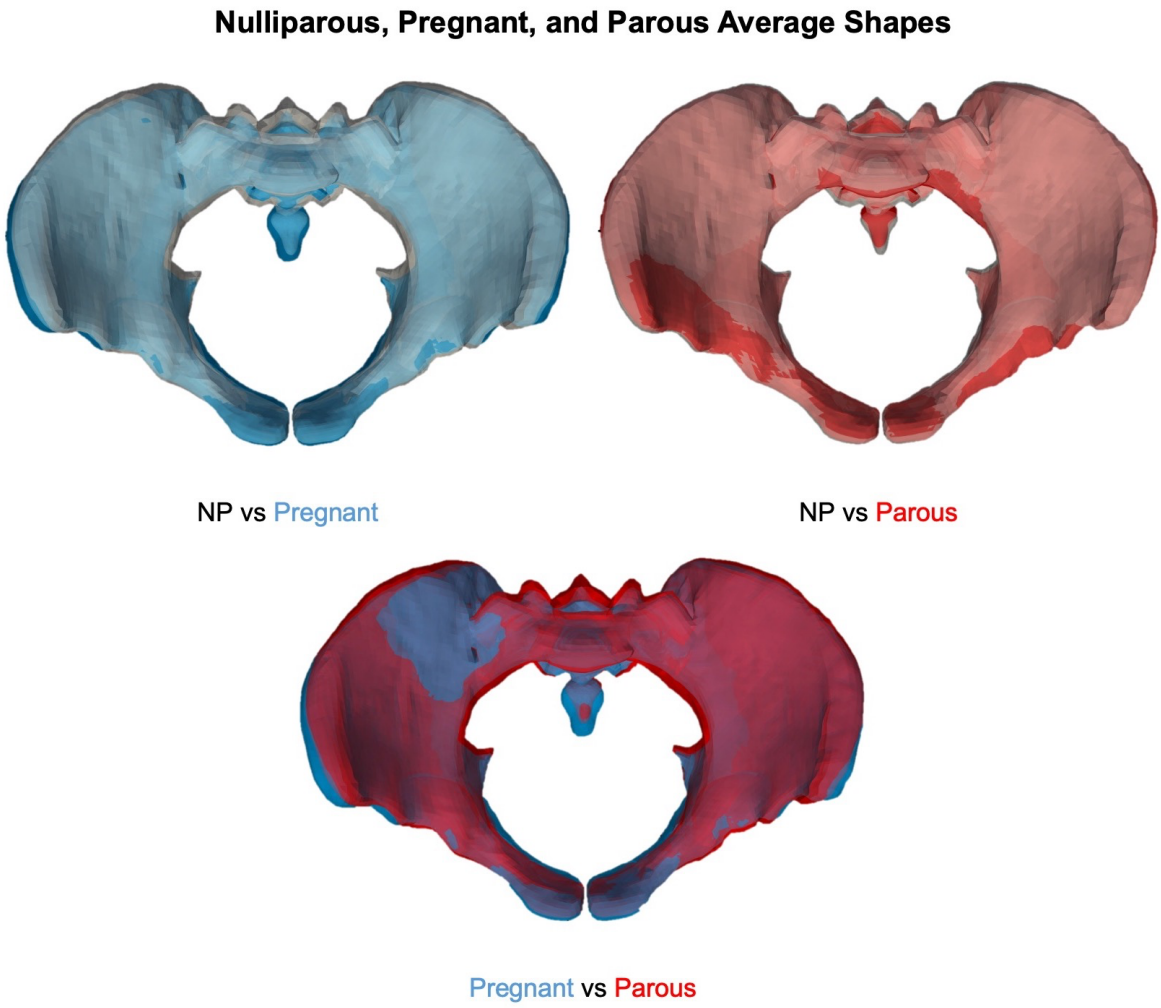

Figure 5.3: Visualizations of group differences by overlaying the average shape of each group: nulliparous (white), pregnant (blue), parous (red). The most notable differences are in the coccyx, ischial spines, pubis, and iliac crests. The pregnant average had the widest coccyx, while the parous coccyx was the most superior with respect to the sacrum; the parous average had the most posterior and the pregnant average the most anterior ischial spines; the pregnant pubis had the most anterior relative position, while the parous had the most posterior; and the pregnant average shape had the most lateral iliac crests.

tionally wider obstetric inlet and a larger angle between the left and right superior pubic rami at the pubic symphysis in addition to a larger proportional distance between the right and left iliac crests. This larger pelvic width in pregnant women also appears at the anterior superior iliac crests—just inferior and anterior to the iliac crests—which have also been

found to be further apart in pregnant women compared to nulligravid and parous women as measured directly via calipers [200]. Additionally, transverse pelvic measurements taken via magnetic resonance imaging have also been found to be larger in pregnant compared to non–pregnant women [153]. Together, these findings suggest that the pelvis becomes both wider and proportionally wider (meaning these increased dimensions are not the result of uniform growth) in pregnant women, creating more room in the pelvis that would better accommodate the fetus during vaginal childbirth. While one prospective, longitudinal study noted that the anterior pelvis was wider 1 month postpartum than at 12 weeks of pregnancy [129], our findings suggest that the pelvic morphology of parous women will return to nulliparous values with time given that our parous group (with all women being at least 1 year postpartum) was statistically similar to the nulliparous while significantly differing from the pregnant group.

The superior sacrum also demonstrated significant shape variation between nulliparous, pregnant, and parous women, as visualized by mode 2. This is the part of the sacrum that composes the lumbosacral joint, the joint between the lumbar spine and sacrum. We noted a relatively inferior sacral promontory with respect to the surrounding ischium and sacrum, which is likely a result of altered mechanical loads and gait in late pregnancy. As the fetus and uterus grow larger and heavier, the mother's center of mass is translated anteriorly, increasing lumbar lordosis [182]. Our study demonstrates the results of this on the superior sacral morphology specifically, but this would also influence surrounding ligaments and intervertebral discs and contribute to lumbosacral pain experienced by pregnant women [182]. The fact that the parous group differed from the pregnant but was similar to the nulliparous group suggests that the superior sacral shape (and likely corresponding lordosis), returns to nulliparous values postpartum.

Though not as drastic as the previous two findings, the coccyx was also influenced by modes 1 and 2. Pregnant women had proportionally larger (wider and taller) coccyxes with respect to the rest of the bony pelvis. The coccyx is not commonly studied, especially with regards to morphology and pregnancy/childbirth. A previous study did note that pregnant women had straighter coccyxes than and decreased sacrococcygeal curvature compared to nulliparous or parous women [120], though we did not. It is possible that this effect may

have been present in this dataset, but the morphology too small to be detected with respect to the total bony pelvis shape variance described by these modes. What was observed in this study could be a result of remodeling due to the increased mechanical loads experienced by the pelvic floor. The coccyx may remodel in order to better support the pelvic floor muscles (the levator ani and coccygeus muscles) attached to it, which is a suspected source of the increased relative dimensions.

In this study, statistical shape modeling was used to perform a robust assessment of the entire bony pelvis morphology. While statistical shape modeling of the bony pelvis has been performed before, previous studies either did not include the sacrum and coccyx [17] and/or were focused on using the statistical shape model to generate patient–specific geometries from medical imaging [21]. None studied the influence of pregnancy and childbirth on bony pelvic morphology. While this study is limited by its retrospective design, it is innovative in its vigorous methodology to identify subtle shape differences and the final statistical shape model allows for the generation of geometries along the continuous modes that can be used in computational simulations so that findings may represent a population of women of varying age, race, and parity rather than one individual.

5.3 Midsagittal Pelvic Floor Shape Variations

5.3.1 Potential Relationship between Pelvic Floor Shape and Pathophysiology

Of the 4 million childbirths in the US each year, 67% are vaginal deliveries [147]. Approximately 66% of parous women experience perineal body disruption–affecting level III vaginal

support—during vaginal delivery while 18% and 20% of women have a visible pubovisceral muscle or levator ani defect after their first delivery [57, 173]. Levator ani muscle avulsion from the pubic bone results in a larger levator hiatus at rest and during Valsalva which has been associated with the presence of pelvic organ prolapse and its recurrence after reconstructive surgeries [57, 161]. In the US, about a quarter of all women report having one or more pelvic floor disorders, though this prevalence increases to 32% for women 50-59 years old, resulting in over 225,000 surgeries annually [126, 198]. Vaginal delivery is the greatest epidemiologic risk factor for the development of pelvic floor disorders, though the etiology remains unclear [80, 100, 119, 193]. It is hypothesized that soft tissue injuries, including those to the levator ani muscles and perineal body, incurred during vaginal delivery may lead to compromised pelvic floor support, which can eventually progress into a pelvic floor disorder [85, 198]. While some believe that cesarean delivery is protective of pelvic floor damage, approximately 46% of nulliparous, 64% of parous women who delivered by cesarean section, and 77% of vaginally parous women have some form of pelvic floor dysfunction—indicating that both pregnancy and vaginal delivery play a significant role in, but alone do not entirely explain, the etiology of pelvic floor disorders [100].

There is strong evidence to suggest that pregnancy alters the pelvic floor mechanical properties to facilitate vaginal delivery while simultaneously protecting against maternal birth injury [10, 11, 49, 116, 150]. Conversely, a failure to achieve these changes may predispose to injury. Currently, it is not known how these changes affect the pelvic floor shape. If known, shape metrics could be used to quantify and compare the pelvic floor during pregnancy and after delivery in order to predict future shape alterations. The pelvic floor is composed of muscles and connective tissues that mechanically act as a unit, enduring changes in material properties during pregnancy—due to remodeling resulting from hormonal changes and increased intraabdominal loads resulting from a growing fetus—and after vaginal delivery—due to acute injury. By using shape as a proxy for the degree of remodeling that has occurred, one could potentially determine which women are more or less likely to sustain an injury or complication during vaginal delivery or recover afterward.

The goal of this study was to quantify the impact of pregnancy and vaginal delivery on the pelvic floor shape in the midsagittal plane. We did this by performing statistical shape

analyses on the pelvic floors of nulliparous (have never given birth), gravid and vaginally nulliparous (pregnant with no prior vaginal deliveries), and vaginally parous (have given birth vaginally) women. We hypothesized that the pelvic floor shape would be significantly affected by both pregnancy and delivery: specifically, that, in pregnancy, the pelvic floor would demonstrate relaxation meant to facilitate vaginal delivery, vaginal parity would significantly impact shape, and that the parous shapes would fall in between the nulliparous and gravid shapes—suggesting some, but not all, women recover their nulliparous shape after pregnancy and vaginal delivery.

5.3.2 Subject Recruitment

Table 5.2: Patient Demographics [169]. This table was reprinted by permission from Elsevier B.V.: Elsevier; Computer Methods and Programs in Biomedicine; Megan R Routzong, Ghazaleh Rostaminia, Pamela A Moalli, and Steven D Abramowitch. Pelvic Floor Shape Variations during Pregnancy and after Vaginal Delivery. *Computer Methods and Programs in Biomedicine* 194:105516, 2020; © 2020 Published by Elsevier B.V.

	Nulliparous	**Gravid**		**Parous**		**All women**
N	22		29		18	**69**
Subgroup N		1st Trimester	3	VP1	9	
		2nd Trimester	12	VP2	4	
		3rd Trimester	14	VP3	4	
				VP4	1	
Age (years)	30 +/- 6.8	32 +/- 5.7		33 +/- 7.7		**32 +/- 6.6**
BMI (kg/m2)	26.0 +/- 6.31	26.6 +/- 6.52		25.7 +/- 4.61		**26.2 +/- 5.93**
Parity	0 +/- 0	1 +/- 2		2 +/- 1		**1 +/- 2**
Vaginal Parity	0 +/- 0	0 +/- 0		2 +/- 1		**0.5 +/- 1**

This retrospective study was approved by the Institutional Review Board at the University of Pittsburgh (19050362) and considered exempt by the Institutional Review Board at Northshore University HealthSystem. The images of 22 nulliparous, 29 gravid (vaginally nulliparous), and 18 vaginally parous (more than 6 months post-delivery) women age 20-49

who underwent pelvic MRI with or without contrast for medical indications (such as abdominal/pelvic pain, appendicitis, abnormal placentation, or fetus anomalies) at Magee-womens Hospital or Northshore University HealthSystem between 2005 and 2018 were included in this study (Table 5.2). Exclusion criteria were history of pelvic surgery (not including cesarean delivery), pelvic masses, scans that did not completely capture the pelvis, and incomplete birth history information. Parous women were not excluded if forceps (N=1), vacuum (N=1), or episiotomies were noted as being used during past vaginal deliveries, nor were they excluded for levator ani muscle avulsions (N=2 for partial avulsion) or other muscle defects (N=1 unilateral). Nongravid women were imaged in the supine position while gravid patients were imaged in a lateral decubitus position.

5.3.3 2D Pelvic Floor Statistical Shape Modelling

Pelvic floor traces—from the inferior posterior pubic symphysis to the inferior anterior coccyx—were segmented from midsagittal MRI slices for each subject. This pelvic floor definition included level III support—which excludes the labia but includes the perineal body—anteriorly, the levator plate posteriorly, and the anal sphincter in between (Figure 5.4). Fiducial points were placed along the pelvic floor and 3D spline curves generated using 3D Slicer v4.10.1 were exported as mesh geometries [64]. The 3D geometries were converted to 2D polylines to reduce computational costs. As we were only interested in the midsagittal portion of the pelvic floor in this study, reducing these shapes to 2D ensured that only shape differences in the midsagittal plane would be calculated by the following statistical shape analyses.

After initially rigidly aligning shapes using a custom iterative closest point algorithm written in Python (Python Software Foundation, Wilmington, DE, USA), corresponding points were calculated using the deterministic atlas application within Deformetrica which implements a control–points–based large deformation diffeomorphic metric mapping framework and has proven to be robust to variations in parameter settings when utilized in statistical shape modeling (SSM) [33, 67]. In this study, an approximate average pelvic floor polyline defined by 100 evenly distributed points was used as the initial, input template.

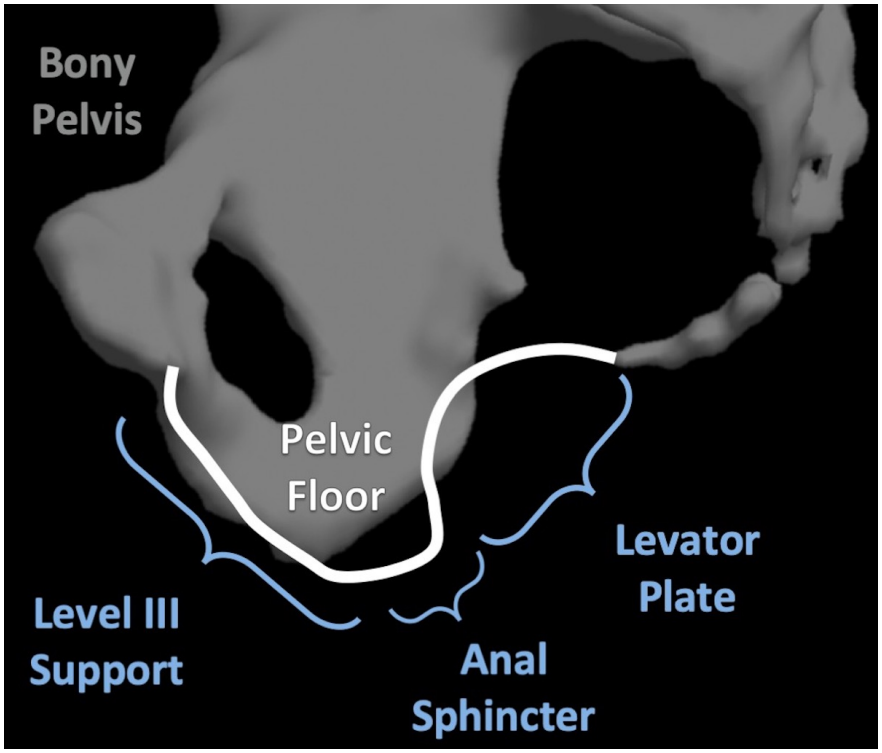

Figure 5.4: An illustration of the 2D pelvic floor traces that were segmented for this study. Level III support is located anteriorly and the levator plate posteriorly [169]. This figure was reprinted by permission from Elsevier B.V.: Elsevier; Computer Methods and Programs in Biomedicine; Megan R Routzong, Ghazaleh Rostaminia, Pamela A Moalli, and Steven D Abramowitch. Pelvic Floor Shape Variations during Pregnancy and after Vaginal Delivery. *Computer Methods and Programs in Biomedicine* 194:105516, 2020; © 2020 Published by Elsevier B.V.

In Deformetrica, the varifold metric and torch kernel type were used while the deformation kernel width and kernel width set to 5 and 10 respectively, the downsampling factor to 1, and the noise standard deviation to 0.1. This resulted in 192 control points. These settings were determined by iterating kernel and deformation kernel width values until the fit of the Deformetrica generated shapes closely matched those of the original shapes through qualitative assessment. The final Deformetrica outputs were then imported into Mathematica where the Procrustes method was implemented using the Procrustes function within the Geometric Morphometrics for Mathematica v12.3 add-on package for Mathematica [148, 158].

A principal component analysis (PCA) was then performed on the corresponding point coordinates using a custom Mathematica script. The number of modes of variation, or prin-

cipal components (PCs), used in the subsequent statistical analyses can alter the significance calculated between groups, thus it is important to only use significant modes. A mode was considered significant if it explained a greater amount of shape variance than that explained by noise. The variance due to noise was determined by randomly sampling a unit Gaussian distribution 10,000 times, performing a PCA on each iteration, and then averaging the percent variance explained for each iteration across corresponding modes [46]. PC scores—projections of the subject–specific coordinate data onto eigenvectors—were calculated for each significant mode and used as the dependent variables in the following statistical analyses.

Three SSMs were performed in this study, each resulting in significant modes of variation and PC scores for the subset of women included. The overall goal was to compare nulliparous, gravid, and parous shapes, but an SSM calculates the shape variance across all inputs without taking study group into consideration. This meant that these groups needed to be chosen carefully and in such a way that emphasized the potential shape differences of interest.

In this study, one objective was to quantify shape variance induced by pregnancy, but if the shape variance across trimesters is much smaller than that between the nulliparous and 3rd trimester, then running statistics to isolate the influence of pregnancy on data from nulliparous, gravid, and parous women risks falsely concluding that there are no significant differences. To avoid this pitfall, a separate SSM was performed on the gravid women only to determine if the pelvic floor shape differed between 1st/2nd and 3rd trimester women. This same rationale was applied when considering the effects of vaginal delivery on pelvic floor shape. Again, a separate SSM was performed on only the parous women to determine if vaginal parity (1 vs 2–4) significantly affected pelvic floor shape.

These initial two SSMs determined which gravid and parous women were included in the overall SSM calculating the variance across nulliparous, gravid, and vaginally parous pelvic floor shapes. The final SSM was meant to answer the overarching question related to the influence of both pregnancy and vaginal delivery on pelvic floor shape by comparing the gravid and parous groups to nulliparous controls.

5.3.4 Post–SSM Statistics and Visualizations

All statistics were performed in IBM SPSS Statistics v26 (International Business Machines Corporation, Armonk, New York, USA). As there were only 3 1st trimester women, the gravid shapes were dichotomized into 1st and 2nd trimester vs 3rd trimester groups. For similar reasons, the vaginally parous group was dichotomized into vaginal parity of 1 vs vaginal parity of 2–4. The gravid and parous PC scores were each analyzed using a multivariate independent t–test with univariate, independent t–tests post hoc to look at each significant mode individually. For the modes describing significant differences between groups, linear regressions were performed to determine whether gestational age (weeks) significantly predicted pelvic floor shape.

For the main and final analysis, the PC scores from the three groups—nulliparous, gravid, and parous—were compared using a One–Way Independent MANOVA with univariate ANOVAs and Benjamini–Hochberg (B–H) corrections post hoc. These corrections, like Bonferroni corrections, account for the error associated with making multiple comparisons, but B–H corrections do so by controlling the false discovery rate—the rate of false positives—which was set to 10% for this study [24, 124, 188]. Original p–values were then compared to B–H corrected values (BHCV) to determine if they were significant (less than the BHCV) after accounting for multiple comparisons.

In this study, SSMs were summarized visually by representing eigenvectors as horizontal line segments scaled by the standard deviation (equal to the square root of the eigenvalue) of the variance being explained by each mode. Individual PC scores were shown as points along those line segments color–coded by group, demonstrating the projections of subject–specific data onto the eigenvectors. As each PC score corresponds to a specific shape, the mean shape and shapes representing each standard deviation from the mean (within ± 3 standard deviations) were displayed below the line segments. Finally, to emphasize differences between groups of interest, group distributions were depicted as color-coded normal curves.

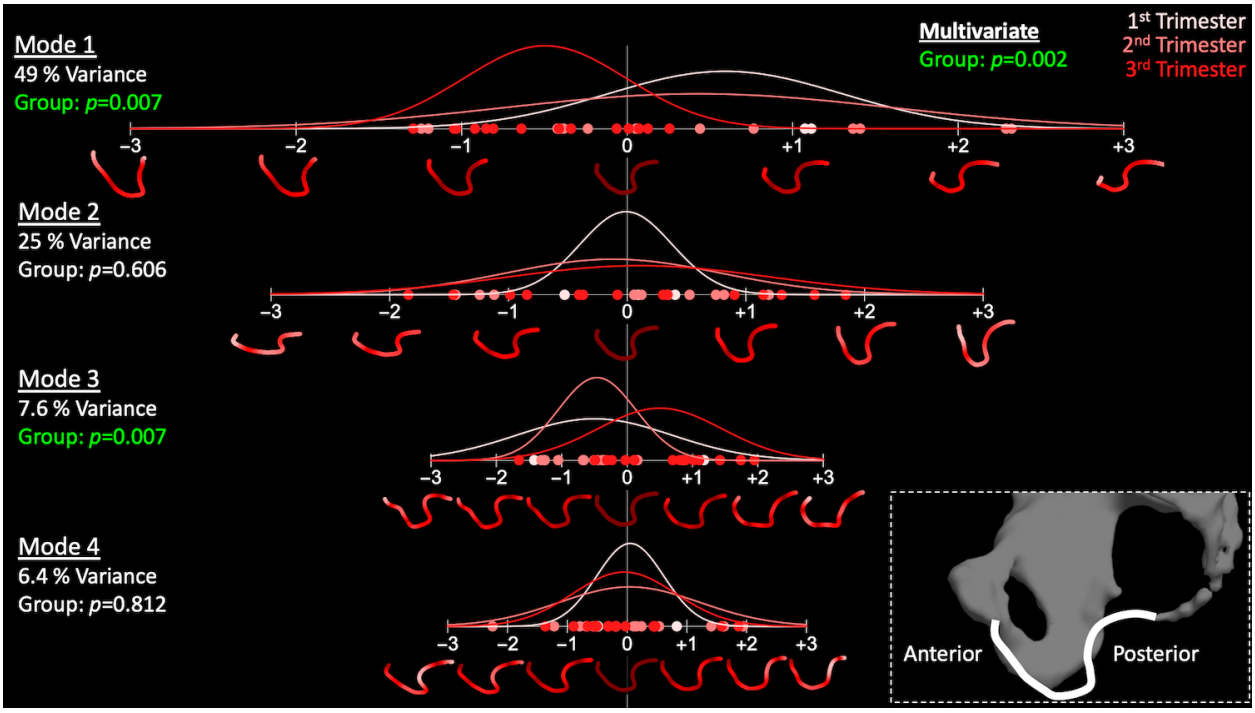

Figure 5.5: The 4 significant modes of variation are depicted, with the variance explained by each mode to the left. Normal curves and points representing PC scores are color coded as signified by the legend in the top right, though the 1st and 2nd trimester shapes were combined into one group when running statistics. The legend in the bottom right corner demonstrates the orientation of the pelvic floor shapes. The p–value of the multivariate, independent t–test is shown in the top right and univariate t–test p–values are given along the left, with significant values indicated by green font. Mode 1 describes levator plate relaxation and anal sphincter descent while mode 3 demonstrates anterior bulging of the level III support in the 3rd trimester [169]. This figure was reprinted by permission from Elsevier B.V.: Elsevier; Computer Methods and Programs in Biomedicine; Megan R Routzong, Ghazaleh Rostaminia, Pamela A Moalli, and Steven D Abramowitch. Pelvic Floor Shape Variations during Pregnancy and after Vaginal Delivery. *Computer Methods and Programs in Biomedicine* 194:105516, 2020; © 2020 Published by Elsevier B.V.

5.3.5 2D Gravid SSM Results

Four modes of variation explained variance greater than that explained by noise when analyzing gravid women alone (1st/2nd semester vs 3rd trimester groups). These modes described 49%, 25%, 7.6%, and 6.4% of the total shape variance between gravid women. The multivariate and univariate independent t–tests revealed that the 1st/2nd trimester and 3rd trimester groups differed significantly at the multivariate level (p=0.002) and for modes 1 (p=0.007) and 3 (p=0.007) specifically. Mode 1 predominantly described levator

plate relaxation and elongation of level III support and mode 3 demonstrated anterior bulging of level III support and levator plate relaxation in the 3rd trimester compared to the 1st and 2nd trimester shapes (Figure 5.5). Levator plate relaxation is denoted by straightening and a more vertical orientation of the levator plate. Additionally, gestational age significantly predicted mode 3 PC scores (p=0.006, R2=0.252) (Figure 5.6). As the goal of this study was to emphasize the influence of pregnancy on pelvic floor shape and shape was found to differ significantly in the 3rd trimester, only 3rd trimester pelvic floor shapes were included in the gravid group in the final SSM.

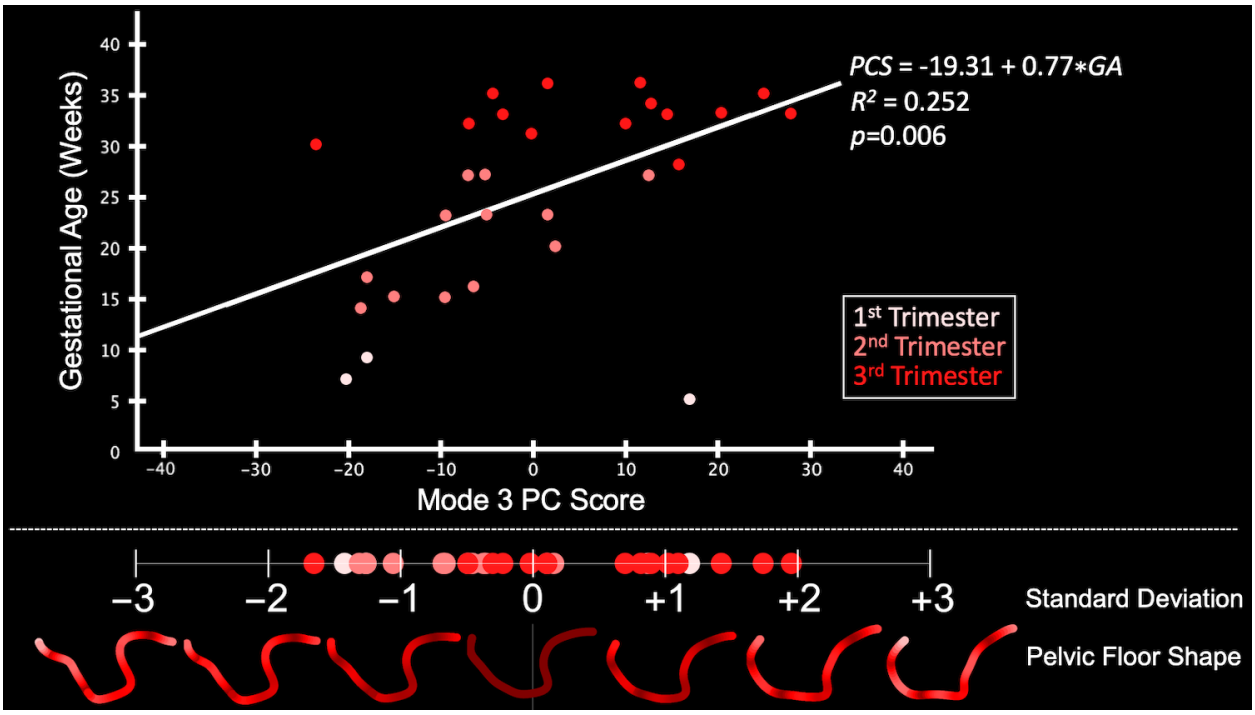

Figure 5.6: This visualizes how gestational age predicts mode 3 PC scores with the regression model in the top right corner. The illustration of mode 3 from Figure 5.5 is reshown here to demonstrate how the shapes correspond to these PC scores and gestational age [169]. This figure was reprinted by permission from Elsevier B.V.: Elsevier; Computer Methods and Programs in Biomedicine; Megan R Routzong, Ghazaleh Rostaminia, Pamela A Moalli, and Steven D Abramowitch. Pelvic Floor Shape Variations during Pregnancy and after Vaginal Delivery. *Computer Methods and Programs in Biomedicine* 194:105516, 2020; © 2020 Published by Elsevier B.V.

5.3.6 2D Parous SSM Results

Three modes of variation were found to explain shape variance greater than that explained by noise, describing 51%, 22%, and 8.7% of the total shape variance within the parous group. A multivariate t–test demonstrated that there were no significant differences due to vaginal parity of 1 vs 2-4 (p=0.713), so all vaginally parous women were included in the final SSM.

5.3.7 2D Nulliparous vs 3rd Trimester Gravid vs Parous SSM Results

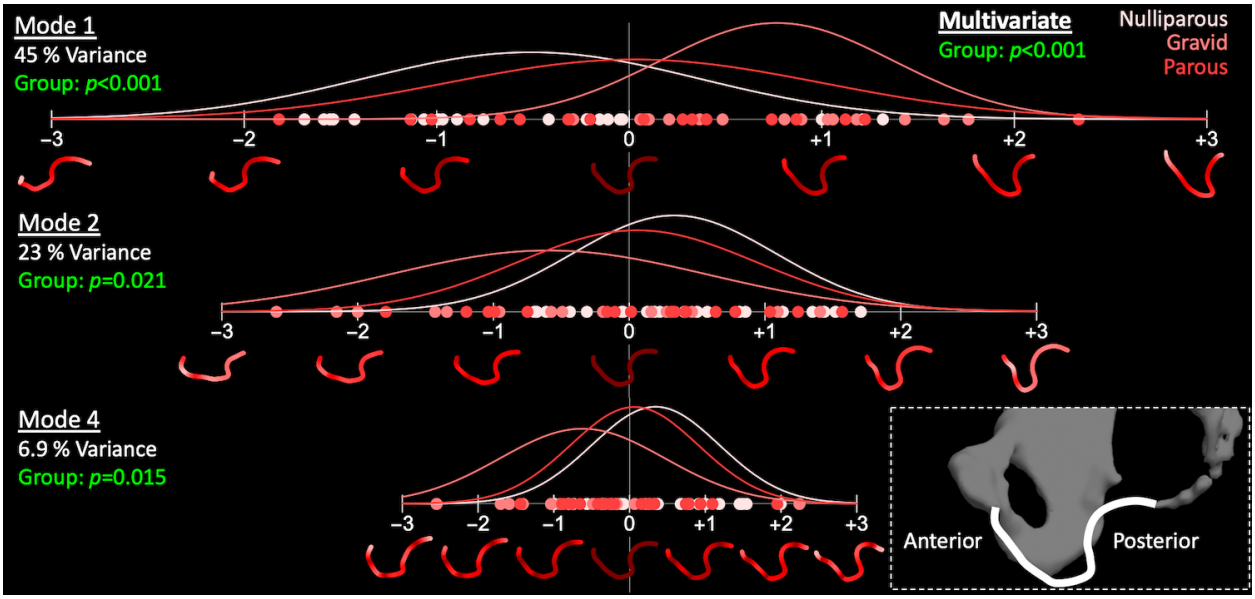

Figure 5.7: The results of the combined nulliparous, 3rd trimester gravid, and vaginally parous SSM. Three of the 6 significant modes of variations are depicted, with the variance explained by each mode to the left. These are the only three modes where Group differed significantly. The normal curves for each group and points representing individual PC scores are color coded as signified by the legend in the top right corner. The p–values of the MANOVA and follow–up univariate ANOVAs are given, with significant values indicated by green font. The legend in the bottom right corner demonstrates the orientation of the pelvic floor shapes. These modes describe more levator plate relaxation, anal sphincter descent, and anterior bulging of the level III support in the gravid subjects compared to the other two groups [169]. This figure was reprinted by permission from Elsevier B.V.: Elsevier; Computer Methods and Programs in Biomedicine; Megan R Routzong, Ghazaleh Rostaminia, Pamela A Moalli, and Steven D Abramowitch. Pelvic Floor Shape Variations during Pregnancy and after Vaginal Delivery. *Computer Methods and Programs in Biomedicine* 194:105516, 2020; © 2020 Published by Elsevier B.V.

In this final analysis, the first six modes explained shape variance greater than that explained by noise. These modes explained 45%, 23%, 8.4%, 6.9%, 5.0%, and 3.9% of the total variance, respectively. According to a One–Way Independent MANOVA, these groups differed significantly at the multivariate level ($p<0.001$) and for modes 1 ($p<0.001$, BHCV=0.017), 2 ($p=0.021$, BHCV=0.050), and 4 ($p=0.015$, BHCV=0.033) at the univariate level (Figure 5.7). Performing Hochberg G2 multiple comparisons with B–H corrections post hoc revealed that the nulliparous group significantly differed from the gravid group for modes 1 ($p<0.001$, BHCV=0.011), 2 ($p=0.018$, BHCV=0.033), and 4 ($p=0.012$, BHCV=0.022) (Figure 5.8). Anatomically, mode 1 described levator plate relaxation and dropping of the anal sphincter in pregnant and some parous women compared to the nulliparous controls, consistent with the results of the pregnancy SSM. Mode 2, on the other hand, described a more horizontal orientation and anterior bulging of the level III support in the gravid compared to the nulliparous group, but the parous women straddled both of these groups. Mode 4 also describes anterior level III support bulging and levator plate relaxation in gravid and some parous women compared to controls. Overall, this SSM suggests that the pelvic floor shape of nulliparous women significantly differed from gravid women. Meanwhile, some parous women had a pelvic floor shape more similar to the nulliparous group and others a shape more similar to the gravid group, which would explain the lack of statistical significance when comparing the parous women to the other two groups. It should be noted that for mode 1, the two largest parous values were from one of the women with a partial avulsion and the one with a muscle defect, while the other partial avulsion value was the third smallest. The levator ani muscle avulsion and defect values are evenly distributed throughout mode 2. The second largest and smallest parous mode 4 PC scores belonged to the women with partial avulsions.

5.3.8 Pregnancy and Vaginal Delivery Influence Midsagittal Pelvic Floor Shape

The final SSM supported the hypothesis that some women may recover their nulliparous shape after pregnancy and vaginal delivery while others do not as the nulliparous subjects differed from the gravid while the parous group straddled the other two. This demonstrates

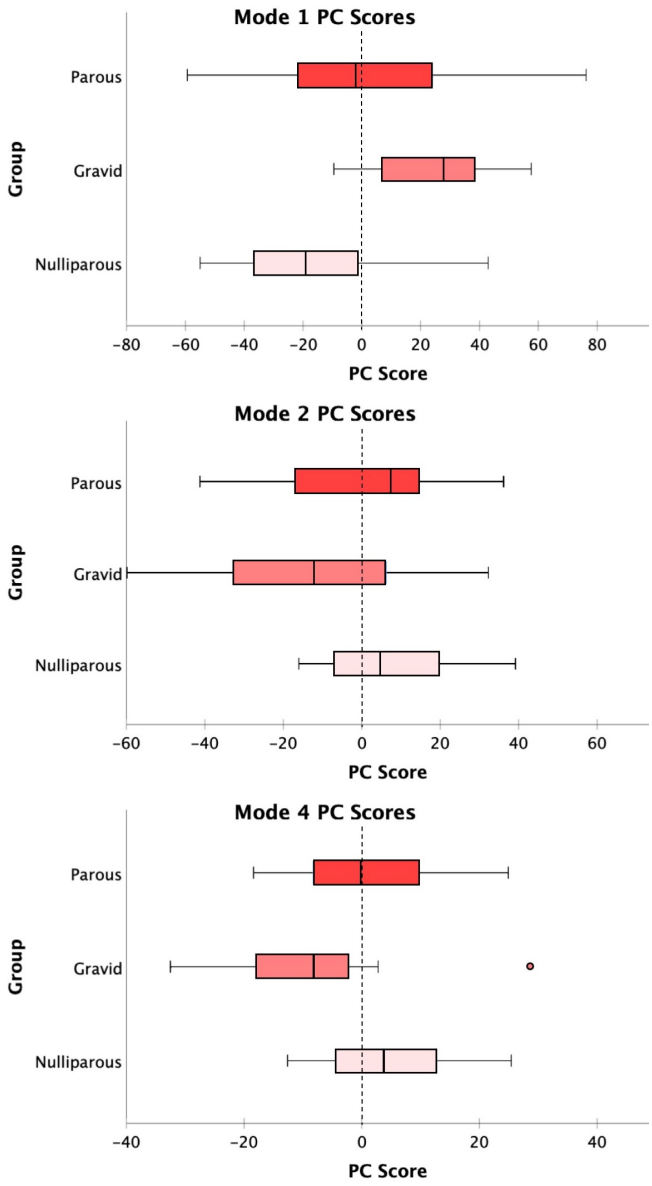

Figure 5.8: This demonstrates the differences between Groups for modes 1, 2, and 4 of the final SSM. For each of these modes, only the gravid and nulliparous groups differ significantly while the parous group is similar to both. Note the varying range in PC score values (corresponding with the horizontal line segments in Figure 4) across modes as the PC score ranges differ for each mode as they explain different percentages of the total shape variance [169]. This figure was reprinted by permission from Elsevier B.V.: Elsevier; Computer Methods and Programs in Biomedicine; Megan R Routzong, Ghazaleh Rostaminia, Pamela A Moalli, and Steven D Abramowitch. Pelvic Floor Shape Variations during Pregnancy and after Vaginal Delivery. *Computer Methods and Programs in Biomedicine* 194:105516, 2020; © 2020 Published by Elsevier B.V.

that pregnancy and vaginal delivery may induce long–term changes to the shape of the pelvic floor. During pregnancy, the levator plate became straighter and more vertical, the anal sphincter dropped, and the level III support bulged anteriorly in the 3rd trimester. This confirms our second hypothesis and suggests that the levator plate relaxes while the level III support moves anteriorly during pregnancy to create more space for the fetus presumably as a mechanism to facilitate vaginal delivery. The parous SSM refuted our third hypothesis as increasing vaginal parity did not influence the pelvic floor shape, suggesting that once a woman has had a single vaginal delivery the changes resulting from subsequent deliveries may not have been detected by this method and study design or that the first vaginal delivery has the greatest impact on the shape of the pelvic floor.

The relaxed levator plate in the 3rd trimester quantified by this study agrees with findings of previous research. Our results correspond with POPQ measures (a clinical way of quantifying and assessing pelvic organ prolapse) made longitudinally in nulliparous, gravid women demonstrating increasing POPQ stage during pregnancy [137, 138]. An increased POPQ stage indicates the presence of more severe pelvic organ prolapse, which agrees with our findings of a more relaxed pelvic floor and bulging level III support. The differences noted between 1st/2nd and 3rd trimester subjects support that these shape changes are likely due to remodeling of soft tissues initiated by hormonal/biochemical changes that alter the mechanical properties of tissues, as joint/organ mobility/laxity (specifically urethra/bladder mobility) and soft tissue distensibility (specifically that of the levator hiatus) have been found to significantly increase during pregnancy [59, 191]. The final SSM in this study corroborated these findings—describing levator plate relaxation, anal sphincter descent, and level III support (or perineal) bulging in gravid compared to nulliparous subjects.

Although this study did not detect significant shape differences due to vaginal parity, the final SSM demonstrated that some parous women's shapes were more similar to the gravid group and others more similar to the nulliparous group. This suggests that there is some mechanism of damage or long–lasting remodeling that changes the pelvic floor shape and persists after pregnancy and vaginal delivery. Vaginal delivery is a major risk factor for the later development of pelvic floor disorders and the lifetime risk increases with increasing parity. Previous studies have noted levator ani injury in vaginally parous women not found

in nulliparous controls, which could be one form of injury potentially influencing pelvic floor shape changes [57]. Injury could explain why some parous women have a shape more similar to the gravid group in our study. This is supported qualitatively by the location of the parous women with levator ani muscle partial avulsions and defects within the PC score distributions. One of the pelvic floor shapes with an avulsion is the largest parous value for mode 1 (corresponding to a more "gravid–like" shape) and the second largest parous value for mode 4 (corresponding to a more "nulliparous–like" shape). Additionally, the other shape with an avulsion is the third smallest parous value for mode 1 and the smallest for mode 4. Though further investigation is needed, this demonstrates how levator ani muscle, and other pelvic floor muscle, defects and avulsions could influence the overall pelvic floor shape and suggests that statistical shape modeling is capable of describing these complex changes. Levator hiatus dimensions have been measured previously to assess changes to the pelvic floor during pregnancy, and were found to increase in late pregnancy [176, 180]. Additionally, a longitudinal study design was used previously to discover that levator hiatus distensibility was greater in vaginally parous women compared to those who delivered by cesarean section, although both demonstrated more distensibility postpartum than in the 1st trimester [191]. These changes in levator hiatus dimensions and distensibility during pregnancy could be contributing to the pelvic floor dropping and level III support bulging we observed in this study and are indicative of remodeling that would facilitate vaginal delivery. These previous studies support our results, suggesting that injury during vaginal delivery may be contributing to pelvic floor shape differences seen in parous women, in addition to any persistent shape changes that may be due to pregnancy alone. This also suggests that pelvic floor shape can be used to assess women with pelvic floor disorders that may have resulted from pregnancy and/or childbirth trauma. By performing SSM with longitudinal data, future studies could attempt to quantify the degree of shape recovery after delivery, thereby identifying a cohort of who may warrant long term monitoring and potential intervention to understand how this recovery, or lack thereof, may be related to the later development of certain pelvic floor disorders.

SSM proved to be a novel and effective tool for defining pelvic floor shape changes during pregnancy and after vaginally delivery. Not only did it provide a thorough qualitative

analysis of shape, but a way to quantify and compare shape variations across a population and groups of interest. SSM has been utilized previously on levator ani and bony pelvises to more robustly describe these complex shapes and quantify differences between them, but had yet to be used to assess changes that result from pregnancy and vaginal delivery [21, 108, 125]. Previous studies have determined relationships between anatomy and disease: urinary incontinence has been associated with a wider intertuberous diameter, increasing prolapse with an increasing transverse inlet diameter, obstetrical sphincter laceration with a shorter anteroposterior outlet, and levator ani muscle defects with pelvic floor disorders [57, 58, 81]. While useful, these relationships are limited to the discrete measures used to define them—an issue that SSM overcomes. Additionally, illustrating the modes of variation as was done in Figures 2 and 4—mapping individual PC scores, group distribution normal curves, and shapes along each mode—enhanced the translational aspects of this research as individuals and groups could be assessed quantitatively by PC score and qualitatively by shape. This visualization made it possible to: 1) determine which regions of the shape are most affected by each mode; 2) analyze a single subject to determine where they lie in terms of shape, PC score, and within their group's distribution; 3) easily identify outliers; and 4) associate group means with specific PC scores and shapes. As performed in this study, this visualization is most easily implemented in 2D but could be adapted for 3D shapes.

Though SSM is a very powerful and attractive tool that provided promising results, this study had several limitations. This SSM was only conducted on two–dimensional shapes and the study design was retrospective. Incorporating 3D shapes would provide a more thorough shape variance quantification, as the current design ignores any differences due to midsagittal asymmetry—which could allow for identification of unilateral injuries due to vaginal delivery—and the retrospective design meant that we did not have all details related to the parous women's previous deliveries (i.e. whether vaginal deliveries included the use of forceps, a vacuum, or episiotomy). Additionally, imaging was conducted while women were in the supine position (except for gravid women who must be imaged while lying on their side), which is not ideal for assessing pelvic floor functional anatomy. Although, that indicates that the significant differences noted in the levator plate during pregnancy may actually be an underestimation. The position of the gravid women during imaging could

have introduced out of plane motion that would not have been captured in this midsagittal analysis, but we can assume that the force of gravity applied in the supine position would have resulted in additional posterior levator plate motion/deformation in gravid women compared to nulliparous and parous women—a difference that was already significant with the current imaging position differences. That being said, the fact that significant shape differences were found using only two dimensions with an unpaired, retrospective design supports the usefulness of this type of study design and reinforces the differences found between groups. However, a longitudinal design would strengthen this study by allowing for direct evaluation of the effects of pregnancy and delivery within each subject by comparing to their own nulliparous control shape. While the number of subjects utilized could be considered a limitation, randomly removing patients and repeating analyses showed that our N was sufficient to determine robust modes of variation, as nothing changed qualitatively, and the conclusions of this study were not altered (data not shown). Thus, it is also likely that the main conclusions would hold even if more subjects had been included. Similarly, the initial SSMs to reduce subgroup variance strengthened the results of the final SSM. Nevertheless, we plan to address these limitations in future studies, although, even with the current limitations, the clinical interpretations of the findings of this study are backed by existing literature.

By utilizing SSM, this study found that the shape of the pelvic floor transformed significantly during pregnancy and these changes remained in certain women after vaginal delivery. The pelvic floor relaxed and the level III support bulged during pregnancy, likely creating more space in the anterior pelvis to facilitate vaginal delivery. This study also demonstrated the potential for this type of SSM workflow to be utilized in the development of diagnostic and predictive models for clinical applications.

5.4 Morphological Variation in the Pelvic Floor Muscle Complex of Nulliparous, Pregnant, and Parous Women

5.4.1 Remodeling During Pregnancy and Vaginal Birth–Related Injury

Throughout the progression of pregnancy, both changes in hormone levels and the mechanical loads introduced by the growing fetus and uterus cause alterations to the skeletal muscles and connective tissues of the female pelvic floor [8]. Documented adaptations in the maternal soft tissues during pregnancy include increased muscle fiber length, sarcomere elongation, and increased muscle stiffness in rat pelvic floor skeletal muscles [10, 11, 44], reduced levator ani muscle active force and less shortening during contraction in human skeletal muscles [51, 179], and decreased connective tissue stiffness [8]. Whether initiated by mechanics or hormones, these changes in the microstructure and mechanical behavior of pelvic soft tissues likely result in changes in the morphology of entire muscles and connective tissues. Image analyses are commonly conducted to evaluate female pelvic morphology *in vivo*. For example, imaging studies have associated straighter levator plates and increased levator hiatus dimensions with increased gestational age [169, 176].

Vaginal childbirth is the greatest risk factor for the later development of pelvic floor disorders, so it makes sense that this event may have permanent effects on pelvic floor muscles and connective tissues [80, 119]. Of women giving birth vaginally for the first time, 94% will experience perineal body tearing, 18% a pubovisceral muscle enthesis injury, and 20% a levator ani muscle defect [57, 173]. It is possible that such injuries may impact pelvic floor morphology. Studies have shown that the rat coccygeus muscle fiber length increases with parity (the number of times a woman has given birth) [9] and, in humans, the levator hiatal area increases with vaginal parity (the number of times a woman has given birth vaginally) [94], but the effect of parity on overall pelvic floor muscle morphology has yet to be investigated.

The aim of this study was to quantify shape variation of the entire pelvic floor muscle complex to identify morphological alterations that may result from pregnancy and childbirth by comparing nulliparous, pregnant, and parous women via statistical shape modeling.

Based on previous 2D statistical shape analyses (see Section 5.3), we hypothesized that there would be greater iliococcygeus concavity, more perineal descent, more bulging of the bulbocavernosus muscle, and straighter levator plates in pregnant compared to nulliparous and parous women.

5.4.2 3D Pelvic Floor Shape Acquisition

This retrospective study was approved by the Institutional Review Board at the University of Pittsburgh and considered exempt at Northshore University HealthSystem. Gravid women age 20–49 who underwent pelvic MRI without contrast as instructed by their physician for medical indications (such as abdominal/pelvic pain, appendicitis, abnormal placentation, or fetus anomalies) at Magee–Womens Hospital or Northshore University HealthSystem between 2005 and 2018 were included in this study. Exclusion criteria were history of pelvic surgery (not including cesarean delivery), pelvic masses, scans that did not completely capture the bony pelvis or pelvic floor, and incomplete birth history information. All of the pregnant women in this study were in their 3rd trimester. Pregnant patients were imaged in the lateral decubitus position, while nulliparous and parous women were supine.

The pelvic floor muscle complex, which included the coccygeus, levator ani (composed of the iliococcygeus and pubovisceralis), external anal sphincter, perineal body, and superficial perineal structures (including the bulbocavernosus, ischiocavernosus, superficial and deep transverse perinei, and perineal membrane) was segmented from each patient as one continuous structure (Figure 5.9). To reduce computational costs and improve point correspondence, the perineal membrane, bulbocavernosus, ischiocavernosus, and transverse perinei muscles were segmented as one instead of leaving holes or gaps in between individual structures. This also meant that some of the lateral, posterior portions of the clitoris were segmented as part of the pelvic floor to avoid regions where there would be multiple very thin tissues in close proximity. During segmentation, the levator ani muscles were reviewed for defects so that the potential impact on pelvic floor muscle complex morphology could be evaluated. It should be noted that the defect itself would be removed by the statistical

shape modeling workflow (as the template shape does not have a defect), so this assessment would determine the effect of muscle defects on the remaining pelvic floor muscle complex morphology.

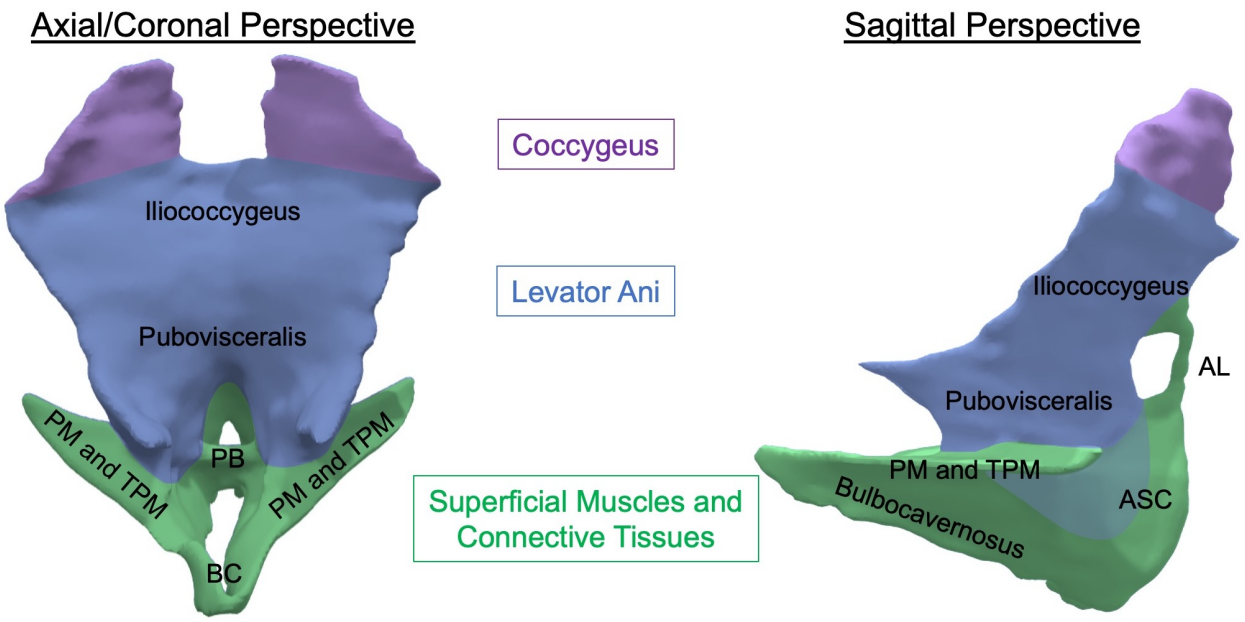

Figure 5.9: The template pelvic floor muscle complex from an angled axial/coronal (left) and a sagittal (right) view color-coded by muscle group. From these perspectives, the left and right coccygeus are the uppermost muscles, the levator ani (composed of the iliococcygeus and pubovisceralis) compose the middle, and the lowermost region is composed of the superficial muscles and connective tissues: the anococcygeal ligament (AL), the anal sphincter complex (ASC), the perineal membrane (PM) and transverse perinei muscles (TPM), and the bulbocavernosus muscle (BC). The shaded region between the pubovisceralis and ASC in the sagittal perspective denotes the region where the levator ani insert into the perineal body (PB) and external anal sphincter.

Segmentations were smoothed while simultaneously determining corresponding points for subsequent statistical shape analyses utilizing the atlas–registration function in Deformetrica [33] (see Section 2.1.2). This requires the use of a high–resolution, smoothed template pelvic floor muscle complex shape which is then deformed into each patient–specific segmentation (Figure 2.2). The pelvic floor template was segmented from the cryosection images obtained from one of the Visible Korean Human female cadaveric pelvises (Korea Institute of Science and Technology Information, Daejeon, South Korea). The segmentation used to create the template was smoothed manually in 3D–Coat (Pilgway, Kiev, Ukraine). The template

pelvic floor muscle complex geometry was composed of a triangular mesh with 16,662 surface elements and 49,986 vertices, which becomes the number of corresponding points in the following statistical shape analysis.

This statistical shape modeling workflow was implemented in Mathematica and has been used in previous 2D and 3D analyses [164, 166, 168, 169]. A statistical shape analysis first requires performing a Procrustes analysis to remove any differences due to translation, rotation, or scale; then a principal component (PC) analysis to calculate eigenvectors, eigenvalues, and modes of variation; and a parallel analysis to determine which modes describe significant shape variance (i.e., those that explain more variance than noise associated with the dataset) (see Section 2.1). The final outputs of the statistical shape model are PC scores—the projections of patient–specific data onto eigenvectors—for each patient and significant mode which were used as the dependent variables in subsequent statistical analyses.

Patient demographics were compared between nulliparous, pregnant, and parous patients via One–Way ANOVAs for continuous and Pearson Chi–Square tests for categorical variables utilizing SPSS v.25 ((InternationalBusiness Machines Corporation, Armonk, New York, USA). Parity, vaginal parity, and gravidity were categorized as either =0, =1, or >1 for these statistics. The morphology of the entire pelvic floor muscle complex was compared across our patient groups using a MANCOVA with maternal age set as the covariate to isolate the influence of gestational age on maternal pelvic floor shape. ANCOVAs with multiple comparisons were performed to assess significant modes individually, allowing for the qualitative and quantitative descriptions of local shape variation between specific patient groups. The Benjamini–Hochberg (BH) method with a false discovery rate of 10% was used to correct ANCOVA p–values for multiple comparisons [24]. A p–value less than the corresponding BH critical value was considered statistically significant.

5.4.3 Significant Differences in Pelvic Floor Muscle Complex Morphology

In total, 48 patients were included in this study: 17 nulliparous, 14 3rd trimester pregnant, and 17 parous women. Age did not significantly differ between our patient groups,

Table 5.3: Patient Demographics and Patient Group Comparisons

	Nulliparous	**Pregnant**	**Parous**	**p-value**
Age (years, mean±SD)	30.0 ± 7.3	33.0 ± 5.8	34.5 ± 7.5	0.178
Parity (median (min-max))	0 (0-0)	1 (0-6)	2 (1-6)	**<0.001**
Vaginal (median (min-max))	0 (0-0)	0 (0-2)	0 (0-3)	**<0.001**
Gravidity (median (min-max))	0 (0-2)	4 (1-10)	3 (1-6)	**<0.001**
Race (N)	Asian 0 Black 0 White 17 White Hispanic/ Latina 0	Asian 1 Black 1 White 8 White Hispanic/ Latina 3	Asian 1 Black 3 White 12 White Hispanic/ Latina 0	**0.034**

although, as expected, parity, vaginal parity, and gravidity did (Table 5.3). Additionally, the race/ethnicity of the patients significantly differed across groups. Two parous women had visible levator ani muscle defects: one partial bilateral avulsion and one unilateral defect.

Table 5.4: ANCOVA and Multiple Comparison p-values

	Mode 1	**Mode 2**	**Mode 3**	**Mode 4**	**Mode 5**	**Mode 6**	**Mode 7**
ANCOVA p-value	0.095	**0.002**	**0.001**	0.110	0.597	0.219	0.224
Nulliparous vs Pregnant Comparison	**0.05**	**0.001**	**0.027**				
Parous vs Pregnant Comparison	0.07	**0.009**	**<0.001**				
Parous vs Nulliparous Comparison	0.854	0.335	0.102				

This statistical shape model resulted in 7 significant modes of variation that described 34.2%, 18.1%, 6.2%, 5.5%, 4.7%, 3.6%, and 3.0% of the total shape variance. The overall pelvic floor muscle complex shape, when all 7 significant modes were considered together, significantly differed between nulliparous, pregnant, and parous women ($p<0.001$). Two modes described significant morphological differences across our groups of interest: modes

2 (p=0.002) and 3 (p=0.001), accounting for almost a quarter of the total shape variance (Table 5.4, Figure 5.10). Within mode 2, the pelvic floor muscle complex shapes of the pregnant patients significantly differed from the nulliparous (p=0.001) and parous (p=0.009) groups (Figure 5.11). Mode 3 was the same, with the pregnant group significantly differing from nulliparous (p=0.027) and parous (p<0.001) groups. Although the ANCOVA was not significant for mode 1 (p=0.095), it was decided to evaluate its pairwise multiple comparisons with modes 2 and 3 as mode 1 described more shape variance than modes 2 and 3 combined, meaning any differences between groups may be more clinically meaningful than the more statistically significant findings of the other two modes. Additionally, visual inspection of the data showed that mode 1 demonstrated similar group trends as modes 2 and 3. As such, the differences between the mode 1 shapes of nulliparous and pregnant women were found to be statistically significant (p=0.05).

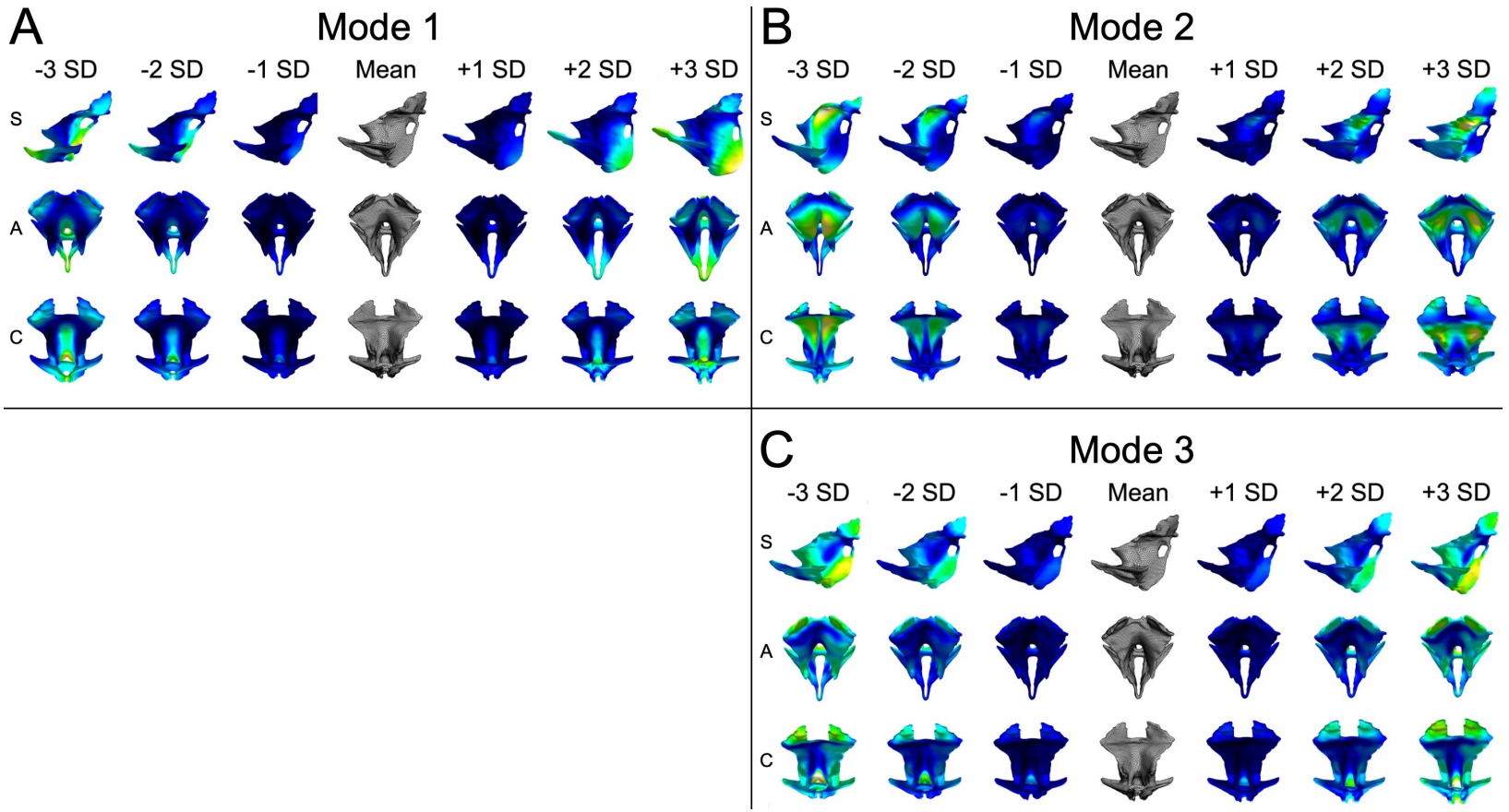

Figure 5.10: Representative shapes from sagittal (S), axial (A), and coronal (C) views within 3 standard deviations (SD) of the mean shape along the first 3 modes of variation. Black/dark blue indicates mesh vertices/regions with minimal displacement from the mean shape while white/yellow indicates maximal displacement. A) Mode 1 describes variation in the elevation/descent of the anal sphincter complex towards and away from the pubic bone (which would be located at the pubovisceralis entheses). B) Mode 2 describes variation in the elevation and concavity of the iliococcygeus muscles and the proportional width of the middle to posterior levator hiatus. C) Mode 3 describes variation in perineal descent (the relative location of the perineal body), the straightness of the anococcygeal ligament, and the relative distance between the left and right pubovisceralis entheses.

Mode 1 described morphological variation, specifically, in the elevation/descent of the anal sphincter complex towards and away from the pubic bone (which would be located at the pubovisceralis entheses), the relative length of the anococcygeal ligament, and the angulation of the bulbocavernosus muscle with respect to the pubovisceralis (Figure 5.10). According to this mode, pregnant women had further posterior descent of the anal sphincter complex, longer anococcygeal ligaments, and straighter, more vertically (superiorly–inferiorly) angled bulbocavernosus muscles (Figure 5.11A). The pelvic floor muscle complexes of parous women did not differ significantly from either other group along this mode. The parous women with levator ani muscle defects were among the larger mode 1 PC scores but were not the largest. Mode 2 described variation in the elevation and concavity of the iliococcygeus muscles, the relative height of the coccygeus muscles, the width/bulging of the bulbocavernosus muscle, and the proportional width of the middle to posterior levator hiatus. This mode demonstrated that pregnant women have more concave iliococcygeus muscles, proportionally taller coccygeus muscles, more bulging of the bulbocavernosus muscle, and proportionally wider mid–posterior levator hiatuses than either nulliparous or parous women (Figure 5.11B). The two parous women with levator ani muscle defects fell relatively close to the mean shape along this mode. Mode 3 described variation in perineal descent (the relative superior–inferior location of the perineal body), the straightness/curvature of the anococcygeal ligament, and the relative distance between the left and right pubovisceralis entheses. Pregnant women had more perineal descent, straighter anococcygeal ligaments, and less distance between the left and right pubovisceral muscle entheses than either nulliparous or parous women. This mode had the most meaningful relationship with the presence of levator ani muscle defects, as both women with visible defects were outliers and had the smallest mode 3 PC scores (Figure 5.11C).

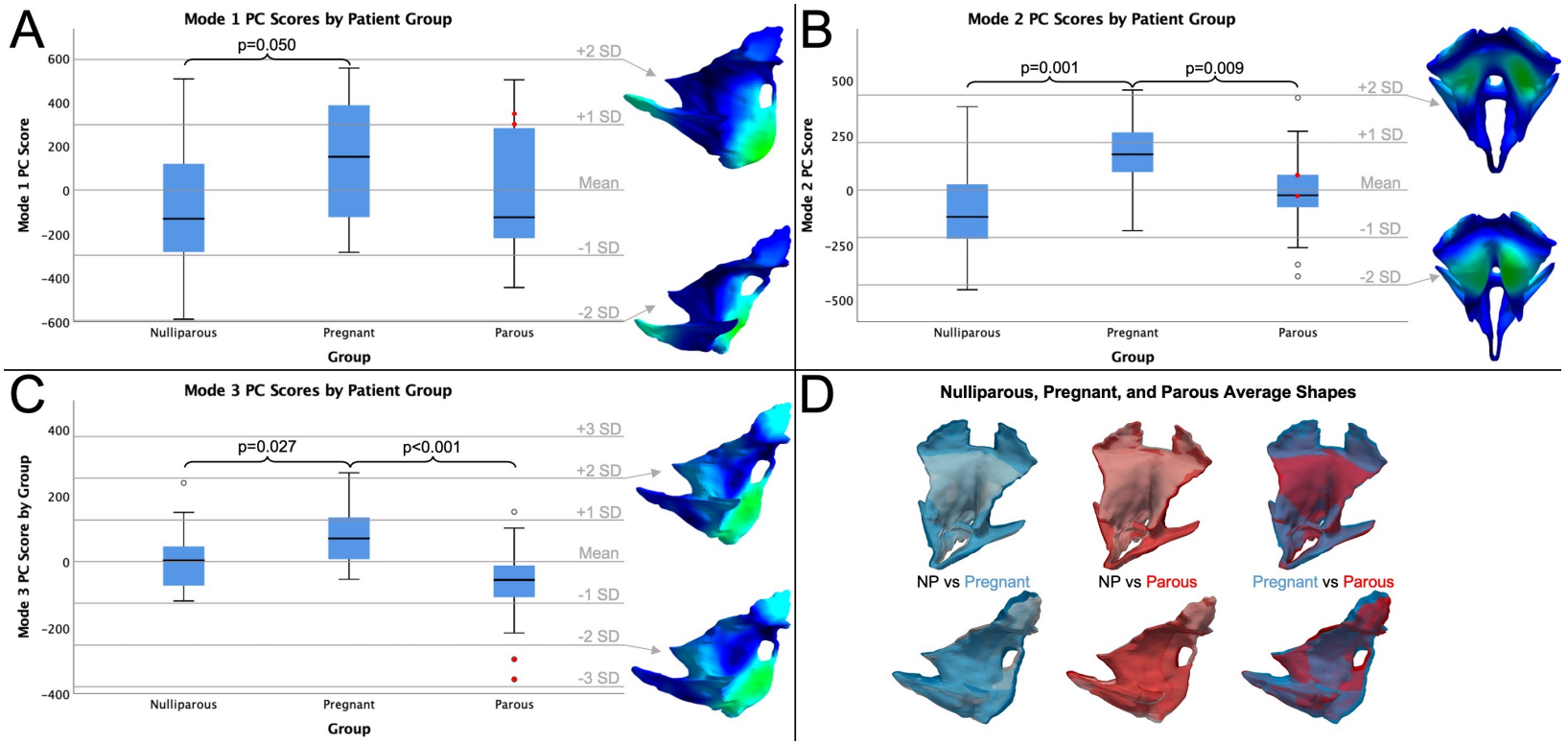

Figure 5.11: Horizontal boxplots demonstrating the group distributions of A) mode 1, B) mode 2, and C) mode 3 principal component scores, and D) the average nulliparous, pregnant, and parous pelvic floor overlaid to demonstrate group differences. Next to each boxplot are the shapes 2 standard deviations (SD) from the mean along each mode from the perspective that best represented the morphological variation defined by that mode. Significant multiple comparison p-values are shown, and the red dots indicate the values of parous women who had visible levator ani muscle defects. Pregnant women had significantly more descended anal sphincter complexes than nulliparous women, more coccygeus/iliococcygeus concavity and proportionally wider levator hiatuses, and more perineal descent and proportionally straighter anococcygeal ligaments. Panel D illustrates that nulliparous women had the most elevated/convex and pregnant women the most descended/concave iliococcygeus muscles, pregnant women had the most perineal descent, nulliparous women had the smallest and pregnant women the greatest proportional width of the levator hiatus, and pregnant women had the most relatively medial while parous women had the most lateral left and right puboviscerales entheses.

By comparing the average nulliparous, pregnant, and parous shapes to one another directly, it can be seen that the average nulliparous shape had the most convex iliococcygeus muscles and most narrow mid–posterior levator hiatus (Figure 5.11D). The average pregnant shape had the most perineal descent, the most bulging of the bulbocavernosus muscle, the most posterior and proportionally the longest anococcygeal ligament, proportionally the tallest coccygeus muscles, and the widest mid–posterior levator hiatus. Meanwhile, the parous average shape had the most lateral pubovisceral muscle entheses. This is likely the morphological feature corresponding with the two parous women with levator ani muscle defects who had the smallest mode 3 PC scores.

5.4.4 Pelvic Floor Descent, Elongation, and Widening in Pregnancy

Our hypothesis, informed by previous 2D findings and the literature, that the pelvic floor muscle complex morphology would significantly differ in pregnant women was supported by the results of this study. In addition to the specific hypothesized results—the presence of greater iliococcygeus concavity, perineal descent, bulbocavernosus bulging, and levator plate straightness in pregnant women compared to the nulliparous and parous groups—we also observed greater anal sphincter complex descent, wider mid–posterior levator hiatuses, straighter anococcygeal ligaments, and proportionally taller coccygeus muscles in the pregnant pelvic floor muscle complexes. The greatest changes were between the pregnant and the other two groups, however the fact that the parous group differed from neither of the other two groups across mode 1 indicates that some shape attributes affected by pregnancy may not fully recover to their nulliparous value postpartum. Although, the fact that the pregnancy and parous groups differed significantly for modes 2 and 3 suggests that most pregnancy–induced morphological alterations recover after childbirth.

The most prominent morphological changes associated with pregnancy were descent and elongation of specific pelvic floor tissues: descent of the perineal body (corresponding with bulging of the bulbocavernosus muscle) and anal sphincter complex (corresponding with straightening and elongation of the anococcygeal ligament), increased iliococcygeus concavity (which involves descent of that muscle), and proportionally taller coccygeus muscles

(suggesting some descent at their attachment to the levator ani). The descent of superficial muscles and connective tissues is likely a result of the increased intraabdominal pressures and loads introduced by the growing fetus. This is supported by the fact that the variation in anal sphincter complex descent described by increasing mode 1 PC scores closely resembles changes in mid–sagittal pelvic floor muscle shape that occur during defecation [168]. Naturally, as the anococcygeal ligament is attached to the coccyx and anal sphincter complex, descent of the anal sphincter would result in elongation and straightening of that ligament. Additionally, the reduced stiffness of connective tissues documented during pregnancy may contribute to the descent of attached pelvic floor muscles [8]. The descent and corresponding morphological changes in the levator ani and coccygeus are likely influenced by the changes in size and weight of the pelvic organs and fetus. The vagina and rectum rest on the "shelf" of the levator ani—the region that varies in concavity along mode 2. As fetal and uterine weight and size increase, the downward loads acting on this shelf would also increase. Pregnancy has been shown to alter the angulation of the vagina (the vaginal angle is reduced/straighter later in pregnancy) [140], so it is easy to imagine how this would also result in greater iliococcygeus concavity (corresponding with the loss of the convex angle that contributed to the angulation of the vagina) and potentially pull the coccygeus muscles (via their attachment to the levator ani) downward.

The second most evident type of shape alterations associated with pregnancy were changes in the medio–lateral width/relative location of specific structures: widening of the mid–posterior levator hiatus and more medial positioning of the pubovisceral muscle enthes-es. Similar to descent of specific muscles and connective tissues relative to the rest of the pelvic floor muscle complex described previously, the widening of the levator hiatus observed in pregnant women is likely a result of increased intraabdominal pressures and forces. As organs and tissues are displaced by the growing fetus and uterus, some are pushed downward and laterally, which would transfer those loads to the surrounding pelvic floor muscles. This is supported by increased pelvic organ descent [73] and levator hiatal dimensions [176] recognized via clinical imaging of pregnant women. This widening would also likely reduce the

burden of vaginal childbirth, as evidenced by the association between larger hiatal dimensions in late pregnancy with a shorter second stage of labor and non–complicated vaginal birth and that between smaller hiatal dimensions with levator ani muscle defects [179, 180].

5.4.5 Pubovisceral Muscle Enthesis Variation and Levator Ani Muscle Defects

While the described morphological features of the pelvic floor muscle complexes of pregnant women create more open space within the pelvis which would likely reduce the amount of strain those soft tissues experience during vaginal childbirth, the more medial location of the left and right muscle entheses would conversely increase the stretch those tissues undergo during childbirth. We suspect that this is a result of mechanically– (and potentially hormone–) induced remodeling meant to improve mechanical support to the larger fetus and uterus and the organs being forced downward in late pregnancy. The fact that this shape attribute is associated with the greatest differences between pregnant and parous women (particularly those with a levator ani muscle defect), demonstrated by mode 3, suggests this does have a negative impact on the biomechanics of vaginal childbirth and may contribute to maternal birth injury.

Generally, the parous group significantly differed from the pregnant group and was statistically similar to the nulliparous group. However, for mode 1, which describes a third of the total shape variance, the parous group did not significantly differ from either group. This suggests varying amounts of soft tissue healing and shape recovery postpartum—some parous women have anal sphincter complex descent that is more reminiscent of a pregnant woman, and others descent more suggestive of a nulliparous woman. This idea is reinforced by the large mode 1 PC scores of the two parous women with levator ani defects. Yet, mode 3 describes the most distinct results with regards to levator ani muscle defects, with those two PC scores being the smallest and outliers. Interestingly, much of the shape variance demonstrated by mode 3 involves the left and right pubovisceral muscles, which run from the left and right pubic bones and meet medially behind the rectum, with some fibers inserting into the pelvic viscera, perineal body, and external anal sphincter. As neither mode 1 nor 2, which describe more shape variance, involve the puboviscerallis entheses, we can infer

that this mode is the cause of the differences between the average nulliparous, pregnant, and parous shapes in this region of the pelvic floor muscle complex. Following that logic, we can conclude that the levator ani defects contributed to pubovisceral muscle enthesis morphology of the parous average. Parous women had the most lateral puboviscerallis entheses relative to the rest of the pelvic floor muscle complex with parous women with levator ani muscle defects having the most lateral entheses. Interestingly, these women presented with two very different defects—one was a partial bilateral avulsion of the puboviscerallis (which would quite blatantly have this effect on the entheses), while the other was a unilateral defect near the middle of the levator ani—but had similar mode 1, 2, and 3 PC scores. This suggests that levator ani muscle defects of different locations and severity may have comparable impacts on the remaining pelvic floor muscle complex morphology, meaning, in the future, shape could potentially be used as a diagnostic and predictive measure of pelvic floor muscle dysfunction/injury.

5.4.6 Innovation and Future Directions

This study used statistical shape modeling to perform an innovative morphological analysis of the female pelvic floor muscle complex. Previous studies have investigated two–dimensional measures (such as areas and angles) [94, 176] and/or performed two dimensional analysis (e.g., statistical shape models of the midsagittal pelvic floor) [169], to evaluate the pelvic floor with respect to pregnancy and parity, but shape modeling of the 3D pelvic floor muscle complex shape provides a more robust description of variation in the entire structure. Previously, a 3D statistical shape analyses was performed on the levator ani muscles, but these shapes did not include the superficial muscles and connective tissues or the coccygeus muscles, the study had a much smaller sample size, and the clinical focus was on obstructed defecation rather than pregnancy or childbirth [108]. These features in our analysis make the study quite innovative, although, it is limited by its retrospective study design and the difference in imaging position for late pregnant women. However, this means that any of the results involving greater inferior and/or posterior descent in the pregnant group were

likely understated here and may be more dramatic *in vivo* while standing. Nevertheless, the current study is exceptionally novel and provides important morphological findings and data that can be used in future computational analyses (e.g., finite element simulations).

In conclusion, the shape of the pelvic floor muscle complex significantly differs between nulliparous, pregnant, and parous women, with a quarter of the total shape variance describing significant morphological disparities. Many pelvic floor structures are descended and wider in late pregnancy—which likely reduces the burden of vaginal childbirth—except for the pubovisceralis entheses which are more medial in a way that may better support the mounting forces from the uterus and fetus. Interestingly, many shape attributes appear to reach the nulliparous range postpartum, as the nulliparous and parous groups were frequently statistically similar, although pelvic floor muscle defects (even once the defects themselves are not considered, as is the case with this statistical shape analysis) appear to meaningfully impact the pelvic floor muscle complex shape—notably the pubovisceralis entheses. Future studies will investigate the role of this shape variation on the mechanics of the pelvic floor muscle complex and surrounding tissues.

5.5 Quantification of Female Cadaveric Pelvic Floor Muscle Fascicle Orientations

5.5.1 Female Pelvic Floor Muscle Fascicle/Fiber Evaluation Methods

The female pelvic floor muscles (PFMs) are composed of the coccygeus posteriorly and the levator ani anteriorly. The levator ani attach anteriorly to the periosteum of the pubic rami and to the lateral walls of the pelvis via the arcus tendineus of the levator ani, while the left and right sides meet posteriorly to the rectum/anus at the midsagittal aponeurosis, which attaches to the coccyx. Meanwhile, the more posterior coccygeus originates at the ischial spines and inserts onto the lateral sides of the coccyx and inferior portion of the sacrum. The levator hiatus, located medially, allows for the passage of the urethra, vagina, and rectum. Together, the PFMs mechanically support the abdominal and pelvic organs through coordinated contraction and relaxation, when required for events such as defecation or intercourse, to maintain physiologic function.

Currently, little is known about the muscle fascicle arrangement of the female PFMs. The lack of data on PFM fascicle orientations, a key determinant of force vectors and resulting lines of action, reduces the accuracy and predictive capability of existing computational models, such as those simulating PFM injury during vaginal delivery [111, 167] and the role of the PFMs in the pathogenesis of pelvic organ prolapse [77, 151]. Without detailed fascicle or fiber orientations, not only is accurate simulation of active muscle contraction impossible, but the specific functions of individual components of the PFM complex may be misunderstood.

Efforts have been made to quantify PFM fascicle and fiber orientations, but progress has been hindered by restricted sample size and technological limitations. For instance, researchers have utilized the Visible Human Project dataset (National Library of Medicine, Bethesda, MD, USA) and a structure tensor method to thoroughly quantify the fiber orientations of the levator ani muscles [201]. While this method provides the predominant fiber direction of each voxel of muscle, the image dataset is expensive and very time consuming to obtain as a frozen cadaver must be divided into thin (1–3 mm) slices in order to attain the level of detail required to calculate fiber orientations. Thus, only one dataset was used to perform these calculations. In one study, left and right halves of cadaveric PFM complexes were photographed, and two-dimensional muscle fascicles were digitally traced in order to

qualitatively describe PFM morphology, however quantification of 3D PFM fascicle orientations was not included [178]. Other methods utilizing magnetic resonance imaging (MRI) are more widespread with larger sample sizes but are limited by image resolution, muscle fiber/fascicle visibility, or lack of repeatability and validation. MR images have been analyzed to determine fiber orientations of the levator ani, but PFMs are often simplified with fibers represented as straight lines restricted to what is visible in individual image slices and the resulting angles often limited to a single plane [28]. In the case of diffusion tensor imaging and fiber tractography, more robust orientation quantification is possible and has been carried out for portions of the pelvic floor connective tissues and PFMs [36, 163, 202, 203]. Although these studies have been important first steps for the field and show great potential [35], validation for the female PFMs is required before diffusion tensor imaging could be used with confidence.

To overcome the limitations of existing methods and to potentially validate and build upon published findings, we developed a novel approach that utilizes close–range photogrammetry to quantify 3D PFM surface fascicle orientations. We chose to use photogrammetry as it allows for direct visualization of surface muscle fascicles, providing more detail than MRI. Furthermore, this method is devoid of limitations associated with extensive post–image processing required for diffusion tensor imaging studies. It has been used successfully in orthopedics to evaluate soleus muscle fiber bundles [3] and in neurology to map white matter pathways [53] with the goal of improving future force generation predictions and success of neurosurgeries, respectively. For easy interpretation of results and statistical comparisons, these orientation vectors were quantified as angles in the axial and sagittal planes. To robustly quantify PFM fascicle orientations for future computational modeling applications, orientation vectors were interpolated to define continuous, 3D vector fields.

5.5.2 Anatomic Dissections of Female Cadaveric Pelvises

This study was exempt from institutional review board approval due to exclusion of living human subjects. Specimens were obtained from female cadaveric donors (N=5) provided by the Anatomy Bequest Program at the University of Minnesota. Donors with history of

pelvic organ or rectal prolapse, pelvic radiation, gynecologic or colorectal malignancy, pelvic metastasis, connective tissue disorder, myopathy, colectomy, or proctectomy were excluded to eliminate potential confounding effects of these conditions on the fascicle orientations. The donors were embalmed with a solution of 70% isopropyl alcohol, 13.25% phenol, 8% sorbitol, 7.5% formaldehyde, and 1.25% barquat MB–50 diluted in water (50:50). Perfusion fixation of the PFMs *in situ* attached to the skeleton preserved *in vivo* muscle architecture.

Prior to dissection, T1 weighted MR images were obtained using a GE Signa 3.0T MRI machine. The levator ani and coccygeus were manually segmented from these images to establish the*in situ* 3D PFM geometry. Anatomic dissections of the cadaveric pelvises were performed to expose the coccygeus and levator ani muscles (composed of the iliococcygeus and the pubovisceralis, which includes the pubococcygeus nd puborectalis). The dissection started posteriorly with the removal of the gluteal muscles and fat from the ischiorectal fossa. This revealed the cone of the levator ani posteriorly. The dissection proceeded with the removal of the urinary bladder, uterus, and rectum. The epimysium covering the PFMs was removed with care as not to damage the muscles. Once the PFMs were exposed anteriorly and posteriorly, they were removed *en bloc*. The levator ani muscles were detached from the pubic rami and the arcus tendineus of the levator ani; the coccygeus was detached from the ischial spines; and the sacrum was sectioned just superior to the attachment of the sacrotuberous and sacrospinous ligaments and the ligaments were then detached from the pelvis. The tips of the ischial spines were retained with the sacrospinous ligaments to use as landmarks. In addition to the ischial spines, the symphysis pubis, sacrococcygeal joint, and the PFM attachment sites to the bony pelvis were identified and used as landmarks in subsequent analyses. Sutures were used to mark relevant landmarks and PFM anatomy *in situ*.

5.5.3 Close–Range Photogrammetry

Once all PFMs were adequately exposed, a close–range photogrammetry protocol was implemented. Photogrammetry utilizes collinearity equations in order to transform sets of 2D images into their 3D configuration so that geometric analyses can be performed [1, 197].

This involves mapping the light rays reflected off of the object(s) being imaged to the sensor of the camera [1]. Photogrammetric reconstruction must take into account the angle of the camera with respect to the object, the camera's orientation, and its distance from the target object. With this information, over–lapping 2D images taken from various angles, orientations, and distances can be reconfigured to generate a3D reconstruction of the target object *in silico*.

The photogrammetry protocol was performed twice on each specimen, once with the PFMs *in situ* and a second time with the PFMs removed en bloc, as described above. Before imaging, pins were placed in the pubic symphysis 1 cm apart in order to accurately determine the scale of the photogrammetric reconstructions *in silico*. Approximately 40 images were captured of each PFM complex using a tripod mounted digital single–lens reflex (DSLR) camera (Canon, EOS Rebel T3, Melville, NY) equipped with a 60 mm macro lens (Canon, EFS f/2.8, Melville, NY). All images were captured with an f–stop of F8.0, ISO400, and a shutter speed of 1/50. For each specimen, images of the *in situ* PFMs were collected at 3 heights and 5 angles centered about the pelvis. Images were then reviewed to confirm that all surfaces of interest were visible in at least one image. For pelvises that required additional surface detail, 2 to 5 supplementary images were captured with the camera placed a shorter distance to the pelvis. The PFM complex was then carefully removed *en bloc* and the photogrammetry protocol was repeated on the excised "PFM cones". Approximately 25 images were taken of each PFM cone while suspended via sutures, allowing the dorsal and ventral surfaces of the PFM cone to be visualized from all directions (Figure 5.12A).

To reconstruct the 3D pelvic floor geometry, images were imported into Photoscan Pro (Agisoft, LLC, St. Petersburg, Russia), which has been validated for surfaces of various degrees of curvature [20], and a textured surface model was generated using nearest point–to–surface correspondences. Upon reconstruction, textured, 3D surface models of the *in situ* pelvis and excised PFM cone were exported for analysis (Figure 5.12B). The PFM geometries obtained from MRI and photogrammetry were manually co–registered using a regional distance–mapping algorithm implemented as a plugin for Paraview (Kitware Inc., Clifton Park, NY) with feedback to establish optimal mutual surface conformity. This was done to ensure that the excised PFM cone geometry reasonably maintained its *in situ* shape.

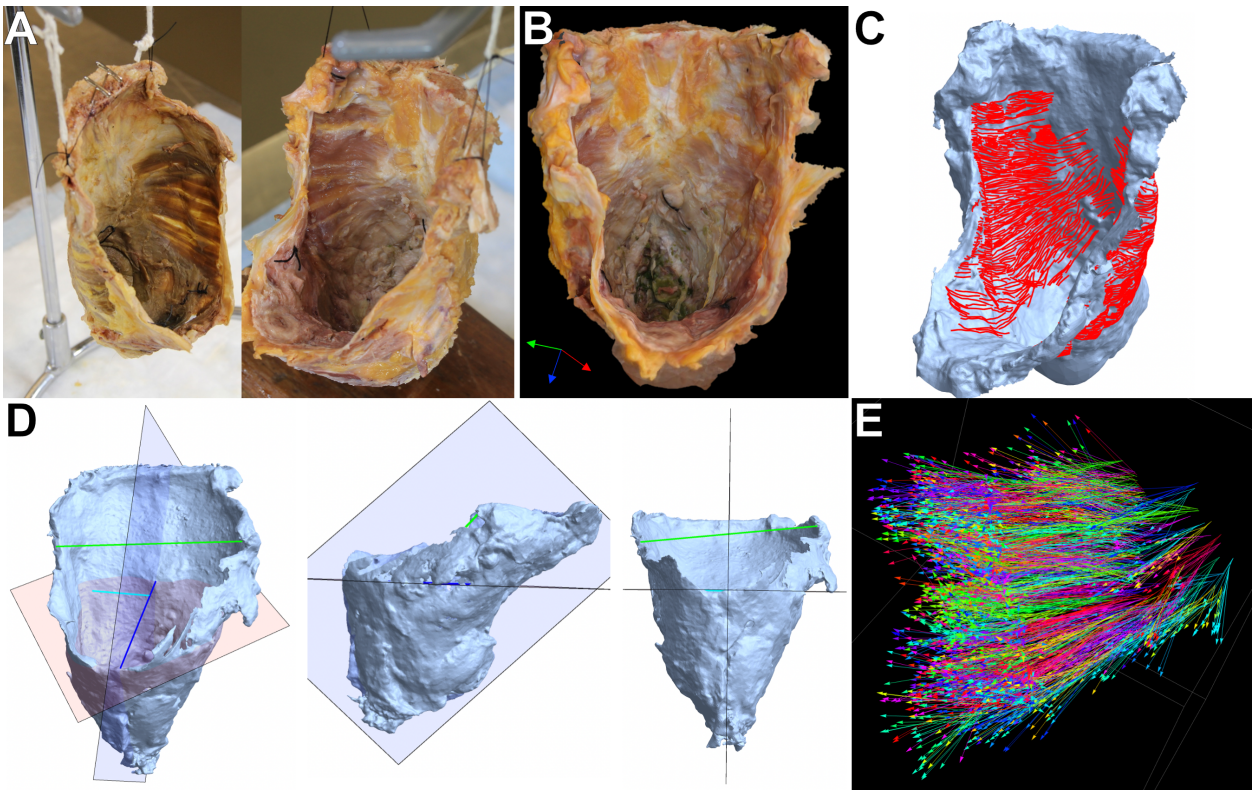

Figure 5.12: A) Sample images of two excised pelvic floor muscle (PFM) cones used to create photogrammetric reconstructions. B) A virtual, textured surface model of a PFM cone demonstrating the quality of the photogrammetric reconstructions. C) A virtual PFM cone (light blue) visualized with the exported PFM fascicles (red) that were traced manually from B. D) Three images depicting the axial (red) and sagittal (blue) planes and their orthogonality. The dark blue line connects the pubic symphysis and coccyx landmarks, the green line connects the ischial spines, and the light blue line demonstrates the vector that was rotated from the sagittal plane to define the axial plane. E) Resulting tangent vectors calculated for the right iliococcygeus for the same PFM complex shown in C from a similar view. This can be referred to as a discrete vector field [165]. This figure was reprinted by permission from the Biomedical Engineering Society: Springer Nature; Annals of Biomedical Engineering; Megan R Routzong, Mark S Cook, William Barone, Steven D Abramowitch, and Marianna Alperin. Novel Application of Photogrammetry to Quantify Fascicle Orientations of Female Cadaveric Pelvic Floor Muscles. *Annals of Biomedical Engineering*, 1–12, 2021; © 2021 Biomedical Engineering Society.

5.5.4 PFM Fascicle Angle and Vector Field Quantification

The textured PFM cone geometries created from photogrammetric reconstructions were imported into Blender v2.79b (Blender Foundation, Amsterdam, Netherlands), where bilateral PFM fascicles were traced manually along the dorsal and ventral surfaces. Tracing was completed with the polyline grease pencil tool which allows the user to draw along an ob-

ject's surface and export the drawing as a Bezier curve. The PFMs' origin and insertion sites as well as relevant bony landmarks were identified, and individual muscles were demarcated *in silico*. Each fascicle trace (Figure 5.12C) was imported into Mathematica v12 (Wolfram, Champaign, IL), where all orientation calculations were performed (see Appendix E).

The arc lengths of these traces were scaled by the length of the pubococcygeal line for each PFM cone. Tangent vectors were calculated along each trace at an interval of 1/100th of the pubococcygeal line to ensure comparable sampling across PFM cones of variable sizes (Figure 5.12E). The x, y, and z components of the tangent vectors calculated along each trace were used as inputs into Mathematica's interpolation function to generate a continuous, 3D vector field for each PFM complex. These vector fields were smoothed using SMOOTHN v2.3 [72] and visualized in Houdini FX v18.0.416 (SideFX, Toronto, CA).

The identified bony landmarks defined axial and sagittal planes. The sagittal plane passed through the center of the pubic symphysis at the level of the enthesis of the pubovisceralis, the tip of the coccyx, and the midpoint between the ischial spines (Figure 5.12D). The axial plane was defined by rotating the sagittal plane by 90° about the pubococcygeal line (modified in this study to define the line that runs from the medial pubic symphysis landmark to the tip of the coccyx) ensuring that the axial and sagittal planes were orthogonal to one another. The tangent vectors were projected onto these planes to calculate angles with respect to the pubococcygeal line. Lines connecting the tip of the coccyx to each ischial spine were also projected onto these planes in order to compare PFM fascicle orientations relative to bony morphology—specifically the location of the ischial spines with respect to the pubic symphysis and coccyx. This was done by subtracting corresponding angles describing the orientation of the ischial spines with respect to the pubococcygeal line from the mean PFM angles.

5.5.5 PFM Fascicle Angle Visualization and Statistics

The axial and sagittal angles were visualized with polar histograms for each PFM (bilateral PFMs treated individually) for all donors in both planes using the CircHist function [204] implemented in Matlab R2018a (MathWorks, Natick, MA). As these data are ax-

ial/bidirectional (i.e. angles 180°apart are considered equivalent), all original angles were duplicated, then added to 180°, and recombined with the original vector dataset—ensuring perfectly symmetric circular distributions as displayed in the polar histograms.

Circular statistics were performed using CircStat v1.21.0.0—a circular statistics toolbox for Matlab [26]. To perform the statistical analyses, the bimodal angular data were doubled, and the resulting means and standard deviations were then divided by two to ensure that the mean would fall in line with the bimodal distribution rather than perpendicular to it. Circular means and standard deviations were calculated for each PFM and PFM complex individually and for the data from all donors combined in both planes. Rayleigh tests, which identify whether a preferred direction is present, were performed for each distribution. Kuiper's tests (the circular equivalent of Kolmogorov–Smirnov tests) were performed to compare circular distributions of corresponding left and right PFMs and ipsilateral PFMs within each donor individually. As Kuiper's tests are very sensitive to differences in the cumulative distribution functions of circular data (i.e. distributions with means within 1° of each other may still be statistically different due to varying standard deviations), comparisons were also made using a threshold of 10° to evaluate whether differences maybe meaningful regardless of statistical significance. Parametric Watson–Williams multi–sample tests for equal means—the circular equivalent of an ANOVA—were used to compare contralateral PFMs as well as the ipsilateral components of the PFM complex. These were performed on the original mean angles and those taken with respect to the ischial spines. As each distribution has 2 means exactly 180° apart, the means used in the statistical comparisons were those closest to one another. This ensured that any differences measured were not artificially inflated. In the axial plane, differences between the left and right PFMs were evaluated by reflecting the right sided mean angle about the pubococcygeal line (by subtracting that angle from 360°)—referred to as the left equivalent angles.

5.5.6 Donor Demographics and Geometry Co–Registration

Donors were white with a mean age of 53.6 ± 20.5 years. The mean body mass index was 18.8 ± 4.3 kg/m^2. Two out of 5 donors were parous with a median parity of 0 (range 0–4).

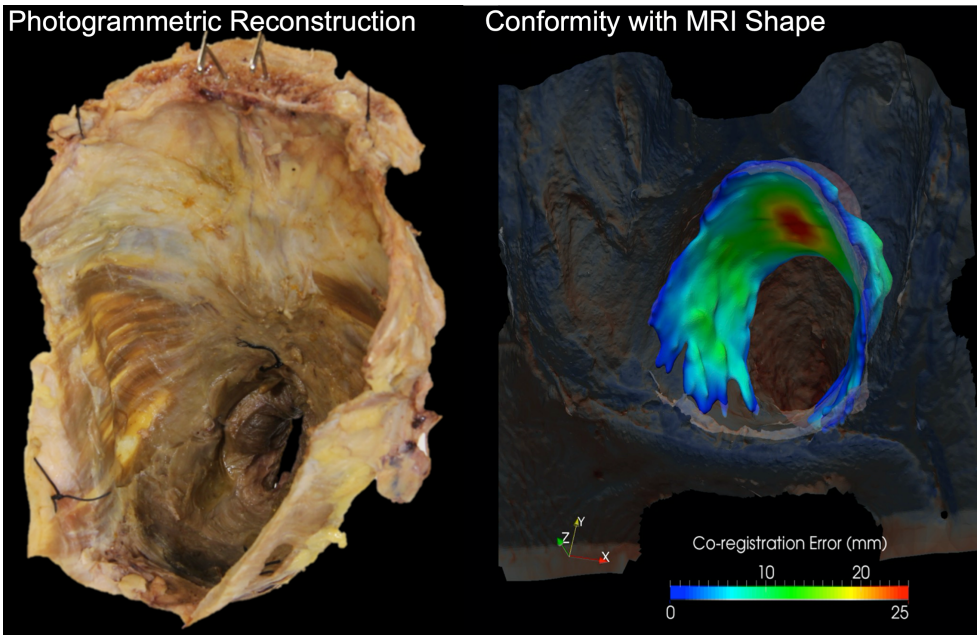

Figure 5.13: A photogrammetric reconstruction of a pelvic floor muscle cone shown next to its virtual geometry segmented from MRI. The color map depicts good shape conformity between the photogrammetric reconstruction and pelvic floor muscle complex segmentation as determined by the low co–registration error [165]. This figure was reprinted by permission from the Biomedical Engineering Society: Springer Nature; Annals of Biomedical Engineering; Megan R Routzong, Mark S Cook, William Barone, Steven D Abramowitch, and Marianna Alperin. Novel Application of Photogrammetry to Quantify Fascicle Orientations of Female Cadaveric Pelvic Floor Muscles. *Annals of Biomedical Engineering*, 1–12, 2021; © 2021 Biomedical Engineering Society.

None of the PFMs had gross disruptions at their aponeurotic origins or the muscle bellies. Distance mapping histograms comparing the optimally co–registered MR and photogrammetry PFM geometries demonstrated good shape conformity with a grand mean error of 2.7 mm (and variance of 2.8-11.5 mm) across all 5 specimens (Figure 5.13).

5.5.7 Continuous 3D Vector Fields

Continuous, 3D vector fields were generated for each PFM cone and visualized with a color map defined by their 3D orientation (Figure 5.14). Qualitatively, we noted that most of the vectors in the posterior region of the PFM complex near insertion of coccygeus muscles onto the sacrum and coccyx were predominantly parallel to the axial plane and were the most laterally (left–right) oriented, the combination of these orientations is indicated

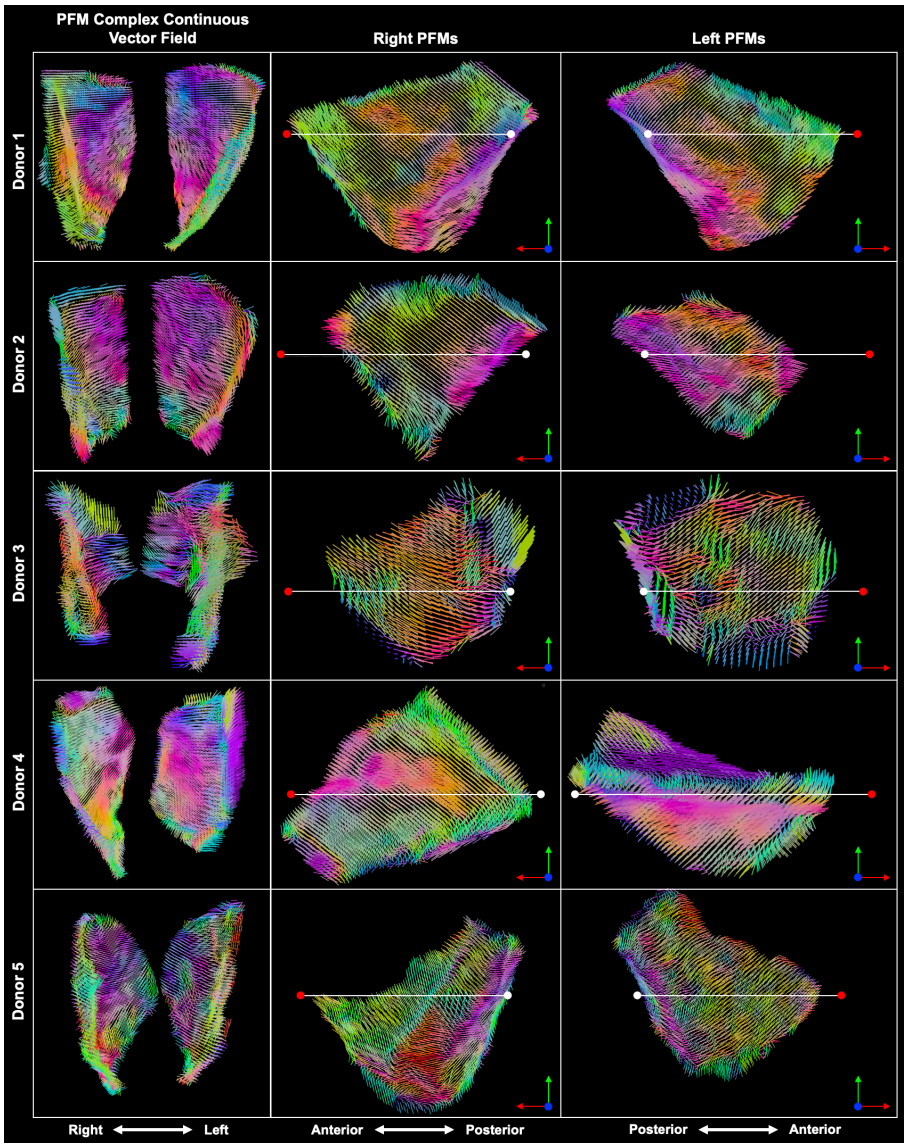

Figure 5.14: The donor–specific continuous, 3D vector fields defining the entire pelvic floor muscle complex (coccygeus and levator ani) from an anterior–superior view. The corresponding left and right pelvic floor muscles are shown from a medial, sagittal view. Relevant anatomical directions are indicated below each column and each pubococcygeal line (white) is visualized connecting the pubic symphysis landmark (red point) to the tip of the coccyx (white point). The color of each vector is indicative of its 3D orientation: vectors parallel to the pubococcygeal line (anteriorly–posteriorly oriented) are red, left–right vectors are blue, inferiorly–superiorly oriented vectors are green, and those colors are blended to label orientations in between [165]. This figure was reprinted by permission from the Biomedical Engineering Society: Springer Nature; Annals of Biomedical Engineering; Megan R Routzong, Mark S Cook, William Barone, Steven D Abramowitch, and Marianna Alperin. Novel Application of Photogrammetry to Quantify Fascicle Orientations of Female Cadaveric Pelvic Floor Muscles. *Annals of Biomedical Engineering*, 1–12, 2021; © 2021 Biomedical Engineering Society.

by the purple/pink colored vectors in these regions. In the middle regions of the PFM complex, corresponding to the position of the iliococcygeus, most fibers ran roughly parallel to the midsagittal plane and pointed anteriorly–superiorly, indicated by orange vectors. The pubovisceralis demonstrated the greatest diversity in vector orientations and the most superiorly–inferiorly aligned fascicles, represented by green and light blue vectors. Though trends were similar across the PFMs bilaterally, there was noticeable left–right asymmetry in most PFM complexes—in both shape and fascicle arrangement.

5.5.8 PFM Fascicle Angle Comparisons

Every individual PFM for each donor had a preferred fascicle orientation ($p<0.001$) (Figure 5.15). In Table 5.5, the data from all donors are summarized using two approaches: average and combined. Combined refers to the mean and standard deviation of the data from all donors, while average refers to the mean of the donor–specific means and standard deviations. The combined approach accounts for every angle measured in all donors, while the average approach only considers a single mean and standard deviation from each donor. Corresponding contralateral PFMs differed significantly within each donor ($p<0.001$), but not when all 5 donors were considered collectively. On average, contralateral PFMs differed by more than 10° in both planes (Table 5.6). The left PFMs tended to be more laterally oriented than the right as indicated by predominantly negative left–right axial angle differences. When looking at the axial angles, corresponding contralateral PFMs differed by more than 10° in 2 donors each. In the sagittal plane, contralateral iliococcygeus and pubovisceral muscles differed by more than 10° in 2 donors while the coccygeus differed in 4 donors.

Combined values describe the overall results across all 5 PFM cones (Figure 5.16). The contralateral PFMs were fairly symmetrical about the midsagittal plane as only the iliococcygeus surpassed the 10° threshold (by 0.4°) in the axial plane and only the coccygeus in the sagittal plane (by 19.4°). Contralateral ischial spine angles were more similar than contralateral PFMs (on average, within 10° of one another in both planes) but comparing mean PFM angles across donors with respect to the ischial spines did not change the significance of these differences.

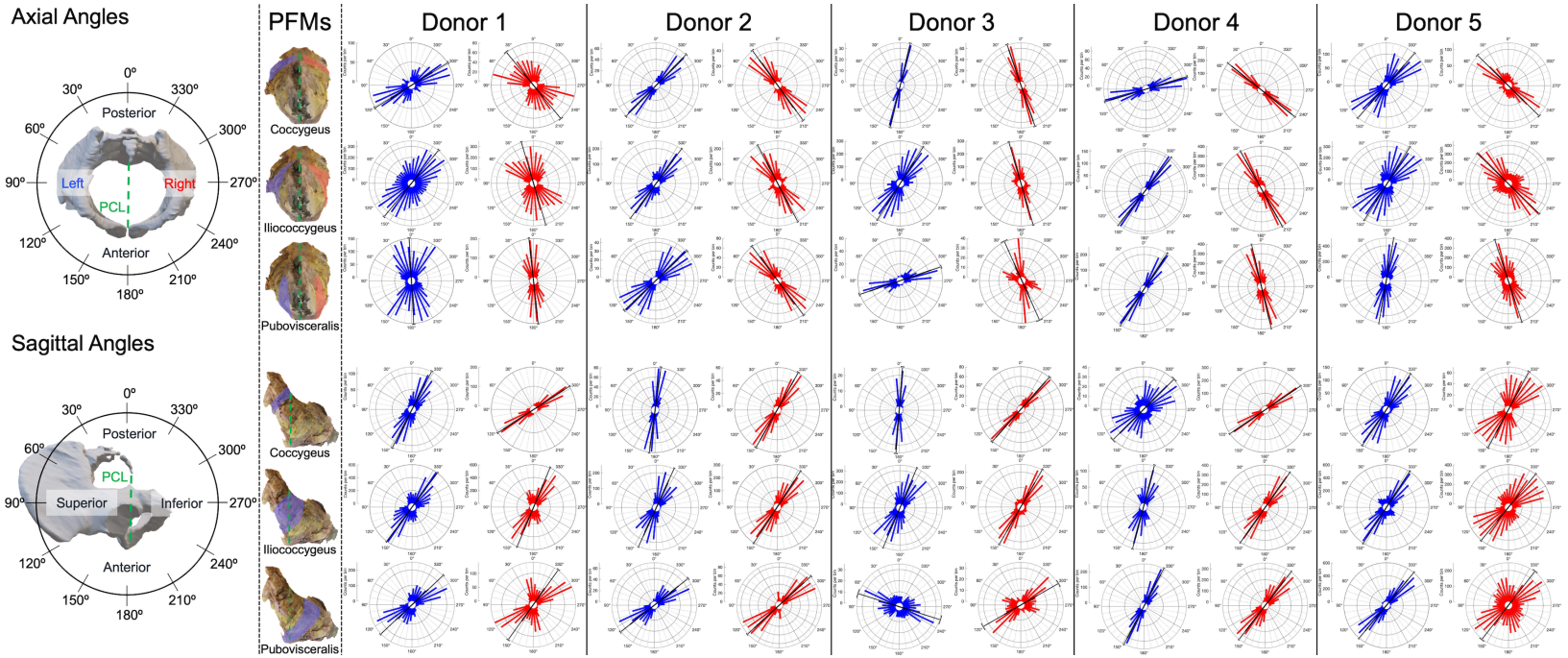

Figure 5.15: Polar histograms depicting the distributions of axial and sagittal angles for each pelvic floor muscle (coccygeus, iliococcygeus, and puboviscerali from top to bottom, respectively, in each section) and donor. Red indicates right–sided pelvic floor muscles and angles while blue represents those on the left. The black lines denote the mean angle and the standard deviation of the mean. Angle values are shown with respect to the bony pelvis and anatomical directions on the left [165]. This figure was reprinted by permission from the Biomedical Engineering Society: Springer Nature; Annals of Biomedical Engineering; Megan R Routzong, Mark S Cook, William Barone, Steven D Abramowitch, and Marianna Alperin. Novel Application of Photogrammetry to Quantify Fascicle Orientations of Female Cadaveric Pelvic Floor Muscles. *Annals of Biomedical Engineering*, 1–12, 2021; © 2021 Biomedical Engineering Society.

Table 5.5: Means and standard deviations (in degrees) of the angular data from each donor and pelvic floor muscle and the ischial spine angles. For right–sided PFM axial angles, original values are given with left equivalent angles in parentheses [165]. This table was reprinted by permission from the Biomedical Engineering Society: Springer Nature; Annals of Biomedical Engineering; Megan R Routzong, Mark S Cook, William Barone, Steven D Abramowitch, and Marianna Alperin. Novel Application of Photogrammetry to Quantify Fascicle Orientations of Female Cadaveric Pelvic Floor Muscles. *Annals of Biomedical Engineering*, 1–12, 2021; © 2021 Biomedical Engineering Society.

		Donor 1		**Donor 2**		**Donor 3**		**Donor 4**		**Donor 5**			**Average**		**Combined**	
		Mean	SD	Mean	SD	Mean	SD	Mean	SD	Mean	SD	**p–value**	Mean	SD	Mean	SD
Axial	Left C	121.8	29.8	135.8	16.0	166.5	9.0	107.1	14.3	138.6	26.9		134.0	19.2	130.5	28.2
	Left IC	140.7	46.2	143.6	25.6	147.8	28.7	141.9	11.6	147.9	33.1	0.551[1]	144.4	29.0	144.4	36.6
	Left PV	183.1	36.0	133.4	22.6	108.7	20.8	147.0	13.6	170.1	22.0		148.5	23.0	166.5	45.1
	Right C	39.4	40.2	36.0	21.9	18.8	13.8	51.4	12.8	45.6	33.2		38.2	24.4	32.1	32.2
		(140.6)		(144.0)		(162.2)		(128.6)		(134.4)			(141.8)		(134.4)	
	Right IC	16.6	39.1	27.7	30.3	16.4	28.1	29.1	21.2	46.0	40.1	0.991[1]	27.2	31.8	19.9	34.8
		(163.4)		(152.3)		(163.6)		(150.9)		(134.0)			(152.8)		(134.0)	
	Right PV	6.3	20.4	37.0	23.7	24.1	35.6	13.2	20.2	18.3	34.3		19.8	26.8	15.4	27.0
		(186.3)		(143.0)		(155.9)		(166.8)		(161.7)			(160.2)		(161.7)	
	Left IS	105.5		132.1		118.1		104.6		106.2			113.3	11.9	113.3	11.9
	Right IS	252.3		232.7		243.0		241.6		246.8		0.592[2]	243.3	7.2	243.3	7.2
		(107.7)		(127.3)		(117.0)		(118.4)		(113.2)			(116.7)		(116.7)	
Sagittal	Left C	152.7	25.5	172.2	13.1	175.6	11.8	134.7	39.3	146.0	25.6		156.2	23.1	161.2	23.8
	Left IC	143.3	31.9	155.4	23.0	157.0	28.6	165.2	20.1	147.0	32.5	0.091[1]	153.6	27.2	150.2	30.0
	Left PV	133.2	32.3	128.3	22.7	72.4	41.4	152.2	16.1	140.1	19.9		125.2	26.5	130.1	34.4
	Right C	122.9	16.2	150.5	18.1	138.3	14.6	124.0	13.4	151.8	29.6		137.5	18.4	131.8	20.0
	Right IC	157.3	29.5	146.9	22.1	150.1	26.1	144.7	19.4	140.6	37.8	0.201[1]	147.9	27.0	152.7	27.3
	Right PV	144.3	36.7	132.3	19.5	119.8	36.3	142.3	20.7	142.0	54.0		136.1	33.4	137.1	33.0
	Left IS	110.4		135.5		109.6		118.5		103.4		0.472[2]	115.5	12.4		
	Right IS	120.5		129.3		112.8		124.9		113.6			120.2	7.1		
Axial–IS	Left C	16.3		3.7		48.4		2.5		32.4			20.7		17.2	
	Left IC	35.2		11.5		29.7		37.3		41.7		0.651[1]	31.1		31.1	
	Left PV	77.6		1.3		-9.4		42.4		63.9			35.2		53.2	
	Right C	-32.9		-16.7		-44.2		-10.2		-21.2			-25.0		-31.2	
	Right IC	-55.7		-25.0		-46.6		-32.5		-20.8		0.211[1]	-36.1		-43.4	
	Right PV	-66.0		-15.7		-38.9		-48.4		-48.5			-43.5		-47.9	
Sagittal–IS	Left C	42.3		36.7		66.0		16.2		42.6			40.8		45.7	
	Left IC	32.9		19.9		47.4		46.7		43.6		0.101[1]	38.1		34.7	
	Left PV	22.8		-7.2		-37.2		33.7		36.7			9.8		14.6	
	Right C	2.4		21.2		25.5		-0.9		38.2			17.3		11.6	
	Right IC	36.8		17.6		37.3		19.8		27.0		0.301[1]	27.7		32.5	
	Right PV	23.8		3.0		7.0		17.4		28.4			15.9		16.9	

C, coccygeus; IC, iliococcygeus; PV, pubovisceralis; IS, ischial spine; Axial–IS, mean axial angles recalculated with respect to the ischial spine angles; Sagittal–IS, mean sagittal angles recalculated with respect to the ischial spine angles

[1]Watson-Williams test p–values for ipsilateral PFMs; [2]Watson-Williams test p–values for contralateral ischial spines

Table 5.6: Differences (in degrees) between contralateral (left–right) and ipsilateral (same–sided) pelvic floor muscles and the ischial spines [165]. This table was reprinted by permission from the Biomedical Engineering Society: Springer Nature; Annals of Biomedical Engineering; Megan R Routzong, Mark S Cook, William Barone, Steven D Abramowitch, and Marianna Alperin. Novel Application of Photogrammetry to Quantify Fascicle Orientations of Female Cadaveric Pelvic Floor Muscles. *Annals of Biomedical Engineering*, 1–12, 2021; © 2021 Biomedical Engineering Society.

	Donor 1	Donor 2	Donor 3	Donor 4	Donor 5	Combined	Average[1]	p–value[2]	IS p-value[3]
Axial									
Left–Right C	**-18.8**	-8.2	5.3	**-31.5**	4.2	-3.9	**13.6**	0.50	0.67
Left–Right IC	**-22.7**	-8.7	**-15.8**	-9	**13.9**	**10.4**	**14.0**	0.17	0.57
Left–Right PV	-3.2	-9.6	**-47.2**	**-19.8**	8.4	4.8	**17.6**	0.37	0.68
Left–Right IS	-2.2	4.8	1.1	**-13.8**	-7		5.8		
Left C–IC	**-18.9**	-7.8	**18.7**	**-34.8**	-9.3	**-13.9**	**17.9**		
Left IC–PV	**137.6**	**10.2**	**39.1**	-5.1	**-22.2**	**-22.1**	**42.8**		
Left C–PV	**118.7**	2.4	**57.8**	**-39.9**	**-31.5**	**-36**	**50.1**		
Right C–IC	**22.8**	8.3	2.4	**22.3**	-0.4	**12.2**	**11.2**		
Right IC–PV	**10.3**	-9.3	-7.7	**15.9**	**27.7**	4.5	**14.2**		
Right C–PV	**33.1**	-1	-5.3	**38.2**	**27.3**	**16.7**	**21.0**		
Sagittal									
Left–Right C	**29.8**	**21.7**	**37.3**	**10.7**	-5.8	**29.4**	**21.1**	0.10	0.06
Left–Right IC	**-14**	8.5	6.9	**20.5**	6.4	-2.5	**11.3**	0.27	0.18
Left–Right PV	**-11.1**	-4	**-47.4**	9.9	-1.9	-7	**14.9**	0.52	0.73
Left–Right IS	**-10.1**	6.2	-3.2	-6.4	**-10.2**		7.2		
Left C–IC	9.4	**16.8**	**18.6**	**-30.5**	-1	**11**	**15.3**		
Left IC–PV	**10.1**	**27.1**	**84.6**	**13**	6.9	**20.1**	**28.3**		
Left C–PV	**19.5**	**43.9**	**103.2**	**-17.5**	5.9	**31.1**	**38.0**		
Right C–IC	**-34.4**	3.6	**-11.8**	**-20.7**	**11.2**	**-20.9**	**16.3**		
Right IC–PV	**13.0**	**14.6**	**30.3**	2.4	-1.4	**15.6**	**12.3**		
Right C–PV	**-21.4**	**18.2**	**18.5**	**-18.3**	9.8	-5.3	**17.2**		

C, coccygeus; IC, iliococcygeus; PV, pubovisceralis; IS, ischial spine; Differences greater than 10° in **bold**.

[1]The absolute value of the average difference; [2]Watson–Williams test p–values for contralateral pelvic floor muscles

[3]Watson–Williams test p–values for contralateral pelvic floor muscle mean angles recalculated with respect to the ischial spine angles

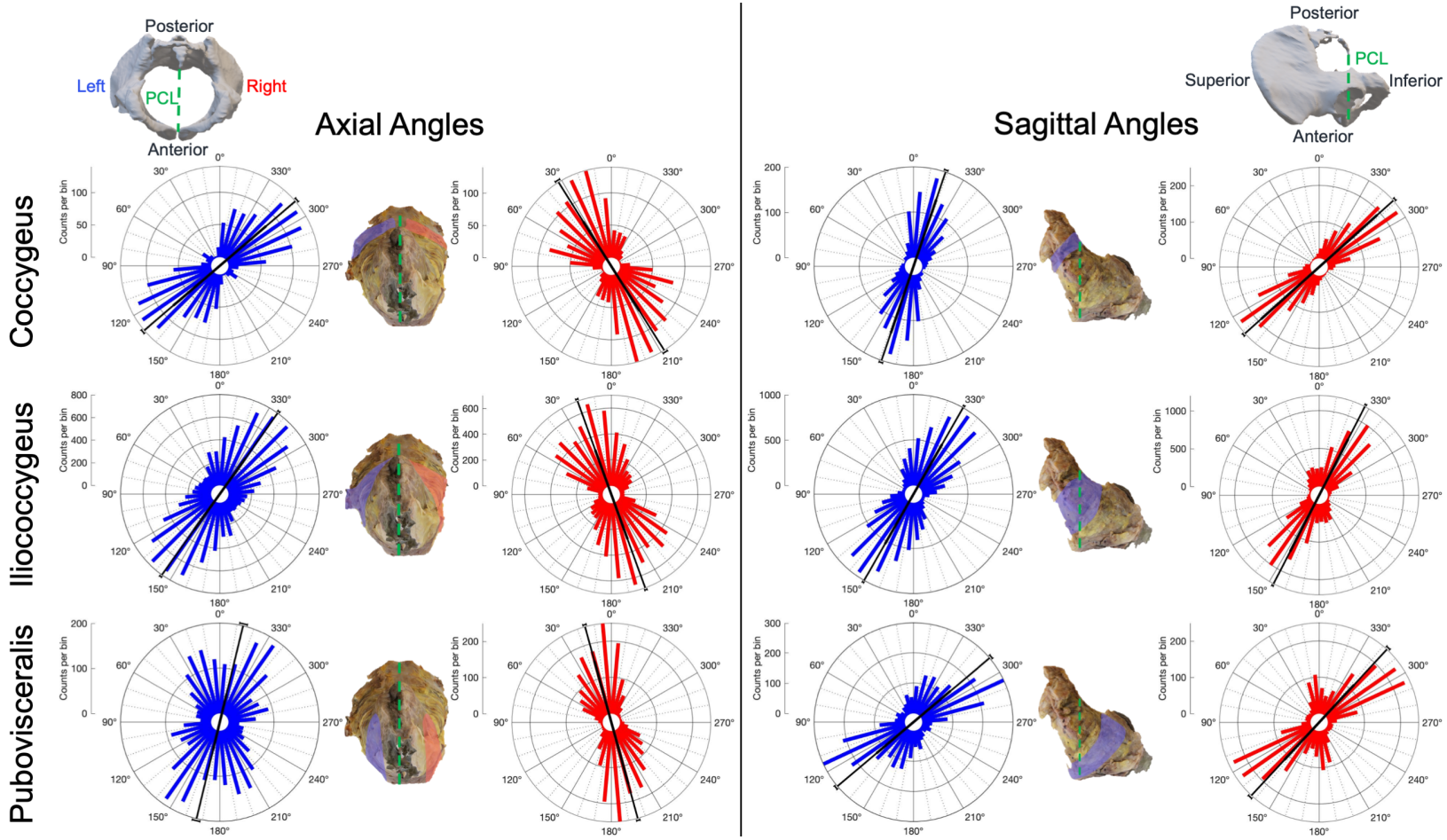

Figure 5.16: Polar histograms similar to those described in Figure 5.15 but generated with angles combined from all 5 donors for more generalizable comparisons of contralateral and ipsilateral pelvic floor muscle fascicle distributions [165]. This figure was reprinted by permission from the Biomedical Engineering Society: Springer Nature; Annals of Biomedical Engineering; Megan R Routzong, Mark S Cook, William Barone, Steven D Abramowitch, and Marianna Alperin. Novel Application of Photogrammetry to Quantify Fascicle Orientations of Female Cadaveric Pelvic Floor Muscles. *Annals of Biomedical Engineering*, 1–12, 2021; © 2021 Biomedical Engineering Society.

Out of all pairs of circular distributions compared within each donor, only the right coccygeus and pubovisceralis of Donor 2 were statistically similar. All others differed significantly ($p<0.001$). On average, ipsilateral PFMs differed by more than 10° in both planes (Table 5.6). In the axial plane, the number of differences across ipsilateral PFMs per donor that surpassed our threshold ranged from 1 to 5. In the sagittal plane, this ranged from 1 to 6, demonstrating variability across individuals. Combining the data of all 5 donors revealed that, in general, the coccygeus was the most laterally oriented PFM (with mean axial values closest to 90° and 270°), the pubovisceralis was the most anteriorly–posteriorly oriented (with mean axial values closest to 0° and 180°), and the iliococcygeus fell in between (Figure 5.16). On average when looking at both sides, the pubovisceralis was the most superiorly–inferiorly oriented (with mean sagittal angles closest to 90° and 270°).

The pubovisceralis bilaterally demonstrated the largest variation across donors in both planes with a summed range (left and right, axial and sagittal) of 209.4° (Table 5.7). The iliococcygeus and coccygeus had summed ranges of 75.4° and 161.8°, respectively. Generally, the range in mean values across donors did not decrease when angles were measured with respect to the ischial spines. In many cases, the range increased or the change was negligible when calculated across angles measured with respect to the ischial spines, suggesting that bony morphology was not the major contributor to the variations observed in this study.

5.5.9 Fascicle Orientations Differed Across the Pelvic Floor Muscles

In this study, we utilized close–range photogrammetry to robustly quantify PFM surface fascicle orientations, which provides data necessary to enhance our understanding of the functional anatomy of the female PFMs and to more accurately simulate their function. The PFM fascicle orientations predict the direction of the forces resulting from active muscle contraction and passive tension generated by the intramuscular extracellular matrix. Our overall results demonstrate how contraction of the PFM complex generates lateral tension, with the bilateral PFMs pulling on the midsagittal portion of the pelvic floor, termed the levator plate. The above allows the PFMs to pull the levator plate anteriorly, with the more inferior PFMs pulling the anus superiorly and anteriorly towards the pubis.

Table 5.7: Ranges (in degrees) of mean pelvic floor muscle (PFM) angles and those taken with respect to the ischial spines across all 5 donors [165]. This table was reprinted by permission from the Biomedical Engineering Society: Springer Nature; Annals of Biomedical Engineering; Megan R Routzong, Mark S Cook, William Barone, Steven D Abramowitch, and Marianna Alperin. Novel Application of Photogrammetry to Quantify Fascicle Orientations of Female Cadaveric Pelvic Floor Muscles. *Annals of Biomedical Engineering*, 1–12, 2021; © 2021 Biomedical Engineering Society.

	Axial	**Axial–IS**[1]	**Sagittal**	**Sagittal–IS**[2]
Left PFMs				
Coccygeus	59.4	45.9	40.9	49.8
Iliococcygeus	7.2	30.2	21.9	27.5
Pubovisceralis	74.4	87.0	79.8	73.9
Right PFMs				
Coccygeus	32.6	34.0	28.9	39.1
Iliococcygeus	29.6	34.9	16.7	19.7
Pubovisceralis	30.7	50.3	24.5	25.4
Ischial Spines				
Left	27.5		32.1	
Right	19.6		16.5	

[1]The range of mean axial angles recalculated with respect to the ischial spine angles

[2]The range of mean sagittal angles recalculated with respect to the ischial spine angles

The coccygeus was the most laterally and the least superior–inferiorly oriented PFM in 5 of the 10 axial and sagittal ipsilateral PFM comparisons, respectively. Note that this varied bilaterally within individual donors and across all donors as sometimes the pubovisceralis was the most lateral or the iliococcygeus the least superiorly–inferiorly oriented. Thus, for most PFM complexes, the coccygeus appears to predominantly contribute to pelvic floor and coccyx motion and stabilization within the axial plane. The vector fields suggest that lateral tension during contraction of the coccygeus muscles pulls the tip of the coccyx anteriorly as it rotates about the sacrum. Conversely, relaxation would then allow posterior motion of the coccyx, which has been observed during straining (i.e. increases in intraabdominal

pressure) via dynamic MRI. This is a novel finding given the lack of focus on the coccygeus in previous research and suggests that the coccygeus plays an important role in pelvic floor support and the pathogenesis of pelvic floor disorders, such as pelvic organ prolapse.

The levator ani contained the most superiorly–inferiorly oriented fascicles. This was more apparent in the puboviscerali as the combined angles and vector fields demonstrate how the iliococcygeus serves as a transition between the more diverse fascicle orientations of the coccygeus and puboviscerali (with a mean axial angle between the coccygeus and puboviscerali in 6 of the 10 axial ipsilateral comparisons made). The puboviscerali specifically was the most superiorly–inferiorly oriented in 6 of the 10 sagittal ipsilateral PFM comparisons made and is the most anteriorly located PFM, indicating that it would be the main contributor to the superior–inferior motion of the pelvic floor observed during dynamic MRI. This also confirms previous findings where the Modified Oxford Scale, which provides guidance on how to grade PFM function via digital assessment, demonstrated anterior displacement of the examiner's fingers during contraction of the puboviscerali [32]. The puboviscerali had the most diversity in muscle fascicle orientations of the PFMs evaluated, which is likely due to the fact that it is composed of multiple smaller, variably oriented medial (pubococcygeus) and lateral (puborectalis) muscles and its fibers lack a fixed point of insertion.

These fascicle orientations appear to concur with existing findings and build upon previous studies where the same muscles were evaluated. Though PFMs were grouped and angles quantified differently, Yan et. al. via analysis of digital images of fresh–frozen cryosections also showed that the coccygeus falls predominantly within the axial plane, especially compared to the other PFMs, though they combined their coccygeus and iliococcygeus angles making further comparisons difficult [201]. Yan et. al.'s resulting vector field demonstrated more superiorly–inferiorly oriented muscle fibers in the puboviscerali compared to the coccygeus and iliococcygeus and in the more anterior regions of the levator ani, which we also observed in our continuous vector fields [201]. Betschart et. al. presented similar puboviscerali sagittal orientations measured from MRI, however their puboviscerali and iliococcygeus were more similar (mean difference of 7.6°across 14 women) than we measured on average in this study (28.3° on the left and 13.3° on the right) [28]. While our combined results agree with the existing literature, we robustly quantified variations between donors and generated

angles (in multiple planes) and vector fields for all donors, obtaining more detailed data from each PFM complex than provided by these previous studies. Importantly, our assessments included the coccygeus muscle, which has frequently been ignored in the past PFM orientation quantification studies.

5.5.10 Pelvic Floor Muscle Fascicle Orientation Variation Across Donors was not due to Bony Morphology

In addition to quantifying and comparing differences between PFMs within individual donors in multiple planes, we also evaluated PFM fascicle orientation variability across donors and with respect to bony morphology. The variation across the 5 donors examined in this study highlights the need for these more robust quantification methods, as differences between individuals and across PFMs could have been missed if muscles were simplified and described by only a few angles. This explains why the Watson-Williams tests, which only consider mean angles, were insignificant, while the Kuiper's tests, which look at entire distributions, were significant for almost every pair of PFMs compared. Furthermore, while variability in the ischial spine angles was identified, this variation in bony morphology did not directly account for the differences in PFM fascicle orientations. If variations in bony morphology did directly explain the differences in PFM orientations across donors, then we would have expected the range in angle values across donors to decrease (for the angles to become more similar) when measured with respect to the ischial spines. These results suggest that the relationship between the PFM fascicle orientations and bony morphology is complex. Both muscle fascicle configuration and bony pelvic shape need to be considered in order to fully understand the mechanical functions of the PFMs and accurately simulate the pelvic floor.

Our study demonstrates a wide range in PFM mean angles and relationships across individual components of the PFM complex within each donor. For example, Donor 2's PFMs were all very similarly oriented within the axial plane, but not in the sagittal plane. Meanwhile, Donor 5 had almost no PFM differences in the sagittal plane, with large variability in the axial plane. Interestingly, these trends were inconsistent across individuals. This

indicates that a single definition of PFM fascicle orientations that can accurately describe every PFM complex is unlikely and that interactions between PFMs vary more across individuals than previously considered. Less variation in orientations across ipsilateral PFMs would result in more uniform linear motion of the PFM complex and supported pelvic organs. Whether this is beneficial or detrimental or associated with factors such as age, parity, or disease progression would need to be determined with future studies. These unique relationships between PFMs, in addition to our more generalizable findings, are important for generating accurate, patient-specific simulations of PFM complex (dys)function.

5.5.11 Photogrammetry is a Viable Methodology for Pelvic Floor Muscle Fascicle Orientation Quantification

Although this novel implementation of a close–range photogrammetry methodology is quite powerful, there are limitations to consider. Most importantly, this protocol could only be performed on cadaveric tissues. That being said, an important aspect of this work is validation of existing methods for PFM fiber/fascicle quantification, such as MRI and diffusion tensor imaging both of which could be performed on cadaveric specimens and compared with the current study. Although vector fields are more useful for computational models, our axial and sagittal angle definitions would allow for more direct comparisons between these PFM fascicle/fiber orientation methodologies. Validating *in vivo* PFM fascicle orientation quantification methods is an important purpose of the current photogrammetry approach that could only be accomplished utilizing cadaveric data. Another limitation stems from the assumption of PFM fascicle orientations calculated by interpolating between those that we were able to visualize and trace manually. For the vectors interpolated through the PFMs (between the dorsal and ventral surfaces) we consider this a safe assumption given the 2–4 mm thickness of the PFMs [8, 190]. Finally, the PFM fascicle orientation data in this study were obtained from digital images of cadaveric tissues after dissection. Some of the differences observed could possibly have been influenced by muscle fascicle visibility (i.e. some regions could have been partially obscured by fat and other tissues), though this does not affect the accuracy of the regions that could be visualized clearly and traced. Despite

these limitations, the results of the current study are important for informing and improving future computational models of female pelvic floor function and the pathogenesis of pelvic floor disorders.

In conclusion, close–range photogrammetry provides robust quantification of the female PFM surface fascicle orientations and contributes critical data to the field of female pelvic medicine. As this method allows PFM fascicles to be viewed in three dimensions and quantified in multiple ways, it affords the ability to view the PFMs and PFM cone geometry virtually in 3D, visualize the muscle fascicles in enough detail to see and quantify the range in orientations within a single PFM, and to validate orientations calculated from MRI and diffusion tensor imaging. The 3D vector fields generated in this study could be used to simulate the PFMs and compare resulting PFM motion and predicted stresses and strains across donors. Additionally, because these vector fields are continuous, they could be modified to define the PFM fascicle arrangement in simulations of other individuals. These vector field equations only require coordinates as inputs, meaning they could be transformed and scaled by the pubococcygeal line to approximate the fascicle orientations of PFM complexes obtained outside of this study (i.e. from MRI). While this study was descriptive and focused on the feasibility of the methods and usability of the resulting dataset for computational research, future studies will expand upon these findings by elucidating the influence of the PFM fascicle orientations on PFM function and quantifying PFM fascicles in women with and without specific pelvic floor disorders and/or injuries to improve our understanding of potential mechanisms of PFM dysfunction.

5.6 Conclusions

These studies revealed that there is a significant amount of shape variation across a broad population of adult women. Only 43% of the total bony pelvis and 24% of the total pelvic floor muscle complex shape variation were described by modes that significantly differed between nulliparous, late pregnant, and parous women, meaning the remaining 57% and 76% of the total shape variance described general population variation. Notably, a larger

proportion of the bony pelvis morphology differed between these groups of interest compared to the pelvic floor muscle complex morphology. Additionally, not only did muscle fascicle orientations vary across individual donors, but that variation was not explained by bony pelvis morphology. These computational analyses established geometric and muscle fascicle orientation means and standard deviations meant to describe a general population of women. However, it should be noted that these analyses did not account for potential effects of aging and menopause. Nevertheless, this data can be used to augment existing and improve future computational simulations and analyses by providing data that can be used to generate results and draw conclusions that apply to a wider range of women.

6.0 Conclusions

6.1 Major Findings

In this dissertation, we quantified morphological variation of the female urethra, pelvic floor muscle complex, and bony pelvis. That shape variation was then associated with stress urinary incontinence, pregnancy, and childbirth and its relationship with the biomechanics of urethral passive closure and vaginal childbirth were determined.

In Section 3, urethral shape as assessed via endovaginal ultrasound was found to be a significant predictor of stress urinary incontinence while the urethra experienced a greater amount of swinging in women with stress urinary incontinence compared to controls. Finite element simulations of Valsalva determined that the urethra and perineal membrane had the greatest impact on simulated urethral passive closure. By measuring the urethral shape and swing variables associated with stress urinary incontinence in Section 3.2 in the finite element simulations generated in Section 3.3, we were also able to determine that the properties of the urethra and perineal membrane *in vivo* likely contribute to the presentation and severity of stress urinary incontinence.

In Section 4, pregnancy–induced shape remodeling was quantified and determined to reduce the mechanical burden of vaginal childbirth. Statistical shape modeling was used in Section 4.3 to quantify variation in the shape of the pelvic floor muscle complex, bony pelvis, and combined pelvic floor–bony pelvis across pregnant women of varying gestational ages. As the superficial perineal muscles and connective tissues were previously determined (Section 4.2) to meaningfully impact biomechanical simulations of vaginal childbirth, they were included as part of the pelvic floor muscle complex. To summarize, women in their 3rd trimester had wider bony pelvises and greater descent in specific regions of and wider pelvic floor muscle complexes. The sensitivity analysis in Section 4.4 determined that maternal pelvic morphological variation significantly impacts the biomechanics of vaginal childbirth (i.e., predicted perineal body and pubovisceral muscle strains). Additionally, the 3rd

trimester average simulation experienced smaller strains than those of the 1st/2nd trimester average simulation, demonstrating how pelvic shape remodeling during pregnancy may be protective of stretch–induced birth injury.

In Section 5, meaningful variation in the shape of the bony pelvis and pelvic floor and in pelvic floor muscle fascicle orientations was quantified. In general, Sections 5.2, 5.3, and 5.4 revealed that pelvic morphology in women in the 3rd trimester of pregnancy significantly differs from that of nulliparous and parous women. In the bony pelvis, these alterations seem to completely recover to within the nulliparous range in parous women, but the pelvic floor muscle complex demonstrates certain shape attributes in some parous women that do not return to the nulliparous range. The fact that less recovery was demonstrated by the soft tissues compared to the bony pelvis is likely indicative of the potential lasting impact of pregnancy and childbirth on the pelvic floor muscle complex and its shape. These quantitative descriptions of variation in female pelvic morphology and pelvic floor muscle fascicles (determined in Section 5.5) provide information that is important to improving the geometry and material property inputs of future computational models of female pelvic floor biomechanics.

The studies laid out in this dissertation are first steps towards combined statistical and computational models that we one day hope to use to predict stress urinary incontinence, outcomes/effectiveness of surgical treatments for pelvic floor disorders (e.g., midurethral sling implantation), vaginal birth–related injuries, postpartum recovery, and the development of pelvic floor disorders. Although this was the focus of Section 5, all three specific aims contribute data to the field that will allow for future improvements to computational models of urethral passive closure, vaginal childbirth, and any number of scenarios/conditions involving the female pelvis and/or pelvic floor. Together, these studies demonstrate the importance and biomechanical implications of morphological and material property variation—specifically on female pelvic floor biomechanics, but also in general. Our findings highlight the need for more critical evaluation of single, patient–specific finite element models. We need to collectively move towards simulations that are designed such that they can be

appropriately applied to a broad population of women (e.g., women of various ages, parity, weight, height, race/ethnicity, etc.), rather than individuals. If designed well, those models could then be tuned to make patient–specific predictions, diagnoses, and treatment decisions.

Likely the most important finding of the work in this dissertation collectively is the importance of critical evaluation of computational models. Clinicians cannot afford to disregard work such as this that may not have direct clinical applications (e.g., basic science and/or computational studies). That kills innovation. At the same time, computational models with many limitations and little validation should not be portrayed as something greater or more pivotal than they truly are (e.g., claiming the results of one patient–specific model can be assumed true for any woman). Although repeatability studies are often shot down and/or not able to publish in impactful journals, such studies by groups other than that who originally published a method or finding should be highly encouraged. Taking the findings of a single study, no matter who the authors are or how innovative and seemingly sound the methods were, without assessing repeatability objectively is a grave error that leads to the disproof of biomechanical theories that had been treated as law for decades. The culture of making the methods sections of manuscripts as short as possible or assuming (sadly often correctly) that they will never be read is doing the field a great disservice. Just as we should critically evaluate computational models, we should critically evaluate research methods and findings in general. Now, this is not to say that faults and limitations of a study should become its focus, but, while both reading and writing any scientific manuscript, it is important to always consider how the limitations and biases of a study influence its results and the interpretation of those results.

6.2 Clinical and Engineering Implications

The statistical shape models in this dissertation have demonstrated that pelvic organ and tissue shape may be indicative of the degree of disease progression (e.g., the urethra with respect to stress urinary incontinence) and of remodeling during pregnancy. While most computational studies are not immediately clinically relevant, this sets the stage for the use

of statistical shape models and other measures of pelvic morphology as variables in predictive tools. In these examples, the goal of these predictive models would be to determine if a continent/asymptomatic woman is at a higher risk of developing stress urinary incontinence or if a woman has remodeled adequately enough during pregnancy to avoid injury during vaginal childbirth. The shape attributes identified in this study in conjunction with the sensitivity analyses of finite element simulations identify risk factors for the development of stress urinary incontinence and maternal birth injury. With additional research, this knowledge could allow for patient–specific conservative and surgical treatment plans that improve patient outcomes.

Although many of these methodologies are especially important for and quite novel to the field of women's health as compared to other fields (given that such methods may have already been applied extensively, as is the case with the field of orthopedics), the described computational methods in this dissertation also benefit the engineering community at large.

We utilized this statistical shape modeling workflow to evaluate pelvic floor muscle morphology. Not many statistical shape models have been performed on soft tissues nor have they been as complex as the combined bony pelvis–pelvic floor muscle complex. Typically, statistical shape modeling of human anatomy is only used to evaluate bones. Throughout most of the body, muscles are fairly simplistic, flat or cylindrical shapes and do not require a technique as complex and potentially computationally expensive as statistical shape modeling to adequately describe their morphology. This dissertation demonstrates the usefulness and benefits of applying such a methodology to the geometrically complex and variable pelvic floor muscle complex and could be applied to other geometrically complex muscles. Additionally, even to engineers who do not study the pelvis, the potential demonstrated by the combined bony pelvis–pelvic floor shape model, where bony and soft tissue anatomy were evaluated together, should serve as motivation for more complex shape models in other fields. Especially given the finite element modeling applications of such models.

Similar to soft tissue shape models, 2D statistical shape models are uncommon, especially of human anatomy. The ideal scenario in which to utilize a 2D shape model is when you are collecting dynamic imaging data that can only be 2D. The pro of the dynamic shape data is that, as shown by our study of the urethra in Section 3.2, it can be used to draw conclusions

about biomechanical function. While 2D shape models may be limited and ignore potential out–of–plan effects, our 3D finite element models of the urethra (in the case of the 2D urethra SSM) and 3D statistical shape models of the pelvic floor corroborated our 2D, midsagittal shape findings. This demonstrates the usefulness of 2D shape models and suggests that the 2D limitations, in these cases, do not significantly impact our findings.

6.3 Limitations

Our analysis of the urethra in Chapter 3 largely ignored potential shape variation and indicators of stress urinary incontinence that may lie outside of the midsagittal plane. Because the urethra was visualized via dynamic endovaginal ultrasound, it could only be captured in 2D. That being said, this demonstrates the utility of 2D statistical shape models as it would have otherwise been impossible to perform such a robust evaluation of urethral shape during active and passive urethral closure.

The largest limitation of the bony pelvis and pelvic floor muscle complex statistical shape models in this dissertation is the use of retrospectively collected patient data. This led to the elimination of many patient scans due to the lack or ambiguity of their demographic or other relevant data. For example, vaginal parity was not always indicated or their chart may have contained conflicting birth history information. This contributed to the number of women included in these studies. However, these statistical shape models still contain more individuals than existing pelvic floor [108] and bony pelvis [21] shape models, which typically analyze fewer than 20 shapes. While the group comparisons could be made more robust, this speaks to the quality of the resulting modes of variation and descriptions of general morphological variation of that patient population.

Inherently, the study of true shape variation ignores any differences in scale. This means that these studies did not have the ability to detect size–related effects. This could be remedied with follow–up analyses targeted to evaluate size specifically. Additionally, the

research presented in Section 3.2 where urethral shape, motion, and length were evaluated simultaneously serves as an example for evaluating true shape and scale variables together to draw conclusions that may not have been reached with separate analyses.

6.4 Future Directions

Although Chapter 3, established trends between urethral shape, motion, and deformation and SUI and identified which tissue material properties likely contribute to the presence of SUI, there still remains a paucity of data on female pelvic floor organ and tissue material properties. In Section 3.3, the literature review resulted in a wide range of material property values, and for some tissues no data existed at all. Considering that many finite element models prioritize studying the influence of material properties over geometry, it is astounding to think that that influence is being evaluated based on such little knowledge. The material properties of every female pelvic tissue needs to be more robustly defined via *in vivo* and *ex vivo* mechanical testing and these study findings need to be determined as repeatable before those values can be trusted with confidence.

As stated previously, the computational methods described in this work could easily be adapted and applied to other areas of female pelvic floor biomechanics research and to the study of anatomical variation in general. In Chapter 2, we described a statistical shape modeling workflow that has many possible applications and could be used to evaluate the morphology of any number of biological and non–biological shapes. Specifically for female reproductive science applications, additional pelvic organs could be incorporated along with surgical implants—such as mesh or native tissue grafts—in order to analyze additional morphology and shape variation with regards to surgical treatments. To address the cross–sectional design limitation of several of these studies, statistical shape models could also be developed to track morphological changes in individuals over time (such as during pregnancy).

These studies also set the stage for combined statistical, computational models of the female pelvis. Imagine scrolling through variation in the morphology of every female pelvic

organ and tissue in order to create a digital population of women. Within this robustly defined female pelvic morphology, imagine being able to generate an average shape at every week of gestation, at every stage of pelvic organ prolapse, at every decade of life. And then being able to evaluate a normal distribution of variation within each category of interest. This would reduce the barrier of needing funding and IRB approval to obtain human imaging data and provide endless opportunities and allow for more consistency across studies than the conflicting findings that may result from everyone using different, single, patient–specific geometries.

6.5 Acknowledgements

The material in this dissertation is based upon work supported by the National Science Foundation Graduate Research Fellowship Program under Grant #1747452. Any opinions, findings, and conclusions or recommendations expressed in this material are those of the author(s) and do not necessarily reflect the views of the National Science Foundation.

Additionally, we'd like to acknowledge the following people and organizations for their contributions to aspects of this work:

- Dr. Andrew Feola for recommending the LHS–PRCC methodology and answering our initial questions regarding that process.
- The National Library of Medicine for access to the Visible Human Project image database that was used to generate the anatomy for the childbirth simulations in Section 4.2.
- The Korea Institute of Science and Technology Information for access to the Visible Korean Human data that was used to generate the female pelvic floor muscle complex template for segmentation smoothing and corresponding point quantification. The research findings and related outcomes of Sections 4.3 and 5.4 are in part the result of the use of that data.

- Undergraduate and graduate students who contributed to the segmentation of the 3D bony pelvises and 3D pelvic floor muscle complexes that appear in Sections 4.3, 5.2, and/or 5.4. This includes Liam Martin, Shaniel Bowen, Alyssa Jordan, Meredith Lie-Atjam, Oreoluwa Odeniyi, and Vincenzia Vargo.
- The University of Pittsburgh Center for Research Computing advanced computing resources which were used to complete Sections 4.3, 4.4, 5.2, and 5.4 of this dissertation.

Appendix A : Statistical Shape Modeling

This Mathematica^{TM} code was started in June of 2018 and developed through February of 2019. It was edited to incorporate more data types and to improve the generated visualizations through August of 2019. The Procrustes function used was developed by Polly et. al. [148].

A.1 Working Directory and Importing Data

```
(*Set working directory to that which contains the vtk outputs from deformetrica.*)

workingdirectory =
  "FILEPATH TO DESIRED WORKING DIRECTORY";
outputdirectory =
  "FILEPATH TO DESIRED OUTPUT DIRECTORY";
studyname =
  "STUDY IDENTIFIER";(*Name to add an identifier to the filenames of files being exported.*)

filenames =
  FileNames["*.vtk",
   workingdirectory];(*Importing only vtk files from the working directory.*)

filenames =
  Last /@ Sort[{Characters@#, #} & /@ filenames];
     (*Ordering filenames in numerical and/or alphabetical order. Is also filename length dependent.*)

(*Importing the vertex data from the vtk files and flattening that data into a matrix where the columns are
each individual shape in the format {x1,y1,z1,x2,y2,z2,....xn,yn,zn}.*)

datashapespace = Flatten[Import[#, "VertexData"]] & /@ filenames;

(*Importing the polygon connectivity data from the vtk files (should be the same for all files) to
reconstruct the surface geometry for the shapes output by the statistical shape model.*)

connectivity =
  Import[filenames[[1]],
   "PolygonData"];(*Use "PolygonData" for surface mesh vtk files and "LineData" for polyline vtk files.*)
```

A.2 Procrustes

Again, this Procrustes function was developed by Polly et. al. [148].

A.2.1 Defining the Procrustes Function

```
Procrustes[data_, nlandmarks_, ndims_] :=
 Module[{l, II, PP,(*SS,*)x, y, u, w, v, hh, ResidSS, NewResidSS,
   shape1},(*Module makes variables local, so commenting them out makes them global*)
  (*partitions data according to dims and landmarks*)

  l = Partition[Partition[Flatten[data], ndims], nlandmarks];

  II = IdentityMatrix[nlandmarks, SparseArray];

  PP = SparseArray[{}, {nlandmarks, nlandmarks}, N[1/nlandmarks]];

  SS = Table[
    N[Sqrt[Tr[(II - PP).l[[x]].Transpose[l[[x]]].(II - PP)]]], {x, Length[l]}];
  (*normalizes each shape by scale*)

  l = Table[((II - PP).l[[x]])/SS[[x]], {x, Length[l]}];
  (*calculates the mean of all shapes*)

  y = Mean[l];
  (*subtracts the mean from each scaled shape to center them*)

  ResidSS =
   Plus @@ Flatten[Table[(Flatten[l[[x]]] - Flatten[y])^2, {x, Length[l]}]];
  (*realigns each shape relative to the mean shape*)
  While[True,
                  For[x = 1, x <= Length[l], x++,
                           {u, w, v} =
     SingularValueDecomposition[Transpose[l[[x]]].y(*,Min[Dimensions[
      Transpose[l[[x]]].y]]*)];
                           hh = u.(w*Inverse[Abs[w]]).Transpose[v];
                           l[[x]] = l[[x]].hh;];
                  y = Mean[l];
   NewResidSS =
    Plus @@ Flatten[
      Table[(Flatten[l[[x]]] - Flatten[y])^2, {x, Length[l]}]];
          If[Abs[NewResidSS - ResidSS] < 0.0001, Break[]];
          ResidSS = NewResidSS;];
  l = Partition[PrincipalComponents[Partition[Flatten[l], ndims]],
    nlandmarks];
  If[ndims == 2, shape1 = Partition[Flatten[data[[1]]], ndims];
          shape1 = # - Mean[shape1] & /@ shape1;
          shape1 = shape1/Sqrt[Plus @@ Plus @@ (shape1^2)] // N;
          {u, w, v} =
    SingularValueDecomposition[
     Transpose[PrincipalComponents[shape1]].shape1(*,Min[Dimensions[
     Transpose[PrincipalComponents[shape1]].shape1]]*)];
          hh = u.(w*Inverse[Abs[w]]).Transpose[v];
          l = Partition[#, 2].hh & /@
     Partition[Flatten[l], ndims*nlandmarks];];
  l = Partition[Flatten[l], ndims*nlandmarks];
  l = l.(IdentityMatrix[ndims*nlandmarks] - Mean[l].Mean[l]);
  Return[l]]
```

A.2.2 Performing the Procrustes Analysis

This line of code must be used to transform 2D shape data so that the Procrustes function can run without error.

```
(*This is to handle 2D data defined by 3D coordinates.*)

datashapespace2d = datashapespace;
datashapespace2d =
 Delete[datashapespace2d,
  Position[datashapespace2d,
   0.]];
(*deleting 0's to avoid Procrustes error and make the data truly 2D*)
```

The following is formatted for 3D shapes, but can be modified to analyze 2D shapes.

```
(*Performs the procrustes analysis on the imported shapes. It requires the number of data points which is
Length[datashapespace[[1]]]/3 and the dimensions of those data points. *)
(*Run on datashapespace2d if data is 2D and change the dimension input to 2,
otherwise run on datashapespace.*)
procrustesshapes =
 Procrustes[datashapespace, Length[datashapespace[[1]]]/3, 3]

 (*Scaling shapes by the average normalized scale*)
(*SS is a list of the scaling values used to normailze each of the input shapes in the Procrustes function.*)
avgscale =
 Mean[SS];(*the average scaling value*)
procrustesshapes =
 procrustesshapes*avgscale;
```

Incorporate this section if you analyzed 2D data. This transforms the data back into a form defined by 3D coordinates.

```
(*Adding the zeros back in to make the data 3D again. You may need to
alter where the zeros are added back in depending on your original data.*)
procrustesshapes =
  Table[Riffle[procrustesshapes[[i]], 0, {1, -3, 3}], {i, 1, Dimensions[procrustesshapes][[1]]}];
```

A.2.3 Calculation of the Mean Shape and File Export

This section of code calculates the mean shape and establishes the bounds of the data for visualization.

```
(*calculates the mean shape from the procrustesshapes*)

meanshape = Mean[procrustesshapes];
(*creates an array of the (x,y,z) vertices of the procrustesshapes for plotting*)

lands = Transpose[
   Partition[Partition[Flatten[procrustesshapes], 3],
    Length[procrustesshapes[[1]]]/3]];
(*finds max & min x,y,z value to establish a plot range*)

xmax = Max[lands[[All, All, 1]]];
xmin = Min[lands[[All, All, 1]]];
ymax = Max[lands[[All, All, 2]]];
ymin = Min[lands[[All, All, 2]]];
```

```
zmax = Max[lands[[All, All, 3]]];
zmin = Min[lands[[All, All, 3]]];
(*plots each of the individual procrustes aligned shapes*)

individualshapes =
  Table[Graphics3D[
    GraphicsComplex[lands[[All, i]], Polygon[connectivity]],
    PlotRange -> {{xmin, xmax}, {ymin, ymax}, {zmin, zmax}}], {i, 1,
    Length[procrustesshapes]}];
(*Polygon[connectivity] for 3D and Line[connectivity] for 2D shapes*)

(*generates the graphics object of the mean procustes shape*)
averageshape =
  Graphics3D[
   GraphicsComplex[Partition[meanshape, 3], Polygon[connectivity]],
   PlotRange -> {{xmin, xmax}, {ymin, ymax}, {zmin, zmax}}];

(*Exporting the Procrustes shapes.*)
Do[Export[
   StringJoin[outputdirectory,
    StringJoin[studyname, "_procrustes", ToString[i], ".vtk"]],
   individualshapes[[i]]], {i, 1, Length[individualshapes]}];

(*Exporting the average Procrustes shape.*)
Export[StringJoin[outputdirectory, studyname, "_average.vtk"],
  averageshape];
```

A.3 Principal Component Analysis and Determination of Significant Modes

A.3.1 Principal Component Analysis

This principal component analysis (PCA) is performed on the residuals (distances between each shape and the mean shape) but you get the same eigenvectors and eigenvalues if you perform the PCA on the Procrustes aligned shape coordinates.

```
residuals = # - meanshape & /@ procrustesshapes;
(*x,y, and z differences between the mean shape and each subject*)

pca = PrincipalComponents[residuals];
covar = Covariance[residuals];

eigenvalues = Variance[pca];
eigenvalues[[
 1 ;; Length[individualshapes]]](*displaying the eigenvalues*)

percentvariation = eigenvalues/Plus @@ eigenvalues;
percentvariation[[ 1 ;; Length[individualshapes]]]
(*displaying the variance as percent of total shape variance*)

eigenvectors =
  Eigenvectors[Covariance[residuals], Length[individualshapes]];
```

A.3.2 Parallel Analysis to Determine Significant Modes

```
(*This cell can take hours to run for large datasets.*)

AbsoluteTiming[(*timing how long the calculations in this cell take in real time*)
  its = 10000;(*assigning number of iterations*)

  mcpercentvariation = {};(*resetting the variable*)

  mcpercentvariation =
   Reap[(*to save all values within Sow functions outside of the loop*)

        Do[(*To iterate thousands of times*)
      (*Selecting random values within a multivariate, unit normal distribution.*)
      modepts =
       RandomVariate[
        MultinormalDistribution[
         ConstantArray[0, Length[individualshapes]],
         IdentityMatrix[Length[individualshapes]]],
        Length[meanshape]];
      newresiduals = Transpose[modepts];
      (*Running a PCA for each iteration.*)

      newpca = PrincipalComponents[newresiduals];
      newcovar = Covariance[newresiduals];
      neweigenvalues = Variance[newpca];
      newpercentvariation = neweigenvalues/Plus @@ neweigenvalues;
      (*Saving the percent variance values from each iteration.*)

      Sow[newpercentvariation[[1 ;; Length[individualshapes]]]];
      , {i, 1, its}]];
  Mean[mcpercentvariation[[2]][[1]][[1 ;;]]] // MatrixForm];
```

This generates the scree plot that visualizes the noise of the dataset compared to the original PCA (Figure **??**).

```
ListLinePlot[{Mean[mcpercentvariation[[2]][[1]]][[
   1 ;; Length[individualshapes] - 1]],
  percentvariation[[1 ;; Length[individualshapes] - 1]]},
 PlotLegends ->
  Placed[{"Monte Carlo Gaussian Noise", "Original Data"}, Center],
 PlotStyle -> {{Blend[{Blue, Cyan}, 0.5],
    Thickness[0.0075]}, {Blend[{Red, Pink}, 0.5], Thickness[0.0075]}},
  PlotMarkers -> {Automatic, Offset[10]}, PlotRange -> All,
 AxesLabel -> {"Mode", "Percent of the Total Variance"},
 AxesStyle -> Directive[Black, 18],
 TicksStyle -> Directive[Black, 18],
 LabelStyle -> Directive[Black, 18], PlotLabel -> "Scree Plot",
 PlotMarkers -> Automatic , ImageSize -> Large]
```

This generates a zoomed in version of the scree plot so that you only see the first 15 modes of variation (Figure A2).

```
ListLinePlot[{Mean[mcpercentvariation[[2]][[1]]][[1 ;; 15]],
  percentvariation[[1 ;; 15]]},
 PlotLegends ->
  Placed[{"Monte Carlo Gaussian Noise", "Original Data"}, Center],
 PlotStyle -> {{Blend[{Blue, Cyan}, 0.5],
    Thickness[0.0075]}, {Blend[{Red, Pink}, 0.5], Thickness[0.0075]}},
  PlotMarkers -> {Automatic, Offset[10]}, PlotRange -> All,
 AxesLabel -> {"Mode", "Percent of the Total Variance"},
 AxesStyle -> Directive[Black, 18],
 TicksStyle -> Directive[Black, 18],
```

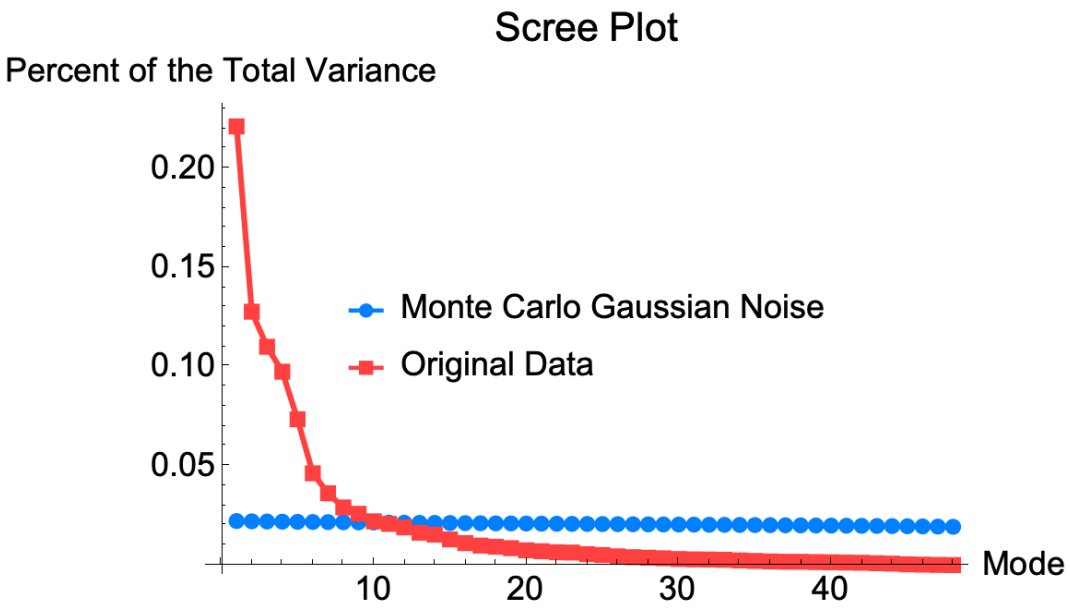

Figure A1: The scree plot that visualizes the results of the parallel analysis which determines the number of significant modes of variation.

```
 LabelStyle -> Directive[Black, 18], PlotLabel -> "Scree Plot",
 PlotMarkers -> Automatic , ImageSize -> Large]


noisedifference =
  Mean[mcpercentvariation[[2]][[1]]][[
    1 ;; Length[individualshapes] - 1]] -
   percentvariation[[1 ;; Length[individualshapes] - 1]];
sigmodes = FirstPosition[noisedifference, n_ /; n > 0] - 1 ;
sigmodes = sigmodes[[1]]
(*finding where on the scree plot the noise surpasses the data to \
determine the number of significant modes*)
```

A.3.3 Principal Component Score Calculation and File Export

```
(*calculating PCA scores = original data projected onto eigenvectors of significant modes of variation*)
pcscores = residuals.Transpose[eigenvectors[[1 ;; sigmodes, ;;]]];

(*Export variables to CSV file for external statistical or other analyses.*)

Export[
 StringJoin[outputdirectory, studyname, "_PCAscores",
  ".csv"], pcscores](*PC scores are used for subsequent statistics*)


(*To export the PC scores for all of the modes of variation, not just the significant ones.*)
allpcascores = residuals.Transpose[eigenvectors];
Export[StringJoin[outputdirectory, studyname, "_allPCAscores",
  ".csv"], allpcscores]
```

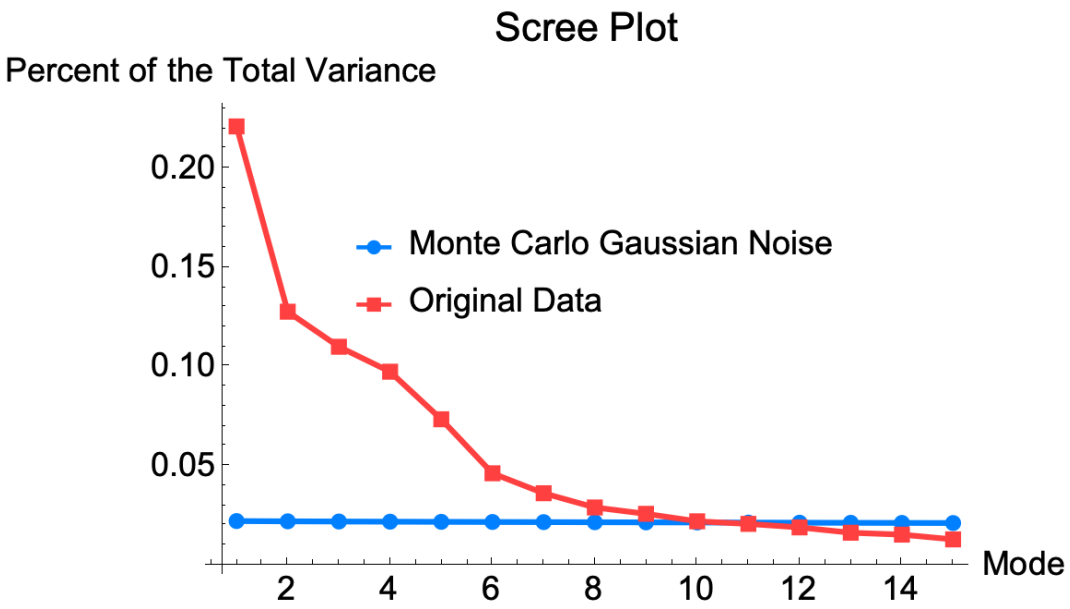

Figure A2: The zoomed in version of the scree plot that visualizes the results of the parallel analysis which determines the number of significant modes of variation.

A.4 Mode Visualizations

A.4.1 View and Boundaries to Establish Mode Figures and Animations

Manually alter values to generate figures and videos from different views (e.g., axial, coronal, sagittal, etc.). Example numerical values have been left in the definition of plotrangevalues, rotdeg1, rotang1, rotdeg2, rotang2, and view.

```
plotrangevalues = {{1.2*xmin, 1.2*xmax}, {1.3*ymin, 1.6*ymax}, {2.2*zmin, 2.2*zmax}};(*to set PlotRange*)
rotdeg1 = 90; rotang1 = {0, 0, 1}; rotdeg2 = -120; rotang2 = {0, 1, 0};(*to set Rotate*)
view = {Infinity, 0, 0};(*to set ViewPoint*)

(*The following computes the specified number of standard deviations from the mean for each mode.*)
std = 3;
(*define the number of standard deviations from the mean you want to include in your model deviation*)
(*If you change this you have to change many other visualization settings
as this is assumed when generating figures.*)

modedev =
  Table[std*Sqrt[eigenvalues[[i]]], {i, 1,
    Length[individualshapes] - 1}];
(*calculates the deviations along each mode of variation*)
```

The following generates and outputs the gray–scale figures and videos.

```
PCmodePts =
```

```
  Table[Table[
    Partition[x*Flatten[eigenvectors[[m]]] + meanshape,
     3], {x, -modedev[[m]], modedev[[m]], 2*modedev[[m]]/18}], {m, 1,
    sigmodes}];

PCmodeptsfigs =
  Table[Table[
    Graphics3D[{White, Thickness[0.01],
      Rotate[Rotate[
        GraphicsComplex[PCmodePts[[m]][[i]], Polygon[connectivity]],
        rotdeg1 Degree, rotang1], rotdeg2 Degree, rotang2]},
     PlotRange -> plotrangevalues, ViewPoint -> view,
     Background -> White, Lighting -> "Neutral"], {i, 1,
     Length[PCmodePts[[m]]]}], {m, 1, sigmodes}];

(*Exports these figures as separate images.*)
Do[
  Do[
   Export[
    StringJoin[outputdirectory,
     StringJoin[studyname, "_Mode", ToString[m], "Fig", ToString[i],
      ".tif"]], PCmodeptsfigs[[m, i]], ImageResolution -> 500],
   {i, 1, Length[PCmodeptsfigs[[m]]], 3}],
  {m, 1, sigmodes}];
```

A.4.2 Locally and Globally Scaled Color Figures and Videos

```
(*Calculating the distance from points on each shape along each significant mode to
corresponding points on the mean shape.*)

modedisps =
  Table[Table[
    EuclideanDistance[PCmodePts[[m]][[j]][[i]],
     Partition[meanshape, 3][[i]]], {i, 1, Length[lands]}, {j, 1,
     Dimensions[PCmodePts[[m]]][[1]]}], {m, 1, sigmodes}];

(*Scaling the displacements separately based on the max of each mode so a color map
can be defined from 0 to 1.*)
{*This will be referred to as local scaling.}
scaledmodedisps =
  Table[modedisps[[m]]/Max[modedisps[[m]]], {m, 1, sigmodes}];

(*Scaling the displacements globally based on the total max so a color map can be defined from 0 to 1.*)
(*This will be referred to as global scaling.}
globalscaledmodedisps =
  Table[modedisps[[m]]/Max[modedisps], {m, 1, sigmodes}];

(*Creating color spectrum to be mapped onto the shapes.*)
(*Left color = 0 displacement and Right color = Max displacement*)

mapcolors = {Black, Blue, Cyan, Green, Yellow, White}; (*blue green yellow spectrum*)

(*Creating locally scaled color shapes.*)

modeconnectivitylines = Table[Table[
    Style[Polygon[connectivity[[i]]],
     Blend[mapcolors,
      Mean[scaledmodedisps[[m]][[connectivity[[i]], j]]]]],
    {i, 1, Length[connectivity]}, {j, 1, Length[PCmodePts[[m]]]}], {m,
     1, sigmodes}];

modecolorfigs = Table[Table[
    Graphics3D[{Thickness[0.01], EdgeForm[],
      Rotate[Rotate[
        GraphicsComplex[PCmodePts[[m]][[i]],
```

```
        modeconnectivitylines[[m]][[All, i]]], rotdeg1 Degree,
       rotang1], rotdeg2 Degree, rotang2]},
    PlotRange -> plotrangevalues, ViewPoint -> view,
    Background -> White, ImageSize -> Large,
    Lighting -> {{"Directional", White, {1, 0, 0}}, {"Ambient",
       GrayLevel[0.5]}}],
   {i, 1, Length[PCmodePts[[m]]], 3}], {m, 1, sigmodes}];

(*Exporting these figures as individual images.*)
Do[
  Do[
   Export[
    StringJoin[outputdirectory,
     StringJoin[studyname, "_Mode", ToString[m], "Fig", ToString[i],
      "Colored", ".tif"]], modecolorfigs[[m, i]],
    ImageResolution -> 500],
   {i, 1, Length[modecolorfigs[[m]]]}],
  {m, 1, sigmodes}];

(*Creating globally scaled colored shapes.*)
globalmodeconnectivitylines = Table[Table[
    Style[Polygon[connectivity[[i]]],
     Blend[mapcolors,
      Mean[globalscaledmodedisps[[m]][[connectivity[[i]], j]]]]],
    {i, 1, Length[connectivity]}, {j, 1, Length[PCmodePts[[m]]]}], {m,
     1, sigmodes}];
globalmodecolorfigs = Table[Table[
    Graphics3D[{Thickness[0.01], EdgeForm[],
      Rotate[Rotate[
        GraphicsComplex[PCmodePts[[m]][[i]],
         globalmodeconnectivitylines[[m]][[All, i]]], rotdeg1 Degree,
        rotang1], rotdeg2 Degree, rotang2]},
     PlotRange -> plotrangevalues, ViewPoint -> view,
     Background -> None, ImageSize -> Large,
     Lighting -> {{"Directional", White, {1, 0, 0}}, {"Ambient",
        GrayLevel[0.5]}}],
    {i, 1, Length[PCmodePts[[m]]], 3}], {m, 1, sigmodes}];

(*Exporting these figures as individual images.*)
Do[
  Do[
   Export[
    StringJoin[outputdirectory,
     StringJoin[studyname, "_Mode", ToString[m], "Fig", ToString[i],
      "GlobalColor", ".tif"]], globalmodecolorfigs[[m, i]],
    ImageResolution -> 500],
   {i, 1, Length[globalmodecolorfigs[[m]]]}],
  {m, 1, sigmodes}];

(*Generating and exporting videos.*)
globalmodecolorfigsfull = Table[Table[
    Graphics3D[{Thickness[0.015], EdgeForm[],
      Rotate[Rotate[
        GraphicsComplex[PCmodePts[[m]][[i]],
         globalmodeconnectivitylines[[m]][[All, i]]], rotdeg1 Degree,
        rotang1], rotdeg2 Degree, rotang2]},
     PlotRange -> plotrangevalues, ViewPoint -> view,
     Background -> Gray],
    {i, 1, Length[PCmodePts[[m]]]}], {m, 1, sigmodes}];

PCmodecolorlistani =
  Table[ListAnimate[globalmodecolorfigs[[m]], 10,
    AnimationDirection -> ForwardBackward], {m, 1, sigmodes}];

Do[
 Export[StringJoin[outputdirectory, studyname, "Mode", ToString[m],
    "Color", ".mov"], PCmodecolorlistani[[m]], "FrameRate" -> 10];
 , {m, 1, sigmodes}]
```

A.5 Principal Component Score Visualizations

```
You shouldn't need to alter the following parameters.

(*Defining scaling term for figure spacing.*)
scaleterm = modedev[[1]]/3;

(*Creating tick marks at the standard deviations.*)

modestdpoints =
  Table[Table[{(modedev[[m]]/3)*i, (m - 1)*-scaleterm}, {i, -std, std}], {m,
    1, sigmodes}];
tickmark = Graphics[{Thickness[0.05], Black, Line[{{0, 0.75}, {0, -0.75}}]}];
tickmarkfig =
  Table[ListPlot[modestdpoints[[m]], PlotMarkers -> {tickmark, 0.02}], {m, 1,
    sigmodes}];

(*Main vertical line.*)

mainlinefig =
  Graphics[{Thin, Black,
    Line[{{0,
       scaleterm/2}, {0, ((sigmodes - 1)*-scaleterm) - (scaleterm/2)}}]},
   ImageSize -> Full, Background -> White];

(*Creating the +/- std lines for each mode.*)

modelinesfig =
  Table[Graphics[{Thin, Black,
     Line[{{-modedev[[m]], (m - 1)*-scaleterm}, {modedev[[
         m]], (m - 1)*-scaleterm}}]}], {m, 1, sigmodes}];


Change the following depending on the number and organization of your groups.
I left previous manual group definitions in this example.

(*Labelling scores according to groups/variables of interest.*)(*User needs to edit.*)
group1 =
  Table[Partition[
    Riffle[pcascores[[(**)1 ;; 17(**), m]], (m - 1)*-scaleterm, {2, -1, 2}],
    2], {m, 1, sigmodes}]; (*parous*)

group2 = Table[
   Partition[
    Riffle[pcascores[[(**)18 ;; 34(**), m]], (m - 1)*-scaleterm, {2, -1, 2}],
    2], {m, 1, sigmodes}]; (*pregnant*)

group3 = Table[
   Partition[
    Riffle[pcascores[[(**)35 ;; 49(**), m]], (m - 1)*-scaleterm, {2, -1, 2}],
    2], {m, 1, sigmodes}]; (*parous*)

group1scores = Table[pcascores[[(**)1 ;; 17(**), m]], {m, 1, sigmodes}];
group2scores = Table[pcascores[[(**)18 ;; 34(**), m]], {m, 1, sigmodes}];
group3scores = Table[pcascores[[(**)35 ;; 49(**), m]], {m, 1, sigmodes}];
(*Partition and Riffle create coordinates out of the scores for figure making purposes.
The (m-1)*200 staggers the y value so each mode has its own row.*)

(*Converting data into list point plots for figures and assigning colors.*)(*User needs to edit.*)

color1 = Blend[{Red, White}, 0.1];
color2 = Blend[{Red, White}, 0.5];
color3 = Blend[{Red, White}, 0.9];

group1fig =
  Table[ListPlot[group1[[m]], PlotStyle -> {PointSize[0.01], color1}], {m, 1,
```

```
    sigmodes}];
group2fig =
  Table[ListPlot[group2[[m]], PlotStyle -> {PointSize[0.01], color2}], {m, 1,
    sigmodes}];
group3fig =
  Table[ListPlot[group3[[m]], PlotStyle -> {PointSize[0.01], color3}], {m, 1,
    sigmodes}];

grouppointsfig = {group1fig, group2fig, group3fig};

Show[mainlinefig, grouppointsfig, tickmarkfig, modelinesfig]
```

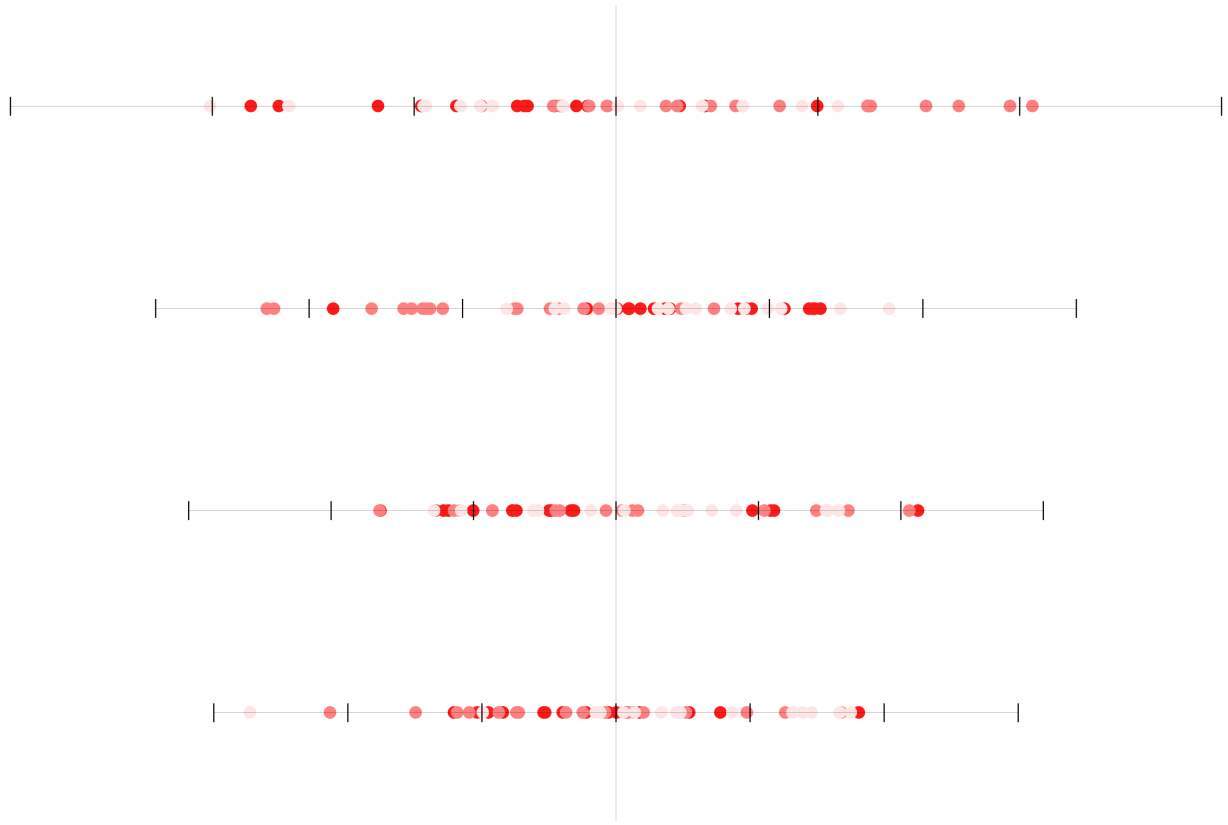

Figure A3: An example of a principal component score visualization before labels and images of corresponding shapes are added. The black vertical tick marks indicate standard deviations from the mean along each mode of variation (in this case there are 4). The dots represent the principal component scores and they are color coded based on manually assigned groups of interest. This makes it easy to determine where the data lies with respect to the standard deviations. Examples of where this type of visualization is used can be found in Figures 3.4, 3.6, 5.5, 5.6, and 5.7.

A.6 Combining Modes of Variation to Generate New Shapes

This section of code is currently formatted to accommodate 10 significant modes of variation, but can be manually edited to incorporate any number of modes. This manipulate appears in Figure 2.5. It is very similar to the code used to generate shapes along each mode, but hear the results of each mode are added together so that all modes can be altered/sampled simultaneously.

```
(*This manipulate allows you to select specific PC scores for each mode
and see and export the resulting shape.*)

Off[
 ViewPoint::nlist3](*to suppress the ViewPoint error message after exporting the shape*)

Manipulate[
 {newshape = Graphics3D[Rotate[Rotate[GraphicsComplex[Partition[
        (Mode1Score*Flatten[eigenvectors[[1]]] +
           Mode2Score*Flatten[eigenvectors[[2]]] +
           Mode3Score*Flatten[eigenvectors[[3]]] +
           Mode4Score*Flatten[eigenvectors[[4]]] +
           Mode5Score*Flatten[eigenvectors[[5]]] +
           Mode6Score*Flatten[eigenvectors[[6]]] +
           Mode7Score*Flatten[eigenvectors[[7]]] +
           Mode8Score*Flatten[eigenvectors[[8]]] +
           Mode9Score*Flatten[eigenvectors[[9]]] +
           Mode10Score*Flatten[eigenvectors[[10]]]) + meanshape, 3],
       Polygon[connectivity]], rotdeg1 Degree, rotang1],
     rotdeg2 Degree, rotang2], PlotRange -> plotrangevalues,
    ViewPoint -> view, ImageSize -> Large]},
 {{Mode1Score, 0}, modestdpoints[[1]][[1]][[1]],
  modestdpoints[[1]][[7]][[1]], 0.0001},
 {{Mode2Score, 0}, modestdpoints[[2]][[1]][[1]],
  modestdpoints[[2]][[7]][[1]], 0.0001},
 {{Mode3Score, 0}, modestdpoints[[3]][[1]][[1]],
  modestdpoints[[3]][[7]][[1]], 0.0001},
 {{Mode4Score, 0}, modestdpoints[[4]][[1]][[1]],
  modestdpoints[[4]][[7]][[1]], 0.0001},
 {{Mode5Score, 0}, modestdpoints[[5]][[1]][[1]],
  modestdpoints[[5]][[7]][[1]], 0.0001},
 {{Mode6Score, 0}, modestdpoints[[6]][[1]][[1]],
  modestdpoints[[6]][[7]][[1]], 0.0001},
 {{Mode7Score, 0}, modestdpoints[[7]][[1]][[1]],
  modestdpoints[[7]][[7]][[1]], 0.0001},
 {{Mode8Score, 0}, modestdpoints[[8]][[1]][[1]],
  modestdpoints[[8]][[7]][[1]], 0.0001},
 {{Mode9Score, 0}, modestdpoints[[9]][[1]][[1]],
  modestdpoints[[9]][[7]][[1]], 0.0001},
 {{Mode10Score, 0}, modestdpoints[[10]][[1]][[1]],
  modestdpoints[[10]][[7]][[1]], 0.0001},
 Row[{Spacer[140],
   Button["Export Shape",
    Export[StringJoin[outputdirectory, studyname, "_NewShape.vtk"],
     newshape], Method -> "Queued"]}]]
```

Appendix B : Latin Hypercube Sampling and Partial Ranked Correlation Coefficients

This Latin hypercube sampling was implemented in Matlab™ and based on the methods described by Feola et. al. [66].

```
%Reads in ranked LHS results to obtain PRCCs
%When ranking in Excel, use Rank(value, full list of values, 1)
%--the 1 ensures that the highest value is given the largest rank
%and the lowest value is given a rank of 1.

%% Inputs and Importing Data

%Input the file name
% The ranked data should be organized with each LHS trial as a row
%and each column as an input and then the output columns

filename='FILEPATH TO EXCEL FILE WITH RANKS';

%Input the number of the Excel sheet and the range of just the
%rank values (not column/row labels) within that sheet
sheet=3;
range='RANGE';

%This imports that data
lhsdata=xlsread(filename,sheet,range);

%To distinguish the input rows from the output rows, give the number of
%inputs and outputs being analyzed
numinputs=NUMBER_OF_INPUTS;
numoutputs=NUMBER_OF_OUTPUTS;

%% Running Partial Rank Correlations
%This organizes the data into a matrix of input ranks and a matrix of
%output ranks
inputmatrix=lhsdata(:,1:numinputs);
outputmatrix=lhsdata(:,numinputs+1:numinputs+numoutputs);

%This runs the Partial Ranked Correlation and gives you a matrix where
%each row is an input variable and each column an output variable
[rho,pval]=partialcorri(outputmatrix,inputmatrix,'Type','Spearman');

%Formatting to match Excel table
rho=transpose(rho);
pval=transpose(pval);
```

Appendix C : Passive Urethral Closure LHS–PRCC Data

The most prominent relationships between ultrasound variables that significantly differed between women with and without SUI listed in Table C1 are also demonstrated visually in Figure 3.11 (see Section 3.3). Here we also list the Latin hypercube sampling and partial ranked correlation coefficient related data for all 50 simulations of urethral passive closure (Tables C2, C3, and C4).

Table C1: Partial rank correlation coefficients (PRCCs) and their p-values (in parentheses) for the rest to peak Valsalva differences in those variables found to significantly differ with SUI severity in Part 1 (Section 3.2) [166]. This table was reprinted by permission from The International Urogynecological Association: Springer; International Urogynecology Journal; Megan R Routzong, Liam C Martin, Ghazaleh Rostaminia, and Steven D Abramowitch. Urethral support in female urinary continence part 2: a computational, biomechanical analysis of Valsalva. *International Urogynecology Journal*, 2021;

	Infrapubic Urethral Length	**Retropubic Bladder Neck Angle**	**Urethral Knee–Pubic Bone angle**
Urethral Stiffness	**0.656 (<0.001)**	**-0.481 (0.001)**	**0.638 (<0.001)**
Perineal Membrane Stiffness	**-0.443 (0.003)**	**-0.388 (0.010)**	-0.197 (0.206)
Paraurethral Connective Tissue Stiffness	**-0.400 (0.008)**	**-0.589 (<0.001)**	**-0.625 (<0.001)**
Bladder Stiffness	**0.320 (0.037)**	**-0.814 (<0.001)**	0.131 (0.401)
Space of Retzius Stiffness	0.133 (0.394)	0.102 (0.513)	0.207 (0.183)
Bladder Soft Constraint	-0.261 (0.091)	-0.280 (0.069)	0.048 (0.761)
Perineal Membrane Soft Constraint	**-0.680 (<0.001)**	-0.265 (0.086)	**-0.893 (<0.001)**
Trigone Factor	0.082 (0.602)	-0.047 (0.765)	0.014 (0.927)

Statistically significant PRCC and p–values ($p<0.05$) are shown in **bold**.

Table C2: Latin hypercube sampling (LHS) input values and their ranks for all 50 simulations [166]. This table was reprinted by permission from The International Urogynecological Association: Springer; International Urogynecology Journal; Megan R Routzong, Liam C Martin, Ghazaleh Rostaminia, and Steven D Abramowitch. Urethral support in female urinary continence part 2: a computational, biomechanical analysis of Valsalva. *International Urogynecology Journal*, 2021; © 2021 The International Urogynecological Association.

		Urethra Stiffness		Perineal Membrane Stiffness		Paraurethral Connective Tissue Stiffness		Bladder Stiffness		Space of Retzius Stiffness		Bladder Soft Constraint		Perineal Membrane Soft Constraint		Trigone Factor	
LHS Iteration	Trial	Young's (kPa)	Rank	Young's (kPa)	Rank	Young's (kPa)	Rank	Young's (kPa)	Rank	Young's (kPa)	Rank	Parameter	Rank	Parameter	Rank	Parameter	Rank
1	1	1762	50	1065	26	573	16	369	41	2.6	28	0.08	15	12.1	14	8.9	43
1	2	420	6	361	7	1215	44	417	46	3.2	35	0.04	6	44.8	45	9.1	45
1	3	1291	35	1447	37	1350	48	259	26	2.5	25	0.25	50	9.3	10	4.3	22
1	4	1630	45	929	24	1132	39	105	10	0.7	3	0.02	2	45.7	46	2.0	10
1	5	952	24	1674	45	749	22	231	24	2.1	20	0.16	31	31.3	31	2.8	15
1	6	1053	26	161	3	473	11	311	32	1.1	8	0.13	26	27.6	28	0.9	4
1	7	258	1	1791	48	291	5	56	3	1.4	12	0.10	20	17.2	18	5.4	28
1	8	1442	40	651	16	835	26	191	19	3.4	36	0.19	37	3.3	4	2.8	14
1	9	540	11	536	12	968	33	123	12	4.2	48	0.20	42	23.1	24	9.6	47
1	10	754	17	1347	35	351	6	354	37	3.7	41	0.11	22	38.3	39	6.6	32
2	11	1336	36	244	5	1172	41	134	14	3.5	38	0.18	36	48.5	50	8.4	40
2	12	1720	48	568	13	368	8	315	33	2.6	27	0.21	43	32.0	32	2.8	16
2	13	1272	33	406	9	608	19	48	1	1.1	7	0.14	28	2.0	2	8.4	40
2	14	488	8	1558	41	680	21	434	48	4.1	46	0.06	9	44.0	43	4.5	23
2	15	1096	28	1288	33	872	28	102	9	2.4	24	0.11	21	20.0	20	9.9	50
2	16	600	13	1882	50	512	14	282	29	0.9	5	0.07	12	35.5	36	6.4	31
2	17	920	22	1162	29	272	3	163	16	3.2	34	0.02	1	5.5	6	5.3	26
2	18	840	20	1504	38	1376	49	356	38	1.6	13	0.10	19	11.0	12	0.8	2
2	19	328	5	658	17	944	32	401	45	2.1	19	0.24	46	26.0	27	7.2	35
2	20	1608	44	964	25	1040	36	225	22	3.8	42	0.16	32	23.5	25	1.7	9
3	21	1352	37	1126	28	584	17	130	13	3.0	32	0.10	17	16.5	17	8.3	39
3	22	616	15	1846	49	788	25	438	49	1.7	15	0.17	33	21.0	21	2.6	12
3	23	824	19	1630	43	500	12	85	7	1.4	11	0.22	45	37.0	38	5.7	29
3	24	1544	41	604	14	212	1	282	29	2.8	29	0.11	23	47.0	47	4.9	24
3	25	984	25	136	1	1100	37	372	42	3.8	43	0.05	7	10.0	11	1.0	5
3	26	264	2	424	10	884	29	192	20	1.0	6	0.24	48	4.5	5	7.2	35
3	27	1272	33	1360	36	1388	50	364	40	2.3	21	0.03	3	6.5	9	6.9	33
3	28	1672	47	838	21	980	34	52	2	0.9	4	0.15	30	42.0	42	1.1	7
3	29	1080	27	766	18	1196	43	315	33	3.5	39	0.19	38	28.0	29	9.3	46
3	30	488	8	1270	31	356	7	237	25	4.1	47	0.07	11	34.5	33	3.4	17
4	31	1560	43	154	2	368	8	438	49	2.5	26	0.20	39	15.5	16	7.6	38
4	32	776	18	820	20	584	17	134	14	4.2	49	0.14	29	5.5	6	3.5	18
4	33	520	10	1108	27	1100	37	81	6	3.1	33	0.24	47	23.0	23	9.8	49

4	34	1256	32	1342	34	1316	46	266	28	0.6	1	0.17	33	36.0	37	9.0	44
4	35	1656	46	622	15	860	27	61	4	2.3	23	0.10	17	25.5	26	0.8	2
4	36	312	4	1504	38	272	3	319	35	1.7	15	0.08	13	47.5	48	4.1	20
4	37	1416	38	352	6	752	23	393	44	3.5	39	0.05	8	1.5	1	5.1	25
4	38	952	23	856	23	1232	45	360	39	1.3	10	0.03	3	35.0	35	2.1	11
4	39	1128	30	1576	42	524	15	225	22	1.7	14	0.22	44	11.0	12	1.3	8
4	40	600	13	1756	46	932	31	179	18	3.8	44	0.13	25	44.5	44	6.2	30
5	41	1544	41	208	4	1028	35	294	31	4.3	50	0.24	48	40.5	41	4.2	21
5	42	904	21	1774	47	1148	40	212	21	2.8	30	0.20	39	34.5	33	9.6	48
5	43	1192	31	1180	30	428	10	339	36	1.2	9	0.20	41	21.5	22	7.2	35
5	44	1752	49	1666	44	608	19	175	17	4.0	45	0.09	16	3.0	3	8.8	42
5	45	1416	38	496	11	260	2	122	11	1.7	15	0.06	9	28.5	30	3.6	19
5	46	1112	29	1522	40	1340	47	261	27	0.6	2	0.03	5	19.0	19	0.5	1
5	47	728	16	388	8	1172	41	372	42	3.5	37	0.08	13	6.0	8	2.7	13
5	48	456	7	1270	31	500	12	69	5	2.3	21	0.13	27	12.5	15	1.0	5
5	49	296	3	802	19	764	24	430	47	1.8	18	0.17	35	47.5	48	6.9	33
5	50	568	12	838	21	908	30	97	8	3.0	31	0.13	24	38.5	40	5.3	26

Table C3: Latin hypercube sampling (LHS) output values and their ranks for all 50 simulations at peak Valsalva (PV) [166]. This table was reprinted by permission from The International Urogynecological Association: Springer; International Urogynecology Journal; Megan R Routzong, Liam C Martin, Ghazaleh Rostaminia, and Steven D Abramowitch. Urethral support in female urinary continence part 2: a computational, biomechanical analysis of Valsalva. *International Urogynecology Journal*, 2021; © 2021 The International Urogynecological Association.

		Urethral Length (cm)		Retropubic Bladder Neck Angle (degrees)		Retropubic Urethral Length (cm)		Bladder Neck–Pubic Bone Angle (degrees)		Meatus–Pubic Bone Angle (degrees)		Urethral Knee–Pubic Bone Angle (degrees)	
LHS Iteration	Trial	PV	Rank	PV	Rank	PV	Rank	PV	Rank	PV	Rank	PV	Rank
1	1	4.48	39	78.9	13	2.43	34	35.9	36	68.9	42	47.2	42
1	2	4.15	7	72.6	4	2.19	5	44.0	47	54.0	1	30.9	2
1	3	4.43	27	77.7	10	2.40	29	38.6	42	64.5	36	41.6	36
1	4	4.45	32	86.6	39	2.45	42	28.2	13	58.3	15	34.5	13
1	5	4.25	16	81.7	23	2.32	14	33.2	31	60.4	25	36.9	22
1	6	4.43	27	80.1	18	2.39	25	34.9	33	61.1	28	39.9	31
1	7	4.23	11	94.6	50	2.30	13	19.0	1	59.0	18	35.9	16
1	8	4.52	43	83.1	26	2.45	42	31.6	26	74.3	46	52.9	47
1	9	4.16	8	85.5	32	2.26	10	28.9	19	59.4	19	35.9	16
1	10	4.25	16	81.4	20	2.29	12	32.7	29	60.0	23	36.9	22
2	11	4.44	31	82.9	25	2.43	34	32.2	27	58.0	14	35.6	15
2	12	4.45	32	81.6	22	2.43	34	32.5	28	63.7	33	41.3	33
2	13	4.64	50	88.5	44	2.52	48	25.8	8	74.5	47	52.8	46
2	14	4.11	5	76.6	7	2.19	5	38.9	43	56.2	5	33.0	7
2	15	4.37	24	86.1	37	2.39	25	28.3	15	62.6	31	39.2	29
2	16	4.14	6	82.7	24	2.21	7	31.3	25	59.8	21	36.7	21
2	17	4.51	41	93.3	49	2.42	32	20.0	2	77.0	50	57.4	50
2	18	4.35	22	71.7	2	2.34	18	45.7	49	61.0	26	38.1	27
2	19	4	2	79.7	17	2.11	3	35.8	34	57.1	9	33.9	9
2	20	4.45	32	79.0	14	2.43	34	37.0	38	61.9	30	39.1	28
3	21	4.45	32	86.9	42	2.43	34	27.3	10	66.9	39	44.3	39
3	22	4.18	10	77.3	9	2.25	9	39.0	44	60.0	23	37.0	24
3	23	4.34	20	90.6	45	2.39	25	23.5	5	59.9	22	36.2	18
3	24	4.43	27	84.3	29	2.42	32	29.3	22	62.7	32	39.6	30
3	25	4.51	41	86.7	41	2.44	39	26.5	9	69.6	44	50.1	44
3	26	4.08	3	85.8	36	2.10	2	27.9	12	67.5	40	45.3	41
3	27	4.47	37	72.2	3	2.41	31	44.6	48	65.0	37	42.3	38
3	28	4.58	48	85.5	32	2.96	50	28.8	18	56.4	6	32.1	5
3	29	4.34	20	76.4	6	2.36	21	39.5	45	59.6	20	36.2	18
3	30	4.24	13	85.4	31	2.27	11	28.2	13	58.9	17	35.1	14
4	31	4.62	49	76.6	7	2.49	46	38.1	41	61.4	29	41.5	34
4	32	4.38	25	88.3	43	2.36	21	25.3	7	73.7	45	52.2	45
4	33	4.24	13	86.6	39	2.33	17	28.3	15	57.9	12	34.2	11
4	34	4.35	22	78.5	12	2.38	23	37.5	40	57.8	11	34.3	12
4	35	4.54	46	85.5	32	2.50	47	29.1	20	61.0	26	37.6	26
4	36	4.17	9	86.2	38	2.17	4	27.3	10	54.5	2	30.0	1
4	37	4.57	47	79.4	16	2.45	42	36.0	37	75.6	48	55.6	48
4	38	4.31	19	73.6	5	2.34	18	43.7	46	57.2	10	33.9	9
4	39	4.4	26	83.9	27	2.38	23	30.3	23	69.1	43	47.3	43
4	40	4.08	3	84.1	28	2.23	8	30.4	24	56.7	8	32.8	6
5	41	4.48	39	78.0	11	2.44	39	37.4	39	58.5	16	37.0	24
5	42	4.24	13	81.4	20	2.32	14	34.0	32	57.9	12	36.3	20
5	43	4.43	27	81.2	19	2.40	29	33.1	30	63.9	35	41.5	34
5	44	4.53	44	85.2	30	2.45	42	29.2	21	76.4	49	55.9	49
5	45	4.47	37	91.8	48	2.44	39	22.0	3	67.5	40	44.7	40
5	46	4.53	44	61.1	1	2.84	49	57.6	50	56.5	7	33.8	8
5	47	4.45	32	90.7	46	2.39	25	23.6	6	65.5	38	41.8	37
5	48	4.23	11	91.3	47	2.32	14	22.6	4	63.7	33	40.6	32
5	49	3.97	1	79.1	15	2.08	1	35.8	34	55.1	3	31.6	3
5	50	4.25	16	85.7	35	2.34	18	28.4	17	55.9	4	31.6	3

Table C4: Latin hypercube sampling (LHS) output values and their ranks for all 50 simulations at peak Valsalva (PV) [166]. This table was reprinted by permission from The International Urogynecological Association: Springer; International Urogynecology Journal; Megan R Routzong, Liam C Martin, Ghazaleh Rostaminia, and Steven D Abramowitch. Urethral support in female urinary continence part 2: a computational, biomechanical analysis of Valsalva. *International Urogynecology Journal*, 2021; © 2021 The International Urogynecological Association.

		Mode 1		Mode 2		Mode 3		Mode 4	
LHS Iteration	Trial	PV	Rank	PV	Rank	PV	Rank	PV	Rank
1	1	0.012	26	-0.043	8	-0.002	22	-0.002	28
1	2	0.013	29	0.017	34	-0.028	8	-0.013	15
1	3	-0.062	13	-0.028	14	-0.005	16	-0.021	8
1	4	-0.195	2	0.022	37	0.003	26	0.019	43
1	5	-0.015	21	0.011	31	-0.003	20	0.016	39
1	6	0.002	25	-0.001	22	0.009	35	0.072	50
1	7	0.139	46	0.060	50	0.054	49	-0.064	1
1	8	-0.029	19	-0.046	5	0.000	25	-0.024	6
1	9	-0.051	16	0.045	47	0.008	34	0.019	42
1	10	0.091	43	0.010	30	-0.018	9	0.026	44
2	11	-0.143	4	0.024	38	0.013	40	0.008	33
2	12	-0.006	22	-0.008	19	0.014	42	0.038	47
2	13	-0.060	14	-0.046	4	0.015	43	-0.033	3
2	14	0.067	40	0.013	32	-0.049	3	0.013	37
2	15	-0.069	11	0.010	29	0.014	41	0.016	38
2	16	0.102	44	0.021	36	-0.028	7	0.008	34
2	17	0.148	47	-0.049	3	0.010	37	-0.027	4
2	18	-0.029	18	-0.029	13	-0.014	10	-0.020	9
2	19	0.025	31	0.028	40	-0.047	4	-0.018	11
2	20	-0.080	10	-0.012	17	0.003	28	-0.011	19
3	21	-0.001	23	-0.015	16	0.017	44	0.001	31
3	22	0.031	33	-0.009	18	-0.039	5	0.001	30
3	23	0.012	27	0.030	42	0.032	47	-0.004	26
3	24	0.028	32	0.005	26	0.024	46	0.040	48
3	25	0.038	35	-0.032	11	-0.004	18	0.068	49
3	26	0.061	39	0.007	28	-0.030	6	-0.034	2
3	27	-0.023	20	-0.045	6	-0.008	13	-0.023	7
3	28	-0.214	1	0.015	33	0.007	30	-0.018	12
3	29	-0.066	12	-0.003	21	-0.007	15	-0.015	13
3	30	0.178	48	0.036	43	0.000	24	0.011	36
4	31	0.012	28	-0.041	9	0.013	39	0.028	45
4	32	0.041	36	-0.033	10	-0.004	17	-0.009	21
4	33	-0.098	8	0.030	41	0.003	27	-0.026	5
4	34	-0.106	7	0.006	27	-0.003	21	-0.014	14
4	35	-0.149	3	0.001	23	0.009	36	-0.019	10
4	36	0.229	50	0.043	46	-0.053	2	-0.009	23
4	37	0.017	30	-0.065	1	-0.003	19	-0.013	16
4	38	-0.044	17	-0.005	20	-0.012	11	-0.006	24
4	39	0.059	38	-0.031	12	-0.001	23	-0.003	27
4	40	-0.054	15	0.047	49	-0.009	12	0.016	40
5	41	-0.112	6	0.005	25	0.008	33	0.000	29
5	42	-0.091	9	0.018	35	-0.007	14	-0.011	18
5	43	0.069	41	-0.022	15	0.007	31	0.030	46
5	44	0.037	34	-0.058	2	0.005	29	-0.005	25
5	45	0.045	37	0.003	24	0.035	48	0.005	32
5	46	0.109	45	-0.044	7	0.018	45	0.011	35
5	47	0.217	49	0.040	45	0.098	50	-0.012	17
5	48	0.002	24	0.024	39	0.012	38	-0.011	20
5	49	0.071	42	0.037	44	-0.062	1	-0.009	22
5	50	-0.122	5	0.045	48	0.007	32	0.017	41

Appendix D : Fetal Head and Perineal Body Angle of Progression Calculations

The following code was originally written in March of 2018 and developed/edited through October of 2018 in Mathematica^{TM}. The text was edited in January of 2019 for publishing purposes [167]. The specific code shown was used to compare two vaginal childbirth simulations: one that included and another that omitted the superficial perineal structures.

D.1 Importing Data

D.1.1 Importing from Excel File

```
(*Importing the Excel file where you copied and pasted the position \
values in the x, y, and z axes from PostView.*)

(*Copy/paste file path of the Excel file inside the " " below.*)
file = Import["Filepath"];
```

D.1.2 Organizing Data based on User Inputs

```
Omitted Time Data

(*Input the sheet of interest within the Excel file (as a number).*)

sheet = 1;

(*Input the rows and columns containing the data of interest.*)

rows = {2, 138}; (*First row, last row.*)
cols = 1;

(*Pulling out time data.*)

ndtime = Transpose[file[[sheet]]][[cols]][[rows[[1]] ;; rows[[2]]]];

Included Time Data

(*Input the sheet of interest within the Excel file (as a number).*)

sheet = 2;

(*Input the rows and columns containing the data of interest.*)

rows = {2, 111}; (*First row, last row.*)
cols = 1;

(*Pulling out x, y, and z data.*)

dtime = Transpose[file[[sheet]]][[cols]][[rows[[1]] ;; rows[[2]]]];
```

```
Omitted Fetal Head Path

(*Input the sheet of interest within the Excel file (as a number).*)

sheet = 1;

(*Input the rows and columns containing the data of interest.*)

xrows = {2, 138}; (*First row, last row.*)
yrows = xrows;
zrows = xrows;
xcols = 5;
ycols = 6;
zcols = 7;

(*Pulling out x, y, and z data.*)

xdata = Transpose[file[[sheet]]][[xcols]][[xrows[[1]] ;; xrows[[2]]]];
ydata = Transpose[file[[sheet]]][[ycols]][[yrows[[1]] ;; yrows[[2]]]];
zdata = Transpose[file[[sheet]]][[zcols]][[zrows[[1]] ;; zrows[[2]]]];

(*Combing as list of 3D coordinates.*)

ndpath = Partition[
   Append[Riffle[Riffle[xdata, ydata], zdata, 3], zdata[[Length[zdata]]]],
   3];
ndpath = ndpath*0.33;(* To convert from 0.33 mm units to mm. *)
(*The *0.33 \
converts from FEBio units to mm for the Visible Human Project Female Anatomy.*)

Included Fetal Head Path

(*Input the sheet of interest within the Excel file (as a number).*)

sheet = 2;

(*Input the rows and columns containing the data of interest.*)

xrows = {2, 111}; (*First row, last row.*)
yrows = xrows;
zrows = xrows;
xcols = 5;
ycols = 6;
zcols = 7;

(*Pulling out x, y, and z data.*)

xdata = Transpose[file[[sheet]]][[xcols]][[xrows[[1]] ;; xrows[[2]]]];
ydata = Transpose[file[[sheet]]][[ycols]][[yrows[[1]] ;; yrows[[2]]]];
zdata = Transpose[file[[sheet]]][[zcols]][[zrows[[1]] ;; zrows[[2]]]];

(*Combing as list of 3D coordinates.*)

dpath = Partition[
   Append[Riffle[Riffle[xdata, ydata], zdata, 3], zdata[[Length[zdata]]]],
   3];
dpath = dpath*0.33;(* To convert from 0.33 mm units to mm. *)

Omitted Perineal Body

(*Input the sheet of interest within the Excel file (as a number).*)

sheet = 1;

(*Input the rows and columns containing the data of interest.*)

xrows = {2, 138}; (*First row, last row.*)
yrows = xrows;
```

```
zrows = xrows;
xcols = 2;
ycols = 3;
zcols = 4;

(*Pulling out x, y, and z data.*)

xdata = Transpose[file[[sheet]]][[xcols]][[xrows[[1]] ;; xrows[[2]]]];
ydata = Transpose[file[[sheet]]][[ycols]][[yrows[[1]] ;; yrows[[2]]]];
zdata = Transpose[file[[sheet]]][[zcols]][[zrows[[1]] ;; zrows[[2]]]];

(*Combing as list of 3D coordinates.*)

ndpbpath =
  Partition[Append[Riffle[Riffle[xdata, ydata], zdata, 3],
    zdata[[Length[zdata]]]], 3];
ndpbpath = ndpbpath*0.33;(* To convert from 0.33 mm units to mm. *)

Included Perineal Body

(*Input the sheet of interest within the Excel file (as a number).*)

sheet = 2;

(*Input the rows and columns containing the data of interest.*)

xrows = {2, 111}; (*First row, last row.*)
yrows = xrows;
zrows = xrows;
xcols = 2;
ycols = 3;
zcols = 4;

(*Pulling out x, y, and z data.*)

xdata = Transpose[file[[sheet]]][[xcols]][[xrows[[1]] ;; xrows[[2]]]];
ydata = Transpose[file[[sheet]]][[ycols]][[yrows[[1]] ;; yrows[[2]]]];
zdata = Transpose[file[[sheet]]][[zcols]][[zrows[[1]] ;; zrows[[2]]]];

(*Combing as list of 3D coordinates.*)

dpbpath = Partition[
   Append[Riffle[Riffle[xdata, ydata], zdata, 3], zdata[[Length[zdata]]]],
   3];
dpbpath = dpbpath*0.33;(* To convert from 0.33 mm units to mm. *)

Right Pubic Symphysis

(*Input the sheet of interest within the Excel file (as a number).*)

sheet = 3;

(*Input the rows and columns containing the data of interest.*)

xrows = {15, 24}; (*First row, last row.*)
yrows = xrows;
zrows = xrows;
xcols = 1;
ycols = 4;
zcols = 7;

(*Pulling out x, y, and z data.*)

xdata = Transpose[file[[sheet]]][[xcols]][[xrows[[1]] ;; xrows[[2]]]];
ydata = Transpose[file[[sheet]]][[ycols]][[yrows[[1]] ;; yrows[[2]]]];
zdata = Transpose[file[[sheet]]][[zcols]][[zrows[[1]] ;; zrows[[2]]]];

(*Combing as list of 3D coordinates.*)
```

```
rps = Partition[
   Append[Riffle[Riffle[xdata, ydata], zdata, 3], zdata[[Length[zdata]]]],
   3];
rps = rps*0.33;
(* To convert from 0.33 mm units to mm. *)

Left Pubic Symphysis

(*Input the sheet of interest within the Excel file (as a number).*)

sheet = 3;

(*Input the rows and columns containing the data of interest.*)

xrows = {2, 11}; (*First row, last row.*)
yrows = xrows;
zrows = xrows;
xcols = 1;
ycols = 4;
zcols = 7;

(*Pulling out x, y, and z data.*)

xdata = Transpose[file[[sheet]]][[xcols]][[xrows[[1]] ;; xrows[[2]]]];
ydata = Transpose[file[[sheet]]][[ycols]][[yrows[[1]] ;; yrows[[2]]]];
zdata = Transpose[file[[sheet]]][[zcols]][[zrows[[1]] ;; zrows[[2]]]];

(*Combing as list of 3D coordinates.*)

lps = Partition[
   Append[Riffle[Riffle[xdata, ydata], zdata, 3], zdata[[Length[zdata]]]],
   3];
lps = lps*0.33;
(* To convert from 0.33 mm units to mm. *)

Right Ischial Spine

(*Input the sheet of interest within the Excel file (as a number).*)

sheet = 1;

(*Input the rows and columns containing the data of interest.*)

xrows = {26, 26}; (*First row, last row.*)
yrows = xrows;
zrows = xrows;
xcols = 1;
ycols = 4;
zcols = 7;

(*Pulling out x, y, and z data.*)

xdata = Transpose[file[[sheet]]][[xcols]][[xrows[[1]] ;; xrows[[2]]]];
ydata = Transpose[file[[sheet]]][[ycols]][[yrows[[1]] ;; yrows[[2]]]];
zdata = Transpose[file[[sheet]]][[zcols]][[zrows[[1]] ;; zrows[[2]]]];

(*Combing as list of 3D coordinates.*)

ris = Partition[Riffle[Riffle[xdata, ydata], zdata, 3], 3];
ris = ris*.33;(* To convert from 0.33 mm units to mm. *)

Left Ischial Spine

(*Input the sheet of interest within the Excel file (as a number).*)

sheet = 1;
```

```
(*Input the rows and columns containing the data of interest.*)

xrows = {13, 13}; (*First row, last row.*)
yrows = xrows;
zrows = xrows;
xcols = 1;
ycols = 4;
zcols = 7;

(*Pulling out x, y, and z data.*)

xdata = Transpose[file[[sheet]]][[xcols]][[xrows[[1]] ;; xrows[[2]]]];
ydata = Transpose[file[[sheet]]][[ycols]][[yrows[[1]] ;; yrows[[2]]]];
zdata = Transpose[file[[sheet]]][[zcols]][[zrows[[1]] ;; zrows[[2]]]];

(*Combing as list of 3D coordinates.*)

lis = Partition[Riffle[Riffle[xdata, ydata], zdata, 3], 3];
lis = lis*0.33;
(* To convert from 0.33 mm units to mm. *)
```

D.2 Fetal Head and Perineal Body Paths

```
(*Changing points into lines.*)
ndpathline = {};
dpathline = {};
ndpbpathline = {};
dpbpathline = {};
isline = {};
Do[AppendTo[ndpathline, Line[{ndpath[[i]], ndpath[[i + 1]]}]], {i, 1,
   Length[ndpath] - 1}];
Do[AppendTo[dpathline, Line[{dpath[[i]], dpath[[i + 1]]}]], {i, 1,
   Length[dpath] - 1}];
Do[AppendTo[ndpbpathline,
   Line[{ndpbpath[[i]], ndpbpath[[i + 1]]}]], {i, 1,
   Length[ndpbpath] - 1}];
Do[AppendTo[dpbpathline, Line[{dpbpath[[i]], dpbpath[[i + 1]]}]], {i,
   1, Length[dpbpath] - 1}];
Do[AppendTo[isline, Line[{ris[[i]], lis[[i]]}]], {i, 1,
   Length[ris]}];
rpsline = BSplineCurve[{Append[rps, rps[[1]]]}];
lpsline = BSplineCurve[{Append[lps, lps[[1]]]}];
```

D.3 Measuring Differences

D.3.1 Prep

Forming Single Pubic Symphysis

```
(* Averaging the left and right pubic symphysis points.*)

ps = Mean[{rps, lps}];

(*From points to splines.*)
```

```
psline = BSplineCurve[{Append[ps, ps[[1]]]}];

Pubic Symphysis Axis Line

(*Connecting top and bottom point.*)

psaxis = {ps[[1]](*top*), ps[[6]](*bottom*)};
psaxisline = Line[psaxis];


3D to 2D

(*As the geometries were aligned beforehand, we'll project onto the YZ plane \
by reducing all x terms to zero. This is most representative of the \
midsagittal plane for this dataset.*)
(*First we'll do this for the fetal \
head paths.*)
pstop = {ps[[1]][[2]], ps[[1]][[3]]};
psbottom = {ps[[6]][[2]], ps[[6]][[3]]};
dpath2d = {};
ndpath2d = {};
Do[AppendTo[dpath2d, {dpath[[i]][[2]], dpath[[i]][[3]]}], {i, 1,
  Length[dpath]}]
Do[AppendTo[ndpath2d, {ndpath[[i]][[2]], ndpath[[i]][[3]]}], {i, 1,
  Length[ndpath]}]

(*We'll do the same for the PB data.*)
dpbpath2d = {};
ndpbpath2d = {};
Do[AppendTo[dpbpath2d, {dpbpath[[i]][[2]], dpbpath[[i]][[3]]}], {i, 1,
  Length[dpbpath]}]
Do[AppendTo[ndpbpath2d, {ndpbpath[[i]][[2]], ndpbpath[[i]][[3]]}], {i, 1,
  Length[ndpbpath]}]
```

D.3.2 Angle of Progression

```
Omitted Head

(*Defining vectors.*)
v1 = pstop - psbottom;
ndv2 = {};
Do[AppendTo[ndv2, ndpath2d[[i]] - psbottom], {i, 1, Length[ndpath2d]}]

(*Calculating Angle of Progression.*)
ndaop1 = {};
Do[AppendTo[ndaop1, VectorAngle[v1, ndv2[[i]]]], {i, 1, Length[ndpath2d]}]
ndaop1 = ndaop1/Degree;
ndaop = ndaop1[[
   1 ;; 77]];(*Setting up AOP to account for angles greater than 180 degrees.*)
Do[AppendTo[ndaop, 180 - ndaop1[[i]] + 180], {i, 78, Length[ndaop1]}]

(*Converting to lines.*)
ndaoplines = {};
Do[AppendTo[ndaoplines, Line[{ndpath2d[[i]], psbottom}]], {i, 1,
  Length[ndpath2d]}]

Omitted PB

(*Defining vectors.*)
v1 = pstop - psbottom;
ndpbv2 = {};
Do[AppendTo[ndpbv2, ndpbpath2d[[i]] - psbottom], {i, 1, Length[ndpbpath2d]}]

(*Calculating Angle of Progression.*)
ndpbaop1 = {};
```

```
Do[AppendTo[ndpbaop1, VectorAngle[v1, ndpbv2[[i]]]], {i, 1,
  Length[ndpbpath2d]}]
ndpbaop1 = ndpbaop1/Degree;
ndpbaop = ndpbaop1[[
   1 ;; 71]];(*Setting up AOP to account for angles greater than 180 degrees.*)
Do[AppendTo[ndpbaop, 180 - ndpbaop1[[i]] + 180], {i, 72, 113}]
Do[AppendTo[ndpbaop, ndpbaop1[[i]]], {i, 114, Length[ndpbaop1]}]

(*Converting to lines.*)
ndpbaoplines = {};
Do[AppendTo[ndpbaoplines, Line[{ndpbpath2d[[i]], psbottom}]], {i, 1,
  Length[ndpbpath2d]}]

Included Head

(*Defining vectors.*)
v1 = pstop - psbottom;
dv2 = {};
Do[AppendTo[dv2, dpath2d[[i]] - psbottom], {i, 1, Length[dpath2d]}]

(*Calculating Angle of Progression.*)
daop1 = {};
Do[AppendTo[daop1, VectorAngle[v1, dv2[[i]]]], {i, 1, Length[dpath2d]}]
daop1 = daop1/Degree;
daop = daop1[[
   1 ;; 19]];(*Setting up AOP to account for angles greater than 180 degrees.*)
Do[AppendTo[daop, 180 - daop1[[i]] + 180], {i, 20, Length[daop1]}]

(*Converting to lines.*)
daoplines = {};
Do[AppendTo[daoplines, Line[{dpath2d[[i]], psbottom}]], {i, 1,
  Length[dpath2d]}]

Included PB

(*Defining vectors.*)
v1 = pstop - psbottom;
dpbv2 = {};
Do[AppendTo[dpbv2, dpbpath2d[[i]] - psbottom], {i, 1, Length[dpbpath2d]}]

(*Calculating Angle of Progression.*)
dpbaop1 = {};
Do[AppendTo[dpbaop1, VectorAngle[v1, dpbv2[[i]]]], {i, 1, Length[dpbpath2d]}]
dpbaop1 = dpbaop1/Degree;
dpbaop = dpbaop1[[
   1 ;; 10]];(*Setting up AOP to account for angles greater than 180 degrees.*)
Do[AppendTo[dpbaop, 180 - dpbaop1[[i]] + 180], {i, 11, 78}]
Do[AppendTo[dpbaop, dpbaop1[[i]]], {i, 79, Length[dpbaop1]}]

(*Converting to lines.*)
dpbaoplines = {};
Do[AppendTo[dpbaoplines, Line[{dpbpath2d[[i]], psbottom}]], {i, 1,
  Length[dpbpath2d]}]
```

D.4 Visualizations

D.4.1 Angle of Progression Plots

```
ListPlot[{Partition[Riffle[ndtime, ndaop], 2],
  Partition[Riffle[dtime, daop], 2]}, PlotStyle -> {Blue, Red},
 PlotLegends -> {"Omitted", "Included"},
 AxesLabel -> {"Time (s)", "Angle Of Progression (\[Degree])"},
 PlotLabel -> "Fetal Head Descent", AxesOrigin -> {0, 80}]
```

```
Max[ndtime]
Max[ndaop]
Max[dtime]
Max[daop]
```

```
4843.88
```

```
192.319
```

```
6146.16
```

```
203.295
```

```
(203.295 - 192.319)/
  192.319*100 (*percent difference*)
203.295 - 192.319 (*difference*)
```

```
5.70718
```

```
10.976
```

```
ListPlot[{Partition[Riffle[ndtime, ndpbaop], 2],
  Partition[Riffle[dtime, dpbaop], 2]}, PlotStyle -> {Blue, Red},
 PlotLegends -> {"Omitted", "Included"},
 AxesLabel -> {"Time (s)", "Angle Of Progression (\[Degree])"},
 PlotLabel -> "Perineal Body Movement"]
```

```
Max[ndpbaop]
Max[dpbaop]
```

```
182.328
```

```
196.909
```

```
(196.909 - 182.328)/
  182.328*100 (*percent difference*)
196.909 - 182.328 (*difference*)
```

```
7.99713
```

```
14.581
```

D.4.2 Displacement Plots

```
Fetal Head
```

```
ListPlot[{Partition[Riffle[ndtime, ndpath[[;; , 1]] - ndpath[[1, 1]]],
    2], Partition[Riffle[dtime, dpath[[;; , 1]] - dpath[[1, 1]]], 2]},
  PlotStyle -> {Blue, Red}, PlotLegends -> {"Omitted", "Included"},
 AxesLabel -> {"Time (s)", "X Displacement (mm)"},
 PlotLabel -> "Fetal Head X Displacement"]
```

```
ListPlot[{Partition[Riffle[ndtime, ndpath[[;; , 2]] - ndpath[[1, 2]]],
    2], Partition[Riffle[dtime, dpath[[;; , 2]] - dpath[[1, 2]]], 2]},
  PlotStyle -> {Blue, Red}, PlotLegends -> {"Omitted", "Included"},
 AxesLabel -> {"Time (s)", "Y Displacement (mm)"},
 PlotLabel -> "Fetal Head Y Displacement"]

Max[ndpath[[;; , 2]] - ndpath[[1, 2]]]
Max[dpath[[;; , 2]] - dpath[[1, 2]]]
```

```
8.92062
```

```
8.96582
```

```
ListPlot[{Partition[Riffle[ndtime, ndpath[[;; , 3]] - ndpath[[1, 3]]],
    2], Partition[Riffle[dtime, dpath[[;; , 3]] - dpath[[1, 3]]], 2]},
  PlotStyle -> {Blue, Red}, PlotLegends -> {"Omitted", "Included"},
 AxesLabel -> {"Time (s)", "Z Displacement (mm)"},
 PlotLabel -> "Fetal Head Z Displacement"]

Max[ndpath[[;; , 3]] - ndpath[[1, 3]]]
Max[dpath[[;; , 3]] - dpath[[1, 3]]]
```

```
31.9698
```

```
40.5646
```

```
(40.5646 - 31.9698)/31.9698*100 (*percent difference*)
```

```
26.8841
```

```
Perineal Body

ListPlot[{Partition[
   Riffle[ndtime, ndpbpath[[;; , 1]] - ndpbpath[[1, 1]]], 2],
  Partition[Riffle[dtime, dpbpath[[;; , 1]] - dpbpath[[1, 1]]], 2]},
 PlotStyle -> {Blue, Red}, PlotLegends -> {"Omitted", "Included"},
 AxesLabel -> {"Time (s)", "X Displacement (mm)"},
 PlotLabel -> "Perineal Body X Displacement"]

ListPlot[{Partition[
   Riffle[ndtime, ndpbpath[[;; , 2]] - ndpbpath[[1, 2]]], 2],
  Partition[Riffle[dtime, dpbpath[[;; , 2]] - dpbpath[[1, 2]]], 2]},
 PlotStyle -> {Blue, Red}, PlotLegends -> {"Omitted", "Included"},
 AxesLabel -> {"Time (s)", "Y Displacement (mm)"},
 PlotLabel -> "Perineal Body Y Displacement"]

Max[ndpbpath[[;; , 2]] - ndpbpath[[1, 2]]]
Max[ndtime]
Max[dpbpath[[;; , 2]] - dpbpath[[1, 2]]]
Max[dtime]
```

```
24.2065
```

```
4843.88
```

```
25.3385
```

```
6146.16
```

```
ListPlot[{Partition[
   Riffle[ndtime, ndpbpath[[;; , 3]] - ndpbpath[[1, 3]]], 2],
  Partition[Riffle[dtime, dpbpath[[;; , 3]] - dpbpath[[1, 3]]], 2]},
 PlotStyle -> {Blue, Red}, PlotLegends -> {"Omitted", "Included"},
 AxesLabel -> {"Time (s)", "Z Displacement (mm)"},
 PlotLabel -> "Perineal Body Z Displacement"]

Max[ndpbpath[[;; , 3]] - ndpbpath[[1, 3]]]
Max[dpbpath[[;; , 3]] - dpbpath[[1, 3]]]
```

```
10.7042

18.4685

(18.4685 - 10.7042)/
  10.7042*100 (*percent difference*)
18.4685 - 10.7042(*difference*)

72.5351

7.7643
```

D.4.3 Displacement/Angle of Progression Visualizations

```
(*Creating lines for visualization.*)
ndpath2dline = {};
dpath2dline = {};
ndpbpath2dline = {};
dpbpath2dline = {};
Do[AppendTo[ndpath2dline,
   Line[{ndpath2d[[i]], ndpath2d[[i + 1]]}]], {i, 1,
   Length[ndpath2d] - 1}];
Do[AppendTo[dpath2dline, Line[{dpath2d[[i]], dpath2d[[i + 1]]}]], {i,
   1, Length[dpath2d] - 1}];
Do[AppendTo[ndpbpath2dline,
   Line[{ndpbpath2d[[i]], ndpbpath2d[[i + 1]]}]], {i, 1,
   Length[ndpbpath2d] - 1}];
Do[AppendTo[dpbpath2dline,
   Line[{dpbpath2d[[i]], dpbpath2d[[i + 1]]}]], {i, 1,
   Length[dpbpath2d] - 1}];

(*Displaying both fetal head paths as one 2d graphics object.*)
Graphics[{Blue, ndpath2dline, Red, dpath2dline, Green,
  Line[{pstop, psbottom}], Red, daoplines, Blue, ndaoplines}]

(*Displaying both perineal body paths as one 2d graphics object.*)
Graphics[{Blue, ndpbpath2dline, Red, dpbpath2dline, Green,
  Line[{pstop, psbottom}], Red, dpbaoplines, Blue, ndpbaoplines}]
```

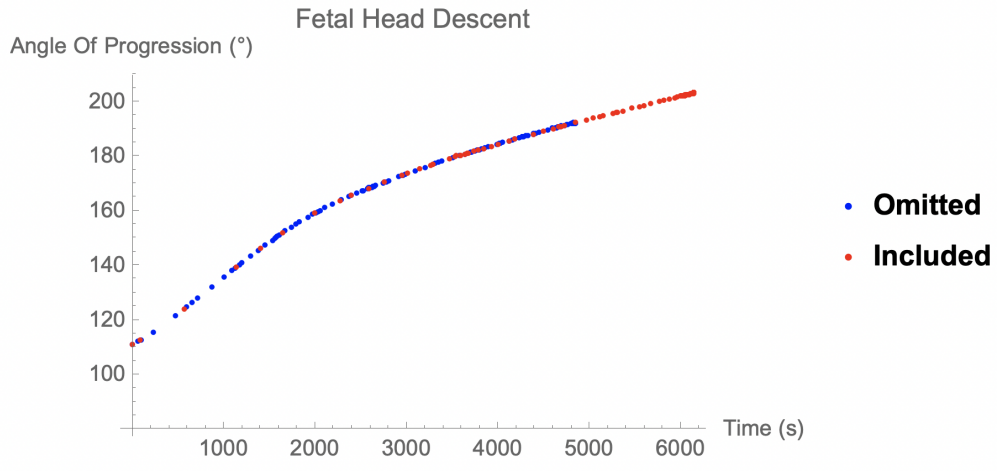

Figure D1: The output of the first angle of progression ListPlot. This plot appears in Figure 4.5 [167].

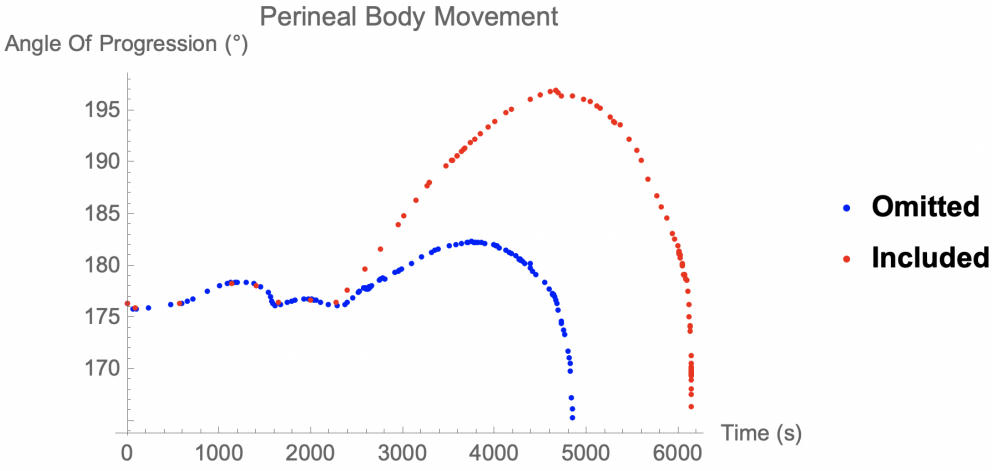

Figure D2: The output of the second angle of progression ListPlot. This plot appears in Figure 4.6 [167].

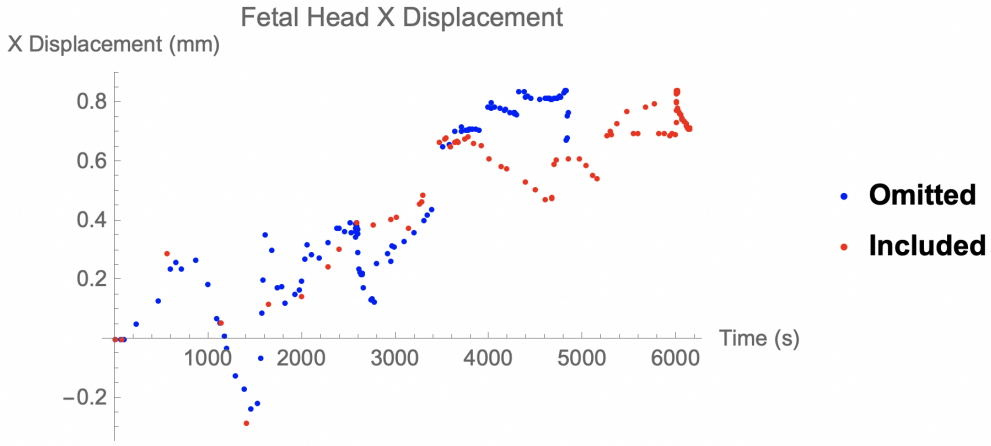

Figure D3: The output of the first displacement ListPlot.

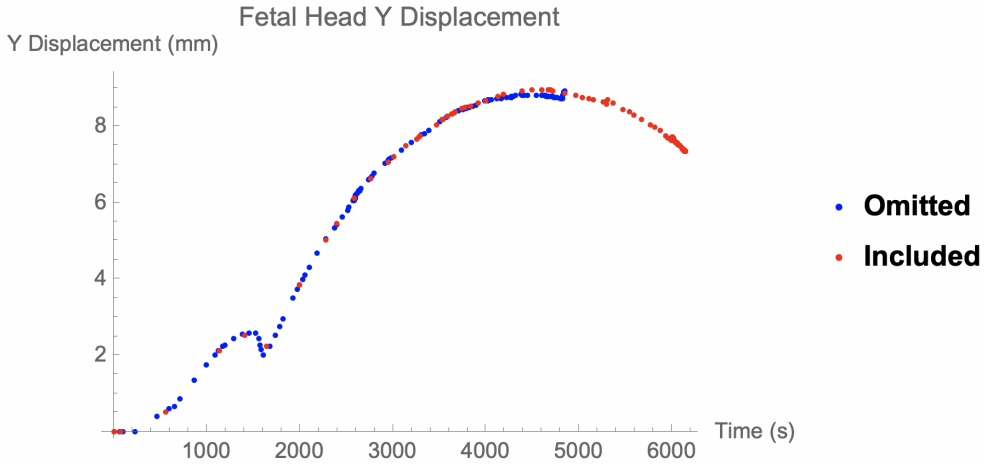

Figure D4: The output of the second displacement ListPlot. This plot appears in Figure 4.5 [167].

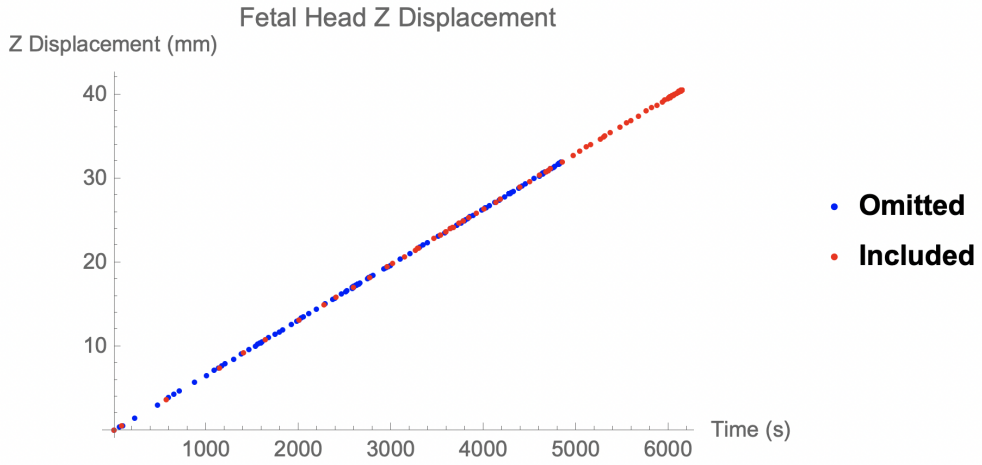

Figure D5: The output of the third displacement ListPlot.

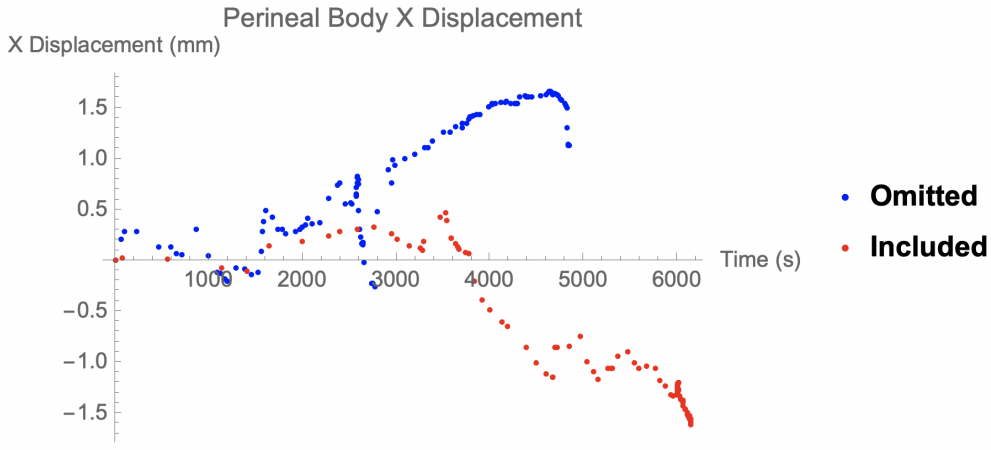

Figure D6: The output of the fourth displacement ListPlot.

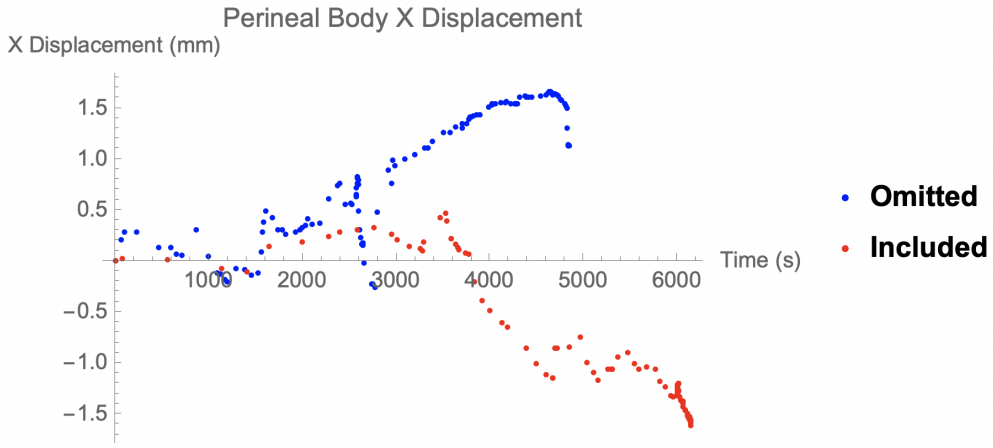

Figure D7: The output of the fifth displacement ListPlot. This plot appears in Figure 4.6 [167].

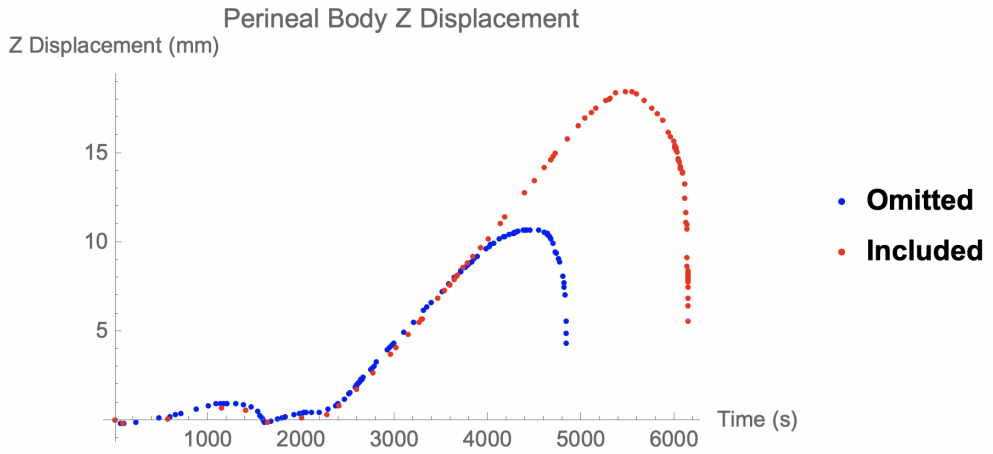

Figure D8: The output of the sixth displacement ListPlot. This plot appears in Figure 4.6 [167].

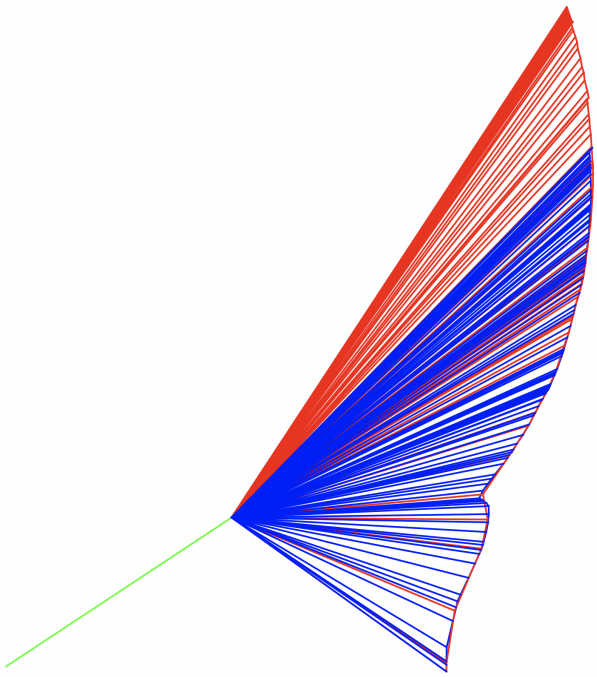

Figure D9: The output of the first Graphics which visually displays the fetal head angles of progression throughout the finite element simulations of the 2nd stage of vaginal childbirth. Blue represents Omitted and red represents Included Model values. The green line is the long axis of the pubic symphysis. The rotated version of this image appears in Figure 4.5 [167].

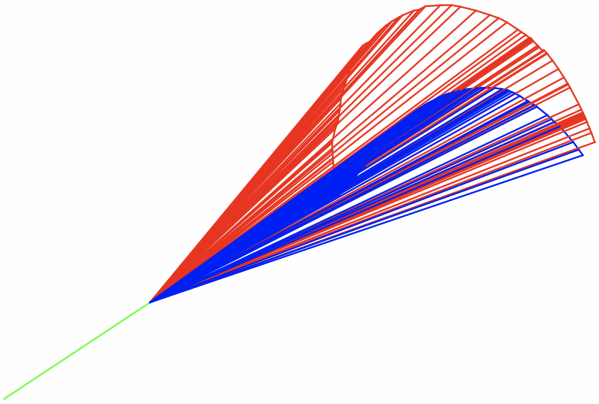

Figure D10: The output of the second Graphics which visually displays the perineal body angles of progression throughout the finite element simulations of the 2nd stage of vaginal childbirth. Blue represents Omitted and red represents Included Model values. The green line is the long axis of the pubic symphysis. The rotated version of this image appears in Figure 4.6 [167].

Appendix E : Quantification of Pelvic Floor Muscle Fascicle Angles and Vector Fields from Photogrammetric Reconstructions

E.1 Custom Mathematica Script for Angle and Vector Field Calculation

This code was written in October of 2019 and revised through October of 2020 in Mathematica™. Some text (e.g., directories and file names) were edited for the purpose of publication in this dissertation. Note that some variable names include "fiber" though this code evaluated muscle fascicles [165], fiber was used only because it is shorter.

E.1.1 Importing Pelvic Floor Shape and Fibers

```
workingdirectory =
  "Directory with fascicle .obj files";(*Each donor and muscle were
evaluated one at a time.*)

filenames =
  FileNames["*IDENTIFIER.obj",
   workingdirectory];(*Importing all .obj files with the defined
identifier from that folder. The identifier was used to distinguish
fascicles from a specific pelvic floor muscle.*)

fiberpoints =
 Flatten[Import[#, "VertexData"]] & /@
  filenames;(*Importing the points that define each fascicle.*)

fiberpoints =
 Table[Partition[fiberpoints[[i]], 3], {i, 1, Length[filenames]}];
fiberlines =
  Table[Line[fiberpoints[[i]]], {i, 1,
    Length[filenames]}];(*Generating lines between the points.*)

coneshape =
 Import[StringJoin[workingdirectory,
   "PELVIC FLOOR GEOMETRY.obj"]]; (*Importing the .obj file of the
photogrammetric reconstruction of the pelvic floor muscle complex
"cone".*)
shapevertices =
 Import[StringJoin[workingdirectory, "PELVIC FLOOR GEOMETRY.obj"],
  "VertexData"];

landmarkfilenames =
 FileNames["*LANDMARK.obj",
  workingdirectory];(*Importing the .obj files which contain the
coordinates of relevant landmarks for orientation calculations.*)

landmarkpoints =
 Flatten[Import[#, "VertexData"]] & /@ landmarkfilenames;
landmarkpoints =
  Table[Partition[landmarkpoints[[i]], 3], {i, 1,
    Length[landmarkfilenames]}];
```

E.1.2 Calculating Fascicle Characteristics

```
arclengths = ArcLength[fiberlines];

straightlengths =
  Table[EuclideanDistance[First[fiberpoints[[i]]],
    Last[fiberpoints[[i]]]], {i, 1,
    Length[filenames]}];(*Distance between first and last fiber \
points*)

curvatureindices =
  straightlengths/
   arclengths;(*Straight length / curved length = curvature index*)
```

E.1.3 Calculating Tangent Vectors and the Discrete Vector Field

```
Calculating Tangent Vectors

(*Defining fibers as spline curves/functions*)

fibercurves =
  Table[BSplineFunction[fiberpoints[[i]]], {i, 1, Length[filenames]}];

(*calculating tangent vectors along each fiber curve*)

tangentvectorfunctions[i_, t_] :=
  0.1*Simplify[fibercurves[[i]]'[t]/Norm[fibercurves[[i]]'[t]],
    t \[Element]
     Reals]; (*where i is the fiber identifyer and t is the
percentage of the distance along that fiber (0 to 1)*)

Sampling Number of Tangent Vectors Proportional to Fiber Length

(*Normalizing the fiber arc lengths by the length of the
pubococcygeal line*)
coccyx = Mean[landmarkpoints[[3]]];
pubic = Mean[landmarkpoints[[4]]];
pclLength = EuclideanDistance[coccyx, pubic];
normarclengths = arclengths/pclLength;

(*These PCLs are about 10cm. If we want to sample a tangent vector
for approximately each mm of length, then we'll want to sample about
every 1/100 of the PCL*)
(*Once the arc lengths are normalzed, PCL=1
so "1 mm"= 0.01*)
tangentvectors = {};
tangentvectors =
  Table[tangentvectorfunctions[i, t], {i, 1, Length[filenames]}, {t,
    0, 1, 1/(normarclengths[[i]]/0.01)}];

Visualizing Discrete Vector Field

(*sampling the points along the fibers that correspond to the sampled
tangent vectors*)


tangentvectorpoints =
  Table[fibercurves[[i]][t], {i, 1, Length[filenames]}, {t, 0, 1,
    1/(normarclengths[[i]]/0.01)}];


discretefieldarrows =
  Table[Line[{tangentvectorpoints[[i]][[n]],
     tangentvectorpoints[[i]][[n]] + (tangentvectors[[i]][[n]])/20}]
   , {i, 1, Length[filenames]}, {n, 1, Length[tangentvectors[[i]]]}];
```

```
tangentvectorarrows =
 Graphics3D[
  Table[{Thickness[0.001], Hue[Random[]],(*Arrowheads[0.01],*)
    discretefieldarrows[[i]]}, {i, 1, Length[filenames]}],
  Background -> Black];
```

E.1.4 Calculating Clinically Relevant Fascicle Angles

```
Import Landmark Positions from Blender and Define Planes

(*Get values by selecting points in Blender*)

isright = Mean[landmarkpoints[[1]]];
isleft = Mean[landmarkpoints[[2]]];
ismid = Midpoint[{isright, isleft}];
Show[coneshape,
 ListPointPlot3D[{isright, isleft, ismid, coccyx, pubic},
  PlotStyle -> Red], PlotRange -> All]

(*Defining lines of interest*)
ischline = Line[{isright, isleft}];
pcl = Line[{pubic, coccyx}];

(*Finding closest points between PCL and IschLine to create an
orthogonal line to the PCL to define the axial plane*)

pclpoint = Projection[ismid - coccyx, pubic - coccyx] + coccyx;
newline = Line[{pclpoint, ismid}];
pclrotated =
  GeometricTransformation[
   GeometricTransformation[newline, TranslationTransform[-pclpoint]],
   RotationMatrix[90 Degree, pubic - pclpoint]];
pclrotated =
  GeometricTransformation[pclrotated,
   TranslationTransform[pclpoint]];
pclrotatedpoint = (RotationMatrix[90 Degree,
      pubic - pclpoint].(ismid - pclpoint)) + pclpoint;

(*Defining Planes*)

sagittalplane = InfinitePlane[{ismid, coccyx, pubic}];
axialplane = InfinitePlane[{pubic, coccyx, pclrotatedpoint}];

(*Showing reference lines and  planes*)
Show[coneshape,
 Graphics3D[{Red, Thick, fiberlines}],
 Graphics3D[{Green, Thick, ischline}], Graphics3D[{Blue, Thick, pcl}],
  Graphics3D[{Cyan, Thick, pclrotated}],
 Graphics3D[{Opacity[0.1, Red], axialplane}],
 Graphics3D[{Opacity[0.1, Blue], sagittalplane}]]

Projecting Fiber Tangent Vectors onto the Axial Plane

*reorganizing fiber tangent vectors*)

fibervectors = Flatten[tangentvectors, 1];
tanvectorpoints = Flatten[tangentvectorpoints, 1];

(*vector normal to the axial plane*)

normalvector = Cross[pubic - coccyx, coccyx - pclrotatedpoint];


(*point of intersection betweeen fiber vector and the axial plane*)
```

```
pin = Table[
   First[RegionIntersection[axialplane,
     InfiniteLine[{tanvectorpoints[[i]],
       tanvectorpoints[[i]] + fibervectors[[i]]}]]], {i, 1,
    Length[fibervectors]}];

(*generating arrows representing fibers and projections pointing
laterally*)

fiberarrows =
  Table[Arrow[
    Tube[{tanvectorpoints[[i]],
      tanvectorpoints[[i]] + fibervectors[[i]]}]], {i, 1,
    Length[fibervectors]}];

fiberarrowlines =
  Table[InfiniteLine[{tanvectorpoints[[i]],
     tanvectorpoints[[i]] + fibervectors[[i]]}], {i, 1,
    Length[fibervectors]}];

fiberprojections =
  Table[{pin[[i]] + fibervectors[[i]] -
     Projection[fibervectors[[i]], normalvector], pin[[i]]}, {i, 1,
    Length[fibervectors]}];

fiberprojectionarrows = Arrow[Tube[fiberprojections]];

normalvectorarrows =
  Table[Arrow[
    Tube[{pin[[i]], pin[[i]] + Normalize[normalvector]/2}]], {i, 1,
    Length[fibervectors]}];

Calculating Axial Angles

(*Calculating angles within axial plane with respect to the
pubococcygeal line*)

apangles =
  Table[VectorAngle[pubic - coccyx,
     fiberprojections[[i]][[2]] - fiberprojections[[i]][[1]]], {i, 1,
     Length[fibervectors]}]/Degree;
(*Adjusting this method using the determinant of each angle, as this
Mathematica function doesn't distinguish from clockwise and
counterclockwise directions from the PCL, so we'll subtract the angle
from 360 if the determinant is positive.*)

unitnormalaxial = Cross[pubic - coccyx, coccyx - pclrotatedpoint];
unitnormalaxial = unitnormalaxial/Sqrt[Total[unitnormalaxial^2]];

detaxial =
  Table[Dot[unitnormalaxial,
    Cross[pubic - coccyx,
     fiberprojections[[i]][[2]] - fiberprojections[[i]][[1]]]], {i, 1,
     Length[fibervectors]}];

apangles =
  Table[If[detaxial[[i]] > 0, 360 - apangles[[i]], apangles[[i]]], {i,
     1, Length[fibervectors]}];

(*Anterior-posterior angles (in degrees): 180=pointing anteriorly,
0/360=pointing posteriorly, 90=pointing left, 270=pointing right*)

Projecting Fiber Tangent Vectors onto the Sagittal Plane

(*vector normal to the sagittal plane*)

normalvectorsag = Cross[ismid - coccyx, coccyx - pubic];
```

```
(*point of intersection betweeen fiber vector and the sagittal plane*)

pinsag = Table[
   First[RegionIntersection[sagittalplane,
     InfiniteLine[{tanvectorpoints[[i]],
       tanvectorpoints[[i]] + fibervectors[[i]]}]]], {i, 1,
    Length[fibervectors]}];

(*generating arrows representing fibers and projections pointing
laterally*)

fiberprojectionssag =
  Table[{pinsag[[i]] + fibervectors[[i]] -
     Projection[fibervectors[[i]], normalvectorsag], pinsag[[i]]}, {i,
     1, Length[fibervectors]}];

fiberprojectionarrowssag = Arrow[Tube[fiberprojectionssag]];

normalvectorarrowssag =
  Table[Arrow[
    Tube[{pinsag[[i]],
      pinsag[[i]] + Normalize[normalvectorsag]/2}]], {i, 1,
    Length[fibervectors]}];

Calculating Sagittal Angles

(*Calculating angles within the sagittal plane with respect to the PCL*)

(*Now we have to bring both of our vectors to the origin to determine the angles*)
siangles =
  Table[VectorAngle[pubic - coccyx,
     fiberprojectionssag[[i]][[2]] -
      fiberprojectionssag[[i]][[1]]], {i, 1, Length[fibervectors]}]/
   Degree;
(*Adjusting as this method doesn't distinguish from clockwise and
counterclockwise directions from the PCL, so we'll subtract the angel
from 360 if the determinant is positive.*)

unitnormalsag = Cross[pubic - coccyx, ismid - coccyx];
unitnormalsag = unitnormalsag/Sqrt[Total[unitnormalsag^2]];

detsag = Table[
   Dot[unitnormalsag,
    Cross[pubic - coccyx,
     fiberprojectionssag[[i]][[2]] -
      fiberprojectionssag[[i]][[1]]]], {i, 1, Length[fibervectors]}];

siangles =
  Table[If[detsag[[i]] > 0, 360 - siangles[[i]], siangles[[i]]], {i,
    1, Length[fibervectors]}];

(*Anterior-posterior angles (in degrees): 180=pointing anteriorly,
0/360=pointing posteriorly, 90=pointing superiorly, 270=pointing
inferiorly*)
```

E.1.5 Exporting Angle Data

```
Export[StringJoin[workingdirectory, "AXIAL ANGLES",
  ".csv"], apangles]
Export[StringJoin[workingdirectory, "SAGITTAL ANGLES",
  ".csv"], siangles]
Export[StringJoin[workingdirectory, "VECTORS", ".csv"],
 Flatten[tangentvectors, 1]]
Export[StringJoin[workingdirectory, "VECTOR POINTS", ".csv"],
 Flatten[tangentvectorpoints, 1]]
```

E.1.6 Vector Field Calculation

Continuous vector fields were calculated for each pelvic floor muscle cone using fascicle data from all muscles simultaneously, meaning the identifier was not used to select individual muscles for this section of the code. The vector fields were exported for visualization in Houdini FX (SideFX, Toronto, CA).

```
Defining the Discrete Vector Field

(*joining the coordinates and vectors into one array for interpolation*)

discretefield =
  Table[Join[tangentvectorpoints[[i, n]],
    tangentvectors[[i]][[n]]], {i, 1, Length[filenames]}, {n, 1,
    Length[tangentvectors[[i]]]}];
discretefield = Flatten[discretefield, 1];
(*discretefield = x-coordinate, y-coordinate, z-coordinate, x-vector
component, y-vector component, z-vector component*)

(*setting bounds using the min and max x, y, and z tangent vector
point coordinates*)
{{xmin, xmax}, {ymin, ymax}, {zmin, zmax}} =
  MinMax /@ Transpose[Flatten[tangentvectorpoints, 1]][[;; 3]];

First Order Interpolation to Define a Continuous Vector Field

*interpolating for continuous definition of the vector field*)

xfunc = Interpolation[(discretefield[[All, ;; 4]]),
   InterpolationOrder -> 1];
yfunc = Interpolation[(discretefield[[All, {1, 2, 3, 5}]]),
   InterpolationOrder -> 1];
zfunc = Interpolation[(discretefield[[All, {1, 2, 3, 6}]]),
   InterpolationOrder -> 1];

Sampling the First Order Interpolation Field to Define a Uniform Grid of Vectors

(*To decide what to round to in order to define the lxwxh of the
uniform grid.*)
{{xmin, xmax}, {ymin, ymax}, {zmin, zmax}}
xrange = Abs[xmin - xmax]
yrange = Abs[ymin - ymax]
zrange = Abs[zmin - zmax]

(*Identifying integer bounds of the 1st order vector field by
rounding up.*)
roundedbounds = {{Floor[xmin, 0.1],
   Ceiling[xmax, 0.1]}, {Floor[ymin, 0.1],
   Ceiling[ymax, 0.1]}, {Floor[zmin, 0.1], Ceiling[zmax, 0.1]}}

(*To decide the x/y/z intervals within the grid.*)(*so I picked 0.01*)
pclLength/100

(*Generating the coordinates that form a uniform grid.*)
firstordergrid =
  Table[{x, y, z}, {x, roundedbounds[[1]][[1]],
    roundedbounds[[1]][[2]], 0.017}, {y, roundedbounds[[2]][[1]],
    roundedbounds[[2]][[2]], 0.017}, {z, roundedbounds[[3]][[1]],
    roundedbounds[[3]][[2]], 0.017}];
firstordergrid = Flatten[firstordergrid, 2];

(*retrieving x,y,z vector values at those grid points*)
```

```
firstordergridx =
 Table[xfunc[firstordergrid[[i]][[1]], firstordergrid[[i]][[2]],
   firstordergrid[[i]][[3]]], {i, 1,
   Dimensions[firstordergrid, 1][[
    1]]}];(*will get error messages because you are extrapolating a
bit outside of the interpolation bounds*)
firstordergridy =
 Table[yfunc[firstordergrid[[i]][[1]], firstordergrid[[i]][[2]],
   firstordergrid[[i]][[3]]], {i, 1,
   Dimensions[firstordergrid, 1][[
    1]]}];(*will get error messages because you are extrapolating a
bit outside of the interpolation bounds*)
firstordergridz =
 Table[zfunc[firstordergrid[[i]][[1]], firstordergrid[[i]][[2]],
   firstordergrid[[i]][[3]]], {i, 1,
   Dimensions[firstordergrid, 1][[
    1]]}];(*will get error messages because you are extrapolating a
bit outside of the interpolation bounds*)

(*organizing the 1st order vector field as a uniform grid of discrete
vectors*)
firstorderfield =
  Transpose[{firstordergrid[[All, 1]], firstordergrid[[All, 2]],
    firstordergrid[[All, 3]], firstordergridx, firstordergridy,
    firstordergridz}];

Export[StringJoin[workingdirectory,
  "VECTOR FIELD NAME",
  ".csv"], firstorderfield]
```

E.2 Matlab Script for Polar Histogram Generation for Fascicle Orientations of Individual Muscles

This code (written in Matlab™) visualizes the fascicle orientation angle outputs from the previous Mathematica™ script. It was written in December of 2019 and revised through April of 2020.

```
clear all
close all

%% Inputs
filelocation=['DIRECTORY TO .csv FILES OF ANGLES'];

%% Importing Data
cd(filelocation)
apanglefiles=dir('*apangles.csv');
sianglefiles=dir('*siangles.csv');
numfiles=length(apanglefiles);

apangledata=cell(1,6);
siangledata=cell(1,6);
for i=1:numfiles
    apcell=struct2cell(apanglefiles(i));
    sicell=struct2cell(sianglefiles(i));

    apfilename=apcell{1,1};
    sifilename=sicell{1,1};
```

```
    apangledata{1,i}=importdata(apfilename);
    siangledata{1,i}=importdata(sifilename);

    apangles=cell2mat(apangledata(i));
    siangles=cell2mat(siangledata(i));

    %% Plotting Angle Data
    color={'blue','blue','blue','red','red','red'};

    plotapangles=[apangles-90;apangles+180-90];
    figure('Name',apfilename)
    aphist=polarhistogram(deg2rad(plotapangles),50,'FaceColor',color{i})
    apax=gca;
    apax.FontSize=14;
    apax.FontWeight='bold';
    set(gca,'ThetaZeroLocation','top',...
        'ThetaDir','counterclockwise');
    apname=strsplit(apfilename,'.');
    saveas(aphist,apname{1},'jpeg')

    plotsiangles=[siangles-90;siangles+180-90];
    figure('Name',sifilename)
    sihist=polarhistogram(deg2rad(plotsiangles),50,'FaceColor',color{i})
    siax=gca;
    siax.FontSize=14;
    siax.FontWeight='bold';
    set(gca,'ThetaZeroLocation','top',...
        'ThetaDir','counterclockwise');
    siname=strsplit(sifilename,'.');
    saveas(sihist,siname{1},'jpeg')

    clear apangles siangles
end
```

E.3 Matlab Script to Run Descriptive Statistics and Generate Combined Histograms

This code (written in Matlab™) performs descriptive statistics of the fascicle orientation angle outputs from the previous Mathematica™ script. It was written in April of 2020 and revised through October of 2020. This code utilizes CircHist [204] and CircStat [26].

```
clear all
close all

% to save CircHist property outputs
diary on

%% Inputs
filelocation=['DIRECTORY TO ALL .csv FILES OF ANGLE DATA'];

%% Importing Data and Individual Descriptive Statistics
cd(filelocation)
apanglefiles=dir('*apangles.csv');
sianglefiles=dir('*siangles.csv');
numfiles=length(apanglefiles);
```

```
apangledata=cell(1,size(apanglefiles,1));
siangledata=cell(1,size(sianglefiles,1));
apmedian=zeros(1,size(apanglefiles,1));
simedian=zeros(1,size(sianglefiles,1));
color={'b','b','b','r','r','r','b','b','b','r','r','r','b','b','b','r','r','r',...
    'b','b','b','r','r','r','b','b','b','r','r','r'};
for i=1:numfiles
    apcell=struct2cell(apanglefiles(i));
    sicell=struct2cell(sianglefiles(i));

    apfilename=apcell{1,1};
    sifilename=sicell{1,1};
    %reading in angles, duplicating to force radial symmetry, and wrapping
    %between 0 and 360
    apangledata{1,i}=wrapTo360(vertcat(importdata(apfilename),importdata(apfilename)+180));
    siangledata{1,i}=wrapTo360(vertcat(importdata(sifilename),importdata(sifilename)+180));

    %plotting the data with statistics
    figure('Name',apfilename)
    aphist=CircHist(apangledata{1,i}, 36, 'areAxialData', true,...
        'baseLineOffset',10,'colorAvgAng','k','colorBar',color{i})
    apname=strsplit(apfilename,'.');
    saveas(aphist.figH,apname{1},'jpeg')

    figure('Name',sifilename)
    sihist=CircHist(siangledata{1,i}, 36, 'areAxialData', true,...
        'baseLineOffset',10,'colorAvgAng','k','colorBar',color{i})
    siname=strsplit(sifilename,'.');
    saveas(sihist.figH,siname{1},'jpeg')
end
diary 'CircHist_Properties.txt'
diary off

%% Calculating Averages Across Subjects
diary on
averageapangledata=cell(1,6);
averagesiangledata=cell(1,6);
for i=1:6
    apcell=struct2cell(apanglefiles(i));
    sicell=struct2cell(sianglefiles(i));

    apfilename=apcell{1,1};
    sifilename=sicell{1,1};

    averageapangledata{1,i}=vertcat(apangledata{1,i},apangledata{1,i+6},apangledata{1,i+12});
    averagesiangledata{1,i}=vertcat(siangledata{1,i},siangledata{1,i+6},siangledata{1,i+12});

    %plotting the data with statistics
    figure('Name',apfilename(7:end))
    avgaphist=CircHist(averageapangledata{1,i}, 36, 'areAxialData', true,...
        'baseLineOffset',10,'colorAvgAng','k','colorBar',color{i})
    apname=strsplit(apfilename,'.');
    saveas(avgaphist.figH,apname{1}(7:end),'jpeg')

    figure('Name',sifilename(7:end))
    avgsihist=CircHist(averagesiangledata{1,i}, 36, 'areAxialData', true,...
        'baseLineOffset',10,'colorAvgAng','k','colorBar',color{i})
    siname=strsplit(sifilename,'.');
    saveas(avgsihist.figH,siname{1}(7:end),'jpeg')
end
diary 'CircHist_Properties_AveragesAcrossSubjects'
diary off

%% Doubling Bimodal Data and Performing Descriptive Statistics
%To accurately calculate the mean and standard deviations across all
%subjects. Also performing Rayleigh tests for non-uniformity.
apdoubleaverageangles=cell(1,6);
sidoubleaverageangles=cell(1,6);
```

```
apmean=zeros(1,6);
simean=zeros(1,6);
apstd=zeros(1,6);
sistd=zeros(1,6);
apraydistp=zeros(1,6);
apraydistz=zeros(1,6);
siraydistp=zeros(1,6);
siraydistz=zeros(1,6);
for i=1:6
    apdoubleaverageangles{1,i}=wrapTo360(averageapangledata{i}*2);
    sidoubleaverageangles{1,i}=wrapTo360(averagesiangledata{i}*2);

    apmean(1,i)=wrapTo360(rad2deg(circ_mean(deg2rad(apdoubleaverageangles{1,i})))/2;
    simean(1,i)=wrapTo360(rad2deg(circ_mean(deg2rad(sidoubleaverageangles{1,i})))/2;

    [~,tempapstd]=circ_std(deg2rad(apdoubleaverageangles{1,i}));
    apstd(1,i)=rad2deg(tempapstd)/2;
    [~,tempsistd]=circ_std(deg2rad(sidoubleaverageangles{1,i}));
    sistd(1,i)=rad2deg(tempsistd)/2;

    [apraydistp(1,i),apraydistz(1,i)]=circ_rtest(deg2rad(apdoubleaverageangles{1,i}));
    [siraydistp(1,i),siraydistz(1,i)]=circ_rtest(deg2rad(sidoubleaverageangles{1,i}));
end

%Cacluating subject-specific means and standard deviations
%Also performing Rayleigh z tests for non-uniformity.
apdoublespecangles=cell(size(apangledata));
sidoublespecangles=cell(size(siangledata));
apmeanspec=zeros(1,length(apangledata));
simeanspec=zeros(1,length(apangledata));
apstdspec=zeros(1,length(apangledata));
sistdspec=zeros(1,length(apangledata));
apraydistpspec=zeros(1,6);
apraydistzspec=zeros(1,6);
siraydistpspec=zeros(1,6);
siraydistzspec=zeros(1,6);
for k=1:length(apangledata)
    apdoublespecangles{1,k}=wrapTo360(apangledata{k}*2);
    sidoublespecangles{1,k}=wrapTo360(siangledata{k}*2);

    apmeanspec(1,k)=wrapTo360(rad2deg(circ_mean(deg2rad(apdoublespecangles{1,k})))/2;
    simeanspec(1,k)=wrapTo360(rad2deg(circ_mean(deg2rad(sidoublespecangles{1,k})))/2;

    [~,tempapstd]=circ_std(deg2rad(apdoublespecangles{1,k}));
    apstdspec(1,k)=rad2deg(tempapstd)/2;
    [~,tempsistd]=circ_std(deg2rad(sidoublespecangles{1,k}));
    sistdspec(1,k)=rad2deg(tempsistd)/2;

    [apraydistpspec(1,k),apraydistzspec(1,k)]=...
        circ_rtest(deg2rad(apdoublespecangles{1,k}));
    [siraydistpspec(1,k),siraydistzspec(1,k)]=...
        circ_rtest(deg2rad(sidoublespecangles{1,k}));
end
```

E.4 Comparative Statistics Across Pelvic Floor Muscles and Corresponding Left and Right Muscles

This Matlab^{TM} code performed One-Way ANOVAs across pelvic floor muscles and to evaluate differences between left and right corresponding muscles. Average angle values copied and pasted into this code were calculated from the previous descriptive statistics Matlab^{TM} script. This code was written in August of 2020 and revised through October of 2020.

```
%% Evaluating axial left/right
cangles=[121.8;135.8;166.5;107.1;138.6;140.6;144.0;161.2;128.6;134.4];
icangles=[140.7;143.6;147.8;141.9;147.9;163.4;152.3;163.6;150.9;134.0];
pvangles=[183.1;133.4;108.7;147;170.1;186.3;143.0;155.9;166.8;161.7];

group=[1;1;1;1;1;2;2;2;2;2];
%1 for left and 2 for right

%Running the ANOVAs
[cleftrightww_pval,cleftrightapww_table]=circ_wwtest(deg2rad(cangles),group);
[icleftrightww_pval,icleftrightapww_table]=circ_wwtest(deg2rad(icangles),group);
[pvleftrightww_pval,pvleftrightapww_table]=circ_wwtest(deg2rad(pvangles),group);
%% Evaluating sagittal left/right
cangles=[152.7;172.2;175.6;134.7;146.0;122.9;150.5;138.3;124.0;151.8];
icangles=[143.3;155.4;157.0;165.2;147.0;157.3;146.9;150.1;144.7;140.6];
pvangles=[133.2;128.3;72.4;152.2;140.1;144.3;132.3;119.8;142.3;142.0];

group=[1;1;1;1;1;2;2;2;2;2];
%1 for left and 2 for right

%Running the ANOVAs
[cleftrightww_pval,cleftrightww_table]=circ_wwtest(deg2rad(cangles),group);
[icleftrightww_pval,icleftrightww_table]=circ_wwtest(deg2rad(icangles),group);
[pvleftrightww_pval,pvleftrightww_table]=circ_wwtest(deg2rad(pvangles),group);
%% Evaluating axial PFM differences
leftpfms=[121.8;135.8;166.5;107.1;138.6;140.7;143.6;147.8;141.9;147.9;...
    183.1;133.4;108.7;147.0;170.1];
rightpfms=[39.4;36.0;18.8;51.4;45.6;16.6;27.7;16.4;29.1;46.0;...
    6.3;37.0;24.1;13.2;18.3];

pfmgroup=[1;1;1;1;1;2;2;2;2;3;3;3;3;3];
%1 for coccygeus, 2 for iliococcygeus, and 3 for pubovisceralis

%Running the ANOVAS
[leftpfmww_pval,leftpfmww_table]=circ_wwtest(deg2rad(leftpfms),pfmgroup);
[rightpfmww_pval,rightpfmww_table]=circ_wwtest(deg2rad(rightpfms),pfmgroup);
%% Evaluating sagittal PFM differences
leftpfms=[152.7;172.2;175.6;134.7;146.0;143.3;155.4;157.0;165.2;147.0;...
    133.2;128.3;72.4;152.2;140.1];
rightpfms=[122.9;150.5;138.3;124.0;151.8;157.3;146.9;150.1;144.7;140.6;...
    144.3;132.3;119.8;142.3;142.0];

pfmgroup=[1;1;1;1;1;2;2;2;2;3;3;3;3;3];
%1 for coccygeus, 2 for iliococcygeus, and 3 for pubovisceralis

%Running the ANOVAS
[leftpfmww_pval,leftpfmww_table]=circ_wwtest(deg2rad(leftpfms),pfmgroup);
[rightpfmww_pval,rightpfmww_table]=circ_wwtest(deg2rad(rightpfms),pfmgroup);
%% Evaluating ischial spine differences
axis=[105.5;132.1;118.1;104.6;106.2;107.7;127.3;117.0;118.4;113.2];
```

```
sagis=[110.4;135.5;109.6;118.5;103.4;120.5;129.3;112.8;124.9;113.6];

isgroup=[1;1;1;1;1;2;2;2;2;2];
%1 for left and 2 for right

%Running the ANOVAS
[axisww_pval,axisww_table]=circ_wwtest(deg2rad(axis),isgroup);
[sagisww_pval,sagisww_table]=circ_wwtest(deg2rad(sagis),isgroup);
%% Repeating evaluations on angles taken WRT the ischial spines
%% Evaluating axial left/right
cangles=[16.3;3.7;48.4;2.5;32.4;32.9;16.7;44.2;10.2;21.2];
icangles=[35.2;11.5;29.7;37.3;41.7;55.7;25.0;46.6;32.5;20.8];
pvangles=[77.6;1.3;-9.4;42.4;63.9;66.0;15.7;38.9;48.4;48.5];

group=[1;1;1;1;1;2;2;2;2;2];
%1 for left and 2 for right

%Running the ANOVAs
[cleftrightww_pval,cleftrightapww_table]=circ_wwtest(deg2rad(cangles),group);
[icleftrightww_pval,icleftrightapww_table]=circ_wwtest(deg2rad(icangles),group);
[pvleftrightww_pval,pvleftrightapww_table]=circ_wwtest(deg2rad(pvangles),group);
%% Evaluating sagittal left/right
cangles=[42.3;36.7;66.0;16.2;42.6;2.4;21.2;25.5;-0.9;38.2];
icangles=[32.9;19.9;42.4;46.7;43.6;36.8;17.6;37.3;19.8;27.0];
pvangles=[22.8;-7.2;-37.2;33.7;36.7;23.8;3.0;7.0;17.4;28.4];

group=[1;1;1;1;1;2;2;2;2;2];
%1 for left and 2 for right

%Running the ANOVAs
[cleftrightww_pval,cleftrightww_table]=circ_wwtest(deg2rad(cangles),group);
[icleftrightww_pval,icleftrightww_table]=circ_wwtest(deg2rad(icangles),group);
[pvleftrightww_pval,pvleftrightww_table]=circ_wwtest(deg2rad(pvangles),group);
%% Evaluating axial PFM differences
leftpfms=[16.3;3.7;48.4;2.5;32.4;35.2;11.5;29.7;37.3;41.7;...
    77.6;1.3;-9.4;42.4;63.9];
rightpfms=[-32.9;-16.7;-44.2;-10.2;-21.2;-55.7;-25.0;-46.6;-32.5;-20.8;...
    -66.0;-15.7;-38.9;-48.4;-48.5];

pfmgroup=[1;1;1;1;1;2;2;2;2;3;3;3;3;3];
%1 for coccygeus, 2 for iliococcygeus, and 3 for pubovisceralis

%Running the ANOVAS
[leftpfmww_pval,leftpfmww_table]=circ_wwtest(deg2rad(leftpfms),pfmgroup);
[rightpfmww_pval,rightpfmww_table]=circ_wwtest(deg2rad(rightpfms),pfmgroup);
%% Evaluating sagittal PFM differences
leftpfms=[42.3;36.7;66.0;16.2;42.6;32.9;19.9;47.4;46.7;43.6;...
    22.8;-7.2;-37.2;33.7;36.7];
rightpfms=[2.4;21.2;25.5;-0.9;38.2;36.8;17.6;37.3;19.8;27.0;...
    23.8;3.0;7.0;17.4;28.4];

pfmgroup=[1;1;1;1;1;2;2;2;2;3;3;3;3;3];
%1 for coccygeus, 2 for iliococcygeus, and 3 for pubovisceralis

%Running the ANOVAS
[leftpfmww_pval,leftpfmww_table]=circ_wwtest(deg2rad(leftpfms),pfmgroup);
[rightpfmww_pval,rightpfmww_table]=circ_wwtest(deg2rad(rightpfms),pfmgroup);
```

E.5 Matlab Script for Smoothing Mathmatica Generated Vector Fields

The purpose of this code is to smooth an evenly distributed 3D grid of 3D vectors generated from first order interpolations of muscle fascicles from the previous Mathematica™ script. It was writtten in May of 2020 in Matlab™ and revised through October of 2020. It utilizes SMOOTHN [72].

```
clear all
close all

%% Inputs
filelocation=['DIRECTORY CONTAINING CONTINUOUS VECTOR FIELD DATA'];

%% Import Grid of Discrete Vectors
cd(filelocation)
vectorfile=dir('*32053.csv');
vectorcell=struct2cell(vectorfile);
vectorfilename=vectorcell{1,1};
vectorgrid=importdata(vectorfilename);

%% Reorganize Data to Expected Smoothn Input Formats

%Identifying min and max values
minx=min(vectorgrid(:,1));
maxx=max(vectorgrid(:,1));
miny=min(vectorgrid(:,2));
maxy=max(vectorgrid(:,2));
minz=min(vectorgrid(:,3));
maxz=max(vectorgrid(:,3));

%defining the range of the vector field's coordinate values--interval must
%be >= that used to generate the discrete 1st order interpolated vector field
interval=0.008;
xrange=minx:interval:maxx;
yrange=miny:interval:maxy;
zrange=minz:interval:maxz;

%arranging those in the way expected by smoothn
[gridx,gridy,gridz]=meshgrid(xrange,yrange,zrange);

grid_long = [gridx(:), gridy(:),gridz(:)];

vectorxyz=zeros(size(grid_long));
disp('Starting loop...')
for i=1:length(grid_long)
    rowvalue = sum(abs(vectorgrid(:,1:3) - grid_long(i,:)),2) < 3e-6;
    vectorxyz(i,:)=vectorgrid(rowvalue,4:6)/max(abs(vectorgrid(rowvalue,4:6)));
end
disp('loop finished')
vectorx = reshape(vectorxyz(:,1),size(gridx));
vectory = reshape(vectorxyz(:,2),size(gridx));
vectorz = reshape(vectorxyz(:,3),size(gridx));

%% Plotting the original vector field
disp('making fig 1')
figure('Name','Original Vector Field')
ogvectorfield=coneplot(gridx,gridy,gridz,vectorx,vectory,vectorz,interval,'nointerp');

%% Smoothing the vector field
disp('making fig 2')
smoothvectors=smoothn({vectorx,vectory,vectorz},'robust');
figure('Name','Smoothed Vector Field')
```

```
smoothvectorfield=coneplot(gridx,gridy,gridz,smoothvectors{1},smoothvectors{2},...
    smoothvectors{3},interval,'nointerp');

%% Exporting the smoothed vector field
%the interval needs to match that used in Mathematica to generate the
%interpolated vector field for this to export only smoothed vectors
disp('export loop start')
%formatting new data like the imported vectorgrid
newvectorgrid=vectorgrid;
for i=1:size(gridx,1)
    for j=1:size(gridx,2)
        for k=1:size(gridx,3)
            %identifying coordinate values
            xcoor=gridx(i,j,k);
            ycoor=gridy(i,j,k);
            zcoor=gridz(i,j,k);
            %finding where these values are located in vectorgrid with a
            %tolerance to keep to a reasonable decimal place
            logmatx= abs(vectorgrid(:,1) - xcoor) < 1e-6;
            logmaty= abs(vectorgrid(:,2) - ycoor) < 1e-6;
            logmatz= abs(vectorgrid(:,3) - zcoor) < 1e-6;
            %isolating the only row where all three appear
            rowvalue=logmatx & logmaty & logmatz;
            %inserting the new vector values into that row of newvectorgrid
            newvectorgrid(rowvalue,4)=smoothvectors{1}(i,j,k);
            newvectorgrid(rowvalue,5)=smoothvectors{2}(i,j,k);
            newvectorgrid(rowvalue,6)=smoothvectors{3}(i,j,k);
        end
    end
end
disp('exporting')
%exporting newvectorgrid with the smoothed vectors and desired filename
justfilename=strsplit(vectorfilename,'.');
dlmwrite(strjoin({justfilename{1},'_smoothed.csv'}),newvectorgrid,'delimiter',',')
```

Bibliography

[1] James S. Aber, Irene Marzolff, Johannes B. Ries, and Susan E.W. Aber. Principles of Photogrammetry. In *Small-Format Aerial Photography and UAS Imagery*, pages 19–38. Elsevier, 2019.

[2] Paul Abrams, Linda Cardozo, Magnus Fall, Derek Griffiths, Peter Rosier, Ulf Ulmsten, Philip Van Kerrebroeck, Arne Victor, and Alan Wein. The standardisation of terminology in lower urinary tract function: Report from the standardisation subcommittee of the International Continence Society. *Urology*, 61(1):37–49, 2003.

[3] Anne M Agur, Victor Ng-Thow-Hing, Kevin A Ball, Eugene Fiume, and Nancy Hunt McKee. Documentation and three-dimensional modelling of human soleus muscle architecture. *Clinical Anatomy*, 16(4):285–293, 2003.

[4] Michael E. Albo, Holly E. Richter, Linda Brubaker, Peggy Norton, Stephen R. Kraus, Philippe E. Zimmern, Toby C. Chai, Halina Zyczynski, Ananias C. Diokno, Sharon Tennstedt, Charles Nager, L. Keith Lloyd, Marypat Fitzgerald, Gary E. Lemack, Harry W. Johnson, Wendy Leng, Veronica Mallett, Anne M. Stoddard, Shawn Menefee, R. Edward Varner, Kimberly Kenton, Pam Moalli, Larry Sirls, Kimberly J. Dandreo, John W. Kusek, Leroy M. Nyberg, William Steers, A. Diokno, S. Khandwala, Linda Brubaker, M. Fitzgerald, Holly E. Richter, L. Keith Lloyd, M. Albo, Charles Nager, Harry W. Johnson, H. M. Zyczynski, Wendy Leng, P. Zimmern, G. Lemack, S. Kraus, T. Rozanski, Peggy Norton, L. Kerr, Sharon Tennstedt, A. Stoddard, D. Chang, John W. Kusek, Leroy M. Nyberg, A. M. Weber, R. S. Ashford, J. Baker, D. Borello-France, K. L. Burgio, S. Chiang, A. Dabbous, P. S. Goode, L. N. Hammontree, Kimberly Kenton, D. Lesser, K. Luber, E. Lukacz, A. Markland, Shawn Menefee, Pam Moalli, K. Peters, E. Sagan, J. Schaffer, A. Simsiman, Larry Sirls, R. Starr, R. Edward Varner, R. Bradt, K. Debes, R. Dinh, J. Gruss, L. Hall, A. Howell, K. Jesse, D. L. Kalinoski, K. Koches, B. Leemon, K. Mislanovich, S. O'Meara, J. Parent, N. Pope, C. Prather, T. Rogers, S. Sluder, M. Tulke, Kimberly J. Dandreo, C. J. Leifer, S. McDermott, A. Stoddard, Sharon Tennstedt, L. Tinsley, L. Wruck, Y. Xu, E. A. Gormley, P. Abrams, D. Bland, J. Q. Clemens, J. Connett, W. Henderson, D. Fenner, S. Kelsey, D. Myers, J. Mostwin, and B. Wadie. Burch colposuspension versus fascial sling to reduce urinary stress incontinence. *New England Journal of Medicine*, 356(21):2143–2155, 2007.

[5] Nadia Alkhouli, Jessica Mansfield, Ellen Green, James Bel, Beatrice Knight, Neil Liversedge, Ji Chung Tham, Richard Welbourn, Angela C. Shore, Katarina Kos, and

C. Peter Winlove. The mechanical properties of human adipose tissues and their relationships to the structure and composition of the extracellular matrix. *American Journal of Physiology - Endocrinology and Metabolism*, 305(12):1427–1435, 2013.

[6] Blake C. Alkire, Jeffrey R. Vincent, Christy Turlington Burns, Ian S. Metzler, Paul E. Farmer, and John G. Meara. Obstructed labor and caesarean delivery: the cost and benefit of surgical intervention. *PloS one*, 7:e34595, 2012.

[7] V Allen. Maternal morbidity associated with cesarean delivery without labor compared with spontaneous onset of labor at term. *Obstetrics Gynecology*, 102(3):477–482, 2003.

[8] Marianna Alperin, Mark Cook, Lori J. Tuttle, Mary C. Esparza, and Richard L. Lieber. Impact of vaginal parity and aging on the architectural design of pelvic floor muscles. *American Journal of Obstetrics and Gynecology*, 215(3):312.e1–312.e9, 2016.

[9] Marianna Alperin, Mark Cook, Lori J. Tuttle, Mary C. Esparza, and Richard L. Lieber. Impact of vaginal parity and aging on the architectural design of pelvic floor muscles. *American Journal of Obstetrics and Gynecology*, 215:312.e1–312.e9, 2016.

[10] Marianna Alperin, Timothy Kaddis, Rajeswari Pichika, Mary C. Esparza, and Richard L. Lieber. Pregnancy-induced adaptations in intramuscular extracellular matrix of rat pelvic floor muscles. *American Journal of Obstetrics and Gynecology*, 215(2):210.e1–210.e7, 2016.

[11] Marianna Alperin, Danielle M. Lawley, Mary C. Esparza, and Richard L. Lieber. Pregnancy-induced adaptations in the intrinsic structure of rat pelvic floor muscles. *American Journal of Obstetrics and Gynecology*, 213(2):191.e1–191.e7, 2015.

[12] Olivier Ami, Jean Christophe Maran, Petra Gabor, Eric B Whitacre, Dominique Musset, Claude Dubray, Gérard Mage, and Louis Boyer. Three-dimensional magnetic resonance imaging of fetal head molding and brain shape changes during the second stage of labor. *PLoS ONE*, 14(5), 2019.

[13] Yoshitaka Aoki, Heidi W. Brown, Linda Brubaker, Jean Nicolas Cornu, J. Oliver Daly, and Rufus Cartwright. Urinary incontinence in women. *Nature Reviews Disease Primers*, 3(1):1–20, 2017.

[14] James A Ashton-Miller and John O.L. DeLancey. On the Biomechanics of Vaginal Birth and Common Sequelae. *Annual Review of Biomedical Engineering*, 11(1):163–176, 2009.

[15] James A. Ashton-Miller and John O.L. L DeLancey. Functional anatomy of the female pelvic floor. *Annals of the New York Academy of Sciences*, 1101(1):266–296, 2007.

[16] James A. Ashton-Miller, Denise Howard, and John O.L. DeLancey. The functional anatomy of the female pelvic floor and stress continence control system. *Scandinavian Journal of Urology and Nephrology, Supplement*, 35(207):1–7, 2001.

[17] E. A. Audenaert, C. Pattyn, G. Steenackers, J. De Roeck, D. Vandermeulen, and P. Claes. Statistical shape modeling of skeletal anatomy for sex discrimination: Their training size, sexual dimorphism, and asymmetry. *Frontiers in Bioengineering and Biotechnology*, 7:302, 2019.

[18] Adwoa Baah-Dwomoh, Marianna Alperin, Mark Cook, and Raffaella De Vita. Mechanical analysis of the uterosacral ligament: Swine vs. human. *Annals of Biomedical Engineering*, 46:2036–2047, 2018.

[19] Matthew D Barber and Christopher Maher. Epidemiology and outcome assessment of pelvic organ prolapse. *International urogynecology journal*, 24(11):1783–1790, 2013.

[20] William R. Barone, Rouzbeh Amini, Spandan Maiti, Pamela A. Moalli, and Steven D. Abramowitch. The impact of boundary conditions on surface curvature of polypropylene mesh in response to uniaxial loading. *Journal of Biomechanics*, 48(9):1566–1574, 2015.

[21] Dean C. Barratt, Carolyn S.K. Chan, Philip J. Edwards, Graeme P. Penney, Mike Slomczykowski, Timothy J. Carter, and David J. Hawkes. Instantiation and registration of statistical shape models of the femur and pelvis using 3D ultrasound imaging. *Medical Image Analysis*, 12(3):358–374, 2008.

[22] Mojtaba Barzegari, Bahman Vahidi, Mohammad Reza Safarinejad, and Mahtab Ebad. A computational analysis of the effect of supporting organs on predicted vesical pressure in stress urinary incontinence. *Medical and Biological Engineering and Computing*, 2020.

[23] Ines Becker, Stephanie J Woodley, and Mark D Stringer. The adult human pubic symphysis: a systematic review. *Journal of anatomy*, 217(5):475–487, 2010.

[24] Yoav Benjamini and Yosef Hochberg. Controlling the False Discovery Rate: A Practical and Powerful Approach to Multiple Testing. *Journal of the Royal Statistical Society: Series B (Methodological)*, 57(1):289–300, 1995.

[25] Julie Bennington, James Koudy Williams, and Karl Erik Andersson. New concepts in regenerative medicine approaches to the treatment of female stress urinary incontinence. *Current Opinion in Urology*, 29(4):380–384, 2019.

[26] Philipp Berens. CircStat: Circular Statistics Toolbox (Directional Statistics), 2020.

[27] Alexander A Berger, Steven Abramowitch, and Pamela A Moalli. 3d vascular anatomy of the presacral space: impact of age and adiposity. *International urogynecology journal*, 30(3):401–407, 2019.

[28] Cornelia Betschart, Jinyong Kim, Janis M. Miller, James A. Ashton-Miller, and John O. L. DeLancey. Comparison of muscle fiber directions between different levator ani muscle subdivisions: In vivo MRI measurements in women. *International Urogynecology Journal and Pelvic Floor Dysfunction*, 25(9):1263–1268, 2014.

[29] Adil E. Bharucha, Alan R. Zinsmeister, G. Richard Locke, Barbara M. Seide, Kimberly McKeon, Cathy D. Schleck, and L. Joseph Melton. Risk Factors for Fecal Incontinence: A Population-based Study in Women. *The American Journal of Gastroenterology*, 101(6):1305–1312, 2006.

[30] Carolina Bibbo, Caroline E Rouse, David E Cantonwine, Sarah E Little, Thomas F. McElrath, and Julian N Robinson. Angle of Progression on Ultrasound in the Second Stage of Labor and Spontaneous Vaginal Delivery. *American Journal of Perinatology*, 35(4):413–420, 2018.

[31] Jeffrey E Bischoff, Yifei Dai, Casey Goodlett, Brad Davis, and Marc Bandi. Incorporating population-level variability in orthopedic biomechanical analysis: a review. *Journal of biomechanical engineering*, 136(2):021004, 2014.

[32] Kari Bø and Margaret Sherburn. Evaluation of female pelvic-floor muscle function and strength. *Physical Therapy*, 85(3):269–282, 2005.

[33] Alexandre Bône, Maxime Louis, Benoît Martin, and Stanley Durrleman. Deformetrica 4: An Open-Source Software for Statistical Shape Analysis. In *ShapeMI @ MICCAI 2018 - Workshop on Shape in Medical Imaging*, volume 11167 LNCS, pages 3–13, 2018.

[34] Victor Bonney. On Diurnal Incontinence of Urine in Women. *BJOG: An International Journal of Obstetrics Gynaecology*, 30(3):358–365, 1923.

[35] Sofia Brandão, Thuane Da Roza, Marco Parente, Isabel Ramos, Teresa Mascarenhas, and Renato M.Natal Jorge. Magnetic resonance imaging of the pelvic floor: From clinical to biomechanical imaging, 2013.

[36] Sofia Brandão, Marco Parente, Elisabete Silva, Thuane Da Roza, Teresa Mascarenhas, João Leitão, João Cunha, Renato Natal Jorge, and Rita Gouveia Nunes. Pubovisceralis Muscle Fiber Architecture Determination: Comparison Between Biomechanical Modeling and Diffusion Tensor Imaging. *Annals of Biomedical Engineering*, 45(5):1255–1265, 2017.

[37] L. Brubaker, H. E. Richter, P. A. Norton, M. Albo, H. M. Zyczynski, T. C. Chai, P. Zimmern, S. Kraus, L. Sirls, J. W. Kusek, A. Stoddard, S. Tennstedt, and E. Ann Gormley. 5-year continence rates, satisfaction and adverse events of burch urethropexy and fascial sling surgery for urinary incontinence. *Journal of Urology*, 187(4):1324–1330, 2012.

[38] Linda Brubaker, Peggy A Norton, Michael E Albo, Toby C Chai, Kimberly J Dandreo, Keith L Lloyd, Jerry L Lowder, Larry T Sirls, Gary E Lemack, Amy M Arisco, et al. Adverse events over two years after retropubic or transobturator midurethral sling surgery: findings from the trial of midurethral slings (tomus) study. *American journal of obstetrics and gynecology*, 205(5):498–e1, 2011.

[39] Elena Brunelli, Biancamaria Del Prete, Paolo Casadio, Gianluigi Pilu, and Aly Youssef. The dynamic change of the anteroposterior diameter of the levator hiatus under valsalva maneuver at term and labor outcome. *Neurourology and Urodynamics*, 39(8):2353–2360, 2020.

[40] Lindsey A. Burnett, Mark Cook, Sameer Shah, Ms Michelle Wong, Deborah M. Kado, and Marianna Alperin. Age-associated changes in the mechanical properties of human cadaveric pelvic floor muscles. *Journal of Biomechanics*, 98:109436, 2020.

[41] Lara J. Burrows, Leslie A. Meyn, and Anne M. Weber. Maternal Morbidity Associated With Vaginal Versus Cesarean Delivery. *Obstetrics Gynecology*, 103(5, Part 1):907–912, 2000.

[42] Romain Buttin, Florence Zara, Behzad Shariat, Tanneguy Redarce, and Gilles Grangé. Biomechanical simulation of the fetal descent without imposed theoretical trajectory. *Computer Methods and Programs in Biomedicine*, 111(2):389–401, 2013.

[43] J.Q. Q. Campbell and A.J. J. Petrella. Automated finite element modeling of the lumbar spine: Using a statistical shape model to generate a virtual population of models. *Journal of Biomechanics*, 49(13):2593–2599, 2016.

[44] Tatiana Catanzarite, Shannon Bremner, Caitlin L. Barlow, Laura Bou-Malham, Shawn O'Connor, and Marianna Alperin. Pelvic muscles' mechanical response to strains in the absence and presence of pregnancy-induced adaptations in a rat model. *American Journal of Obstetrics and Gynecology*, 218:512.e1–512.e9, 2018.

[45] Joshua Cates. *SHAPE MODELING AND ANALYSIS WITH ENTROPY-BASED PARTICLE SYSTEMS*. Doctor of philosophy, University of Utah, 2010.

[46] Joshua Cates, Thomas Fletcher, and Ross Whitaker. A Hypothesis Testing Framework for High-Dimensional Shape Models. *2nd MICCAI Workshop on Mathematical Foundations of Computational Anatomy*, pages 170–181, 2008.

[47] P. Chantereau, M. Brieu, M. Kammal, J. Farthmann, B. Gabriel, and M. Cosson. Mechanical properties of pelvic soft tissue of young women and impact of aging. *International Urogynecology Journal*, 25(11):1547–1553, 2014.

[48] Lyn S. Chitty, Douglas G. Altman, Annabel Henderson, and Stuart Campbell. Charts of fetal size: 2. Head measurements. *BJOG: An International Journal of Obstetrics & Gynaecology*, 101(1):35–43, 1994.

[49] James F. Clapp, Brian L. Seaward, Robert H. Sleamaker, and John Hiser. Maternal physiologic adaptations to early human pregnancy. *American Journal of Obstetrics and Gynecology*, 159(6):1456–1460, 1988.

[50] Kerstyn Comley and Norman A. Fleck. A micromechanical model for the Young's modulus of adipose tissue. *International Journal of Solids and Structures*, 47(21):2982–2990, 2010.

[51] Melissa J. Davidson, Poul M.F. Nielsen, Andrew J. Taberner, and Jennifer A. Kruger. Change in levator ani muscle stiffness and active force during pregnancy and postpartum. *International Urogynecology Journal*, pages 1–7, 2020.

[52] Rhodri Davies, Carole Twining, and Chris Taylor. *Statistical models of shape: Optimisation and evaluation*. Springer Science & Business Media, 2008.

[53] Alessandro De Benedictis, Erica Nocerino, Fabio Menna, Fabio Remondino, Mattia Barbareschi, Umberto Rozzanigo, Francesco Corsini, Emanuele Olivetti, Carlo Efisio Marras, Franco Chioffi, Paolo Avesani, and Silvio Sarubbo. Photogrammetry of the Human Brain: A Novel Method for Three-Dimensional Quantitative Exploration of the Structural Connectivity in Neurosurgery and Neurosciences. *World Neurosurgery*, 115:e279–e291, 2018.

[54] Allert M de Vries, Pieter L Venema, and John PFA Heesakkers. Midurethral support is also necessary for reflex closure of the urethra. *Neurourology and urodynamics*, 37(8):2965–2972, 2018.

[55] John O.L. DeLancey. Structural support of the urethra as it relates to stress urinary incontinence: The hammock hypothesis. *American Journal of Obstetrics and Gynecology*, 170(5):1713–1723, 1994.

[56] John OL DeLancey. Structural anatomy of the posterior pelvic compartment as it relates to rectocele. *American Journal of Obstetrics and Gynecology*, 180(4):815–823, 1999.

[57] John O.L L DeLancey, Rohna Kearney, Queena Chou, Steven Speights, and Shereen Binno. The appearance of levator ani muscle abnormalities in magnetic resonance images after vaginal delivery. *Obstetrics and Gynecology*, 101(1):46–53, 2003.

[58] H. P. Dietz and A. B. Steensma. The prevalence of major abnormalities of the levator ani in urogynaecological patients. *BJOG: An International Journal of Obstetrics and Gynaecology*, 113(2):225–230, 2006.

[59] Hans Peter Dietz, Ann Eldridge, Marlene Grace, and Barton Clarke. Does pregnancy affect pelvic organ mobility? *Australian and New Zealand Journal of Obstetrics and Gynaecology*, 44(6):517–520, 2004.

[60] HP Dietz, R Bhalla, V Chantarasorn, and KL Shek. Avulsion of the puborectalis muscle is associated with asymmetry of the levator hiatus. *Ultrasound in obstetrics & gynecology*, 37(6):723–726, 2011.

[61] Carmen Dolea and Carla Abouzahr. Global burden of obstructed labour in the year 2000, 2003.

[62] Ian L Dryden and Kanti V Mardia. *Statistical shape analysis: with applications in R*, volume 995. John Wiley & Sons, 2016.

[63] G Enhorning. Simultaneous recording of intravesical and intra-urethral pressure. A study on urethral closure in normal and stress incontinent women. *Acta Chirurgica Scandinavica*, 1, 1961.

[64] Andriy Fedorov, Reinhard Beichel, Jayashree Kalpathy-Cramer, Julien Finet, Jean Christophe Fillion-Robin, Sonia Pujol, Christian Bauer, Dominique Jennings, Fiona Fennessy, Milan Sonka, John Buatti, Stephen Aylward, James V Miller, Steve Pieper, and Ron Kikinis. 3D Slicer as an image computing platform for the Quantitative Imaging Network. *Magnetic Resonance Imaging*, 30(9):1323–1341, 2012.

[65] Tanis R Fenton and Jae H Kim. A systematic review and meta-analysis to revise the Fenton growth chart for preterm infants. *BMC Pediatrics*, 13(1):59, 2013.

[66] Andrew J. Feola, Jerry G. Myers, Julia Raykin, Lealem Mulugeta, Emily S. Nelson, Brian C. Samuels, and C. Ross Ethier. Finite element modeling of factors influencing optic nerve head deformation due to intracranial pressure. *Investigative Ophthalmology and Visual Science*, 57(4):1901–1911, 2016.

[67] James Fishbaugh, Stanley Durrleman, Marcel Prastawa, and Guido Gerig. Geodesic shape regression with multiple geometries and sparse parameters. *Medical Image Analysis*, 39:1–17, 2017.

[68] Abigail A Ford, Lynne Rogerson, June D Cody, Patricia Aluko, and Joseph A Ogah. Mid-urethral sling operations for stress urinary incontinence in women. *Cochrane Database of Systematic Reviews*, (7), 2017.

[69] M. A. R. Freeman. Strength of Biological Materials. *The Journal of Bone and Joint Surgery. British volume*, 1971.

[70] Boris Friedman. Conservative treatment for female stress urinary incontinence: simple, reasonable and safe. *Canadian Urological Association Journal*, 6(1):61, 2012.

[71] Y. C. Fung and Richard Skalak. Biomechanics: Mechanical Properties of Living Tissues. In *Journal of Biomechanical Engineering*, volume 103, pages 231–298. 1981.

[72] Damien Garcia. SMOOTHN, 2020.

[73] Hans Van Geelen, Donald Ostergard, and Peter Sand. A review of the impact of pregnancy and childbirth on pelvic floor function as assessed by objective measurement techniques. *International Urogynecology Journal*, 29:327–338, 2018.

[74] T Ghi, Am Youssef, F Martelli, F Bellussi, E Aiello, G Pilu, N Rizzo, T Frusca, D Arduini, and G Rizzo. Narrow subpubic arch angle is associated with higher risk of persistent occiput posterior position at delivery. *Ultrasound in Obstetrics & Gynecology*, 48(4):511–515, 2016.

[75] Tullio Ghi, Andrea Dall'Asta, Alice Suprani, Elisa Aiello, Andrea Musaro, Costanza Bosi, Giuseppe Pedrazzi, Ariane Kiener, Domenico Arduini, Tiziana Frusca, et al. Correlation between subpubic arch angle and mode of delivery in large-for-gestational-age fetuses. *Fetal diagnosis and therapy*, 44(3):221–227, 2018.

[76] Boloye Gomero. *Latin Hypercube Sampling and Partial Rank Correlation Coefficient Analysis Applied to an Optimal Control Problem.* Master's thesis, Unviersity of Tennessee, 2012.

[77] Mark T. Gordon, John O.L. DeLancey, Aaron Renfroe, Andrew Battles, and Luyun Chen. Development of anatomically based customizable three-dimensional finite-element model of pelvic floor support system: POP-Sim1.0. *Interface Focus*, 9(4):20190022, 2019.

[78] J. A. Gosling. Structure of the lower urinary tract and pelvic floor. *Clinics in Obstetrics and Gynaecology*, 12(2):285–294, 1985.

[79] Tuva K. Halle, Kjell Salvesen, and Ingrid Volløyhaug. Obstetric anal sphincter injury and incontinence 15–23 years after vaginal delivery. *Acta Obstetricia et Gynecologica Scandinavica*, 95(8):941–947, 2016.

[80] Victoria L. Handa, Joan L. Blomquist, Leise R. Knoepp, Kay A. Hoskey, Kelly C. McDermott, and Alvaro Muñoz. Pelvic Floor Disorders 5-10 Years After Vaginal or Cesarean Childbirth. *Obstetrics and gynecology*, 118(4):777, 2011.

[81] Victoria L Handa, Mark E Lockhart, Kimberly S Kenton, Catherine S Bradley, Julia R Fielding, Geoffrey W Cundiff, Caryl G Salomon, Christiane Hakim, Wen Ye, and Holly E Richter. Magnetic resonance assessment of pelvic anatomy and pelvic floor disorders after childbirth. *International Urogynecology Journal*, 20(2):133–139, 2009.

[82] Rosemary Harkin, Myra Fitzpatrick, P. Ronan O'Connell, and Colm O'Herlihy. Anal sphincter disruption at vaginal delivery: Is recurrence predictable? *European Journal of Obstetrics Gynecology and Reproductive Biology*, 109(2):149–152, 2003.

[83] Michael D. Harris, Manasi Datar, Ross T. Whitaker, Elizabeth R. Jurrus, Christopher L. Peters, and Andrew E. Anderson. Statistical shape modeling of cam femoroacetabular impingement. *Journal of Orthopaedic Research*, 31(10):1620–1626, 2013.

[84] Bernard T Haylen, Glenn McNALLY, Philippa Ramsay, Warwick Birrell, and Vanessa Logan. A standardised ultrasonic diagnosis and an accurate prevalence for the retroverted uterus in general gynaecology patients. *Australian and New Zealand journal of obstetrics and gynaecology*, 47(4):326–328, 2007.

[85] Sender Herschorn. Female pelvic floor anatomy: the pelvic floor, supporting structures, and pelvic organs. *Reviews in urology*, 6 Suppl 5(3):S2–S10, 2004.

[86] Barbara L. Hoffman, John O. Schorge, Karen D. Bradshaw, Lisa M. Halvorson, Joseph I. Schaffer, and Marlene M. Corton, editors. *Williams Gynecology*. McGraw-Hill Education, 3 edition, 2016.

[87] Yvonne Hsu, Aimee Summers, Hero K. Hussain, Kenneth E. Guire, and John O L Delancey. Levator plate angle in women with pelvic organ prolapse compared to women with normal support using dynamic MR imaging. *American Journal of Obstetrics and Gynecology*, 194(5):1427–1433, 2006.

[88] Arent B. Huisman. Aspects on the anatomy of the female urethra with special relation to urinary continence. *Contributions to Gynecology and Obstetrics*, VOL. 10:1–31, 1983.

[89] Magdalena Jansova, Vladimir Kalis, Zdenek Rusavy, Robert Zemcik, Libor Lobovsky, and Katariina Laine. Modeling manual perineal protection during vaginal delivery. *International Urogynecology Journal*, 25(1):65–71, 2014.

[90] T. N.A. Jeffcoate and H. Roberts. Observations on stress incontinence of urine. *American journal of obstetrics and gynecology*, 64(4):721–738, 1952.

[91] J Eric Jelovsek, Christopher Maher, and Matthew D Barber. Pelvic organ prolapse. *The Lancet*, 369(9566):1027–1038, 2007.

[92] Dejun Jing, James A. Ashton-Miller, and John O.L. L DeLancey. A subject-specific anisotropic visco-hyperelastic finite element model of female pelvic floor stress and strain during the second stage of labor. *Journal of Biomechanics*, 45(3):455–460, 2012.

[93] U Kalkan, T Yoldemir, ES Ozyurek, and A Daniilidis. Native tissue repair versus mesh repair in pelvic organ prolapse surgery. *Climacteric*, 20(6):510–517, 2017.

[94] I Kamisan Atan, B Gerges, K. L. Shek, and H. P. Dietz. The association between vaginal parity and hiatal dimensions: A retrospective observational study in a tertiary urogynaecological centre. *BJOG: An International Journal of Obstetrics and Gynaecology*, 122(6):867–872, 2015.

[95] Rohna Kearney, Raja Sawhney, and John O.L. L DeLancey. Levator ani muscle anatomy evaluated by origin-insertion pairs. *Obstetrics and gynecology*, 104(1):168–73, 2004.

[96] Howard A Kelly and William M Dumm. Urinary incontinence in women, without manifest injury to the bladder. *International Urogynecology Journal*, 9(3):158–164, 1998.

[97] David G Kendall. The diffusion of shape. *Advances in applied probability*, 9(3):428–430, 1977.

[98] Maurice G Kendall. Partial rank correlation. *Biometrika*, 32(3/4):277–283, 1942.

[99] Kimberly Kenton, Anne M. Stoddard, Halina Zyczynski, Michael Albo, Leslie Rickey, Peggy Norton, Clifford Wai, Stephen R. Kraus, Larry T. Sirls, John W. Kusek, Heather J. Litman, Robert P. Chang, and Holly E. Richter. 5-Year Longitudinal Followup after Retropubic and Transobturator Mid Urethral Slings. *Journal of Urology*, 193(1):203–210, 2015.

[100] Ilknur Kepenekci, Betul Keskinkilic, Filiz Akinsu, Petek Cakir, Atilla Halil Elhan, Ayhan Bulent Erkek, and Mehmet Ayhan Kuzu. Prevalence of pelvic floor disorders in the female population and the impact of age, mode of delivery, and parity. *Diseases of the Colon and Rectum*, 54(1):85–94, 2011.

[101] Beomkeun Kim, Seong Beom Lee, Jayone Lee, Sehyun Cho, Hyungmin Park, Sanghoon Yeom, and Sung Han Park. A comparison among neo-hookean model, mooney-rivlin model, and ogden model for chloroprene rubber. *International Journal of Precision Engineering and Manufacturing*, 13(5):759–764, 2012.

[102] Petra Kochová, Robert Cimrman, Magdalena Jansová, Květoslava Michalová, Vladimir Kalis, Tereza Kubíková, and Zbyněk Tonar. The histological microstruc-

ture and in vitro mechanical properties of the human female postmenopausal perineal body. *Menopause*, 2019.

[103] Toril Kolås, Ola D. Saugstad, Anne K. Daltveit, Stein T. Nilsen, and Pål Øian. Planned cesarean versus planned vaginal delivery at term: Comparison of newborn infant outcomes. *American Journal of Obstetrics and Gynecology*, 195(6):1538–1543, 2006.

[104] Bouchra Koullali, Andrea R Westervelt, Kristin M Myers, and Michael D House. Prevention of preterm birth: Novel interventions for the cervix. In *Seminars in perinatology*, volume 41, pages 505–510. Elsevier, 2017.

[105] Alicia S. Kriete, Katsiaryna Prudnikova, and Michele S. Marcolongo. Modulating physical properties of porcine urethra with injection of novel biomimetic proteoglycans ex vivo. *Interface Focus*, 2019.

[106] Kindra A. Larson, Aisha Yousuf, Christina Lewicky-Gaupp, Dee E. Fenner, and John O.L. L Delancey. Perineal body anatomy in living women: 3-dimensional analysis using thin-slice magnetic resonance imaging. *American Journal of Obstetrics and Gynecology*, 203(5):494.e15–494.e21, 2010.

[107] J. O.N. Lawson. Pelvic anatomy. I. Pelvic floor muscles. *Annals of the Royal College of Surgeons of England*, 54(5):244–252, 1974.

[108] Su-Lin Lee, Emile Tan, Vik Khullar, Wladyslaw Gedroyc, Ara Darzi, and Guang-Zhong Yang. Physical-based statistical shape modeling of the levator ani. *IEEE transactions on medical imaging*, 28(6):926–936, 2009.

[109] R Levy, S Zaks, A Ben-Arie, S Perlman, Z Hagay, and E Vaisbuch. Can angle of progression in pregnant women before onset of labor predict mode of delivery? *Ultrasound in Obstetrics and Gynecology*, 40(3):332–337, 2012.

[110] X Li, J A Kruger, M P Nash, and P M F Nielsen. Effects of nonlinear muscle elasticity on pelvic floor mechanics during vaginal childbirth. *Journal of Biomechanical Engineering*, 132(11), 2010.

[111] Xinshan Li, Jennifer A. Kruger, Martyn P. Nash, and Poul M. F. Nielsen. Anisotropic effects of the levator ani muscle during childbirth. *Biomechanics and Modeling in Mechanobiology*, 10(4):485–494, 2011.

[112] Xinshan Li, Jennifer A. Kruger, Martyn P. Nash, and Poul M.F. Nielsen. Modeling childbirth: Elucidating the mechanisms of labor. *Wiley Interdisciplinary Reviews: Systems Biology and Medicine*, 2(4):460–470, 2010.

[113] Kuo-Cheng Lien, Brian Mooney, John O. L. DeLancey, and James A. Ashton-Miller. Levator Ani Muscle Stretch Induced by Simulated Vaginal Birth. *Obstetrics & Gynecology*, 103(1):31–40, 2004.

[114] Shiliang Liu, Robert M Liston, K S Joseph, Maureen Heaman, Reg Sauve, Michael S Kramer, and for the Maternal Health Study Group of the Canadian Perinatal Surveillance Maternal Health Study Group of the Canadian Perinatal Surveillance System. Maternal mortality and severe morbidity associated with low-risk planned cesarean delivery versus planned vaginal delivery at term. *CMAJ : Canadian Medical Association journal = journal de l'Association medicale canadienne*, 176(4):455–60, 2007.

[115] LæGe Gunnar Lose. Simultaneous recording of pressure and cross-sectional area in the female urethra: A study of urethral closure function in healthy and stress incontinent women. *Neurourology and Urodynamics*, 11(2):55–89, 1992.

[116] Jerry L. Lowder, Kristen M. Debes, Daniel K. Moon, Nancy Howden, Steven D. Abramowitch, and Pamela A. Moalli. Biomechanical adaptations of the rat vagina and supportive tissues in pregnancy to accommodate delivery. *Obstetrics and Gynecology*, 109(1):136–143, 2007.

[117] Lula O. Lubchenco, Charlotte Hansman, and Edith Boyd. Intrauterine growth in length and head circumference as estimated from live births at gestational ages from 26 to 42 weeks. *Pediatrics*, 37(3):403–8, 1966.

[118] Karl M Luber. The definition, prevalence, and risk factors for stress urinary incontinence. *Reviews in urology*, 6 Suppl 3(Suppl 3):S3–9, 2004.

[119] Jonathan Mant, Rosemary Painter, and Martin Vessey. Epidemiology of genital prolapse: Observations from the oxford family planning association study. *BJOG: An International Journal of Obstetrics and Gynaecology*, 104(5):579–585, 1997.

[120] Liam Martin, Megan Routzong, Pamela Moalli, Ghazaleh Rostaminia, and Steven Abramowitch. Shape changes in midsagittal sacrum and coccyx shape during pregnancy and after delivery: Main research article. *Authorea Preprints*, 2021.

[121] Liam C. Martin, Megan R. Routzong, Pamela A. Moalli, and Steven D. Abramowitch. Novel Application of a Corresponding Point Algorithm for Unbiased Smoothing. In *17th International Symposium on Computer Methods in Biomechanics and Biomedical Engineering*, 2021.

[122] Jean-Marc Martinez, Yann Collette, Michael Baudin, and Maria Christopoulou. pyDOE, 2017.

[123] Pedro A.L.S. Martins, Agnaldo Lopes Silva Filho, Andrea Moura Rodrigues Mac Iel Fonseca, Agostinho Santos, Liliana Santos, Teresa Mascarenhas, Renato M.Natal Jorge, and António J.M. Ferreira. Uniaxial mechanical behavior of the human female bladder. *International Urogynecology Journal*, 22(8):991–995, 2011.

[124] John H Mcdonald. *Handbook of Biological Statistics*. Sparky House Publishing, Baltimore, 2 edition, 2009.

[125] Sebastian Meller and Willi A Kalender. Building a statistical shape model of the pelvis. *International Congress Series*, 1268:561–566, 2004.

[126] Hafsa U. Memon and Victoria L. Handa. Vaginal childbirth and pelvic floor disorders, 2013.

[127] Lina Michala, Louise Strawbridge, Maligaye Bikoo, Alfred S. Cutner, and Sarah M. Creighton. Lower urinary tract symptoms in women with vaginal agenesis. *International Urogynecology Journal and Pelvic Floor Dysfunction*, 24(3):425–429, 2013.

[128] Paul S. Milley and David H. Nichols. The relationship between the pubo-urethral ligaments and the urogenital diaphragm in the human female. *The Anatomical Record*, 170(3):281–283, 1971.

[129] Saori Morino, Mika Ishihara, Fumiko Umezaki, Hiroko Hatanaka, Mamoru Yamashita, and Tomoki Aoyama. Pelvic alignment changes during the perinatal period. *PloS one*, 14:e0223776, 2019.

[130] Rafael Mendes Moroni, Pedro Sergio Magnani, Jorge Milhem Haddad, Rodrigo de Aquino Castro, and Luiz Gustavo Oliveira Brito. Conservative treatment of stress urinary incontinence: a systematic review with meta-analysis of randomized controlled trials. *Revista Brasileira de Ginecologia e Obstetrícia*, 38(2):97–111, 2016.

[131] S. R. MUELLNER. The physiology of micturition. *The Journal of urology*, 65(5):805–810, 1951.

[132] Bert Müller, Javier Ratia Garcia, Florian Marti, and Thomas Leippold. MECHANICAL PROPERTIES OF URETHRAL TISSUE. *Journal of Biomechanics*, 41:S61, 2008.

[133] Kristin M Myers, Helen Feltovich, Edoardo Mazza, Joy Vink, Michael Bajka, Ronald J Wapner, Timothy J Hall, and Michael House. The mechanical role of the cervix in pregnancy. *Journal of biomechanics*, 48(9):1511–1523, 2015.

[134] Arturo Nicola Natali, Emanuele Luigi Carniel, Alessandro Frigo, Piero Giovanni Pavan, Silvia Todros, Paola Pachera, Chiara Giulia Fontanella, Alessandro Rubini, Laura Cavicchioli, Yochai Avital, and Giulia Maria De Benedictis. Experimental investigation of the biomechanics of urethral tissues and structures. *Experimental Physiology*, 101(5):641–656, 2016.

[135] Ingrid Nygaard. Prevalence of Symptomatic Pelvic Floor Disorders in US Women. *JAMA*, 300(11):1311, 2008.

[136] Ingrid E Nygaard, Rebecca McCreery, Linda Brubaker, AnnaMarie Connolly, Geoff Cundiff, Anne M Weber, and Halina Zyczynski. Abdominal sacrocolpopexy: a comprehensive review. *Obstetrics & Gynecology*, 104(4):805–823, 2004.

[137] A. L. O'Boyle, J. D. O'Boyle, R. E. Ricks, T. H. Patience, B. Calhoun, and G. Davis. The natural history of pelvic organ support in pregnancy. *International Urogynecology Journal*, 14(1):46–49, 2003.

[138] Amy L. O'Boyle, John D. O'Boyle, Byron Calhoun, and Gary D. Davis. Pelvic organ support in pregnancy and postpartum. *International Urogynecology Journal*, 16(1):69–72, 2005.

[139] Thomas M. Oelrich. The striated urogenital sphincter muscle in the female. *The Anatomical Record*, 205(2):223–232, 1983.

[140] Sallie Oliphant, Timothy Canavan, Stacy Palcsey, Leslie Meyn, and Pamela Moalli. Pregnancy and parturition negatively impact vaginal angle and alter expression of vaginal mmp-9. *American Journal of Obstetrics and Gynecology*, 218:242.e1–242.e7, 2018.

[141] Dulce A Oliveira, Marco P L Parente, Begoña Calvo, Teresa Mascarenhas, and Renato M Natal. A biomechanical analysis on the impact of episiotomy during childbirth. *Biomechanics and Modeling in Mechanobiology*, 15(6):1523–1534, 2016.

[142] Dulce A. Oliveira, Maria Elisabete T. Silva, Maria Vila Pouca, Marco P. L. Parente, Teresa Mascarenhas, and Renato M. Natal Jorge. Biomechanical Simulation of Vaginal Childbirth: The Colors of the Pelvic Floor Muscles. In *Computational Biomechanics for Medicine*, pages 1–17. Springer International Publishing, Cham, 2020.

[143] M. P.L. Parente, R. M.Natal Jorge, T. Mascarenhas, A. A. Fernandes, and J. A.C. Martins. Deformation of the pelvic floor muscles during a vaginal delivery. *International Urogynecology Journal*, 19(1):65–71, 2008.

[144] Mihaela Pavličev, Roberto Romero, and Philipp Mitteroecker. Evolution of the human pelvis and obstructed labor: new explanations of an old obstetrical dilemma. *American Journal of Obstetrics and Gynecology*, 222:3–16, 2020.

[145] Yun Peng, Rose Khavari, Nissrine A. Nakib, Julie N. Stewart, Timothy B. Boone, and Yingchun Zhang. The single-incision sling to treat female stress urinary incontinence: A dynamic computational study of outcomes and risk factors. *Journal of Biomechanical Engineering*, 137(9), 2015.

[146] Peter E.Papa Petros and Ulf I. Ulmsten. AN INTEGRAL THEORY OF FEMALE URINARY INCONTINENCE: Experimental and clinical considerations. *Acta Obstetricia et Gynecologica Scandinavica*, 69(153 S):7–31, 1990.

[147] Jennifer Podulka, Elizabeth Stranges, and Claudia Steiner. Hospitalizations Related to Childbirth, 2008. Technical report, 2011.

[148] P David Polly. Geometric Morphometrics for Mathematica, 2019.

[149] Lieschen H Quiroz, Alvaro Muñoz, Stuart H Shippey, Robert E Gutman, and Victoria L Handa. Vaginal parity and pelvic organ prolapse. *The Journal of reproductive medicine*, 55(3-4):93, 2010.

[150] David D. Rahn, Matthew D. Ruff, Spencer A. Brown, Harry F. Tibbals, and R. Ann Word. Biomechanical properties of the vaginal wall: effect of pregnancy, elastic fiber deficiency, and pelvic organ prolapse. *American Journal of Obstetrics and Gynecology*, 198(5):590.e1–590.e6, 2008.

[151] G. Venugopala Rao, Chrystèle Rubod, Mathias Brieu, Naresh Bhatnagara, and Michel Cosson. Experiments and finite element modelling for the study of prolapse in the pelvic floor system. *Computer Methods in Biomechanics and Biomedical Engineering*, 13(3):349–357, 2010.

[152] Gary C. Reid, John O.L. DeLancey, Michael P. Hopkins, James A. Roberts, and George W. Morley. Urinary incontinence following radical vulvectomy. *Obstetrics and Gynecology*, 75(5):852–858, 1990.

[153] Anke Reitter, Betty Anne Daviss, Andrew Bisits, Astrid Schollenberger, Thomas Vogl, Eva Herrmann, Frank Louwen, and Stephan Zangos. Does pregnancy and/or shifting positions create more room in a woman's pelvis? *American Journal of Obstetrics and Gynecology*, 211:662.e1–662.e9, 2014.

[154] Monica L Richardson and Eric R Sokol. A cost-effectiveness analysis of conservative versus surgical management for the initial treatment of stress urinary incontinence. *American journal of obstetrics and gynecology*, 211(5):565–e1, 2014.

[155] Holly E. Richter, Michael E. Albo, Halina M. Zyczynski, Kimberly Kenton, Peggy A. Norton, Larry T. Sirls, Stephen R. Kraus, Toby C. Chai, Gary E. Lemack, Kimberly J. Dandreo, R. Edward Varner, Shawn Menefee, Chiara Ghetti, Linda Brubaker, Ingrid Nygaard, Salil Khandwala, Thomas A. Rozanski, Harry Johnson, Joseph Schaffer, Anne M. Stoddard, Robert L. Holley, Charles W. Nager, Pamela Moalli, Elizabeth Mueller, Amy M. Arisco, Marlene Corton, Sharon Tennstedt, T. Debuene Chang, E. Ann Gormley, and Heather J. Litman. Retropubic versus Transobturator Midurethral Slings for Stress Incontinence. *New England Journal of Medicine*, 362(22):2066–2076, 2010.

[156] Géraldine Rivaux, Chrystèle Rubod, Bruno Dedet, Mathias Brieu, Boris Gabriel, and Michel Cosson. Comparative analysis of pelvic ligaments: A biomechanics study. *International Urogynecology Journal and Pelvic Floor Dysfunction*, 24(1):135–139, 2013.

[157] Sara Roccabianca and Tamara Reid Bush. Understanding the mechanics of the bladder through experiments and theoretical models: Where we started and where we are heading. *Technology*, 04(01):30–41, 2016.

[158] F. James Rohlf and Dennis Slice. Extensions of the procrustes method for the optimal superimposition of landmarks. *Systematic Zoology*, 39(1):40–59, 1990.

[159] Peter F.W.M. Rosier, Werner Schaefer, Gunnar Lose, Howard B. Goldman, Michael Guralnick, Sharon Eustice, Tamara Dickinson, and Hashim Hashim. Interna-

tional continence society good urodynamic practices and terms 2016: Urodynamics, uroflowmetry, cystometry, and pressure-flow study. *Neurourology and Urodynamics*, 36(5):1243–1260, 2017.

[160] Ghazaleh Rostaminia, Steven Abramowitch, Cecilia Chang, and Roger P. Goldberg. Descent and hypermobility of the rectum in women with obstructed defecation symptoms. *International Urogynecology Journal*, 31(2):337–349, 2020.

[161] Ghazaleh Rostaminia, Dena White, Aparna Hegde, Lieschen H. Quiroz, G. Willy Davila, and S. Abbas Shobeiri. Levator ani deficiency and pelvic organ prolapse severity. *Obstetrics and Gynecology*, 121(5):1017–1024, 2013.

[162] Ghazaleh Rostaminia, Dena E. White, Lieschen H. Quiroz, and S. Abbas Shobeiri. Levator plate descent correlates with levator ani muscle deficiency. *Neurourology and Urodynamics*, 34(1):55–59, 2015.

[163] Pascal Rousset, Vincent Delmas, Jean Noël Buy, Alain Rahmouni, Dominique Vadrot, and Jean François Deux. In vivo visualization of the levator ani muscle subdivisions using MR fiber tractography with diffusion tensor imaging. *Journal of Anatomy*, 221(3):221–228, 2012.

[164] Megan R. Routzong, Cecilia Chang, Roger P. Goldberg, Steven D. Abramowitch, and Ghazaleh Rostaminia. Urethral support in female urinary continence part 1: dynamic measurements of urethral shape and motion. *International Urogynecology Journal*, 2021.

[165] Megan R. Routzong, Mark S. Cook, William Barone, Steven D. Abramowitch, and Marianna Alperin. Novel Application of Photogrammetry to Quantify Fascicle Orientations of Female Cadaveric Pelvic Floor Muscles. *Annals of Biomedical Engineering*, pages 1–12, 2021.

[166] Megan R. Routzong, Liam C. Martin, Ghazaleh Rostaminia, and Steven Abramowitch. Urethral support in female urinary continence part 2: a computational, biomechanical analysis of Valsalva. *International Urogynecology Journal*, 2021.

[167] Megan R. Routzong, Pamela A. Moalli, Spandan Maiti, Raffaella De Vita, and Steven D. Abramowitch. Novel simulations to determine the impact of superficial perineal structures on vaginal delivery. *Interface Focus*, 9(4):20190011, 2019.

[168] Megan R. Routzong, Ghazaleh Rostaminia, Shaniel T. Bowen, Roger P. Goldberg, and Steven D. Abramowitch. Statistical shape modeling of the pelvic floor to evaluate women with obstructed defecation symptoms. *Computer Methods in Biomechanics and Biomedical Engineering*, 24(2):122–130, sep 2021.

[169] Megan R. Routzong, Ghazaleh Rostaminia, Pamela A. Moalli, and Steven D. Abramowitch. Pelvic floor shape variations during pregnancy and after vaginal delivery. *Computer Methods and Programs in Biomedicine*, 194:105516, 2020.

[170] Chrystle Rubod, Mathias Brieu, Michel Cosson, Géraldine Rivaux, Jean Charles Clay, Laurent De Landsheere, and Boris Gabriel. Biomechanical properties of human pelvic organs. *Urology*, 79(4):968.e17–968.e22, 2012.

[171] J P S Ferreira, M P L Parente, M Jabareen, R M Natal Jorge, and B J P S Ferreira. A general framework for the numerical implementation of anisotropic hyperelastic material models including non-local damage. *Biomechanics and Modeling in Mechanobiology*, 16:1119–1140, 2017.

[172] Marie-Louise Saaby. The urethral closure function in continent and stress urinary incontinent women assessed by urethral pressure reflectometry. *Neurourology and Urodynamics*, 31(8):1231–5, 2012.

[173] Ellen Samuelsson, Lars Ladfors, B. G. Lindblom, and Henrik Hagberg. A prospective observational study on tears during vaginal delivery: Occurrences and risk factors. *Acta Obstetricia et Gynecologica Scandinavica*, 81(1):44–49, 2002.

[174] Maurizio Serati, Maria Carmela Di Dedda, Giorgio Bogani, Paola Sorice, Antonella Cromi, Stefano Uccella, Martina Lapenna, Marco Soligo, and Fabio Ghezzi. Position in the second stage of labour and de novo onset of post-partum urinary incontinence. *International Urogynecology Journal*, 27(2):281–286, 2016.

[175] Ali Ahmed Shafik, Olfat El Sibai, Ali Ahmed Shafik, and Ismail A. Shafik. A novel concept for the surgical anatomy of the perineal body. *Diseases of the Colon and Rectum*, 50(12):2120–2125, 2007.

[176] Ka Lai Shek, Jenny Kruger, and Hans Peter Dietz. The effect of pregnancy on hiatal dimensions and urethral mobility: An observational study. *International Urogynecology Journal*, 23(11):1561–1567, 2012.

[177] Kelsey L Shnaekel, Everett F Magann, and Shahryar Ahmadi. Pubic symphysis rupture and separation during pregnancy. *Obstetrical & gynecological survey*, 70(11):713–718, 2015.

[178] S. Abbas Shobeiri, Ralph R. Chesson, and Raymond F. Gasser. The internal innervation and morphology of the human female levator ani muscle. *American Journal of Obstetrics and Gynecology*, 199(6):686.e1–686.e6, 2008.

[179] F Siafarikas, J. Stær-Jensen, G Hilde, K Bø, and M Ellström Engh. The levator ani muscle during pregnancy and major levator ani muscle defects diagnosed postpartum: A three- and four-dimensional transperineal ultrasound study. *BJOG: An International Journal of Obstetrics and Gynaecology*, 122(8):1083–1091, 2015.

[180] Franziska Siafarikas, Jette Stær-Jensen, Gunvor Hilde, Kari Bø, and Marie Ellström Engh. Levator hiatus dimensions in late pregnancy and the process of labor: A 3- and 4-dimensional transperineal ultrasound study. *American Journal of Obstetrics and Gynecology*, 210(5):484.e1–484.e7, 2014.

[181] M.E.T. E T Silva, D.A. A Oliveira, T.H. H Roza, S. Brandão, M.P.L. P L Parente, T. Mascarenhas, and R.M. M Natal Jorge. Study on the influence of the fetus head molding on the biomechanical behavior of the pelvic floor muscles, during vaginal delivery. *Journal of Biomechanics*, 48(9):1600–1605, 2015.

[182] Tomasz Sipko, Dominika Grygier, Katarzyna Barczyk, and Gabriela Eliasz. The Occurrence of Strain Symptoms in the Lumbosacral Region and Pelvis During Pregnancy and After Childbirth. *Journal of Manipulative and Physiological Therapeutics*, 33(5):370–377, 2010.

[183] Wilbur C. Smith. The levator ani muscle; Its structure in man, and its comparative relationships. *The Anatomical Record*, 26(3):175–203, 1923.

[184] Thomas Spirka, Kimberly Kenton, Linda Brubaker, and Margot S. Damaser. Effect of material properties on predicted vesical pressure during a cough in a simplified computational model of the bladder and urethra. *Annals of Biomedical Engineering*, 41(1):185–194, 2013.

[185] Aleksandra Stankiewicz, Andrzej P. Wieczorek, Magdalena M. Wozniak, Michal Bogusiewicz, Konrad Futyma, Giulio A. Santoro, and Tomasz Rechberger. Comparison of accuracy of functional measurements of the urethra in transperineal vs. endovaginal ultrasound in incontinent women. *Pelviperineology*, 27(4):145–147, 2008.

[186] Tamara A. Stein and John O.L. DeLancey. Structure of the perineal membrane in females: Gross and microscopic anatomy. *Obstetrics and Gynecology*, 111(3):686–693, 2008.

[187] Merete Kolberg Tennfjord, Marie Ellström Engh, and Kari Bø. The influence of early exercise postpartum on pelvic floor muscle function and prevalence of pelvic floor dysfunction 12 months postpartum. *Physical therapy*, 100(9):1681–1689, 2020.

[188] David Thissen, Lynne Steinberg, and Daniel Kuang. Quick and Easy Implementation of the Benjamini-Hochberg Procedure for Controlling the False Positive Rate in Multiple Comparisons. *Journal of Educational and Behavioral Statistics*, 27(1):77–83, 2002.

[189] Paige V. Tracy, John O. DeLancey, and James A. Ashton-Miller. A Geometric Capacity–Demand Analysis of Maternal Levator Muscle Stretch Required for Vaginal Delivery. *Journal of Biomechanical Engineering*, 138(2):021001, 2016.

[190] Lori J. Tuttle, Olivia T. Nguyen, Mark S. Cook, Marianna Alperin, Sameer B. Shah, Samuel R. Ward, and Richard L. Lieber. Architectural design of the pelvic floor is consistent with muscle functional subspecialization. *International Urogynecology Journal and Pelvic Floor Dysfunction*, 25(2):205–212, 2014.

[191] G. A. Van Veelen, K. J. Schweitzer, and C. H. Van Der Vaart. Ultrasound imaging of the pelvic floor: Changes in anatomy during and after first pregnancy. *Ultrasound in Obstetrics and Gynecology*, 44(4):476–480, 2014.

[192] E. Versi. Incontinence in the climacteric. In *Clinical Obstetrics and Gynecology*, volume 33, pages 392–398. Clin Obstet Gynecol, 1990.

[193] L Viktrup, G Lose, M Rolff, and K Barfoed. The symptom of stress incontinence caused by pregnancy or delivery in primiparas. *Obstetrics and gynecology*, 79(6):945–9, 1992.

[194] M.C.P. Vila Pouca, J.P.S. Ferreira, D.A. Oliveira, M.P.L. Parente, Teresa Mascarenhas, and R.M. Natal Jorge. On the effect of labour durations using an anisotropic visco-hyperelastic-damage approach to simulate vaginal deliveries. *Journal of the Mechanical Behavior of Biomedical Materials*, 88:120–126, 2018.

[195] Anne M Weber and Holly E Richter. Pelvic organ prolapse. *Obstetrics & Gynecology*, 106(3):615–634, 2005.

[196] Mirjam Weemhoff, Ka Lai Shek, and Hans P Dietz. Effects of age on levator function and morphometry of the levator hiatus in women with pelvic floor disorders. *International urogynecology journal*, 21(9):1137–1142, 2010.

[197] Paul R. Wolf, Bon A. Dewitt, and Benjamin E. Wilkinson. Development of Collinearity Condition Equations. In *Elements of Photogrammetry with Applications in GIS*. McGraw-Hill Education, 4 edition, 2014.

[198] Jennifer M Wu, Camille P Vaughan, Patricia S Goode, David T Redden, Kathryn L Burgio, Holly E Richter, and Alayne D Markland. Prevalence and trends of symptomatic pelvic floor disorders in U.S. women. *Obstetrics and gynecology*, 123(1):141–8, 2014.

[199] You Maria Wu, Natalia McInnes, and Yvonne Leong. Pelvic floor muscle training versus watchful waiting and pelvic floor disorders in postpartum women: a systematic review and meta-analysis. *Female pelvic medicine & reconstructive surgery*, 24(2):142–149, 2018.

[200] Moe Yamaguchi and Saori Morino. Comparison of pelvic alignment among never-pregnant women,pregnant women, and postpartum women (pelvic alignment and pregnancy). *Journal of Womens Health Care*, 05, 2016.

[201] Xiani Yan, Jennifer A. Kruger, Martyn P. Nash, and Poul M. F. Nielsen. A Quantitative Description of Pelvic Floor Muscle Fibre Organisation. In *Computational Biomechanics for Medicine*, pages 119–130. Springer New York, 2011.

[202] Ali Zifan, Marco Reisert, Shantanu Sinha, Melissa Ledgerwood-Lee, Esther Cory, Robert Sah, and Ravinder K. Mittal. Connectivity of the Superficial Muscles of the Human Perineum: A Diffusion Tensor Imaging-Based Global Tractography Study. *Scientific Reports*, 8(1):17867, 2018.

[203] Frank M. Zijta, Martijn Froeling, Aart J. Nederveen, and Jaap Stoker. Diffusion tensor imaging and fiber tractography for the visualization of the female pelvic floor, 2013.

[204] Frederick Zitrell. CircHist- circular / polar / angle histogram, 2020.